Polarization-optimized Heterostructures with Quaternary AlInGaN Layers for Novel Group III Nitride Devices

Von der Fakultät für Elektrotechnik und Informationstechnik
der Rheinisch-Westfälischen Technischen Hochschule Aachen
zur Erlangung des akademischen Grades eines Doktors
der Naturwissenschaften genehmigte Dissertation

vorgelegt von

Dipl.-Phys. Benjamin Reuters
aus Würselen, Deutschland

Berichter: Univ.-Prof. Dr.-Ing. Andrei Vescan
Univ.-Prof. Dr. rer. nat. Ferdinand Scholz

Tag der mündlichen Prüfung: 23.10.2015

Diese Dissertation ist auf den Internetseiten der Hochschulbibliothek online verfügbar.

Contents

1. Introduction **1**

2. Fundamentals of group III nitrides **5**

2.1. Crystal structure and material properties 5
2.2. Elastic deformation in nitride-based heterostructures 9
2.3. Bandgaps of nitride alloys 10
2.4. Polarization effects 13
2.4.1. Spontaneous polarization 13
2.4.2. Piezoelectric polarization 14
2.4.3. Two-dimensional carrier gases 14
2.5. Heterostructure field effect transistors 17
2.6. The quaternary approach 19

3. Epitaxy and characterization methods **23**

3.1. Metal organic vapor phase epitaxy 23
3.1.1. Basic principle and precursors 24
3.1.2. Foreign substrates for GaN epitaxy 26
3.2. X-ray diffraction 27
3.3. Rutherford backscattering spectroscopy 30

I. Growth and structural properties of quaternary AlInGaN **33**

4. Growth and structural properties of AlInGaN layers on GaN **35**

4.1. Buffer layer concept on sapphire 35
4.2. Growth challenges of AlInGaN 37
4.3. Composition range of AlInGaN layers grown on GaN 39
4.3.1. Reactor pressure 41
4.3.2. Growth surface temperature 42
4.3.3. Molar flow of metalorganic precursors 53

5. Growth and structural properties of AlInGaN on AlN 59
5.1. Experimental concept for the comparison of AlInGaN growth on AlN and GaN 59
5.1.1. Addition of Ga precursor to AlInN growth conditions 60
5.1.2. Variation of the growth surface temperature 62

II. Polarization engineering in nitride-based heterostructure field effect transistors with either n- or p-channels 65

6. HFET structures with AlInGaN barriers for 2DEG accumulation 67
6.1. Influence of growth surface temperature on 2DEG properties 67
6.2. Lowering the total polarization in AlInGaN 70
6.2.1. Comparison of 2DEG characterisctics 72
6.3. Fabrication of transistors in depletion and enhancement mode 74
6.3.1. Comparison of enhancement mode transistors 76
6.3.2. E-mode HFETs with lowered on-resistance by multi-layer barriers 77

7. HFET structures with AlInGaN backbarriers for 2DHG accumulation 81
7.1. Preface to Mg doping of GaN 81
7.2. p-channel HFET structures utilizing a 2DHG 84
7.2.1. Mg compensation doping 85
7.3. AlInGaN backbarrier composition 88
7.3.1. Electrical properties 92
7.3.2. p-Channel transistor performance 94

III. Light emitting diodes with polarization-engineered AlInGaN layers 99

8. Light emitting diodes with AlInGaN barrier layers 101
8.1. Internal electric fields 101
8.2. Structural properties of LEDs 102
8.3. Optical properties of LEDs 105

9. LED structures with reversed polarization utilizing a 2DHG 109
9.1. Preface to inversed p-n junctions 109
9.2. Fabrication of inversed LEDs 111
9.2.1. LED stack and its structural properties 111
9.2.2. Optical properties 113

10. Summary and outlook 117

References 121

Publications 159

List of figures 164

List of tables 171

List of abbreviations 173

Acknowledgements/Danksagung 177

Chapter 1

Introduction

Research on group III nitrides recently moved again into the focus of public attention, since the Nobel prize in physics 2014 has been awarded by the Royal Swedish Academy of Sciences to Isamu Akasaki, Hiroshi Amano and Shuji Nakamura

> "for the invention of efficient blue light-emitting diodes which has enabled bright and energy-saving white light sources" [1].

Light-emitting devices in the visible and UV spectrum, i.e. light emitting diodes (LEDs) and laser diodes (LDs), were among the first successful demonstrations of nitride devices more than 20 years ago [2–6]. These devices have recently reached a high level of maturity, which is manifested in large luminous efficacies, high external quantum efficiencies and long lifetimes [7]. In the commercial photonics market, LEDs are widely adopted and replace conventional light sources for the reason of saving energy [8–10].

Owing to the unique inherent material properties of nitrides, the development of nitride research aside from optoelectronics is driven by the large variety of possible applications for GaN-based heterostructure field effect transistors (HFETs)[1]. GaN features a wide bandgap (E_{gap}) of 3.43 eV which enables a large breakdown voltage (V_{bd}). For depletion-mode HFETs a V_{bd} of 8300 V has been demonstrated [11], whereas for enhancement-mode HFETs a V_{bd} of 1600 V has been achieved [12]. The large V_{bd} allows for high-voltage operation (typically 28 V-50 V [13]) at elevated temperatures [14]. High power densities of up to 40 W/mm at 4 GHz have been shown [15]. Moreover, an electron bulk mobility above 1000 cm^2/Vs [16, 17] and a saturation velocity of about $3 \cdot 10^7$ cm/s in GaN enable high-frequency operation. Considering the Johnson figure of merit (JFoM) [18], which is a benchmark of the suitability of a material for high-frequency power applications, GaN is superior to other material systems, e.g. GaAs or InP. Deeply scaled (20 nm gate length) GaN

[1] A synonym for GaN-based transistors is high electron mobility transistor (HEMT).

HFETs have been demonstrated with a transit frequency (f_t) exceeding 450 GHz and a maximum oscillation frequency (f_{max}) of almost 600 GHz [19]. Owing to their high level of maturity, GaN-based HFETs are expected to certainly play an important role in future commercial radio frequency (RF) and microwave applications [20].

Group III nitrides are pyro- and piezoelelectric materials [21–27]. They exhibit an inherent macroscopic total polarization (P_{total}), which is the sum of the spontaneous polarization (P_{spon}) and the piezoelectric polarization (P_{piezo}). Further, it is possible to form heterostructures within the nitride material system [28]. At an interface, an abrupt change of P_{total} results in a fixed sheet charge density, which in turn leads to an accumulation of a two-dimensional electron gas (2DEG). The electron density is proportional to the polarization difference (ΔP) between the constituent layers. A wide variety of potential choices and combinations of alloy compositions allows for a more flexible transistor design (HFET) compared to e.g. SiC (metal semiconductor field effect transistor (MESFET)) [14]. So far, the polarization-induced 2DEG has widely been exploited in n-channel HFETs with typically ternary barriers, i.e. AlGaN or AlInN[2] [30–40].

A more sophisticated approach, which offers unique possibilities for novel heterostructure designs, is to use quaternary AlInGaN layers as barrier layers in devices [29, 41, 42]. The major advantage of AlInGaN is the additional degree of freedom, i.e. two different material properties can be adjusted independently by a variation of the AlInGaN composition. This allows for either a change in E_{gap} at an equal strain state or a change in the strain state at a constant E_{gap}. The case of an increased E_{gap} can be achieved by a larger Al content, which is accompanied by an increased P_{spon}. As a result, P_{total} and, hence, the 2DEG density is increased[3] [46]. The case of a variation in the strain state is in particular interesting, when the lattice parameter of AlInGaN becomes larger than the one of GaN. The compressive strain leads to an opposite sign of P_{piezo} with respect to P_{spon}, which in turn reduces P_{total}. The methodology of changing P_{total} by varying the AlInGaN composition is called polarization-engineering. It is theoretically possible to realize polarization-matched heterostructures with no or a very small 2DEG density [47]. This effect can be ex-

[2] The advantages of AlInN over AlGaN are the in-plane lattice-matching to GaN by employing an In content of about 17 % [29], the larger bandgap of about 4.4 eV, which results in a larger conduction band offset, and the higher P_{spon}, which leads to a larger electron density in the 2DEG.

[3] The larger P_{total} further allows for thinner barrier thicknesses compared to AlGaN while maintaining excellent 2DEG transport properties [43, 44]. A smaller barrier thickness allows for downscaling the gate length, which is beneficial for high-frequency performance [45].

ploited in HFETs to realize enhancement mode (e-mode) behavior, which is required in industry for the reasons of fail-safety and low circuit complexity.

In contrast to the high-performance n-channel HFETs, p-channel HFETs are rather overlooked in nitride research. The main reason for this is found in the inferior properties of holes in a two-dimensional hole gas (2DHG) [48–56]. The effective mass m_{eff} of holes in GaN is one order of magnitude larger than the one of electrons. This results in generally low mobilities. However, a systematic study on the properties of a 2DHG is necessary to understand physical limitations and improve the performance of p-channel HFETs. In particular, the influence of ΔP on 2DHG properties is of highest interest.

The polarization-engineering approach is further interesting for optoelectronic devices. Indeed, it has first been proposed for LEDs, in which conventional GaN barrier layers in the multiple quantum well (MQW) were replaced by AlInGaN to reduce internal electric fields [57]. Such polarization-engineered MQWs show a more stable emission wavelength and a suppression of the efficiency droop with larger drive currents [58–62].

The present thesis is dedicated to the synthesis and characterization of quaternary AlInGaN layers. Moreover, novel polarization-optimized devices, n-channel and p-channel HFETs as well as LEDs, on the basis of AlInGaN-containing heterostructures are presented.

The thesis consists of three parts, which follow a general introduction to fundamentals of group III nitrides (Chap. 2) as well as to epitaxy and characterization (Chap. 3). Part I deals with the epitaxial growth and characterization of structural properties of AlInGaN, deposited either on GaN (Chap. 4) or on AlN (Chap. 5). In Part II, the application of polarization-engineered heterostructures for HFETs is discussed. The investigation of both n-channel HFETs containing a 2DEG (Chap. 6) and p-channel HFETs containing a 2DHG (Chap. 7) is presented. In these chapters, the focus is on the influence of P_{total} on transport properties and HFET characteristics. Part III presents novel concepts for LEDs with polarization-engineered AlInGaN layers. At first, AlInGaN layers are utilized as barriers in the active zone of LEDs (Chap. 8). Finally, LEDs with inversed p-n junctions by utilization of a 2DHG induced by an AlInGaN backbarrier are demonstrated (Chap. 9). Both concepts, the reduction of internal fields in a MQW with AlInGaN barriers and the reversed polarization in an inversed LED present remedies for droop effects. Finally, all results are summarized and a conclusion is drawn (Chap. 10).

Chapter 2

Fundamentals of group III nitrides

This chapter gives a brief overview of fundamentals of group III nitrides and of basic principles of devices. In the beginning, material properties of the nitride alloy system are summarized. The elastic deformation in pseudomorphic heterostructures is discussed. Further, polarization effects leading to fixed interface charges are described. The formation of two-dimensional carrier gases is regarded. In the end, the prospect of using AlInGaN layers as an alternative to conventional binary or ternary layers is elucidated.

2.1. Crystal structure and material properties

The thermodynamically stable phase of group III nitrides under standard ambient conditions is the wurtzite crystal. The crystal is shown as a ball-and-stick model in Fig. 2.1a [28]. The unit cell is described by two lattice parameters: the in-plane lattice parameter a and the out-of-plane parameter c. The wurtzite structure is composed of two hexagonal close-packed lattices for each atom species, which are spatially displaced by $5/8c$ in [0001]-direction[1]. This results in a tetrahedral coordination of atoms, in which each atom of one species is surrounded by four atoms of the other species. This allows an energetically favored sp^3 hybridization of the binding orbitals. The bonds are of ionic character due to different electronegativities for nitrogen and the metal: N (3.04), Ga (1.81), Al (1.61) and In (1.78) after Paulings scale [63]. The strong ionicity is the reason for the high thermal and chemical stability of GaN and related alloys. Further, the strength of the ionic character in a wurtzite crystal leads to a non-ideal crystal, i.e. a deviation from the ideal c-to-a ratio of $\sqrt{8/3}$ for the wurtzite structure. This influences several material properties, e.g. the valence band splitting [64] or internal polarization fields, which will be regarded in more detail in sections 2.4.1 and 2.4.2.

If the long vertical bond from the metal atom to the nitrogen atom points in [0001]-direction, the polarity is defined as metal-polar. Consequently, if the bond

[1] The [0001]-direction is commonly referred to as the c-direction

points in [000$\bar{1}$]-direction, the polarity is defined as N-polar. The length of the vertical bond is important for further considerations and it is commonly denoted as the internal parameter u [24]. u is given in units of the lattice parameter c.

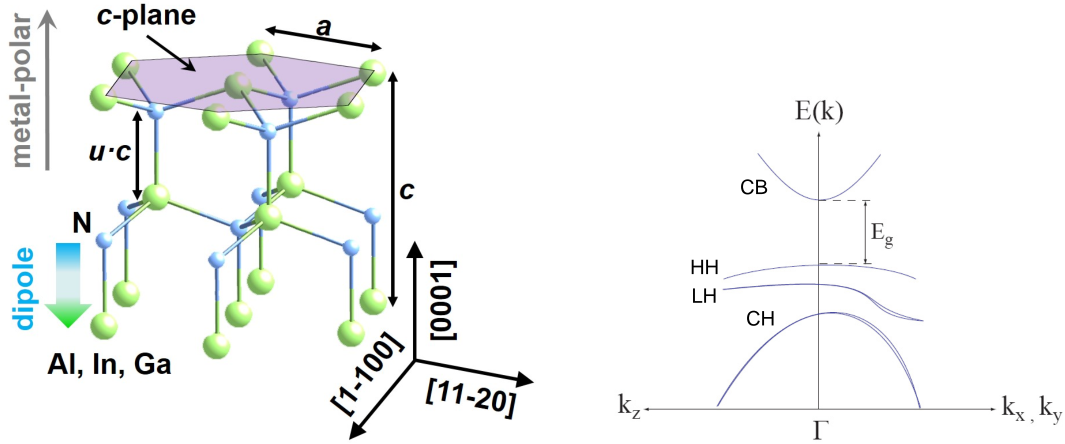

(a) Ball-and-stick model.

(b) Shown are the conduction band (CB) and the three valence bands: heavy-hole (HH), light-hole (LH) and the crystal field split-off band (CH).

Figure 2.1.: Structure of the wurtzite crystal and the simulated bandstructure of GaN at the Γ symmetry point after [65].

The bandstructure is shown exemplarily for GaN at the Γ symmetry point in Fig. 2.1b [65]. Obviously, group III nitrides have a direct bandgap, which allows direct recombinations of electrons and holes. The large recombination probability is important for optical devices and already commercially exploited in e.g. LEDs and LDs [9, 10]. The conduction band consists of 4s orbitals predominantly from the Ga atom and, hence, the excited niveau is isotropic in real space [66]. In contrast, the valence band, which consists of 2p orbitals from the N atom, is apparently split into three bands. While the lowest band (split-off band, CH) stems from the crystal field of the wurtzite phase and represents the p_z state along the c-direction, the two upper valence bands are degenerated with p_x and p_y states. These two upper valence bands reflect the basal plane symmetry and are split into heavy-hole and light-hole bands by spin-orbit coupling [66, 67]. This splitting has a dramatic influence on electronic properties for both electrons and holes in matters of mobility. While for electrons in the conduction band, an effective mass of 0.17 to 0.23 m_0 is observed [64, 68, 69], for holes in the uppermost heavy-hole valence band, the effective mass m_{eff} is 1.61 to 2.27 m_0 [64, 69, 70]. The effective hole mass m_{eff} in the light-hole band and the crystal field split-off band are much lower, namely about 0.16 to 0.20 m_0 [64]. However, c-plane GaN maintains a basal plane symmetry, even when biaxial strain

is applied and, hence, the hole properties discussed in this thesis are dominantly determined by the heavy-hole valence band[2].

An overview of relevant properties of the three binary nitride alloys is given in Tab. 2.1. AlN is the most densely packed crystal followed by GaN and InN. Lattice parameters a and c of ternary and quaternary compounds change linearly with the content of the metal species and can be calculated via Vegard's law [73]. It holds for e.g. a:

$$a_{Al_xIn_yGa_{(1-x-y)}N} = x_{Al} \cdot a_{AlN} + y_{In} \cdot a_{InN} + (1 - x_{Al} - y_{In}) \cdot a_{GaN}. \tag{2.1}$$

In the case of heteroepitaxy, the nitride layer is grown on a possibly lattice-mismatched substrate or buffer with a distinct lattice constant a_{Ref}. Since the lattice mismatch f is not uniquely defined in literature [74], it is defined here as follows:

$$f = \frac{a_{Ref} - a_{nom}}{a_{nom}}, \tag{2.2}$$

in which a_{nom} is the nominal lattice constant of a nitride alloy and a_{Ref} is the effective substrate lattice constant. The lattice mismatch between the nitride binaries is generally large in the range of a few percent. It is larger for InN-on-GaN than for AlN-on-GaN. As an example, for AlN-on-GaN with a mismatch of -2.5 %, the critical thickness for lattice relaxation lies in the range of several nanometers [75]. As a result, thick binary nitrides with a thickness of several tens of nanometers are always fully relaxed on each other. In the case of a small lattice mismatch, a nitride layer may adopt the substrate lattice constant a_{Ref}. Here, an elastic deformation of the crystal occurs. The nominal strain ε_{nom} in a nitride layer can be described as:

$$\varepsilon_{nom} = \frac{a_{strained} - a_{nom}}{a_{nom}}, \tag{2.3}$$

in which $a_{strained}$ is the fully strained lattice constant. In the fully strained case $a_{strained} = a_{Ref}$, which is called pseudomorphic, the nominal strain ε_{nom} is equal to the lattice mismatch f. At the critical thickness of a layer, relaxation occurs. In this case, the in-plane lattice constant starts to change. This is accompanied by a reduction in strain. For this scenario, the residual strain ε_{res} in a nitride layer can

[2] There might be a possibility to shift the light-hole band energetically upwards and, hence, to provoke dominant light-hole conduction by anisotropic and/or shear strain engineering in semi-polar nitrides [71, 72].

Quantity	Unit	**GaN**	**AlN**	**InN**
Real space properties				
a	[Å]	3.189	3.112	3.545
c	[Å]	5.185	4.982	5.703
u [23]	[Å]	0.377	0.382	0.379
Density	10^{22} [cm^{-3}]	8.9	9.6	6.8
$\Delta a/a$ to GaN	[%]	-	-2.5	10.0
$\Delta a/a$ to Al_2O_3	[%]	13.9	11.7	22.5
Electrical properties				
P_{spon}	[µC·cm^{-2}]	-3.4	-9.0	-4.2
μ_e	[cm^2·V^{-1}s^{-1}]	1250 [16, 17]	800 [76]	14000 [77]
$v_{sat,e}$	10^7[cm·s^{-1}]	3.0 [78]	1.4 [78]	5.1 [79]
μ_h	[cm^2·V^{-1}s^{-1}]	25 [80]	-	-
$v_{sat,h}$	10^5[cm·s^{-1}]	2.4 [81]	-	-
E_{BD}	10^6[V·cm^{-1}]	3.3	8.4	-
Optical properties				
E_{gap} (300 K)	[eV]	3.43	6.14	0.65-0.68 [82, 83]
b_{AlGaN}	[eV]	0.9		
b_{InGaN}	[eV]	1.7		
b_{AlInN}	[eV]		2.4-6.3 [84–86]	

Table 2.1.: Structural parameters for the binary nitride alloys in the wurtzite phase. If not otherwise mentioned, taken from [87–89].

be described as:

$$\varepsilon_{res} = \frac{a_{relaxed} - a_{nom}}{a_{nom}}, \tag{2.4}$$

in which $a_{relaxed}$ is the partially relaxed lattice constant. The degree of relaxation in a specific layer is normally calculated by taking the lattice constant of the underlying layer with a_{Ref} into account:

$$R = \frac{a_{relaxed} - a_{Ref}}{a_{nom} - a_{Ref}}. \tag{2.5}$$

At full relaxation, $a_{relaxed}$ becomes equal to a_{nom}. Consequently, it holds $R = 1$ and $\varepsilon_{res} = 0$.

2.2. Elastic deformation in nitride-based heterostructures

In the pseudomorphic case, for which elastic deformation is necessary, the in-plane deformation is counterbalanced by an out-of-plane elastic relaxation. As illustrated in Fig. 2.2, three different cases appear in heteroepitaxy. In the tensile strained case, $a_{nom} < a_{GaN}$, the crystal expands in-plane and shrinks elastically in c-direction. In the special case of lattice-matching, $a_{nom} = a_{GaN}$, no stress exists and, hence, no deformation in the c-direction appears. In the compressively strained case, $a_{nom} > a_{GaN}$, the crystal is compressed in-plane and stretched elastically in c-direction.

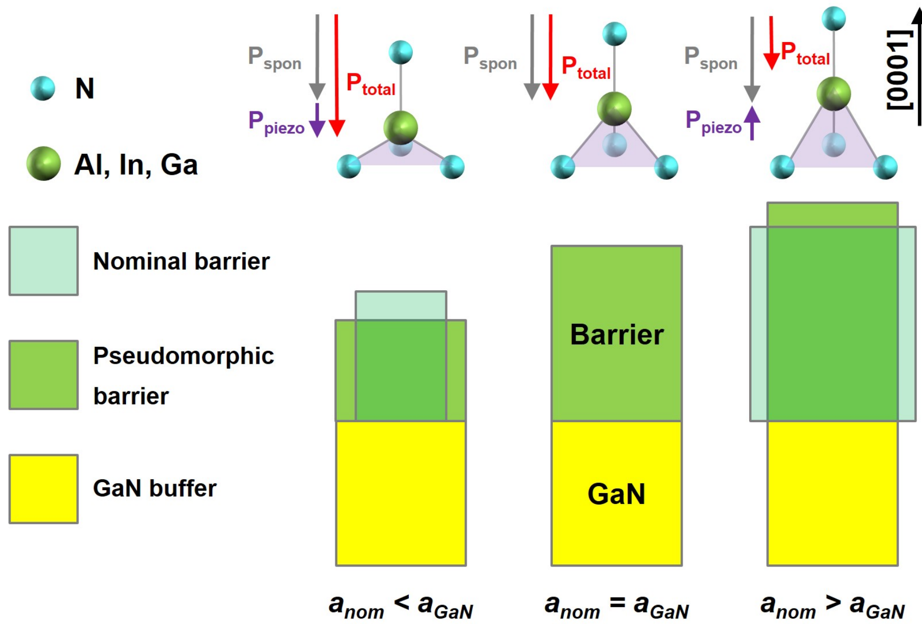

Figure 2.2.: Illustration of the elastic deformation for pseudomorphic growth for three different cases: the tensile strained case $a_{nom} < a_{GaN}$, the lattice-matched case $a_{nom} = a_{GaN}$ and the compressively strained case $a_{nom} > a_{GaN}$. A ball-and-stick model is shown in every case to indicate the changing dipole length.

Generally, for the strain and stress tensors, both normal parts and shear parts have to be considered. Owing to the wurtzite symmetry in the group III nitride system, the strain and stress tensors are connected via a (6×6) matrix, via Hooke's law in Voigt's notation [23, 74]:

$$\begin{pmatrix} \sigma_{xx} \\ \sigma_{yy} \\ \sigma_{zz} \\ \sigma_{yz} \\ \sigma_{xz} \\ \sigma_{xy} \end{pmatrix} = \begin{pmatrix} C_{11} & C_{12} & C_{13} & 0 & 0 & 0 \\ C_{12} & C_{11} & C_{13} & 0 & 0 & 0 \\ C_{13} & C_{13} & C_{33} & 0 & 0 & 0 \\ 0 & 0 & 0 & C_{44} & 0 & 0 \\ 0 & 0 & 0 & 0 & C_{44} & 0 \\ 0 & 0 & 0 & 0 & 0 & \frac{1}{2}(C_{11}-C_{12}) \end{pmatrix} \cdot \begin{pmatrix} \varepsilon_{xx} \\ \varepsilon_{yy} \\ \varepsilon_{zz} \\ \varepsilon_{yz} \\ \varepsilon_{xz} \\ \varepsilon_{yz} \end{pmatrix}. \quad (2.6)$$

Here, σ denotes the stress, ε the strain and C the elastic constants. The (6×6) matrix consists of the elastic constants of the constituent layer. However, for the in-plane isotropic case $\varepsilon_{xx} = \varepsilon_{yy} = \varepsilon_{\|}$ and growth in c-direction, shear parts can be neglected. Thus, the elastic theory can be simplified:

$$\begin{pmatrix} \sigma_{\|} \\ \sigma_{\perp} \end{pmatrix} = \begin{pmatrix} C_{11}+C_{12} & C_{13} \\ 2 \cdot C_{11} & C_{33} \end{pmatrix} \cdot \begin{pmatrix} \varepsilon_{\|} \\ \varepsilon_{\perp} \end{pmatrix} \quad (2.7)$$

$$(2.8)$$

For pseudomorphic growth, the in-plane stress $\sigma_{\|}$ results directly in in-plane strain $\varepsilon_{\|}$. Owing to the free surface in c-direction, the out-of-plane stress $\sigma_{\perp}$ is always zero. Hence, the out-of-plane strain $\varepsilon_{\perp}$ is only determined by the elastic constants. With this assumption, the following relationship can be derived:

$$\sigma_{\perp} = 2\varepsilon_{\|}C_{13} + \varepsilon_{\perp}C_{33} = 0 \qquad \Rightarrow \qquad \varepsilon_{\perp} = -\frac{2\varepsilon_{\|}C_{13}}{C_{33}}. \quad (2.9)$$

The ratio between in-plane and out-of-plane strain is the so-called Poisson ratio and can be calculated with the elastic constants $-2C_{13}/C_{33}$.

2.3. Bandgaps of nitride alloys

The bandgaps for the binary nitrides are given in Tab. 2.1. The values increase from InGaN with 0.65 eV to GaN with 3.43 eV and to AlN with 6.14 eV.

For the calculation of the bandgap of ternary alloys, non-linearities have to be considered. These non-linearities occur due to a non-linear dependence of the internal parameter u on the composition [23]. This results in a smaller bandgap compared to the linear model. The non-linearity is mathematically reflected in bowing parameters. For the calculation of the bandgap $E_{g,Al_xIn_{(1-x)}N}$ of e.g. AlInN the following

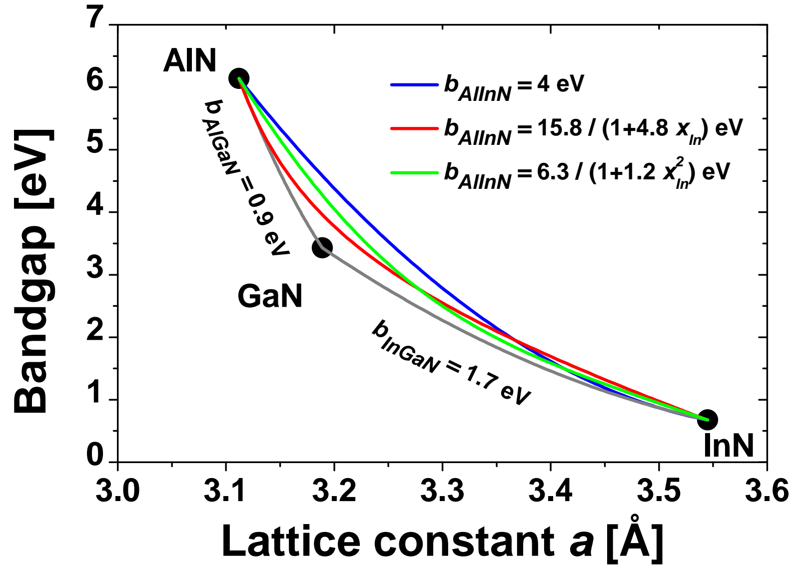

Figure 2.3.: Bandgap of nitride binaries and ternaries plotted against the in-plane lattice constant a. While the bowing for AlGaN and InGaN is commonly accepted to be constant, the bowing for AlInN is controversially discussed.

holds

$$E_{g,Al_xIn_{(1-x)}N} = x_{Al} \cdot E_{g,AlN} + (1 - x_{Al}) \cdot E_{g,InN} - b_{AlInN} \cdot x_{Al} \cdot (1 - x_{Al}). \quad (2.10)$$

The bowing parameters b for each ternary compound are given in Tab. 2.1. In Fig. 2.3, the bandgaps of nitride binaries and ternaries are plotted against the in-plane lattice constant a. The bowing is commonly assumed to be constant. For AlGaN, b_{AlGaN} is quite low with 0.9 eV, whereas for InGaN b_{InGaN} is higher with 1.7 eV [90–92].

For AlInN, there is an ongoing discussion about the wide spread of published values between 2.4 eV and 6.3 eV [84–86]. These discrepancies occur due to several reasons: In reports older than 10 years, the InN bandgap was believed to be much larger (1.8 eV) than it is accepted today (0.7 eV) [93–96]. Reports taking the lower bandgap of 0.7 eV into account still vary in the bowing parameters for reasons which include: variations in crystal quality, different compositions in either Al-rich or In-rich regimes, different methods of composition determination and also a strong Stokes shift in AlInN layers [29, 84, 85, 97]. Investigations on high-quality AlInN layers generally yield larger bowing parameters of about 5 eV [98, 99]. Latest results taking the whole compositional range into account and results on quaternary layers indicate either a linear In-dependent bowing parameter like $b(x_{In}) = A_1/(1 + A_2 \cdot$

x_{In}), with A_1=15.3 eV and A_2=4.8 [100] or a quadratically In-dependent bowing parameter like $b(x_{In}) = A_1/(1 + A_2 \cdot x_{In}^2)$, with A_1=6.4 eV and A_2=1.2 [91, 101]. Calculated bandgap values on basis of the latter two bowing parameters and on basis of a constant bowing parameters of 4 eV [102] are shown for comparison in Fig. 2.3. The moderate value of 4 eV represents the maximum value for which a crossing of the ternary AlInN line and InGaN line in the In-rich regime is prevented. This crossing is unlikely to reflect real behavior. Apparently both approaches with In-dependent bowing parameters overcome this issue. When the whole compositional range of AlInN is regarded, the quadratic In-dependent bowing parameter might be the best solution [91, 101].

For a first-order calculation of the bandgap in the quaternary system, an equation in analogy to Eq. 2.10 could be used [91]:

$$E_{g,Al_xIn_yGa_zN} = x \cdot E_{g,AlN} + y \cdot E_{g,InN} + z \cdot E_{g,GaN} - b_{AlGaN} \cdot xz - b_{InGaN} \cdot yz - b_{AlInN} \cdot xy. \quad (2.11)$$

$$\text{with} \qquad x + y + z = 1. \quad (2.12)$$

Here, x denotes the Al content, y denotes the In content and z denotes the Ga content. It has been discussed that the contribution of a specific ternary bowing parameter (e.g. b_{AlInN}) is too strong when the quaternary composition is far off from the respective ternary composition line (e.g. AlInN). Hence, it has been suggested to use the following equation for the quaternary system, in which each ternary bowing parameter (e.g. b_{AlInN}) is weighted with the associated compositional fraction (e.g. $x + y$) in the quaternary ensemble (i.e. $x + y + z$) [103, 104].

$$E_{g,Al_xIn_yGa_zN} = x \cdot E_{g,AlN} + y \cdot E_{g,InN} + z \cdot E_{g,GaN} - b_{AlGaN} \cdot xz \cdot (x+z) - b_{InGaN} \cdot yz \cdot (y+z) - b_{AlInN} \cdot xy \cdot (x+y). \quad (2.13)$$

For ternary alloys, Eq. 2.13 yields equal values as the non-weighted Eq. 2.11. For quaternary AlInGaN, the calculated bandgap values are different depending on the equation used. This is illustrated with a bandgap contour plot in Fig. 2.4. Compared to the case of a non-weighted bandgap in Fig. 2.4a, the area of AlInGaN compositions featuring a larger bandgap than the one of GaN (yellow-to-red) is slightly increased

in the case of a weighted bandgap in Fig. 2.4b. It is shown in the following paragraphs that the difference of the bandgap values has a tremendous impact on the feasibility of polarization-matching AlInGaN layers to GaN for device applications.

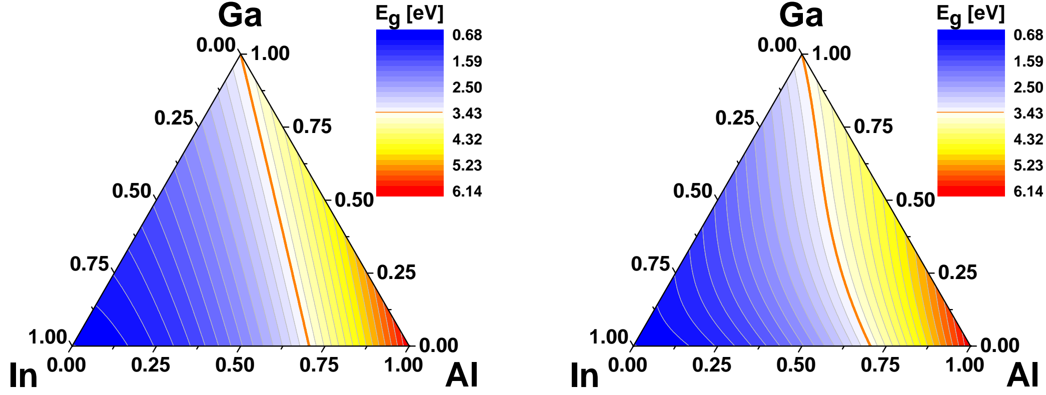

(a) Bandgap calculated with a simple non-weighted Eq. 2.11.

(b) Bandgap calculated with a weighted Eq. 2.13.

Figure 2.4.: Bandgap contour plot in a ternary diagram for all metal contents possible in a quaternary nitride layer. The orange lines mark the compositions with bandgaps equal to that of GaN. The yellow-to-red colored areas indicate larger bandgaps than the one of GaN.

2.4. Polarization effects

Owing to a missing inversion symmetry in c-direction, wurtzite group III nitrides are polar materials. The strong deviation between the electronegativities for nitrogen and the metal atoms leads to a displacement of binding electrons. In the basal plane, which is spanned by the $[1\bar{1}00]$- and $[11\bar{2}0]$-directions, in-plane symmetry results in a compensation of the dipoles. In c-direction, however, the vertical bonds of metal and nitrogen atoms create dipoles $\vec{p}$, which point in the $[000\bar{1}]$-direction. The uncompensated dipoles sum up to a macroscopic polarization component $P_{total,z}$ in the $[000\bar{1}]$-direction.

2.4.1. Spontaneous polarization

The inherent polarization in an unstrained crystal is called the P_{spon}. The value of P_{spon} scales linearly with the internal parameter u and is dependent on the constituent metal atom. As listed in Tab. 2.1, P_{spon} is lower for GaN than for AlN and InN. Since the internal parameter u changes non-linearly with alloy composition, P_{spon} does so as well [23–25].

2.4.2. Piezoelectric polarization

If a crystal is under biaxial elastic stress, as discussed in the previous Sec. 2.2, a P_{piezo} has to be considered. Because of the elastic deformation present in c-direction, the value of the internal parameter u changes. With that, the absolute value of the dipoles change, leading to a P_{piezo}, which has to be added to P_{spon}:

$$P_{total} = P_{spontaneous} + P_{piezo}. \tag{2.14}$$

For metal-polar[3] wurtzite crystals with in-plane symmetry, an equation can be derived, connecting P_{piezo} with the in-plane strain $\varepsilon_{\|}$:

$$P_{piezo,z} = 2\varepsilon_{\|} \cdot \left(e_{31} - \frac{C_{13}}{C_{33}} e_{33} \right), \tag{2.15}$$

with e_{ij} being the piezoelectric constants. The key aspect is that for tensile strained layers, P_{piezo} and P_{spon} are parallel, and for compressively strained layers, P_{piezo} and P_{spon} are anti-parallel. In the first mentioned case, $|P_{total}|$ becomes larger[4], whereas in the latter case, $|P_{total}|$ is lowered [23–25].

2.4.3. Two-dimensional carrier gases

For a homogeneous crystal consisting of only a single layer, the resulting internal fields due to the polarization are compensated by charges of opposite signs at the external surfaces. These charges are not necessarily fixed charges, e.g adsorbed ions from the ambient and charge trapped in surface states [108, 109]. This is not the case, when a heterostructure is considered, which consists of a GaN channel and a barrier layer with P_{total} and E_{gap} both larger than those of GaN. This is shown for metal-polar heterostructures for two cases in Fig. 2.5.

At first, the typical case of metal polar "barrier on GaN" heterostructure is regarded and shown in Fig. 2.5a. According to Gauss' Law, $\rho = \vec{\nabla} \cdot \vec{P}$, a discontinuity of the polarization P leads to a fixed charge density ρ. At the interface, P_{total} changes abruptly in c-direction. The resulting net interface sheet charge density σ_{int} is identical to ΔP between the barrier and the GaN channel:

$$\sigma_{int} = -\Delta P = -(P_{total,barrier} - P_{total,GaN}) \tag{2.16}$$

[3]Nitride layers grown on sapphire by metal-organic vapor phase epitaxy (MOVPE) are typically of metal-polarity owing to a larger decomposition rate for N-polar material [105–107].

[4]The inherent polarization is negative for group III nitrides. For the sake of simplicity in this thesis, it is often referred to the absolute value of the polarization.

For the shown case, σ_{int} is positive and fixed at the upper side of the interface. This leads to an internal electric field and, hence, a slope in the band structure of the barrier. As a result, the band structure in the GaN is pulled downwards. Due to the defined concuction band offset ΔE_C, a potential well is formed in the conduction band. When the potential well, which can be approximated by a triangular shape, reaches the Fermi level, free electrons representing a 2DEG are accumulated.

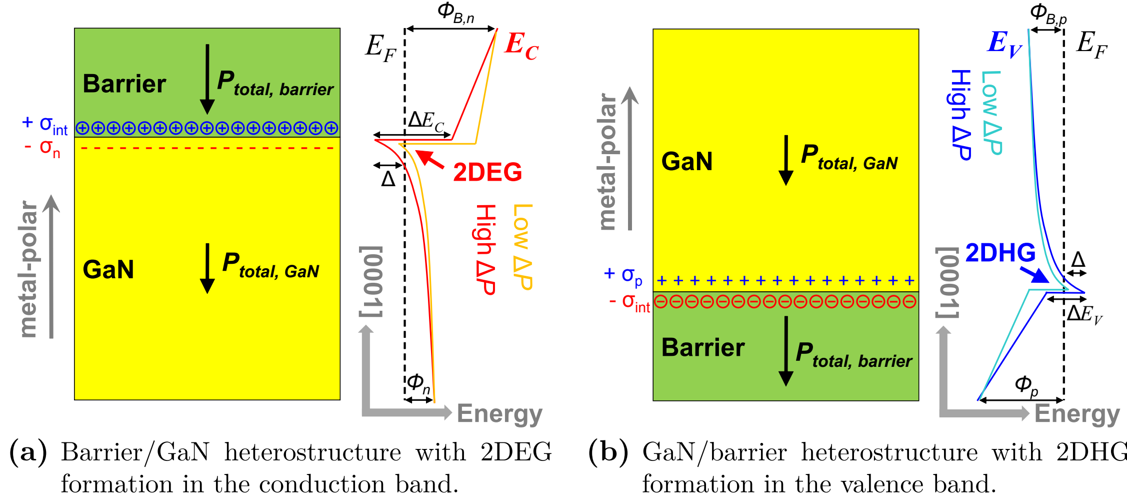

(a) Barrier/GaN heterostructure with 2DEG formation in the conduction band.

(b) GaN/barrier heterostructure with 2DHG formation in the valence band.

Figure 2.5.: Location of fixed interface charges in a metal-polar two-fold heterostructure and the corresponding bandstructure.

Even for a heterostructure with intrinsic material, for which the Fermi level is positioned at midgap, such a 2DEG is formed. The sheet electron density (n_s) is proportional to ΔP and can be understood as a countercharge to the fixed positive σ_{int}. However, for the calculation of the actual value of n_s, self-consistent differential equations have to be solved numerically. A simplified analytical model for n_s follows [32, 110]:

$$n_s = \frac{\Delta P}{e} - \frac{1}{e^2} \cdot C_b \cdot (\Phi_{B,n} - \Delta E_C + \Delta) - \frac{1}{e^2} \cdot C_{ch,n} \cdot \Phi_n. \tag{2.17}$$

Here, e is the elementary charge, $\Phi_{B,n}$ is either the Schottky barrier height or the surface potential, ΔE_C is the conduction band offset at the barrier/GaN interface. Φ_n is the position of the conduction band with respect to the Fermi level at the bottom of the GaN channel. The last term in Eq. 2.17 is negligible for thick GaN buffers ($t_{GaN} > t_{barrier}$). C_b and $C_{ch,n}$ is the area-specific capacitance of the barrier and the GaN n-channel, respectively. It is defined as

$$C_{index} = \frac{\epsilon_0 \cdot \epsilon_{r,index}}{t_{index}}, \tag{2.18}$$

in which ϵ_0 is the permittivity of free space. $\epsilon_{r,index}$ and t_{index} are the relative dielectric constant and the thickness of the constituent layer, respectively. Δ is the penetration depth of the triangular well with respect to the Fermi level. It is a function of n_s itself and inverse proportional to the effective mass m_{eff} of the carriers [111]:

$$\Delta = \frac{\pi\hbar^2}{m_{eff}} \cdot n_s. \tag{2.19}$$

For the case of the metal-polar "GaN on barrier" heterostructure in Fig. 2.5b, an analogous model can be derived. It is still assumed that compared to GaN, the barrier layer features both a higher bandgap and larger P_{total}. Then, the net interface charge density σ_{int} is negative and the associated valence band structure leads to the formation of a 2DHG, as illustrated in 2.5b. An analytical expression to calculate the sheet hole density (p_s) in such a 2DHG has already been derived in [112]. It holds:

$$p_s = \frac{\Delta P}{e} - \frac{1}{e^2} \cdot C_b \cdot (\Phi_p - \Delta E_V) - \frac{1}{e^2} \cdot C_{ch,p} \cdot \Phi_{B,p}. \tag{2.20}$$

Due to the interchanged layer structure, the GaN p-channel capacitance $C_{ch,p}$ is multiplied with the p-type Schottky barrier height $\Phi_{B,p}$. Φ_p denotes the position of the Fermi level with respect to the valence band at the bottom of the barrier. The penetration depth Δ for a 2DHG is negligible, since m_{eff} is one order of magnitude larger for holes compared to electrons [64, 69, 70].

For the actual generation of a 2DHG in the experimental part of this thesis, a double heterostructure is used, which consists of a GaN buffer, a barrier layer and a topmost GaN p-channel[5]. The layer stack and the associated bandstructure of the used double heterostructure is illustrated in Fig. 2.6.

In such a double heterostructure, both a 2DEG and a 2DHG exist. The respective carrier densities are correlated by the following first-order approximation [112, 113]:

$$p_s = n_s - C_{ch,p} \frac{\Phi_{B,p}}{e^2}. \tag{2.21}$$

Here, $\Phi_{B,p}$ is the Schottky barrier height, $C_{ch,p}$ is the area-specific capacitance of the upper p-channel GaN. The 2DHG density depends only on the 2DEG density[6] and a depletion term, the latter accounting for the surface depletion by the p-type Schottky barrier and the p-channel capacitance.

[5] It will be shown in the experimental Part I, that an embedded thin barrier can be deposited in a superior crystal quality compared to thick backbarriers.

[6] The 2DEG density is fixed in the double heterostructure, as long as a 2DHG exists [112, 113].

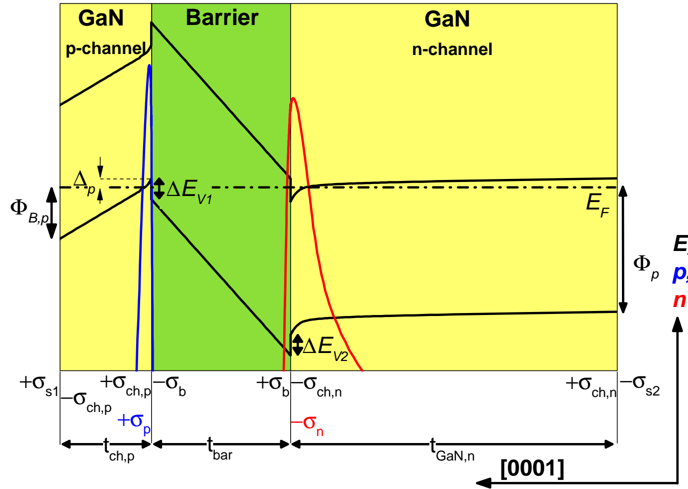

Figure 2.6.: Band diagram of a double heterostructure consisting of a lower GaN n-channel and an upper GaN p-channel with an embedded barrier. Conduction and valence bands as well as the accumulated 2DHG (blue) and 2DEG (red) densities. The associated polarization charges are given at each interface. After [112].

As has been shown, Eq. 2.17 for n_s in a 2DEG and Eq. 2.20 for p_s in a 2DHG contain the term $\frac{\Delta P}{e}$. The intentional adjustment of ΔP is the essential method in this thesis to influence the density of polarization-induced carrier gases and is denoted as polarization engineering.

2.5. Heterostructure field effect transistors

The working principle of GaN-based HFETs is briefly introduced here. These transistors are unipolar devices. Generally, n-channel devices can be realized by using the 2DEG as the channel in "barrier on GaN" heterostructures and p-channel devices can be realized by using the 2DHG as the channel in "GaN on barrier" heterostructures. The basic device structure is schematically shown in Fig. 2.7a for the n-channel HFET and in Fig. 2.7b for the p-channel HFET. In the access region, ohmic contacts to the 2DEG/2DHG form the source and the drain. The intrinsic device is defined as the region below the gate contact, which is realized as a Schottky diode. A potential insulator between the semiconductor and the metal gate contact might be used for the reduction of gate leakage currents.

By applying a gate source voltage V_{GS}, the carrier density n_s/p_s in the channel can be modulated via the field effect. A simple charge control model yields the following relation between n_s and V_{GS} [114, 115]:

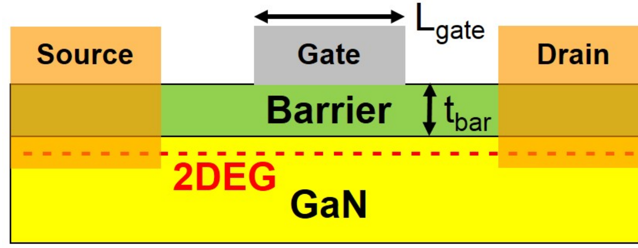

(a) n-Channel (2DEG) HFET on a barrier/GaN heterostructure.

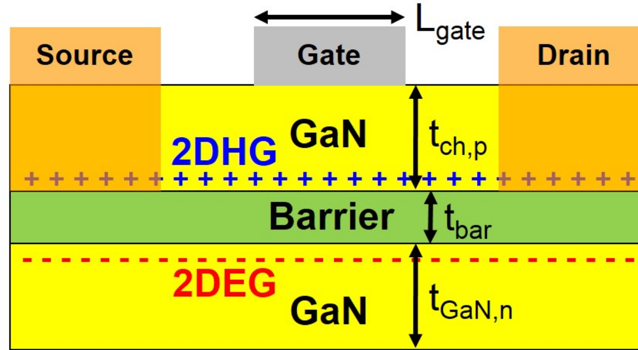

(b) p-Channel (2DHG) HFET on a GaN/barrier/GaN double heterostructure.

Figure 2.7.: Schematic illustration of the HFET device principle including source, drain and gate contacts.

$$n_s = \frac{C_b}{e} \cdot (V_{GS} - V_{th}). \tag{2.22}$$

The threshold voltage (V_{th}) is defined as the gate voltage at which n_s is depleted. With no bias applied on the gate ($V_{GS} = 0$), the following equation is valid for the n-channel heterostructure:

$$V_{th,n} = -\frac{e}{C_b} \cdot n_s. \tag{2.23}$$

For the p-channel double heterostructure, it holds [112]

$$V_{th,p} = \frac{e}{C_{ch,p}} \cdot p_s \tag{2.24}$$

$$= \frac{e}{C_{ch,p}} \cdot n_s - \frac{\Phi_{B,p}}{e}. \tag{2.25}$$

The Eqs. 2.23 and 2.25 obviously show that V_{th} can be changed in either case

by the value of the polarization-induced n_s under the barrier, which is a function of ΔP between barrier and GaN (Eq. 2.17). Hence, the adjustment of ΔP allows for a control over V_{th}. This is especially interesting for HFET applications to gain normally-off behavior. To achieve this, V_{th} must be shifted to positive values for n-channel devices and to negative values for p-channel HFET. It will shown for both n-channel and p-channel HFETs that it is possible to realize either transistor characteristic by polarization engineering: depletion mode (d-mode) and enhancement mode (e-mode) behavior.

2.6. The quaternary approach

Quaternary alloys cover the full parameter space of material properties, e.g. bandgap E_{gap} and lattice constant a, in the nitride system, framed by the binaries and the ternaries. With quaternary AlInGaN, it is theoretically possible to change material parameters (a, E_{gap}, P_{total}) independently of each other. This enables an adjustment of a specific P_{total} in an AlInGaN layer while maintaining a large E_{gap}, which can be exploited in (opto)electronic devices, e.g. HFETs and LEDs.

However, the controversy about the ternary AlInN bowing parameters and the bandgap equations makes the polarization engineering approach a challenging task. To elucidate this issue, the bandgap is plotted as a function of the lattice constant a in Fig. 2.8. Additionally, P_{total}, calculated for pseudomorphic growth on GaN, is shown in the quaternary parameter space as a contour in different colors. The parameters for this calculation are taken from an earlier publication [104]. The black contour lines indicate compositions with equal values of P_{total}. Polarization-matching compositions to GaN are highlighted with a red line. Further, commonly used ternary compositions, which are $Al_{0.25}Ga_{0.75}N$ and $Al_{0.83}In_{0.17}N$, are shown. Additionally, measured bandgap values, determined by spectroscopic ellipsometry (SE) [91, 101], for several AlInN compositions with different In contents between 6 % and 19 % are plotted as red circles for comparison.

A case study for six different parameter sets is presented in Fig. 2.8: The recently published bowing parameters discussed in Sec. 2.1, which are a constant value of 4 eV [102], a linearly In-dependent bowing parameter like $b(x_{In}) = A_1/(1 + A_2 \cdot x_{In})$ [100] and a quadratically In-dependent bowing parameter like $b(x_{In}) = A_1/(1 + A_2 \cdot x_{In}^2)$ [91] are shown here as examples. The case study includes calculations for each bowing parameters with both the non-weighted Eq. 2.11 in Fig. 2.8a, 2.8c, and 2.8e and the weighted bandgap Eq. 2.13 in Fig. 2.8b, 2.8d, and 2.8f.

In the case of the non-weighted bandgaps (Fig. 2.8a, 2.8c, and 2.8e), it is interest-

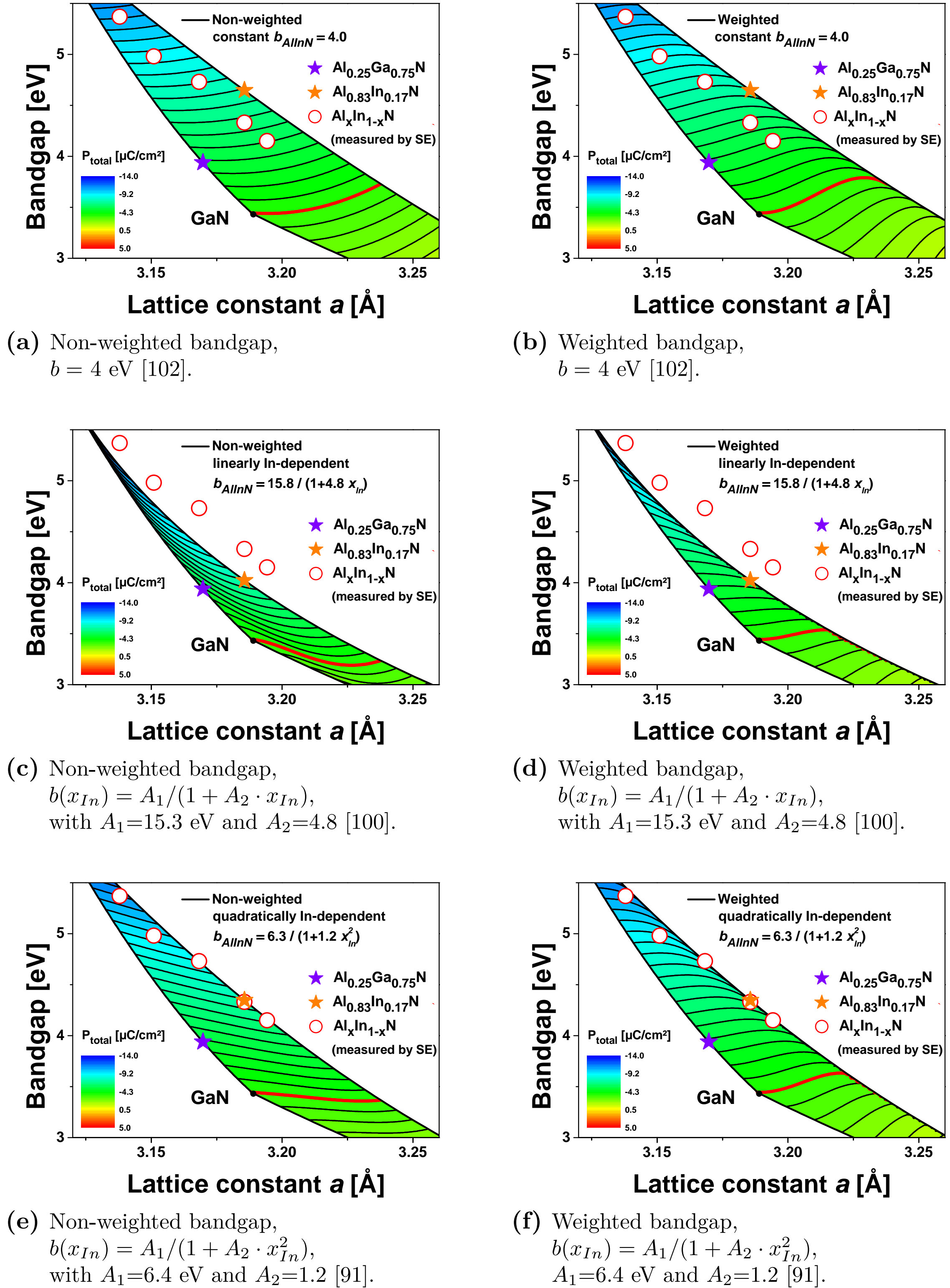

(a) Non-weighted bandgap, $b = 4$ eV [102].

(b) Weighted bandgap, $b = 4$ eV [102].

(c) Non-weighted bandgap, $b(x_{In}) = A_1/(1 + A_2 \cdot x_{In})$, with A_1=15.3 eV and A_2=4.8 [100].

(d) Weighted bandgap, $b(x_{In}) = A_1/(1 + A_2 \cdot x_{In})$, with A_1=15.3 eV and A_2=4.8 [100].

(e) Non-weighted bandgap, $b(x_{In}) = A_1/(1 + A_2 \cdot x_{In}^2)$, with A_1=6.4 eV and A_2=1.2 [91].

(f) Weighted bandgap, $b(x_{In}) = A_1/(1 + A_2 \cdot x_{In}^2)$, A_1=6.4 eV and A_2=1.2 [91].

Figure 2.8.: Bandgap diagrams plotted over the lattice constant a with different bowing parameters for AlInN. Either a non-weighted a), c) and e) or a weighted bandgap equation b), d) and f) is applied. The calculated bandgap values for the typical ternary barrier layers $Al_{0.25}Ga_{0.75}N$ (purple star) and $Al_{0.83}In_{0.17}N$ (orange star) as well as measured bandgap values for several AlInN layers (red circles) with different compositions are shown.

ing that only for the constant bowing parameter (2.8a), the polarization-matching red line shows larger bandgaps than the one of GaN. In both In-dependent cases, compositions with equal polarizations to GaN exhibit smaller bandgaps than the one of GaN. Since the bandgaps of polarization-matched barriers are not large enough to form a positive conduction band offset, this has a detrimental effect on the feasibility for heterostructures with low ΔP. In the case of the weighted bandgap (Fig. 2.8b, 2.8d, and 2.8f), this issue is not observed. In every graph, the polarization-matching line is bending upwards, illustrating larger bandgaps than the one of GaN. In these cases, polarization-matched AlInGaN barriers with sufficiently large conduction band offsets to GaN are possible.

Due to the wide spread of bandgap calculation parameters, the case study presented here shows a quite confusing picture. To identify the most accurate cases, the measured bandgap values for AlInN are regarded. Obviously, for a quadratically In-dependent bowing parameter in the two latter cases in Fig. 2.8e and 2.8f, the ternary line comes closest to the measured values. In particular for lattice-matched $Al_{0.83}In_{0.17}N$ with a measured bandgap of about 4.3 eV the aggreement is very good [91, 101]. Still, it remains rather unclear whether true polarization-matching with quaternary layers is possible while maintaining a larger bandgap than the one of GaN. In the case of a weighted bandgap calculation (Eq. 2.13), which is shown in Fig. 2.8f, polarization-matching AlInGaN/GaN heterostructures are theoretically possible. Despite the uncertain bandgap for polarization-matching AlInGaN, the tendency to lower polarizations with increasing compressive strain can definitely be utilized. It will be discussed in the experimental part of this thesis to what extent this approach is feasible for device applications.

Chapter 3

Epitaxy and characterization methods

In this chapter, the methods for fabrication and charaterization of nitride layers and heterostructures are introduced. A wide range of different analysis methods have been utilized for this thesis. However, detailed descriptions are only given for the most specific and not commonly known analysis methods.

3.1. Metal organic vapor phase epitaxy

For this thesis, all layers and heterostructures were grown by MOVPE[1]. Epitaxial growth was performed in different AIXTRON MOVPE reactors [116]. These reactors are high-temperature systems, which allow for temperatures exceeding 1300 °C. The process set temperature (T_{Set}) is coupled to the power feeded into the system. However, the actual growth surface temperature ($T_{Surface}$) on the wafer differs from T_{Set} due to thermal losses. $T_{Surface}$ is measured by an external in-situ monitoring system produced by LayTec [117]. The system combines a true-temperature pyrometer module with measurements of the optical reflectance at different wavelengths. This enables in-situ monitoring and control of the actual $T_{Surface}$ on the wafer and the growth rate during epitaxy.

If not otherwise mentioned, most of the experiments were performed in an AIX 200/4 RF-S reactor with gas foil rotation in a 2-inch configuration, shown in Fig. 3.1a. The reactor is based on the principle of a horizontal laminar gas flow. All parts guiding the gas flow consist of quartz and can be cleaned easily in KOH and HF baths. The SiC coated graphite parts are inductively heated by an RF coil during epitaxy. Owing to its small size, the AIX 200/4 RF-S is the fastest MOVPE system in terms of heating and cooling time. This allows for a quick change in process conditions, which is advantageous for achieving high interface qualities.

Several experiments were performed in a close-coupled showerhead (CCS) system in a 3 × 2-inch configuration [118]. A side view schematic is shown in Fig. 3.1b.

[1] Other synonyms for this technique used in literature are metal-organic chemical vapor deposition (MOCVD) and organo-metallic vapor phase epitaxy (OMVPE).

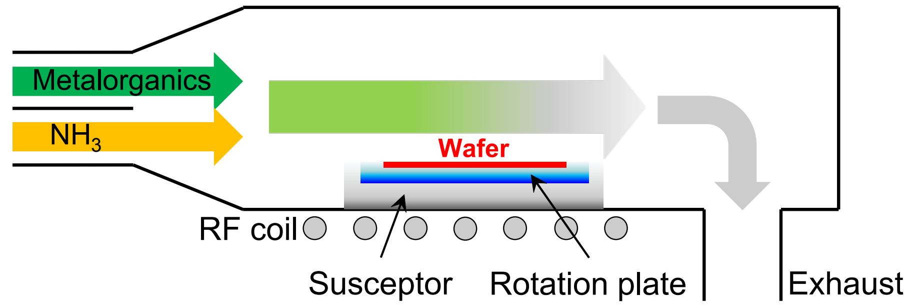

(a) AIX 200/4 RF-S reactor with horizontal gas flow.

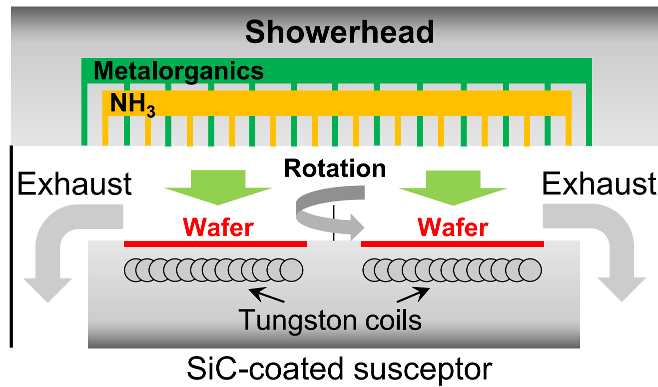

(b) CCS system in a 3 × 2-inch configuration

Figure 3.1.: Schematic drawings of the MOVPE reactors used in this thesis.

The showerhead concept distributes the process gases homogeneously over the entire showerhead lid. The inlets of the group III and V precursors are separated in small tubes in the showerhead surface, which leads to a uniform distribution of gases. Compared to horizontal flow designs, this design allows for a much smaller distance between inlets and wafer. Hence, precursors need to travel a much smaller distance in the process preventing parasitic gas phase pre-reactions. A rotating SiC-coated susceptor is heated by a tungston coil resistive heater in a CCS system.

3.1.1. Basic principle and precursors

For the supply of the group III metal species (Al, In and Ga), the standard precursors trimethylaluminum (TMAl), trimethylindium (TMIn) and trimethylgallium (TMGa) are used. For the Ga incorporation in specific layers, e.g. thin InGaN films, the precursor triethylgallium (TEGa) is more common and it was also used here for this purpose. Owing to the possibility to adjust smaller molar flows than with TMGa because of a small mass flow controller setup of the system, TEGa was tested for some quaternary AlInGaN layers as well.

The growth chemistry of GaN MOVPE contains mainly two fundamental reac-

tion paths [119]: The first pathway is the separate thermal decomposition (pyrolysis) of ammonia (NH_3) to N radicals, and the metalorganics, e.g. TMGa to radical fragments. These are dimethylgallium (DMGa) and finally monomethylgallium (MMGa) [120]. The dissociation energy for MMGa is twice as large as for DMGa leading to a much longer residence time in the gas phase [119]. Due to a temperature gradient towards the wafer surface, a boundary layer exists in proximity to the surface, in which the largest density of MMGa radicals is located. In this boundary layer, more and more MMGa is dissociated. Finally, elemental Ga is present at the wafer surface for adsorption. The second pathway describes the adduct formation of TMGa:NH_3, which can react to DMGa:NH_2 by the elimination of methane. Finally, a trimer [DMGa:NH_2]$_3$ can form, which reacts to 3GaN + 6CH_4 [119]. The adduct formation finally leads to large amounts of GaN and methane molecules and is generally assumed to be a parasitic reaction which degrades the crystal quality and consumes precursor material.

The precursor gas for nitrogen is NH_3. The temperature-dependent cracking efficiency of NH_3 is generally low at typical MOVPE temperatures in the range of 700 °C to 1300 °C with values of only several percent [120–122]. For nitride epitaxy, however, a catalyst effect occurs in the boundary layer due to the high density of Ga atoms and MMGa radicals leading to an enhanced cracking of NH_3 [121]. Further, to establish a sufficient supply of N radicals, the molar flow of NH_3 typically exceeds that of the metalorganics by 2 to 4 orders of magnitude. The choice of such high V/III molar flow ratios along with a high $T_{Surface}$ overcomes the issue that the growth rate is limited by the cracking efficiency of NH_3. Thus, the growth rate can be controlled almost linearly by the metalorganic precursor fluxes.

To reduce the probability of parasitic adduct formation, several measures are to be taken. First, metalorganics and ammonia need to be separated for as long as possible, before they are mixed in the gas phase. Here, the small distance of the CCS is quite advantageous. In the horizontal reactor, a separation plate between the group III and ammonia inlets is installed. Second, the pyrolysis of TMGa should be as fast as possible. Again, the CCS is superior, because it features a stronger temperature gradient. However, beyond the reactor design, the choice of the carrier gas has also an influence on the precursor decomposition rate. Hydrogen (H_2) generally boosts the pyrolysis [123, 124]. For this reason, H_2 is normally used as the carrier gas for nitride epitaxy. For epitaxy of In-containing layers, however, nitrogen (N_2) serves as the carrier gas since H_2 hampers In incorporation strongly [125].

As dopant sources for nitride epitaxy, bis-cyclopentadienyl-magnesium (Cp_2Mg)

and silane (SiH_4) were used for p-type (Mg acceptor) and n-type (Si donor) doping, respectively.

3.1.2. Foreign substrates for GaN epitaxy

Three substrate materials have been mainly utilized for GaN heteroepitaxy and GaN-based devices: sapphire (Al_2O_3), silicon carbide (SiC) and silicon (Si) [28, 89, 126]. Neither of them is a perfect choice. The appropriate substrate has to be selected by considering requirements for each device, e.g. material properties, industry standards or costs.

For nitrides in transistor applications, SiC is superior as a substrate, not only due to the very small lattice mismatch of 3.5 % to GaN, but also from aspects of material properties [126]. The thermal conductivity of 3.0 - 3.8 $W \cdot K^{-1} cm^{-1}$ is one order of magnitude higher than for e.g. sapphire with 0.2 - 0.4 $WK^{-1} cm^{-1}$ [89]. Hence, heat can be dissipated much more efficiently, which is an essential issue for commercial electronics. However, the fabrication process of SiC substrates is very time-consuming and, hence, these substrates are more than 100 times more expensive than sapphire [20]. Thus, SiC is rarely used in university research activities.

From an industry point of view, III nitride growth on Si is very attractive owing to several advantages, e.g. low-cost, availability of large-size substrates and all types of conductivities [127]. Further, one could envision an, although challenging, integration of III nitride devices with Si technology. The mainstream approach is to grow GaN on planar Si(111) substrates for the reason of the trigonal plane symmetry [128]. The large mismatch between the thermal expansion coefficients is a severe obstacle for GaN epitaxy on Si(111) and demands for sophisticated strain-engineering methods [129, 130]. By patterning, the coalesced film deposited by selective area growth can be reduced, which mitigates the necessity for excessive strain-compensation [131–133]. Another approach is to use Si(100) substrates, in which non-planar Si{111} facets can be uncovered by e.g. wet-chemical anisotropic etching in Si. Here, selective area growth is performed on the exposed Si{111} facets.

All heterostructures investigated in this work were deposited on two inch c-plane sapphire substrates with an offcut between 0.2 % and 0.3 % towards m-plane. With the above mentioned substrates for GaN epitaxy, this substrate choice is the most common one for research due to several reasons: First, it is reasonably cheap[2]. Second, for LED industry, sapphire has been developed for over 20 years and still

[2] The price for 2-inch sapphire wafers are comparable to the price for 2-inch silicon wafers. For larger wafer sizes, sapphire substrates are 2 to 5 times more expensive than silicon substrates but 100 times cheaper than SiC substrates.

dominates the market [134]. Thus, commercially available sapphire substrates exhibit a very high quality in terms of material properties and reproducibility. Third, the growth procedure for achieving high crystal quality buffer layers is relatively straight-forward compared to growth on silicon. The small thermal conductivity of sapphire between 0.2 - 0.4 $WK^{-1}cm^{-1}$ is, however, a major drawback for HFET applications.

Like the III nitrides, sapphire features a hexagonal unit cell [28, 89]. The thermal expansion coefficient of $7.5 \cdot 10^{-6}\,K^{-1}$ is only slightly larger than that of GaN with $5.6 \cdot 10^{-6}\,K^{-1}$ [28]. The similar thermal expansion coefficients are beneficial, because the thermal shrinking of the lattices of the sapphire substrate and the epitaxial film during cool-down process is not significant, which prevents cracking of the film. Regarding the lattice mismatch, sapphire is not an ideal candidate to grow on. The nitride crystal is by 30 ° rotated on sapphire. Still, the lattice mismatch remains rather high at -13.2 % and -15.9 % for AlN and GaN, respectively [28, 89]. The resulting large compressive strain results in immediately relaxed nuclei on sapphire. Two major challenges arise from this incoherence of nucleation and substrate: First, different polarities are possible on the Al-terminated sapphire [135], depending strongly on treatment before growth and growth conditions [105, 136–138]. Second, for AlN growth, the so-called step bouncing occurs, which leads to abrupt super steps in the layer with heights of several nm [139–141]. The origin of these super steps is likely to be found in the small surface diffusion length of Al. However, all these issues can be controlled by properly adjusting the growth parameters, which will be presented in Sec. 4.1.

3.2. X-ray diffraction

A powerful technique for the characterization of crystals in terms of structural properties is X-ray diffraction (XRD). It is a non-destructive and fast measurement, which allows for a high level of accuracy. In this thesis, XRD measurements were performed on a Panalytical X'Pert material research diffractometer (MRD) equipped with a channel-cut hybrid 2-crystal Ge(220) monochromator with X-ray mirror. The diffracted beam can either be collected with an open detector or with an additional Ge(220) analyzer crystal. The latter "Triple Axis" geometry works as a filter to reduce the beam divergence. Owing to the increased resolution, this technique is also denoted as high-resolution X-ray diffraction (HRXRD). The X-ray beam has the wavelength λ of the $K_{\alpha,1}$ line of Cu, which is 0.1540598 nm. An elaborated discussion on XRD on III nitrides can be found in literature [142]. Here, only a brief

overview on the methods used in this thesis is given.

A descriptive image for aiding comprehension is presented by a cross section through the reciprocal space in Fig. 3.2. Real lattice planes are represented by reciprocal lattice points in the reciprocal space, e.g. the $(\bar{1}015)$ point displays the constructive interference of the diffracted beam at $(\bar{1}105)$ planes. This correlation is also described by the Ewald sphere shown as a circle with a radius of the length of the incident vector $\underline{\mathbf{k}}_{\mathbf{i}}$. The length is inversely proportional to the wavelength λ of the X-ray beam. If for an appropriate configuration of crystal and diffractometer the circle crosses a reciprocal lattice point, constructive interference occurs. Then, the scattering vector $\underline{\mathbf{S}}$, which is equal to $\underline{\mathbf{k}}_{\mathbf{d}} - \underline{\mathbf{k}}_{\mathbf{i}}$ points to a reciprocal lattice point. The scattering vector $\underline{\mathbf{S}}$ is always perpendicular to the respective real lattice planes and serves as the probe to scan the reciprocal space. In the schematic, only the most relevant reflexes for this thesis are included. To fulfill the Bragg condition for asymmetric reflexes, an ω offset has to be applied. It follows that $\omega \neq \Theta$. However, for some reflexes it is necessary to use a skew geometry, in which the sample has to be tilted in Ψ to perform a quasi-symmetric scan $(\omega = \Theta)$.

In the following, a description of the most important scan-methods in this thesis is given.

Optimization scans For an accurate alignment of the sample's crystal, several optimization scans have to be performed. For this, ϕ, ω and ψ line scans are performed alternately to determine the actual peak position. The offsets, which are finally corrected, are due to several reasons like substrate offcuts, crystal mis-orientation or misalignment of the sample on the wafer holder.

Rocking curve Rocking curve is an alternative notation for an ω scan, normally agreed to be performed with open detector to assess the crystal quality of an epi-layer. The FWHM value of such an ω-scan can be correlated to the crystal quality. From a series of symmetrical (ω=Θ) scans, it is possible to extract the lateral coherence length and the mosaic lattice tilt from screw- and mixed-type dislocations [142]. The mosaic lattice twist caused by edge- and mixed-type dislocations can be assessed by quasi-symmetric scans (skew, compare the $(10\bar{1}2)$ reflex in Fig. 3.2) [142, 143]. Asymmetrical ($\omega \neq \Theta$) scans, e.g. the $(10\bar{1}5)$ scan, are often used when the intensity of skew scans is too low.

However, the exact determination of the dislocation density is a complex issue

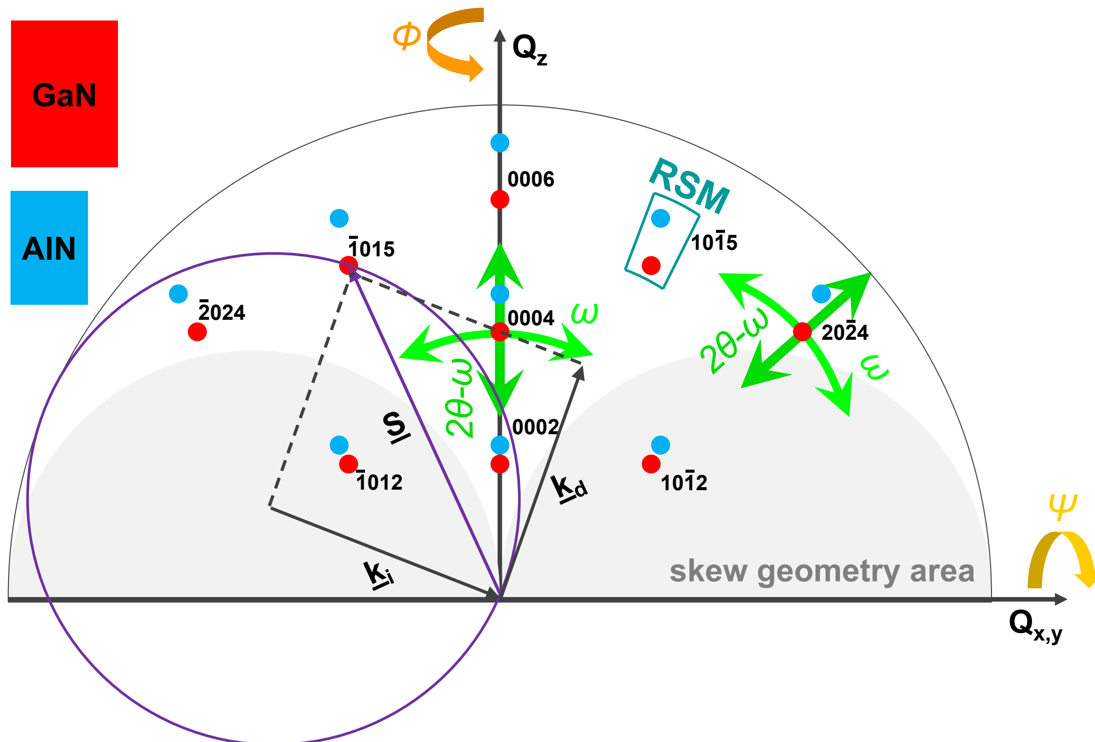

Figure 3.2.: Schematic cross section through the reciprocal space. The Ewald construction with $\underline{\mathbf{S}}=\underline{\mathbf{k}}_{\mathbf{d}}-\underline{\mathbf{k}}_{\mathbf{i}}$ is also included. The relevant reflexes for the analysis in this thesis are shown exemplarily for fully relaxed GaN and AlN schematically. The movement of the scattering vector $\underline{\mathbf{S}}$ with changing goniometer angles is illustrated by the arrows. The grey area is measureable in skew geometry.

which has led to controversial discussions [142]. Simple equations for calculating dislocation densities from full width at half maximum (FWHM) values of only a single reflex have been suggested to be adopted to GaN from other material systems [144–148]. As a result, while the FWHM values can be determined reliable and accurately, the dislocation densities depend strongly on the calculation method. Hence, comparing FWHM values is faster and often more precise within a sample series. In the case, when the exact values for the dislocation density is not needed, the comparison of the FWHM values of a symmetrical scan, e.g. the (0002), and a quasi-symmetrical scan (skew), e.g. $(10\bar{1}2)$, is sufficient.

HRXRD (0002) 2Θ-ω scan The HRXRD 2Θ-ω symmetric scan yields a high degree of information. Since symmetric scans move through all (symmetric) peaks from a heterostructure (compare the (0004) reflex in Fig. 3.2), a compositional analysis of pseudomorphic binary and ternary alloys is possible from

the analysis of the peak positions. Exemplary scans for a AlInN/GaN/AlN heterostructures taken with two different detector setups are given in Fig. 3.3a: first, a scan with an open detector (OD); second, a scan with triple axis geometry, which uses an additional analyzer crystal to define the direction of 2Θ. When the diffracted beam intensity is high enough, the triple axis (TA) geometry should be used to enable a high resolution and to reveal the so-called fringe (Pendellösung) oscillations. The fringe spacing is related to the thickness of a barrier or the periodicity of a superlattice (e.g. MQW).
For heterostructures with more than two separate layers with different compounds, e.g. multi-layer barriers, the observed fringe oscillations are more complex. Absolute peak positions are not distinct anymore. Here, numerical fittings of the measurement curves are necessary to extract structural properties. Asymetrical 2Θ-ω scans are in most cases not very informative, since the scan direction is radial in the reciprocal space and, hence, most peaks are off that line-scan (compare the $(20\bar{2}4)$ reflex in Fig. 3.2).

HRXRD reciprocal space mapping (RSM) A RSM delivers a full cross section of the reciprocal space. It consists most commonly of 2Θ-ω scans, which are taken over a specific ω-range (compare the RSM of the $(10\bar{1}5)$ reflex in Fig. 3.2). Then, a transformation from 2Θ-ω / ω values to reciprocal lattice units Q_x (in-plane) / Q_z (out of plane) is performed. An example of a $(10\bar{1}5)$ RSM for the AlInN/GaN/AlN heterostructures is given in 3.3b.
By analyzing the exact position of the layer peaks, accurate lattice constants can be derived from a RSM and with that, a very precise description of the strain state of each layer in a heterostructure can be performed. In an asymmetrical mapping, the in-plane relaxation to nominal lattice parameters is depicted intuitively by a shift in the Q_x position.

3.3. Rutherford backscattering spectroscopy

Rutherford backscattering spectroscopy (RBS) is a scattering analysis technique which yields depth-resolved information about the exact chemical composition of a crystal film. A high-energy ion beam, using 1.4 MeV He^+ ions, is scattered elastically at target atoms. The energy of the backscattered ions is measured and the energy loss can be correlated to the mass of the target atoms and the depth of the scattering event. More details on the measurement setup and technique can be found in [149].

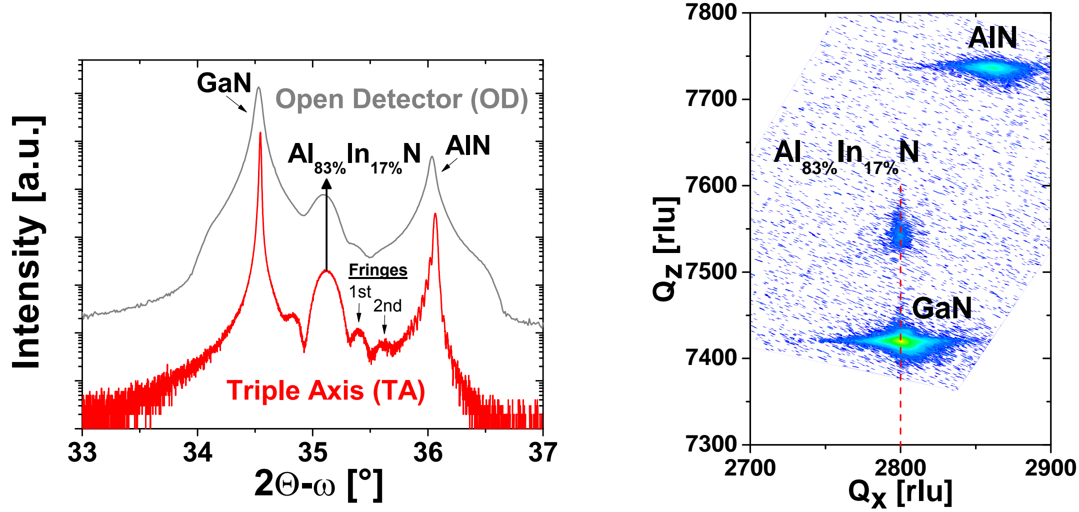

(a) HRXRD (0002) 2Θ-ω scans taken with an open detector (OD) and triple axis geometry (TA).

(b) HRXRD (10$\bar{1}$5) RSM taken in triple axis (TA) geometry.

Figure 3.3.: Exemplary HRXRD measurements on a sample with a lattice-matched $Al_{83\%}In_{17\%}N$ barrier with a thickness of 42 nm on a GaN/AlN buffer.

Exemplarily, a simple layer stack consisting of an AlN buffer with a thickness of 1 µm and a top AlInGaN layer with a thickness of 90 nm is discussed here and shown in Fig. 3.4a. The RBS spectra are shown in Fig. 3.4b.

The random spectrum (blue circles) is recorded at a scattering angle of 170 °. This ensures that the effective cross section is large, because ion channeling is prevented. This results in a large signal, which is beneficial for an accurate analysis. Since scattering events at atoms with large masses lead to a smaller loss in energy of backscattered ions, high-energy ions are correlated to heavy atoms. Hence, the signal belonging to In is located at higher energy values than the signal for Al. Because ions lose energy while moving through the crystal, the buffer structure, here AlN, is detectable at even lower energies. By taking this energy loss into account for the simulation (red curve) of the spectrum, thicknesses of individual layers can also be determined.

The channeling spectrum (green squares) is measured after alignment of the [0001] sample normal with respect to the incoming ion beam. This allows for a dominant channeling effect of ions through the crystal. To evaluate the crystal quality, the ratio of intensities of the channeling spectrum and the random spectrum, also called RBS channeling value ($\chi_{\mathrm{RBS,min}}$), is calculated. A larger $\chi_{\mathrm{RBS,min}}$ displays a weaker channeling effect owing to an inferior crystal structure. This can be related to e.g.

alloy disorder, inhomogeneities, interstitials or impurities.

Especially for quaternary AlInGaN layers, for which several compositions exhibit equal lattice constants and, hence, XRD analysis cannot separate between specific compositions, RBS is an excellent method to acquire a depth-resolved composition profile. This helps not only to determine an accurate composition, but it also reveals changes in composition with thickness. Compositional pulling effects are widely observed for In-containing layers. By using a combined method of XRD and RBS, a very accurate determination of the evolution of composition and relaxation in a quaternary AlInGaN film is possible [150].

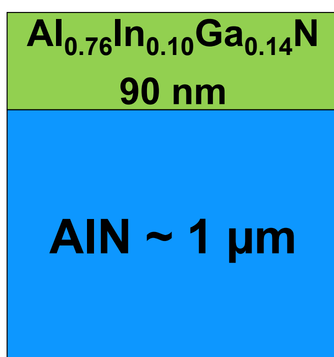

(a) Schematic layer stack.

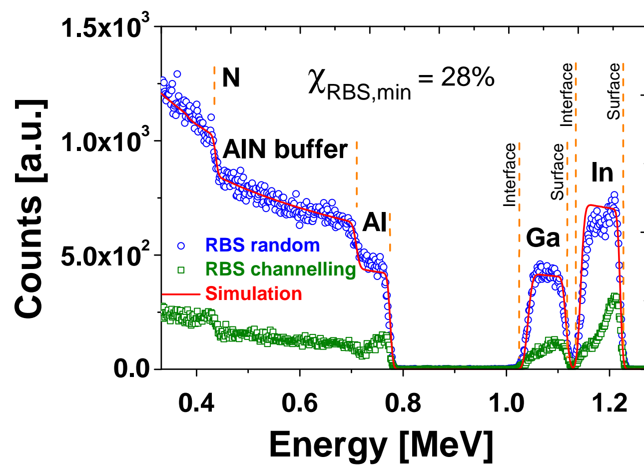

(b) RBS random and channeling spectra. For this sample, a clear separation of Al, Ga and In of the AlInGaN layer and the AlN buffer signal is possible.

Figure 3.4.: Example of RBS measurements of a AlInGaN/AlN heterostructure.

I.

Growth and structural properties of quaternary AlInGaN

Chapter 4

Growth and structural properties of AlInGaN layers on GaN

In this first experimental chapter, basic material investigations on GaN/AlN buffer structures and on quaternary AlInGaN barrier layers are presented. First, the typical GaN/AlN buffer structure on sapphire is discussed. Thereafter, several aspects concerning challenges in epitaxial growth of AlInGaN are highlighted. In the following sections, the influence of the main growth parameters on structural properties and crystal quality of AlInGaN alloys is described.

4.1. Buffer layer concept on sapphire

Prior to the discussion of experimental results on AlInGaN layers, the typical layer stack used for heterostructure field effect transistors (HFETs) is briefly introduced and shown in Fig. 4.1a. The buffer on sapphire consists of a 25 nm low-temperature (LT)-AlN nucleation layer and a 300 nm high-temperature (HT)-AlN layer followed by a 3 µm GaN layer. For the generation of a two-dimensional electron gas (2DEG), a quaternary AlInGaN layer with variable thickness in the range between 10 nm and 500 nm is used together with an interfacial 1 nm AlN spike. The important features of each layer are given in the following.

Owing to the large lattice mismatch and the resulting high compressive strain in nitride nucleation layers on sapphire, the growth sequence needs to be adjusted properly [126, 151]. Therefore, a three-dimensional growth mode is initiated in the beginning of the growth by depositing a LT-nucleation layer. Subsequently, the temperature is ramped up. This annealing step is necessary for the recrystallization of the poly-crystalline nucleation layer. As a result, a single-crystalline orientation necessary for subsequent growth is obtained [151, 152]. Then, a HT-layer can be grown with a high crystal quality. The two-temperature step growth can be applied to either GaN or AlN [153–157]. To achieve a semi-insulating behavior, e.g. for HFET applications, it is advantageous to deposit AlN before GaN. It has been shown

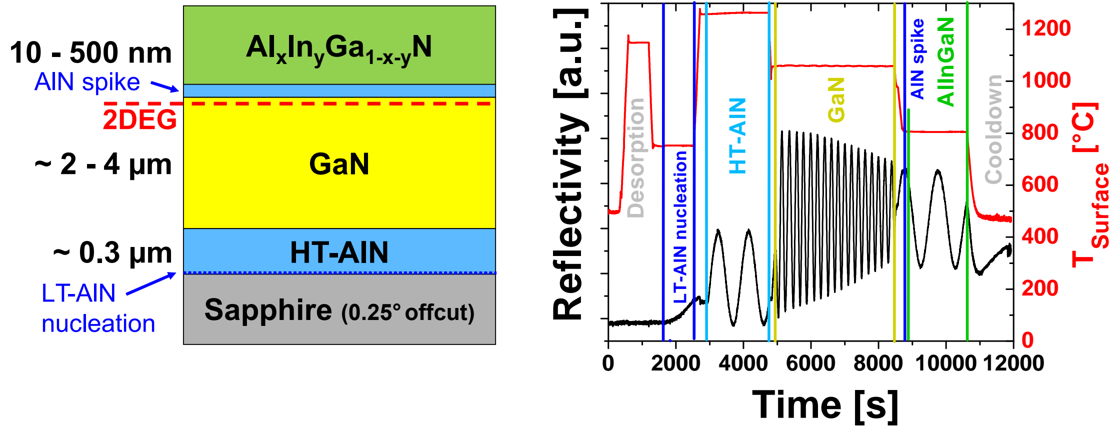

(a) Schematic layer stack of the samples investigated.

(b) Typical process temperatures and reflectance traces.

Figure 4.1.: Typical layer stack sequence on a sapphire substrate.

that oxygen is likely to outdiffuse from the sapphire and that it is incorporated in the adjacent layer up to a few hundred nm [158, 159]. Oxygen acts as a shallow donor in GaN with an ionization energy in the range of the thermal energy at room temperature [160]. Thus, GaN buffers directly grown on sapphire are typically conductive [161, 162].

This can be prevented by using an underlying AlN layer, in which the oxygen donor has a large ionization energy above 2 eV [157]. As indicated in Fig. 4.1, for all samples investigated in this work, a HT-AlN layer (1250 °C and 25 hPa) on top of a LT-AlN nucleation layer (760 °C and 50 hPa) is deposited first. As determined by wet-etch analysis [138, 151], the relatively thick (25 nm) nucleation layer and a TMAl-preflow of 10 sec ensures a pure metal-face polarity of AlN and subsequent layers[1]. The pure polarity in the whole stack is a necessity for accurate polarization engineering in the active layers.

To ensure a low dislocation density, the GaN buffer (1060 °C, 300 hPa) thickness is in the range of 3 µm. Owing to the small critical thickness of GaN on AlN, the GaN buffer layer shows a high degree of relaxation of about 90 % ± 5 % determined by HRXRD [163, 164]. The dislocation density is assessed by FWHM values of XRD rocking curves, as desribed in 3.2. Typically measured FWHM values for both AlN and the GaN buffer are 100-150 arcsec for the (0002) reflex and 500-700 arcsec for the $(10\bar{1}2)$ reflex. These FWHM values for the buffer layers on sapphire are comparable

[1]MOVPE nitride layers grown on sapphire are typically of metal-polarity owing to larger decomposition rate for N-polar material [105–107]. For certain growth conditions, however, mixed polarity of AlN has been observed [151].

to state of the art technology [151, 165]. Taking these values into account, the screw-type dislocation density is calculated to be in the range of low 10^{10} cm^{-2}, which is a typical value for GaN/AlN buffers with 1-5 µm thickness on sapphire [166–168].

On top of GaN, a quaternary AlInGaN barrier is deposited for the generation of a 2DEG at the interface. Electrical properties of such a 2DEG will be investigated in Chap. 6. The growth conditions and structural properties of AlInGaN are presented in the following sections.

A thin AlN spike between the barrier and the GaN buffer has been intensively used in literature for the enhancement of the 2DEG mobility [169–173]. Generally, the insertion of an AlN interlayer leads to a large conduction band offset in the band structure, which reduces the probability for electrons to penetrate into the barrier. Hence, alloy disorder scattering in the barrier becomes less probable. The improved electron confinement at the interface, however, leads to a higher sensitivity to the interface roughness [174]. Several studies on the AlN spike thickness have shown an optimum at around 1.0 nm [169, 174, 175]. For thicker AlN spikes, the interface quality decreases due to plastic deformation of the AlN spike [176, 177]. The determination of the exact thickness of AlN of approximately 1 nm is challenging and cannot be performed on every sample presented here. However, several reference studies by HRXRD, TEM and electrical measurements confirm that the target of 1 nm was successfully achieved by an AlN growth time of about 1 min.

The corresponding growth surface temperature ($T_{Surface}$) and typical reflectance traces at 620 nm for the layer sequence are plotted in Fig. 4.1b. Growth oscillations with a constant average intensity are observed for all layers, which is a clear sign for a stable epitaxial growth process.

4.2. Growth challenges of AlInGaN

The fabrication of quaternary AlInGaN layers is generally challenging. Several issues have to be addressed. The most critical aspect is probably the growth surface temperature ($T_{Surface}$) which determines the In incorporation. Unlike for the binary compounds, GaN and AlN, or for the ternary alloy AlGaN, for which the process window of suitable growth conditions is rather wide, for AlInGaN, it turns out to be quite narrow. AlN is usually grown at high $T_{Surface}$ between 1100 °C and 1400 °C [106, 107]. For GaN, $T_{Surface}$ is lower between 900 °C and 1100 °C [154]. Thus, ternary AlGaN can be grown at high $T_{Surface}$ and in a wide range. For AlGaN, the composition is usually weakly dependent on $T_{Surface}$. It is rather affected by other growth parameters, e.g. precursor flux and reactor pressure [178, 179].

For growth of In-containing nitride layers, the large vapor pressure of In has to be considered. Compared to Ga and Al, In is the most volatile element leading to a strong desorption rate [180, 181]. Further in comparison with the bond strengths of AlN and GaN, the one of InN is weaker. To account for this, $T_{Surface}$ has to be chosen as low as possible. For pure InN growth, a $T_{Surface}$ between 500 °C and 650 °C is used [182, 183]. Further, the gas phase is normally intentionally saturated with the In precursor [184]. To achieve a high crystal quality for ternary InGaN and AlInN, a compromise has to be made in adjusting an intermediate temperature. As an example, for ternary AlInN lattice-matched to GaN, it is generally agreed on a $T_{Surface}$ not larger than 800 °C [151]. Based on results of thermodynamic modeling, it has been suggested to adjust $T_{Surface}$ between 700 °C and 800 °C and to use nitrogen as the carrier gas in order to prevent liquid alloy formation during epitaxy of AlInGaN [185].

Another challenging limitation for the growth of AlInGaN is the reactor pressure. For efficient In incorporation, high reactor pressures are favored. In contrast, the Al precursor has a strong tendency for pre-reactions in the gas phase at high pressure, which leads to an effective loss in Al [186–188]. Depending on the reactor design[2], this effect puts an upper limit to the pressure [188]. The upper pressure limit for effective Al incorporation in AlInGaN is estimated in this work to be 150 hPa for the horizontal-flow AIX 200/4 RF-S reactor [150].

A further complication in the growth of AlInGaN is the different strength of Al-N, Ga-N and In-N bonds. In the ideal case of a homogeneous distribution of atoms, a statistic length variation will result in a mean lattice parameter. For a real crystal, however, locally different bond lengths lead to inhomogeneities in the lattice. These result in strain variations and clustering effects on the nanoscale or even in phase segregation. Theoretical calculations predict a thermodynamically unstable mixing region for both cubic and wurtzite nitride alloys, except for AlGaN [189–194]. For In-containing ternary layers, phase segregation is predicted to start at 12 %-17 % leading to a miscibility gap in the phase diagram. However, experimental results on ternary AlInN MOVPE have overcome the predicted limit showing a much smaller miscibility gap [195]. Up to In contents of 50 %, single-phase crystals have been presented. Biaxial tensile strain is most likely to stabilize a thin single-phase layer [190, 195]. Phase separation occurred experimentally only in the highly compressively strained region. Results on MBE-grown AlInN on N-polar GaN have

[2]The effective distance from precursor inlet to the substrate has to be considered here. As an example, in an horizontal-flow reactor like the AIX 200/4 RF-S, this distance is around 100-150 mm, much larger than for a showerhead design with 5-25 mm.

shown single-crystalline AlInN over the entire composition range [98]. Hence, phase separation in nitride alloys is not an inevitable effect, but only occurs under certain growth conditions.

For quaternary AlInGaN, these considerations are important especially for higher In contents, i.e. when more than 17 % (compare lattice-matched $Al_{83\%}In_{17\%}N$) are regarded. In this case, the layers are compressively strained on GaN. On AlN, quaternary AlInGaN is always compressively strained because the lattice constants of both GaN and InN are larger than the one of AlN [87, 88].

Due to the difficulty to incorporate large In contents while maintaining a sufficient crystal quality, experimental results on compressively strained AlInGaN on GaN are rare so far. Tensile or nearly lattice-matched AlInGaN has shown clustering effects on the nanoscale, rather than a mesoscopic domain formation by phase segregation [196–200]. These In-rich clusters form potential minima, which lead to fluctuations in the bandstructure. The cluster effects are likely to appear for the reason that they compensate local strain peaks. For a specific composition, however, the grade of clustering varies strongly. It is not determined by composition alone, but also by the growth method, the growth conditions, the crystal quality and the substrate choice, which further explains the wide spread of reported material properties of AlInGaN [201].

4.3. Composition range of AlInGaN layers grown on GaN

Compared to ternary alloys, quaternary AlInGaN barrier layers have several advantages, as described in Sec. 2.6. The main aim in this work is to vary the AlInGaN composition to intentionally change the total polarization (P_{total}). This allows for the control of the internal electric field in heterostructures and, hence, it is possible to influence the electrical properties of devices. HFETs utilizing AlInGaN layers are discussed in Part II. It will be shown that by lowering P_{total} of the AlInGaN barriers, it is possible to reduce the polarization-induced carrier density in both n-channel and p-channel HFETs. This allows for a control of the V_{th} of HFETs and, hence, for a change from d-mode to e-mode behavior. Light emitting diodes (LEDs) with AlInGaN as barrier layers are presented in Part III. First, conventional GaN barriers in the multiple quantum well (MQW) are replaced by AlInGaN barrier layers. Finally, AlInGaN backbarrier layers with a large P_{total} are used in inversed p-n junction LED. The resulting large hole density is promising for the p-conductivity of such inversed LED.

In this section, crystal growth and structural characterization of AlInGaN layers

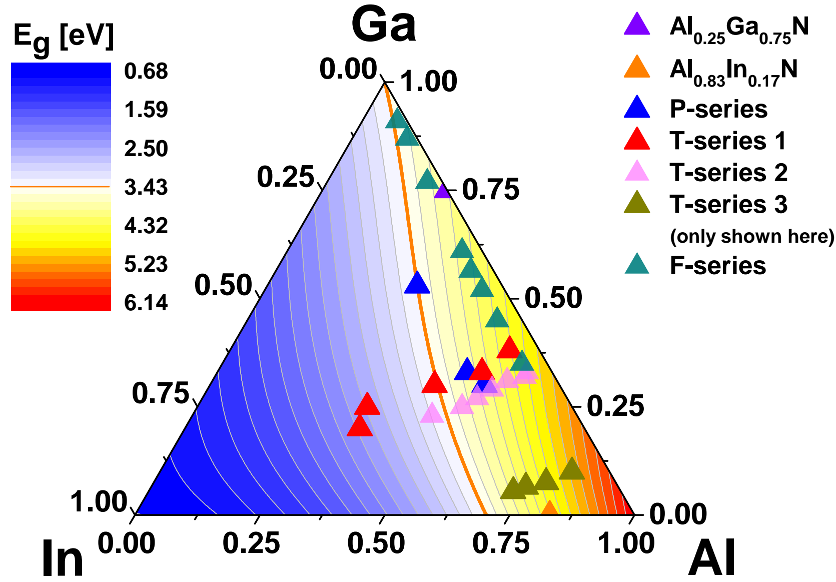

Figure 4.2.: Overview of the different sample series which are most relevant for this thesis. On the underlying bandgap contour plot, the different samples are shown in dependence of composition.

are in focus. For an accurate determination of structural properties, the thicknesses of the AlInGaN layers investigated here were chosen to be in the range of several tens of nanometers. An overview of the composition range covered by these AlInGaN samples is given in Fig. 4.2. Shown is the ternary illustration of the respective metal species of the $Al_xIn_yGa_{1-x-y}N$ with the associated bandgaps as contour lines. As previously discussed in Fig. 2.4, the orange line marks the AlInGaN compositions with bandgaps equal to that of GaN. The yellow-to-red area indicates larger bandgaps than the one of GaN. Compositions in this area are suitable for the utilization in devices: first, as barrier or backbarrier layers in HFET (Chap. 6 and Chap. 7) and second, as barrier layers in MQW in LED (Chap. 8).

Different sample series, in which a specific parameter is investigated, are plotted in different colors. All compositions were realized on similar GaN/AlN buffer structures, as discussed in Sec. 4.1. For comparison, the ternary barriers $Al_{25\%}Ga_{75\%}N$ and $Al_{83\%}In_{17\%}N$, which are commonly used in HFETs, are also shown.

Parameters in the MOVPE process which were identified to have the strongest influence on compositions are the reactor pressure P (P-series), $T_{Surface}$ (T-series 1-3) and the precursor molar flows (F-series). To identify the impact of each parameter on composition and crystal quality, each experimental series will be discussed in detail in a separate section.

4.3.1. Reactor pressure

To identify limits for an appropriate growth window, the impact of the reactor pressure P on structural properties is discussed at first. In the experimental P-series, three samples P1, P2 and P3 were grown at varying reactor pressures of 70 hPa, 125 hPa and 200 hPa, as summarized in Tab. 4.1. This pressure range is chosen to avoid unwanted gas phase pre-reactions of TMAl (compare Sec. 4.2) [186–188]. All other reactor parameters are identical for samples within the P-series.

A quite low $T_{Surface}$ of 750 °C is chosen for the P-series to ensure a sufficient In incorporation. All layers exhibit similar In contents between 15 % and 17 %, showing that In incorporation is almost unaffected by a pressure change in the investigated regime. In contrast and as expected, the Al content shows a significant change for different pressures. While sample P1, grown at 70 hPa, has 55 % Al, the Al content is almost halved to 30 % for sample P3 grown at 200 hPa. This is illustrated in a composition plot in the upper part of Fig. 4.3. As a result, the growth rate decreases from 5.2 nm/min to 3.0 nm/min.

The nominal and residual strain, calculated by the methodology presented in Sec. 2.2, are shown in the bottom plot of Fig. 4.3. Generally, the increasing compressive strain for larger reactor pressures is due to the lower Al content in the layer. While samples P1 and P2 are pseudomorphically grown on GaN with a residual strain equal to the nominal strain of -0.38 % and -0.72 %, respectively, sample P3 with a high nominal strain of 1.19 % is partially relaxed. This is clearly visible in XRD $(10\bar{1}5)$ RSM taken with an open detector, shown in Fig. 4.4. The residual strain is only 1.06 % which corresponds to 35 % relaxation. The XRD peak for this 30 nm AlInGaN layer shifts to lower Q_x values, indicating an increase of the in-plane lattice constant a. The theoretical position of a fully relaxed layer (R = 100 %) is also plotted.

To compare the relaxation behavior of compressively strained AlInGaN layers to ternary InGaN layers, the preudomorphic sample P2 is regarded. An InGaN layer with the same strain state as sample P2 with -0.72 % would contain about 6 % In. Such a layer exhibits a theoretical critical thickness[3] of about 20 nm [204]. The much larger thickness of 34 nm of sample P2 indicates that the critical thickness of AlInGaN might be generally larger compared to InGaN.

For additional information on the crystal quality of these samples, RBS channeling measurements were performed. The RBS channeling values $\chi_{\text{RBS,min}}$ are steadily in-

[3]It is noted here that former models for the critical thickness developed for other material systems are not appropriate for nitrides [202, 203]. The latest published model derived from InGaN is the most relevant one for this thesis [204].

Sample	$T_{Surface}$ [°C]	P [hPa]	Al [%]	In [%]	Ga [%]	$\chi_{\text{RBS,min}}$ [%]	t_{bar} [nm]	r_{Growth} [nm/min]
P-series								
P1	750	**70**	55	15	30	3	52	5.2
P2	750	**125**	50	17	33	5	34	3.4
P3	750	**200**	30	17	53	8	30	3.0
High $T_{Surface}$ and low $T_{Surface}$ samples								
HT	**813**	70	62	5	33	2	70	4.7
LT	**722**	70	48	29	23	22	75	5.0

Table 4.1.: MOVPE conditions and structural properties of AlInGaN layers grown either at varying reactor pressure P (samples P1, P2 and P3) or at varying $T_{Surface}$ (samples HT and LT). Published in [150].

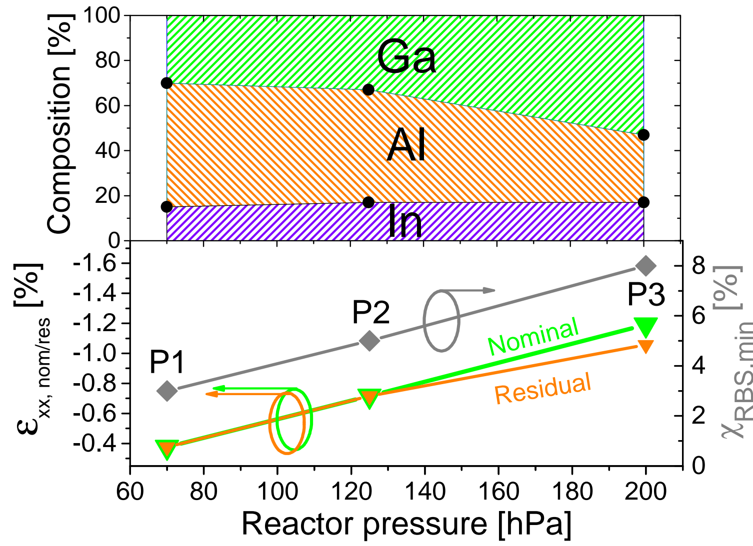

Figure 4.3.: Compositions determined by RBS (upper plot), nominal strain ε_{nom}, residual strain ε_{res} and $\chi_{\text{RBS,min}}$ channeling values (bottom plot) for different reactor pressures.

creasing from sample P1 to P3, visible in the bottom plot of Fig. 4.3. This shows that the AlInGaN crystal quality degrades with larger compressive strain. The stronger gas phase pre-reactions might also be partly responsible for this degradation. Hence, to suppress the pre-reactions and to establish a sufficient Al incorporation, the lowest pressure investigated here (70 hPa) is used for all further experiments.

4.3.2. Growth surface temperature

After the reactor pressure P has been optimized in Sec. 4.3.1, the growth surface temperature $T_{Surface}$ is the most critical parameter in MOVPE processes. The

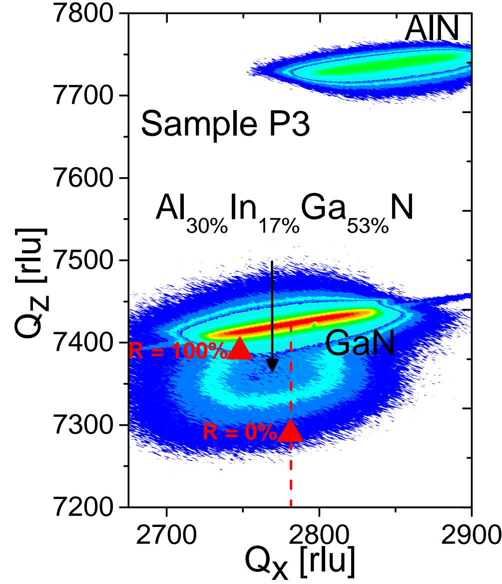

Figure 4.4.: XRD ($10\bar{1}5$) RSM taken with an open detector of sample P3. The dashed red line in the image illustrates the Q_x position of the GaN buffer peak. The red triangles illustrate the theoretical positions of sample P3 assumed to be pseudomorphically grown (R = 0 %) or fully relaxed (R = 100 %).

influence of $T_{Surface}$ on the AlInGaN composition, especially on the In incorporation, is under study here.

Starting from the pseudomorphic sample P1 with the highest crystal quality within the P-series, which was grown at 750 °C, $T_{Surface}$ was both increased to 813 °C for the HT-sample (HT: high temperature) and decreased to 722 °C for the LT-sample (LT: low temperature) [150]. The growth conditions and structural properties of the HT- and LT-sample are listed in Tab. 4.1 (bottom).

As expected, a higher $T_{Surface}$ leads to a strongly reduced In content in the layer due to the increased desorption rate [180, 181]. The In content decreases from 15 % achieved at 750 °C for sample P1 to only 5% achieved at 813 °C for the HT-sample. The reduced In incorporation results in a lowered growth rate from 5.2 nm/min to 4.7 nm/min. The Al-to-Ga content ratio remains constant. Hence, it can be concluded that the incorporation of Al and Ga atoms is uneffected by the change in $T_{Surface}$.

In the case of a reduced $T_{Surface}$ to 722 °C for the LT-sample, the In content reaches a large value of up to 29 %. The Al-to-Ga content ratio changes slightly by about 10 %. For this sample, a very large channeling value $\chi_{\mathrm{RBS,min}}$ of 22 % was measured. The HT-sample shows the highest crystallinity, manifested by the lowest $\chi_{\mathrm{RBS,min}}$ of 2 % of all samples shown here. The larger $\chi_{\mathrm{RBS,min}}$ for samples

with higher In contents is direct evidence for increased alloy disorder. This is in full agreement with several results for other ternary In-containing layers [205]. However, by comparing the $\chi_{\mathrm{RBS,min}}$ value with those of ternary AlInN layers with similar In contents, the quaternary layers appear to have a better crystallinity. This can likely be referred to the presence of Ga, which might enhance miscibility and suppress phase segregation effects in AlInGaN [194].

Direct comparison of HT-sample and LT-sample

The dramatic change in the AlInGaN composition of the HT- and LT-sample has a strong influence on the lattice parameters and, hence, on the strain state of AlInGaN on GaN [150]. To gain insight into the strain, HRXRD RSMs shown in Fig. 4.5, were measured. While the AlInGaN peak of the HT-sample is located between the GaN and AlN buffer peaks, and exactly on a vertical line with the GaN buffer peak indicating pseudomorphic growth, the peak of the LT-sample is shifted to the lower left relative to the GaN peak.

For the fully strained HT-sample, the elastic deformation of AlInGaN can be analyzed to calculate the Poisson ratio and to compare it to the ratio of the elastic constants for AlInGaN. The elastic constants for wurtzite binary nitrides are still controversially discussed [206–209]. From HRXRD (0004) and (20$\bar{2}$4) RSMs, not shown here, the actual lattice parameters were determined to be a = 3.181 Å and c =5.073 Å. Considering the nominal lattice parameters of a_{nom} = 3.189 Å and c_{nom} = 5.185 Å, the Poisson ratio is determined to be -0.536 [88]. The obtained value is in very good agreement with the ratio of the elastic constants $-2C_{13}/C_{33} = -0.540$ with C_{ii} values, calculated with a composition-dependent formula [209].

The AlInGaN peak position of the LT-sample is shifted to lower Q_x values in Fig. 4.5b. This shift indicates an incoherent growth for most of the layer thickness. The agreement of the measured peak, albeit quite broad and weak, with the theoretical position of a fully relaxed lattice, indicated as a red triangle, is reasonable. As the relaxed peak is the only detectable AlInGaN peak with a significant intensity, the relaxation is likely to occur in an early stage of the growth. An excellent agreement between the nominal lattice constant, calculated from RBS composition with Vegard‘s law, and the HRXRD measured ones is found. The relative deviation is in the range of 10^{-4}. Further, the broader and less intense appearance of the peak of the LT-sample confirms the lower crystal quality already determined by RBS.

AFM measurement results are shown in Fig. 4.6. While the HT-sample exhibits a smooth surface with a step flow pattern, a hillock-like morphology is observed

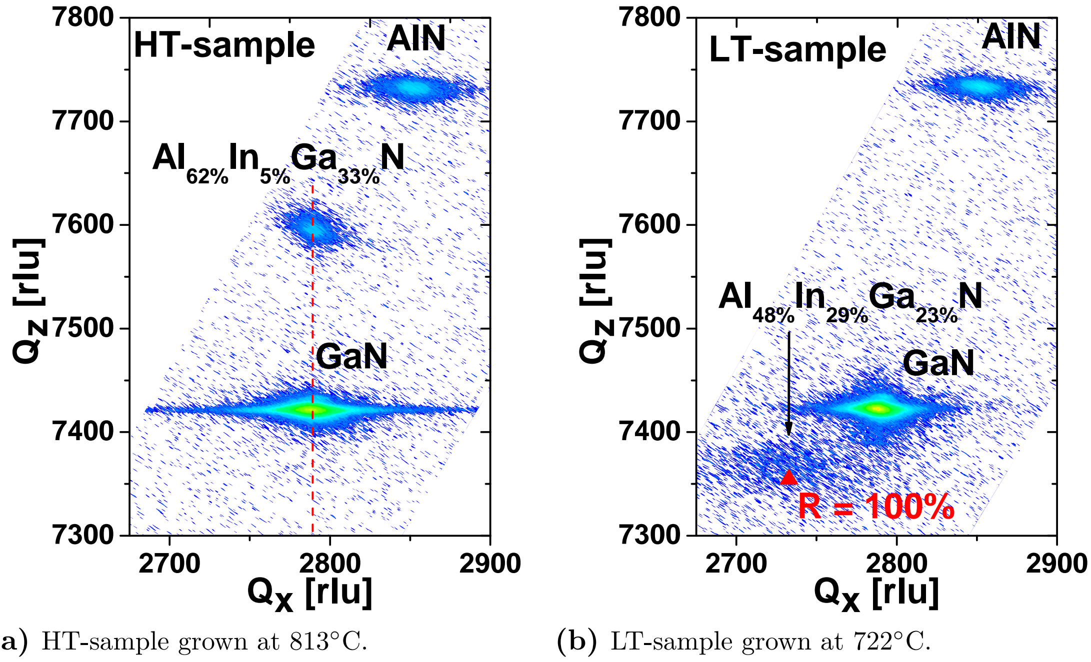

(a) HT-sample grown at 813°C.

(b) LT-sample grown at 722°C.

Figure 4.5.: HRXRD (10$\bar{1}$5) RSMs in triple axis geometry.

for the LT-sample. With this change in morphology, the roughness increases from 0.5 nm for the HT-sample to 1.5 nm for the LT-sample, further confirming the lower crystal quality for the LT-sample with larger In contents. Such a transition from 2D step flow growth during epitaxy at high temperatures to 3D island formation at low temperatures has widely been reported for ternary In-containing layers [205, 210, 211]. Similar findings have been observed for AlInGaN for lower $T_{Surface}$ and are believed to stem from a decreased adatom surface diffusion length [212, 213]. Especially the different bond strengths of the Al-to-N and In-to-N bonds lead to locally Al-rich or In-rich phases, which have a catalytic effect on island formation. This is in agreement to theoretical studies which have stated that island nucleation is correlated to the adatom density [214, 215]. For the LT-sample, the most intuitive root cause for hillock formation is that relaxation leads to local elastic deformations [150]. This relaxation is studied in more detail in the next paragraph.

Relaxation sub-layer model for compressively strained AlInGaN on GaN

In the following, a closer look at the strain evolution and the associated relaxation phenomena in compressively strained AlInGaN is presented. From this discussion, a layer model for relaxation with discrete sub-layers is derived [150].

For both the tensile strained HT- and the initially compressively strained LT-

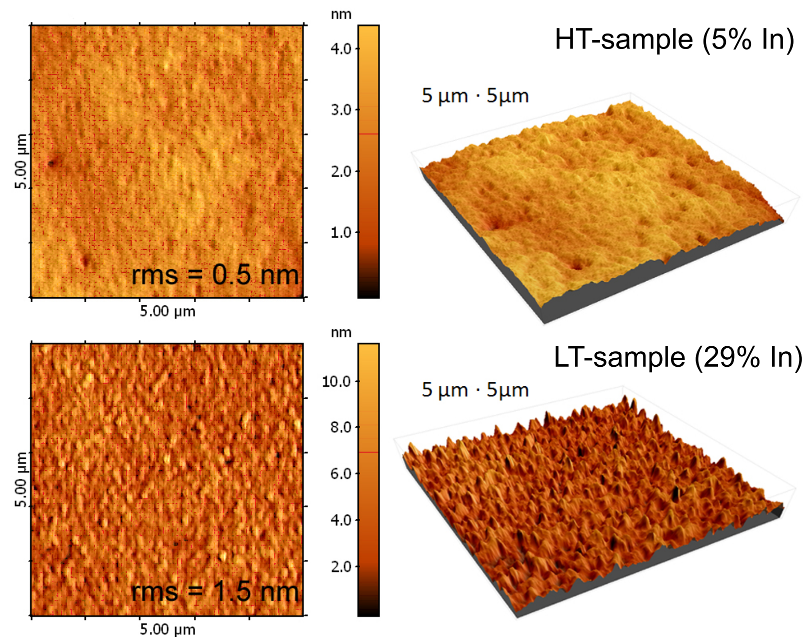

Figure 4.6.: AFM 5 µm · 5 µm scans of the HT-sample (top) and the LT-sample (bottom) in planar illustration (left) and 3D perspective (right).

sample, depth-resolved RBS measurements are shown in Fig. 4.7. The measurement curve of the HT-sample in Fig. 4.7a can be fitted with a 70 nm thick homogeneous $Al_{62\%}In_{5\%}Ga_{33\%}N$ layer. This is not the case for the LT-sample (Fig. 4.7b). The composition is changing strongly with depth. For the In signal, the increase in intensity starting at the AlInGaN/GaN interface at about 1.15 MeV up to the surface at about 1.25 MeV is an obvious feature. To account for this increase, a multi-layer structure, as shown in the inset of Fig. 4.7b, is used to fit the RBS spectrum. A minimum of six discrete sub-layers is necessary for a succesful fit. A larger number of sub-layers would increase the complexity strongly. To increase the accuracy, the increment in thickness of each sub-layers is not constant. The sub-layer structure is separated in 5 nm increments near the interface, followed by four 10 nm sub-layers and a final 30 nm sub-layer. The Al content is constant at 48 % for all sub-layers. The In content increases from 19 % to 29 %, accompanied by a decreasing Ga content from 35 % to 23 %. A competition of Ga and In atoms to be adsorbed on the surface is plausible for the reason that AlGaN layers prefer Ga-terminated surfaces and In-containing layers prefer In-terminated surfaces [216, 217]. Hence, it can be assumed that Al atoms are adsorbed most effectively in AlInGaN layers and that In is likely to replace rather Ga than Al at the surface.

Based on the composition from RBS of 29 % In, 48 % Al and 23 % Ga for the topmost 30 nm layer, the lattice mismatch to GaN is calculated to be -2.10 %. Such

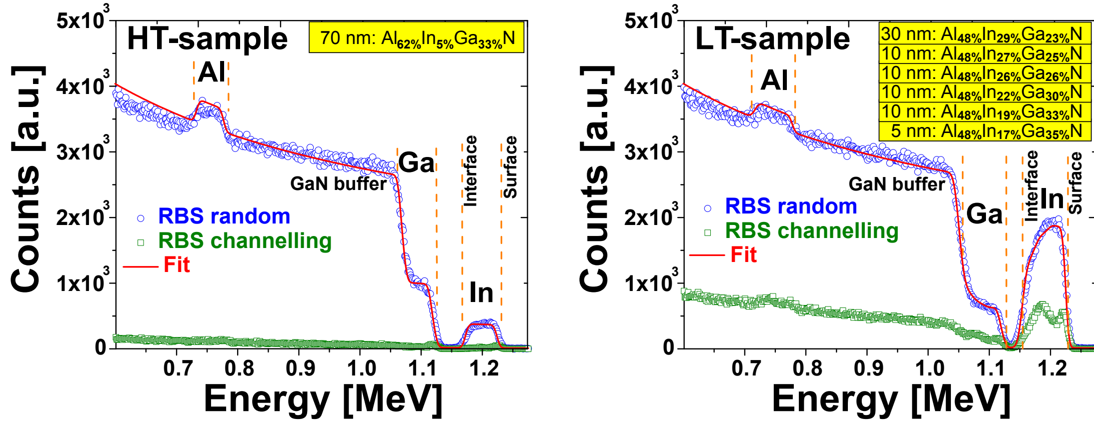

(a) HT-sample: A good fit is obtained for a homogeneous composition.

(b) LT-sample: A good fit is obtained with a multi-layer structure with changing In and Ga contents in AlInGaN.

Figure 4.7.: RBS spectra: The blue dots represent the random measurement, the green squares represent the channeling signal, and the red curves are simulations. The compositions are given in the insets.

a high strain is energetically unfavorable in a thin film, which explains that this composition cannot be realized at the AlInGaN/GaN interface. This strain state would correspond to ternary InGaN with 19 % In with a theoretical critical thickness of around 4 nm [204]. However, there is no experimental evidence that such an InGaN/GaN structure can be grown pseudomorphically at all.

The increasing In content for larger layer thicknesses, also known as "In pulling", has been reported before for thick ternary InGaN layers [218]. When a compressively strained layer reaches a critical thickness, relaxation occurs leading to larger in-plane lattice constants [204, 219]. In atoms segregate to relaxed areas, at which In incorporation is enhanced. The intuitive image of the wider In-N bonds favoring a larger space in the lattice depicts this effect well.

To gain further information regarding the relaxation, the HRXRD 2Θ-ω scan for the LT-sample was fitted, shown in Fig 4.8. Neither a pseudomorphic nor a fully relaxed layer fits the scan well. Therefore, a simulation was performed by taking the previously introduced multi-layer model into account. By splitting the layer into a six-fold stack, the relaxation can now be adjusted for each sub-layer. Although in the measured HRXRD scan only weak fringe oscillations are observed due to an inferior crystal quality and a rough interface, the envelope of the multi-layer fit is after appropriate adjustment of the relaxation of each layer perfectly consistent with the scan. The exact values for the relaxation of each sub-layer are plotted as a function of the layer thickness in the bottom part of Fig. 4.9 together with the graded

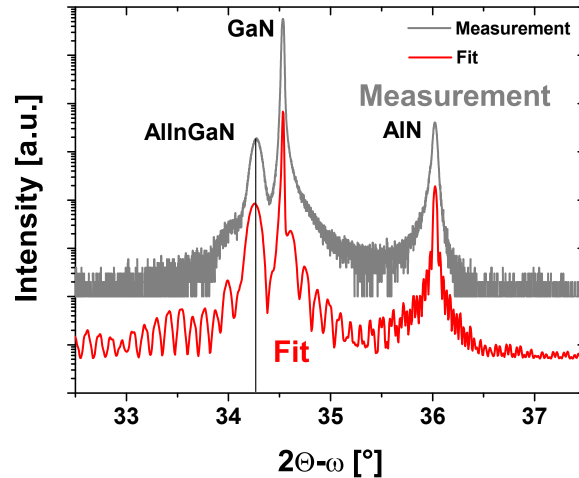

Figure 4.8.: HRXRD (0002) 2Θ-ω scan for the LT-sample (grey curve). The fit based on the six-fold multi-layer model derived by RBS is also shown (red curve).

In content derived from the multi-layer model. The general trend of an increasing relaxation is obvious. The two first sub-layers are grown pseudomorphically up to a critical thickness of 15 nm at which an In content of 19% is reached. In the following 30 nm, the lattice relaxes almost fully with a simultaneous increase in In content to 27 %. The uppermost 30 nm are fully relaxed with an almost constant In content of 29 %.

The fitting results confirm the aforementioned assumption that the uppermost part of the AlInGaN layer is dominant in HRXRD mapping analysis. The lattice of the buried sub-layers likely changes continuously. Thus, constructive interference for these layers is very weak, which explains the lower intensity of the AlInGaN peak in the RSM of the LT-sample in Fig. 4.5 compared to the one of the HT-sample. Additionally, the continuously changing AlInGaN composition makes the complete barrier layer undefined and inhibits the appearance of fringe oscillations in the HRXRD (0002) 2Θ-ω scan.

The upper plot in Fig. 4.9 shows the calculated in-plane nominal strain ϵ_{nom} and the measured residual strain ϵ_{res}, which takes the relaxation determined by HRXRD into account. Owing to the increased In content, the nominal compressive strain shows a steady trend from -0.80 % to -2.10 %. Near the interface, the residual strain is likely to have the same value as the nominal one of -0.80 %, because of fully strained sub-layers. At the specific critical thickness, here at about 15 nm, relaxation and In pulling start. A limitation for strain generation is determined to be about -1.1 % by taking a homogeneous layer with an average composition in lateral

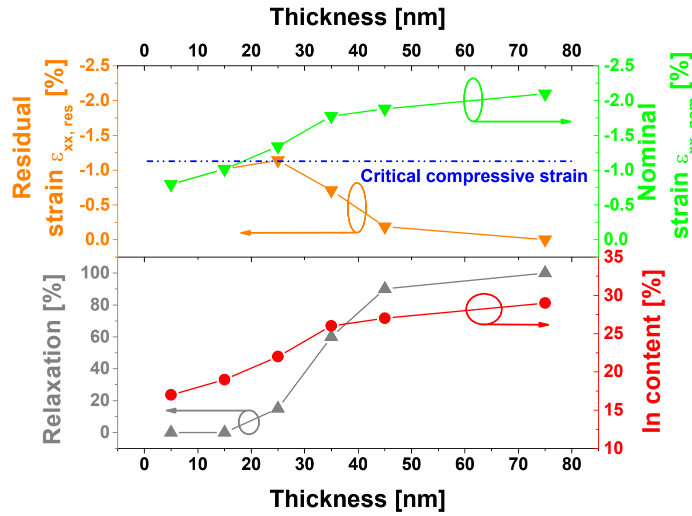

Figure 4.9.: Relaxation (grey curve), In content (red curve), nominal strain (green curve) and residual strain (orange curve) as functions of the AlInGaN layer thickness for the LT-sample.

dimensions into account. These results lead to the assumption that, for AlInGaN layers, compressive strain generation at an interface is limited by a possible change of the initial AlInGaN composition. Although growth conditions would allow for a high In content and high compressive strain of the first monolayers, a pseudomorphic lattice with less In is favored. A similar tendency of a limit for maximum In content has also been found for InGaN layers with thicknesses of about 100 nm [220]. By considering the limit of strain generation at an AlInGaN/GaN interface, it is in principle possible to predict the relaxation of any AlInGaN composition on a GaN buffer and to predict compositional limits, e.g. the maximum In content possible in an AlInGaN layer for pseudomorphic growth. This might help designing strain-dependent polarization-engineered heterostructures, used for devices like HFETs or LEDs.

Crystal quality degradation with relaxation

By regarding the RBS channeling spectrum (green) in Fig. 4.7b, the crystal quality of the LT-sample can be correlated to relaxation phenomena. The relaxation is accompanied by In pulling. Thus, the depth-resolved In content is regarded here in more detail. The In signal of the channeling spectrum (green) reveals a significantly different shape compared to the random spectrum (blue) with a clear peak at the depth, at which the In content is reaching its maximum. This behavior can be understood by the relaxation sub-layer model. The first few monolayers are fully

Sample	$T_{Surface}$ [°C]	P [hPa]	Al [%]	In [%]	Ga [%]	R [%]	t_{bar} [nm]	r_{Growth} [nm/min]
T-series 1								
T1	**786**	70	56	6	38	0	46 (HRXRD)	2.3
T2	**741**	70	53	14	33	0	48 (HRXRD)	2.4
T3	**699**	70	45	25	30	80	54 (HRXRD)	2.7
T4	**654**	70	34	41	25	100	$\sim$ 60 (LayTec)	3.0
T5	**622**	70	35	45	20	100	$\sim$ 60 (LayTec)	3.0

Table 4.2.: MOVPE conditions and structural properties of the T-series 1 with AlInGaN layers grown at varying $T_{Surface}$.

strained on the GaN buffer. Then, the lattice is continuously relaxing after 10 nm to 15 nm, which causes disorder and inhomogeneity in the layer. With that, the channeling signal increases. The maximum, which corresponds to the lowest quality within the crystal, is located at the depth of 45 nm at which the In content saturates due to a fully relaxed crystal. From this depth, the crystal quality slightly improves, which results in a decreasing channeling signal [150].

In incorporation

The prior discussion of the analysis of the structural properties of selected samples revealed the details of strain evolution and relaxation. However, it is further very important to identify the amount of In which can generally be expected in an AlInGaN layer at a specific $T_{Surface}$. This dependence of the In incorporation on $T_{Surface}$ is discussed here.

To present a wider sample base for this analysis, T-series 1 is included here. This series contains samples T1 to T5 with a thickness of about 50 nm, for which $T_{Surface}$ was varied in a wide range of $T_{Surface}$ between 786 °C for sample T1 and 622 °C for sample T5 (Tab. 4.2). For these samples, RBS measurements are used for the initial composition determination, which is further verified by HRXRD.

HRXRD (0002) 2Θ-ω scans of the T-series, shown in Fig. 4.10, reveal a shift of the quaternary peak to lower diffraction angles. This is related to a strongly enhanced In content of 6 % for sample T1 to 45 % for sample T5. While samples T1 and T2 are pseudomorphic, samples T3, T4 and T5 are either partially or fully relaxed.

In Fig. 4.11a, the In contents for the T-series and for the LT- and HT-samples are plotted as a function of $T_{Surface}$. A linear fit has been applied to both series and a similar temperature-dependent In incorporation factor of about -0.25 $\pm$ 0.02 %K^{-1} is determined. This value is consistent with observations in literature for ternary AlInN

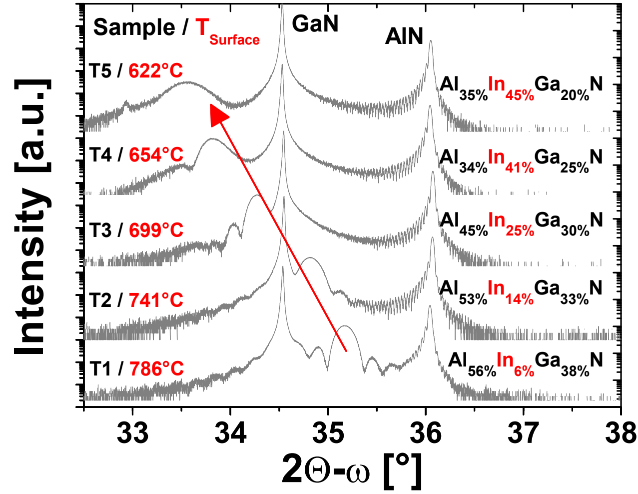

Figure 4.10.: HRXRD (0002) 2Θ-ω scans for a sample series, for which $T_{Surface}$ is different. The quaternary peak is shifted to lower angles for an increasing In content due to a larger nominal lattice constant c.

layers [181]. For InGaN, the factor is slightly smaller in the range of -0.16 %/°C to -0.26 %/°C [221]. The stronger In incorporation in Al-containing alloys is likely caused by the locally-induced tensile strain of AlN, which enhances the probability for InN formation [213]. This also explains the shift towards higher absolute In contents for the LT- and HT-samples (Fig. 4.11a), which exhibit a larger Al-to-Ga content ratio (compare Tab. 4.1 and Tab. 4.2) due to different values of precursor flow, total flow as well as different reactor setups. The influence of the precursor flows on In incorporation is discussed in Sec. 4.3.3 in more detail.

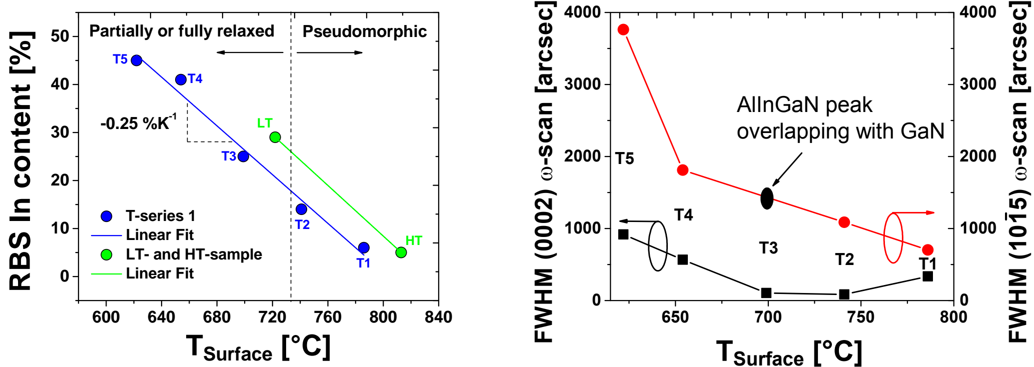

(a) In content, determined by RBS and HRXRD, for two sample series: Samples T1-T5 as well as LT- and HT-sample.

(b) FWHM values of rocking curves for samples T1-T5. The black squares are for (0002) ω-scans and the red circles are for $(10\bar{1}5)$.

Figure 4.11.: Effect of $T_{Surface}$ on In incorporation and crystal quality.

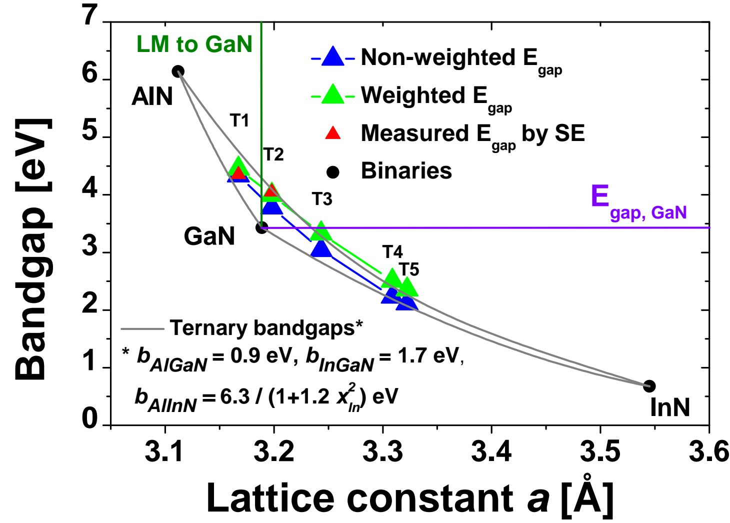

Figure 4.12.: Bandgap diagram plotted over the lattice constant a. Blue triangles represent theoretical values for samples T1 to T5 with a non-weighted bandgap. Green triangles represent values with a weighted bandgap. The red triangles are values measured by SE.

On the basis of the T-series 1 with samples T1-T5, the crystal quality is qualitatively analyzed by XRD FWHM rocking curve measurements, shown in Fig. 4.11b. While the FWHM values of the $(10\bar{1}5)$ reflex is increasing steadily for lower $T_{Surface}$, the FWHM values of the (0002) reflex show a minimum in the range of 700-740 °C. However, the overall trend to higher FWHM values for both the $(10\bar{1}5)$ and the (0002) reflex for lower $T_{Surface}$ are obvious, indicating generally larger dislocation densities. This confirms the inferior crystal quality at lower $T_{Surface}$, already observed in RBS measurements and HRXRD analysis.

Bandgaps

In the following, the bandgaps of samples T1 to T5 are discussed. In Fig. 4.12, measured values by spectroscopic ellipsometry (SE) together with theoretical values calculated by the two versions of bandgap formulas given in Sec. 2.3 are plotted over the lattice constant a. The two versions are a simplified non-weighted bandgap Eq. 2.11 (blue triangles) and a weighted bandgap Eq. 2.13 (green triangles). The following bowing parameters were used: $b_{AlGaN} = 0.9\,\text{eV}$, $b_{InGaN} = 1.4\,\text{eV}$ and $b_{AlInN} = A_1/(1 + A_2 \cdot x_{In}^2)$, with A_1=6.4 eV and A_2=1.2 [91, 101].

Owing to the increasing In content from sample T1 to T5, a decreasing trend from large to small bandgaps is observed in the T-series 1. The bandgaps of samples T1 and T2 are larger than the one of GaN, which is a necessity for a potential barrier application of AlInGaN in GaN-based heterostructures. For these two samples, a

measurement of the bandgaps by SE was possible, also plotted as red triangles [91]. For sample T2, it is obvious that the agreement to the weighted bandgap is better compared to that to the non-weighted bandgap. For sample T1, the difference between the measured value and the weighted bandgap might be caused by the residual tensile strain, which stretches the lattice in-plane resulting in a smaller bandgap [222]. For samples T3 to T5, a measurement by SE was not possible likely due to the inferior crystal quality. However, the bandgap of sample T3 is theoretically almost identical to the one of GaN. The bandgaps of samples T4 and T5 are definitely smaller than the one of GaN. Further, all samples except T1, which is tensile strained, are compressively strained. In the high In-containing region (samples T4 and T5), the weighted bandgap formula delivers values for AlInGaN bandgaps which are larger than the bandgaps of ternary AlInN at an equal lattice constant a. Hence, this formula might not be applicable for AlInGaN compositions with very large In contents ($> 30\,\%$).

Electrical properties of this T-series 1 will be presented in Chap. 6.

4.3.3. Molar flow of metalorganic precursors

As shown in the previous two sections, both $T_{Surface}$ and the reactor pressure have a strong influence on gas phase precursor pre-reactions, mass transport and ad- and desorption rates. The effect on the AlInGaN composition can be briefly summarized as follows: First, the reactor pressure needs to be low enough to suppress Al precursor pre-reactions for sufficient Al supply. Second, the window for $T_{Surface}$ is quite small: $T_{Surface}$ needs to be low enough to prevent desorption of In and, hence, to achieve a large In content and it needs to be high enough to obtain a sufficient crystal quality.

To adjust the relative amount of the metal species Al and Ga effectively, the molar flow of TMAl and TMGa can be varied. To compensate for strong deviations in the growth rate for different AlInGaN compositions due to an additional amount of a specific precursor, the total molar flow should be kept almost constant [223].

In the following, the F-series (F for flow), containing samples F1 to F6, with AlInGaN barriers grown with different TMAl and TMGa fluxes is regarded. Growth conditions and composition, as well as the layer thicknesses and growth rates are given in Tab. 4.3.

These samples are designed to be processed as HFETs. Thus, the AlInGaN barrier thicknesses are chosen to be below 20 nm. Although the total molar flow was kept constant to maintain a similar growth rate, a change from 4.7 nm/min to 6.3 nm/min

Sample	TMAl [µmol/min]	TMGa [µmol/min]	$\frac{TMAl}{TMGa}$	Al [%]	In [%]	Ga [%]	t_{bar} [nm]	r_{Growth} [nm/min]
F-series								
F1	20.9	8.8	2.4	54	5	41	14	4.7
F2	18.3	11.0	1.7	50	5	45	14	4.7
F3 ($F3_{Ref}$)	15.7	13.2	1.2	43	5	52	15 (235)	5.0
F4	13.1	15.4	0.9	36	4	60	15	5.0
F5	10.5	17.6	0.6	28	3	69	16	5.3
F6 ($F6_{Ref}$)	3.9	22.8	0.2	11	2	87	19 (50)	6.3

Table 4.3.: MOVPE conditions and structural properties of AlInGaN layers grown at different TMAl-to-TMGa molar flow ratios. The TMIn flux is constant at 31.5 µmol/min. $T_{Surface}$ and reactor pressure are equal for all samples with values of 815°C and 70 hPa, respectively.

was unavoidable for larger Ga contents with smaller TMAl-to-TMGa ratios as the growth rate for GaN is typically larger than that for AlN. As a result, the AlInGaN thickness increases from 14 nm for sample F1 to 19 nm for sample F6.

Because the determination of a quaternary composition for layers with a thickness of about 20 nm is quite challenging[4], thick reference samples $F3_{Ref}$ (235 nm) and $F6_{Ref}$ (50 nm) were grown under identical reactor conditions as the thinner samples F3 and F6. The thick reference samples can be analyzed depth-resolved by RBS. Taking the composition results at the specific thickness of the associated HFET sample into account, the HRXRD (0002) 2Θ-ω scans of the thinner HFET samples can be fitted accurately.

The change in the Al and Ga content adjusted by different TMAl-to-TMGa molar flow ratios is obvious in Tab. 4.3. While the Al content decreases from 54% for sample F1 to 11 % for sample F6, the Ga content increases from 41 % to 87 %. A reduction in the In content from 5 % to 2 % is most likely caused by the diminishing catalytic effect[5] of Al on In incorporation at such low values of TMAl flow [213, 223–227].

To achieve the highest possible crystal quality, all samples were grown at a quite high $T_{Surface}$ of about 815 °C and at a reactor pressure of 70 hPa. A benchmark for the crystallinity is obtained by RBS channeling of the reference samples. The near-lattice-matched sample $F6_{Ref}$ exhibits a very low $\chi_{RBS,min}$ of 1 %, reaching a value which is typical for binary GaN. This low value is related to the large Ga content

[4]RBS analysis becomes inaccurate on layers with a thickness below 30 nm due to a weak signal. Further, because several compositions exhibit equal lattice constants, the conventional method of HRXRD measurements to determine the lattice constant and to calculate the composition with Vegard's law is not possible for quaternary AlInGaN.

[5]This effect is caused by strain compensation on the nanoscale. Regions with higher Al contents induce higher tensile strain, which enhances the probability of incorporating In atoms.

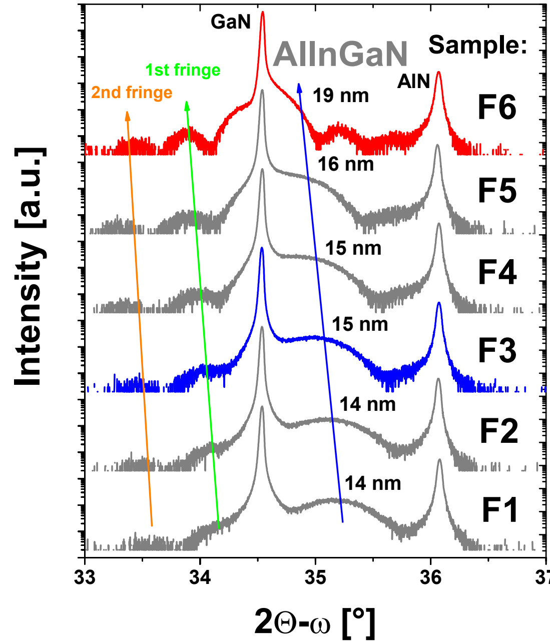

Figure 4.13.: HRXRD (0002) 2Θ-ω scans for sample series F, for which the TMAl-to-TMGa molar flow ratio is changed. The quaternary peak is shifted to lower angles for an increasing Ga content due to a larger nominal lattice constant c. Also shown are the first and the second fringe oscillations, which are of equal intensity indicating a similar interface quality in these heterostructures.

and to the almost lattice-matched composition. Sample $F3_{Ref}$ shows a slightly larger $\chi_{RBS,min}$ of 3 %, which is attributed to partial tensile strain relaxation of this 235 nm layer (observed in RSMs). Still, this value is reasonably low compared to published values, demonstrating the high quality of these quaternary layers. In Fig. 4.13, HRXRD (0002) 2Θ-ω scans are shown. With increasing Ga content, the quaternary peak is shifted to lower diffraction angles indicating the larger nominal lattice constant c. On the lower diffraction angle side, next to the GaN peak, the first and second fringe oscillation are visible. The intensity of these fringes remains almost the same, which confirms a similar interface quality for these heterostructures.

To summarize this section, adjusting the TMAl-to-TMGa molar flow ratio turns out to be most effective to change the composition while maintaining high crystal quality. Electrical properties of this F-series will be presented in Sec. 6.2.

Morphology development for thicker AlInGaN

In the following, the morphology of AlInGaN layers with low In contents is discussed. The change of the morphology during growth is of high interest, especially

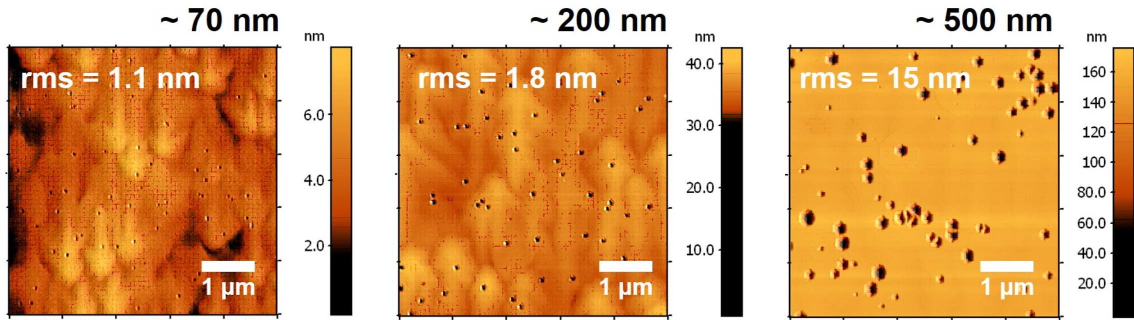

Figure 4.14.: Morphological development of AlInGaN samples with growth conditions of sample F6 and different thicknesses of 70 nm, 200 nm and 500 nm.

for applications of relatively thick AlInGaN of several hundreds of nanometers, e.g. as backbarriers. For this reason, three samples with compositions similar to the one of sample F6 are grown with thicknesses of 70 nm, 200 nm and 500 nm.

For these samples, atomic force microscope (AFM) images are shown in Fig. 4.14. Generally, a step flow pattern on the nanoscale can be observed for all samples. Additionally, the morphology is superimposed with hillock-like features with a size in the µm range. These hillocks are responsible for the overall rougher surface (rms roughness > 1 nm) as compared to binary alloys. Further identifiable on the surface are small pits with a density of around $2.6 \cdot 10^{8}$ cm^{-2}. These pits can be correlated to the dislocation density of the buffer structures on sapphire, which is in a similar range (compare Sec. 4.1). For thicker AlInGaN layers, the pit width increases up to several hundred nm. The morphology of the 500 nm-thick AlInGaN layer clearly shows that these pits exhibit a hexagonal shape. These V-shaped pits have been reported before in In-containing barrier layers and they are assumed to be formed dominantly at dislocations in the buffer due to strain compensation [228–233]. Their side-wall facets are the $\{1\bar{1}01\}$ planes, which have often been reported as a naturally forming plane in MOVPE processes for e.g. semi-polar growth or epitaxial lateral overgrowth (ELOG) processes [234, 235]. It has further been found that In migrates to the edges of these facets leading to a conductive path [236, 237]. Both the hillocks and the V-pits are responsible for the increasing roughness from 1.1 nm to 15 nm with rising thickness from 70 nm to 500 nm.

In summary, optimum reactor conditions for AlInGaN growth by MOVPE have been identified. The reactor pressure P should be chosen below 150 hPa to prevent gas phase pre-reactions of the Al precursor. For the growth surface temperature

($T_{Surface}$), lower values guarantee a sufficient In incorporation. However, with larger In content in the AlInGaN layer, the crystal quality decreases. Moderate $T_{Surface}$ values of about 780 °C - 800 °C result in an In content below 10 % while maintaining a sufficient crystal quality. The Al and Ga contents can effectively be varied by the molar precursor fluxes.

A wide composition range of AlInGaN layers grown on GaN has been covered. The AlInGaN layers exhibit different strain states: first, high tensile strain; second, almost no strain for near-lattice-matched compositions; third, compressive strain. While in the first and second case, a high crystal quality can be achieved, in the latter case, an inferior crystal quality is observed. The reasons can mainly be found in compressive strain limiting In incorporation and relaxation effects leading to an inhomogeneous composition. A multi-layer model has been used to describe the progress of relaxation in these AlInGaN layers.

Chapter 5

Growth and structural properties of AlInGaN on AlN

The previous Chap. 4 focused on the epitaxial growth of quaternary AlInGaN layers on GaN as the buffer layer. The growth of AlInGaN on other nitride buffers has never been investigated so far. In the present chapter, the growth of AlInGaN layers on binary AlN templates is studied for the first time. Compared to growth on GaN, structural properties show significant differences in composition and crystal quality due to large compressive strain in AlInGaN on AlN.

AlInGaN layers on AlN could be employed as backbarriers. These backbarriers are interesting for both, n-channel double heterostructure field effect transistors (DHFETs) or p-channel HFETs. The main advantage for the replacement of conventional backbarriers e.g. of AlGaN by AlInGaN is the high flexibility in adjusting material properties independently of each other in AlInGaN [23, 102, 104, 238]. This allows especially for a control of the polarization difference (ΔP) at the GaN/backbarrier interface, while maintaining a sufficiently large conduction band offset to GaN.

5.1. Experimental concept for the comparison of AlInGaN growth on AlN and GaN

For initial growth studies, which focus on structural properties of AlInGaN, epitaxial growth was separated into two steps. First, two different sets of templates were grown on 2-inch sapphire substrates. The first template consists of a 1 µm thick AlN layer only. The second template features an additional 3 µm thick GaN layer on top of the AlN. Both heterostructure templates were loaded simultaneously in the MOVPE process for AlInGaN growth. As shown in Fig. 5.1, this experiment was performed in a close-coupled showerhead (CCS) reactor in 3 × 2-inch configuration.

An overview on MOVPE conditions and structural properties of the investigated samples is given in Tab. 5.1. The target thickness for the AlInGaN layer is about 100 nm, which allows for an accurate composition determination by RBS. First, a TMGa flow series was investigated. Therefore, the TMGa flow was varied while

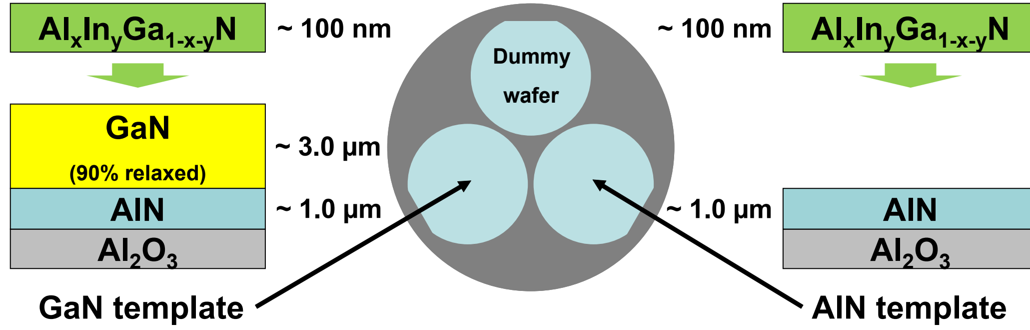

Figure 5.1.: Experimental concept of a MOVPE experiment using different templates grown in previous epitaxy runs on sapphire. The GaN template consists of 1 µm AlN and 3 µm GaN and the AlN template consists of only 1 µm AlN.

Sample	TMGa flux [µmol/min]	$T_{Surface}$ [°C]	Al [%]	In [%]	Ga [%]	$\chi_{\mathrm{RBS,min}}$ [%]	t_{bar} [nm]	r_{Growth} [nm/min]
Samples on GaN templates								
G1	**0**	790	83	17	0	1.5	100	2.2
G2	**2.7**	790	75	13	12	1.5	90	2.3
G3	**8.0**	**790**	56	10	34	1.5	90	2.6
G4	8.0	**775**	50	15	35	2	120	3.4
G5	8.0	**760**	50	17	33	8	125	3.6
Samples on AlN templates								
A1	**0**	790	86	14	0	28	100	2.2
A2	**2.7**	790	76	10	14	28	90	2.3
A3	**8.0**	**790**	57	3	40	6	90	2.6
A4	8.0	**775**	48	20	32	15	110	3.1
A5	8.0	**760**	45	25	30	18	120	3.4

Table 5.1.: MOVPE conditions and structural properties of AlInGaN layers grown with either different TMGa flux or at varying $T_{Surface}$ on both GaN (G1 to G5) and AlN (A1 to A5). Reactor pressure P is equal for all samples at 70 hPa.

keeping the TMAl and TMIn flows constant. This TMGa flow series contains the samples G1, G2 and G3 on GaN and samples A1, A2 and A3 on AlN. In a further "temperature" sample series, $T_{Surface}$ was reduced in steps of 15 K, from 790 °C (G3 on GaN and A3 on AlN) to 760 °C (G5 on GaN and A5 on AlN).

5.1.1. Addition of Ga precursor to AlInN growth conditions

For AlInGaN samples of the TMGa flow series, the starting MOVPE conditions were chosen to result in nearly lattice-matched AlInN on GaN. This is illustrated in the bandgap-vs.-lattice diagram in Fig. 5.2 with sample G1. The arrows indicate the shift in the composition caused by the increased TMGa flux for growth on GaN

(light blue) and growth on AlN (red). For growth on GaN, a compositional range from ternary lattice-matched $Al_{83\%}In_{17\%}N$ (sample G1) to a Ga-richer regime like $Al_{56\%}In_{10\%}Ga_{34\%}N$ (sample G3) was covered. Owing to the increasing TMGa flux, the growth rate increased from 2.2 nm/min to 2.6 nm/min. These layers on GaN exhibit high crystal quality, which is manifested in the low RBS $\chi_{\mathrm{RBS,min}}$ values of 1.5 %. The distinct fringe oscillations in HRXRD (0002) 2Θ-ω scans shown in Fig. 5.3 reflect this high quality. The low defect density is further confirmed by $(10\bar{1}5)$ rocking curve FWHM values down to 384 arcsec for sample G3, which is comparable to values for binary AlN and only a factor of 2 to 3 larger than those of the underlying GaN.

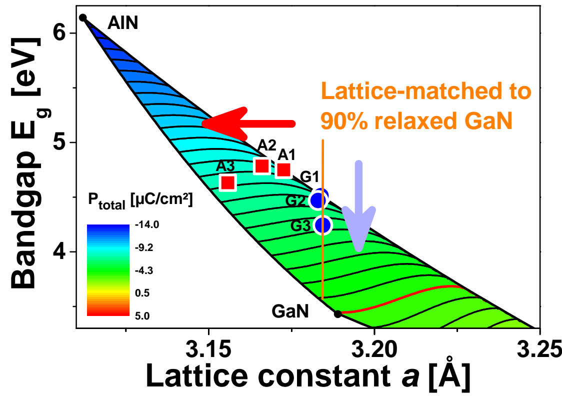

Figure 5.2.: Illustration of the composition in the bandgap-vs.-lattice diagram. The arrows indicate the shift in the composition due to the increased TMGa flow for growth on AlN (red) and for growth on GaN (light blue).

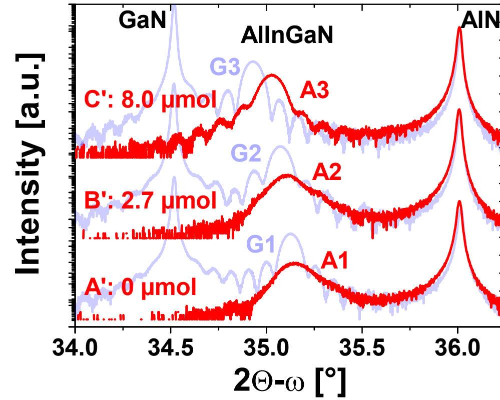

Figure 5.3.: HRXRD (0002) 2Θ-ω scans for samples grown with different TMGa fluxes. The red curves are samples grown on AlN templates. The light blue curves are samples on GaN templates, shown for comparison.

In contrast, AlInGaN layers on AlN templates show a different appearance in HRXRD 2Θ-ω scans (red curves in Fig. 5.3). Apart from the shift of the peak position with increasing TMGa flow to lower angles and, hence, to Ga-richer compositions, compared to scans of AlInGaN on GaN, the peaks are significantly broader. By RBS, In pulling was identified as one reason for this broadening [150]. To achieve a sufficient agreement between HRXRD 2Θ-ω scans and simulations, a relaxation of 50 % and 70 % for samples A1 and A2, respectively, has to be assumed. An interesting observation is the larger intensity and the well-defined fringe oscillations in the scan for sample A3, indicating a superior crystal quality compared to those of samples A1 and A2. This is confirmed by the improved RBS $\chi_{\mathrm{RBS,min}}$ value of 6 %.

Further, the RBS spectrum reveals a homogeneous composition of $Al_{57\%}In_{3\%}Ga_{40\%}N$ for sample A3 and strong In pulling in growth direction for samples A1 and A2. The reason for this phenomena might be found in the nominal strain, which results from the initial lattice mismatch to AlN. As illustrated by the red arrow in Fig. 5.2, the compositions for AlInGaN on AlN are shifted almost horizontally towards AlN, i.e. the bandgap remains almost constant and the in-plane lattice constant becomes smaller, approaching the one of AlN. Thus, the nominal compressive strain is reduced from -1.9 % for sample A1 to -1.4 % for sample A3, leading to pseudomorphic growth and, hence, the higher crystal quality for sample A3. The XRD ($10\bar{1}5$) rocking curve reveals FWHM values of 910 arcsec for sample A3, which is 3 times larger than for sample G3 on GaN. Owing to their homogeneity, samples G3 on GaN and A3 on AlN are chosen to compare the influence of the substrate on the AlInGaN composition. The shift of the AlInGaN peak related to the lowered In content from 10 % to 3 % is obvious. This manifests a strongly hampered In incorporation because of the smaller lattice constant of AlN.

To summarize, a high TMGa flux for AlInGaN growth on AlN, which results in compositions near the AlGaN ternary line, is promising to lower the nominal strain and to achieve a good crystallinity, which is essential for subsequent layer growth.

5.1.2. Variation of the growth surface temperature

Starting from flow conditions of sample A3, a temperature series was grown. As previously discussed in Sec. 4.3.2, enhanced In incorporation for lower $T_{Surface}$ is confirmed for all samples by RBS. This effect is stronger for AlInGaN on AlN and leads to very high In contents exceeding 20 % for samples A4 and A5 (Tab. 5.1). As a result, the growth rate increases for samples grown at lower $T_{Surface}$. Further, the crystal quality decreases, which is manifested by larger RBS $\chi_{\mathrm{RBS,min}}$ values. While for AlInGaN on GaN, the value increases from 1.5 % for sample G3 to 8 % for sample G5, for AlInGaN on AlN, the value increases from 6 % for sample A3 to 18 % for sample A5.

To identify the reason for the very large In contents and the inferior quality, HRXRD ($10\bar{1}5$) RSM were performed and are shown in Fig. 5.4 for samples A3, A4 and A5 on AlN templates. First, the previously mentioned pseudomorphic growth of sample A3 is obvious. A pseudomorphic phase is also observed for all samples grown at lowered $T_{Surface}$. The peak is slightly moving away from the AlN peak, indicating the larger In content. However, for the lowered $T_{Surface}$ (samples A4 and A5), a clear second peak is observed, reflecting the presence of a second phase with a different

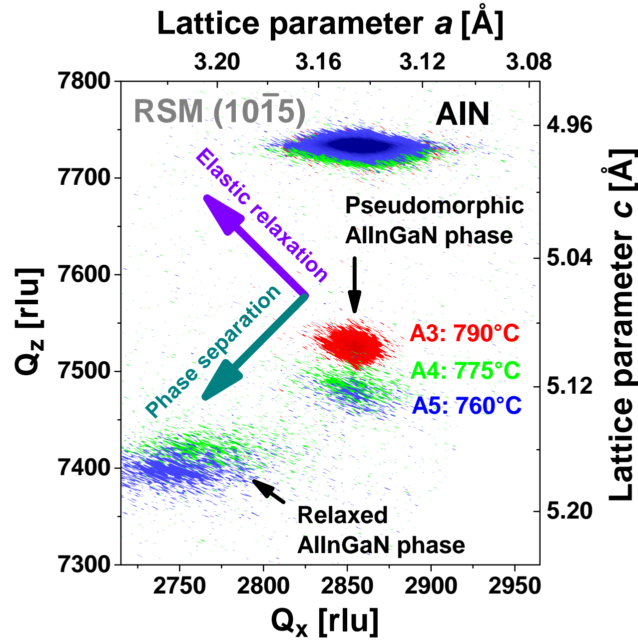

Figure 5.4.: Merged HRXRD (10$\bar{1}$5) RSM of samples of the "temperature" series. A pseudomorphic phase is apparent for all $T_{Surface}$. For lower $T_{Surface}$ phase segregation leads to an additional fully relaxed AlInGaN phase.

composition. Elastic relaxation can be excluded here, since the shift would then appear, although also to smaller Q_x, to larger Q_z values. This is indicated by the light blue arrow pointing to the upper left corner in Fig. 5.4. Further, a relaxation with In pulling would be represented by a single fully relaxed peak or a peak tail in the RSM. With increasing compressive strain from sample A4 to sample A5, the intensity of the peak of the pseudomorphic phase decreases. The phase segregation observed for larger compressive strain is comparable to the trend observed for AlInN grown on GaN and represents evidence for the correlation between the miscibility gap and the strain in an epilayer [190, 195].

Epitaxial growth of AlInGaN directly on AlN remains a challenging task even under optimum reactor conditions. Due to the large lattice mismatch, which results in compressive strain for all AlInGaN compositions, relaxation effects occur. The general trends, which were observed for AlInGaN growth on GaN, have been confirmed for the growth on AlN, i.e. larger In incorporation for lower $T_{Surface}$ and an effective control of the Ga content by the TMGa flux. For $T_{Surface}$ values below 775 °C and, hence, large In contents above 20 %, phase separation has been observed. However, for $T_{Surface}$ values of about 790 °C, a composition near the AlGaN ternary line with sufficient crystal quality could be achieved.

II.

Polarization engineering in nitride-based heterostructure field effect transistors with either n- or p-channels

Chapter 6

HFET structures with AlInGaN barriers for 2DEG accumulation

This chapter deals with the fabrication of heterostructure field effect transistors (HFETs) with AlInGaN barrier layers on GaN buffers. The main focus here is on the investigation of electrical properties of the two-dimensional electron gas (2DEG), which is formed in the GaN buffer in proximity to the AlInGaN barrier due to the polarization difference (ΔP). The electron sheet density and mobility are correlated to the structural properties, i.e. composition and crystal quality, of the barrier. The knowledge of critical structural properties, which could limit device performace, is finally used to realize polarization-optimized heterostructures. This allows for the fabrication of both depletion and enhancement mode HFETs comparable to state-of-the-art performance.

6.1. Influence of growth surface temperature on 2DEG properties

This section deals with the investigation of the influence of different AlInGaN compositions on basic 2DEG characteristics, which are the electron density n_s and the electron mobility μ.

The T-series 1 containing the samples T1 to T5 is investigated with regard to electrical properties of the 2DEG. A comprehensive study on the structural characteristics of exactly this series was already presented in Sec. 4.3.2. Nevertheless, an overview on growth surface temperature ($T_{Surface}$), the AlInGaN composition and the bandgap E_g is given in Tab. 6.1. Additionally, the measured electron density n_s and mobility μ are listed together with the theoretical values of n_s calculated by Eq. 2.17.

Hall and Van der Pauw measurements were performed on these samples. The results are shown in Figs. 6.1a and 6.1b. Starting in Fig. 6.1a from sample T1, n_s decreases with increasing In contents for sample T2 and T3. This trend is well

Sample	$T_{Surface}$ [°C]	Al [%]	In [%]	Ga [%]	t_{bar} [nm]	E_g [eV]	$n_{s,calc./meas.}$ [10^{13}cm^{-2}]	$\mu_{300K/77K}$ [cm^2/Vs]
T-series 1								
T1	786	56	6	38	46	4.35*	1.84 / 2.59	1076 / 3035
T2	741	53	14	33	48	4.05*	0.69 / 1.95	414 / 599
T3	699	45	25	30	54	3.39	- / 1.61⋆	228⋆ / 274⋆
T4	654	34	41	25	60	2.52	- / 5.35⋆	79⋆ / 74⋆
T5	622	35	45	20	60	2.35	- / 22.1⋆	13⋆ / 4⋆

Table 6.1.: Growth surface temperature $T_{Surface}$, AlInGaN composition, thickness t_{bar}, bandgap E_g, theoretical and measured values of the electron density $n_{s,calc./meas.}$ as well as the measured mobility μ for samples T1-T5 in the T-series 1. The bandgap values marked with * are determined by SE. For samples with the bandgap of the barrier smaller than the one of GaN, the measured $n_{s,measured}$ and mobility μ values marked with ⋆. Here, no 2DEG is formed.

correlated to expectations regarding the compositions and the strain states, which were already discussed in the bandgap-over-lattice diagram in Fig. 4.12 in Sec. 4.3.2. While sample T1 with a low In content of 6 % is tensile strained on GaN, sample T2 with a larger In content of 14 % is slightly compressively strained. Hence, sample T1 exhibits a large total polarization (P_{total}) (piezoelectric polarization (P_{piezo}) and spontaneous polarization (P_{spon}) are parallel), whereas sample T2 features a lower P_{total} (P_{piezo} and P_{spon} are anti-parallel).

For these two samples, values of n_s were calculated by Eq. 2.17 (Tab. 6.1). The theoretical values for n_s are smaller compared to the measured ones, which is likely caused by the uncertainties in physical properties, which are used for the calculation, and the AlN interlayer between the barrier and the GaN buffer, which is neglected in the calculations. Such an AlN spike is present in all samples (compare Fig. 4.1a) and generally enhances n_s [175]. However, a smaller n_s for sample T2 compared to sample T1 correlates well to the measured values.

For samples T4 and T5 with large In contents of more than 40 %, n_s rises to very large values above 10^{14} cm^{-2}. These values exceed typical ones in nitride heterostructures with large ΔP: For AlInN/GaN, n_s values up to $3{\cdot}10^{13}$ cm^{-2} have been reported [175, 239, 240] and even for pure AlN barriers on GaN with thicknesses up to the crack-free limit of around 5-7 nm, n_s has not been exceeding $5{\cdot}10^{13}$ cm^{-2} [75, 174, 241]. Due to the lower bandgap of AlInGaN compared to GaN for samples T4 and T5 (compare Tab. 6.1), the formation of a potential well in the conduction band at the AlInGaN/GaN interface for 2DEG accumulation is not possible. As described in Sec. 2.4.3, a potential well could theoretically exist in the valence band

at the upper side of this interface. However, the measured Hall coefficient R_{Hall} is negative, which indicates that the dominant carriers are electrons. Hence, the root cause for the large measured n_s values in the samples T4 and T5 is most likely found in free electrons in the AlInGaN layer. This effect is likely supported by the poor crystal quality of these barriers (compare FWHM values in Fig. 4.11b in Sec. 4.3.2).

An equivalent bulk electron density can be calculated to $0.89{\cdot}10^{19}\,cm^{-2}$ for sample T4 and $3.68{\cdot}10^{19}\,cm^{-2}$ for sample T5. These values are comparable to those of ternary InGaN layers grown at very low $T_{Surface}$ below 700 °C [184]. Because the electron density does not decrease significantly for measurements at 77 K, the AlInGaN semiconductor with a very high average In contents of 45 % must be at least locally degenerated. From very broad undefined AlInGaN peaks in HRXRD RSMs, it follows that the composition in the barrier is non-uniform. Local In-rich clusters might form potential minima in the conduction band leading to the degeneration [196–200].

Sample T3 with its almost identical bandgap to GaN shows a large n_s above $10^{13}\,cm^{-2}$, although P_{total} should be very small. The high n_s is likely to emerge from free electrons in the AlInGaN rather than from electrons in a 2DEG.

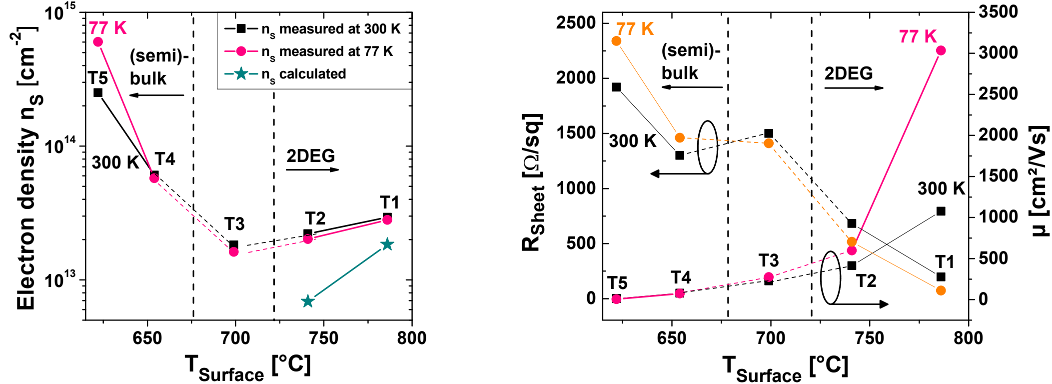

(a) Electron density n_s plotted against $T_{Surface}$.

(b) Sheet resistance R_{Sheet} and electron mobility μ against $T_{Surface}$.

Figure 6.1.: Hall and van der Pauw measurements on samples of the T-series 1.

The behavior of the electron mobility μ is shown in Fig. 6.1b. A reduction of $T_{Surface}$ leads to a steadily decreasing μ at 300 K from 1076 cm^2/Vs for sample T1 to 13 cm^2/Vs for sample T5. This strong reduction is related to a transition from a two-dimensional conductivity in a 2DEG to the (semi-)bulk conductivity in the AlInGaN. For electrons in the AlInGaN layer (samples T3-T5), in dependence on composition, ionized impurity scattering and alloy scattering are the dominant

scattering mechanisms. The inferior crystal quality for lower $T_{Surface}$ (compare FWHM values in Fig. 4.11b in Sec. 4.3.2) generally increases the electron scattering probability for these samples. For electrons in the 2DEG (samples T1, T2), the probability to be scattered at impurities in the barrier or alloy disorder is strongly reduced.

Furthermore, the difference of the measured mobility at 300 K and at 77 K is more pronounced for samples grown at higher $T_{Surface}$. This indicates that phonon scattering at 300 K hampers the mobility in the samples with initially high mobilities to a larger extent. With decreasing $T_{Surface}$, the difference in mobility is less strong. This is a sign for decreasing impact of phonons and increasing contribution of impurity and alloy scattering. The mobility values of samples T1 and T2 are larger at 77 K compared to values at 300 K, which is a typical behavior of a 2DEG. The mobility μ of sample T3 with a value of 274 cm^2/Vs at 77 K is also slightly larger than the value of 228 cm^2/Vs at 300 K. This indicates that a 2DEG might be weakly present in this sample. For samples T4 and T5, the mobility values at 77 K are smaller compared to values at 300 K. This is a further sign for a (semi-)bulk conductivity in the AlInGaN.

As plotted in Fig. 6.1b, the sheet resistance (R_{Sheet}) increases for lower $T_{Surface}$. Only samples T1 and T2 exhibit a 2DEG which leads to a low R_{Sheet} below 1 kΩ/□.

In conclusion, for the T-series 1, $T_{Surface}$ needs to be larger than 700 °C to grow AlInGaN barriers with a bandgap larger than the one of GaN. Otherwise, no 2DEG is formed in the GaN. Generally, a lower $T_{Surface}$ leads to an increased In content, which in turn results in a smaller P_{total} and a smaller n_s. This indicates that by changing $T_{Surface}$, polarization-engineering with AlInGaN barriers is possible. A comprehensive study on polarization-engineering is discussed in the following Sec. 6.2.

6.2. Lowering the total polarization in AlInGaN

To study the influence of ΔP in AlInGaN/GaN heterostructures on n_s further, two series of samples with 8 nm to 19 nm AlInGaN barriers are regarded in the following. The objective is the reduction of n_s by lowering P_{total} in AlInGaN to realize enhancement mode behavior of HFETs.

Therefore, a T-series 2 is introduced with AlInGaN barriers grown at different $T_{Surface}$. The range of $T_{Surface}$ is chosen between 720 °C and 815 °C. For all samples, the AlN spike between the GaN buffer and the AlInGaN barrier was grown at a high $T_{Surface}$ of 815 °C. The second series of interest is the F-series, discussed already in

Sample	T_S [°C]	$\frac{\text{TMAl}}{\text{TMGa}}$	Al [%]	In [%]	Ga [%]	t_{bar} [nm]	E_g [eV]	$n_{s,calc./meas.}$ [10^{13}cm^{-2}]	μ [cm^2/Vs]
T-series 2									
T6	815	2.4	62	5	33	19	4.68	2.17 / 1.87	1490
T7	770		60	10	30	20	4.40	1.44 / 1.59	726
T8	740		55	14	31	20	4.09	0.67 / 1.16	584
T9 (HFET A)	720		48	17	35	8	3.81	<0.01 / 0.19	146
F-series									
F1	815	2.4	54	5	41	14	4.47	1.54 / 1.69	1530
F2		1.7	50	5	45	14	4.36	1.32 / 1.44	1650
F3		1.2	43	5	52	15	4.22	0.98 / 1.15	1760
F4		0.9	36	4	60	15	4.05	0.75 / 0.84	1790
F5		0.6	28	3	69	16	3.89	0.51 / 0.71	1820
F6 (HFET B)		0.2	11	2	87	19	3.56	0.02 / 0.18	1330

Table 6.2.: Growth surface temperature T_S, TMAl-to-TMGa molar flow ratio, AlInGaN composition and bandgap E_g for the T-series 2 and the F-series (F for flow). Additionally, theoretical and measured values of the electron density n_s and the measured mobility μ in the 2DEG are given.

Sec. 4.3.3. For the F-series, the precursor TMAl-to-TMGa ratio was changed to vary mainly the Al and Ga content. The AlInGaN barriers and the AlN spikes were grown under a high temperature of 815 °C. Tab. 6.2 summarizes the important growth conditions: the AlInGaN compositions, the bandgap E_g, the mobility μ, the measured electron density n_s as well as the theoretical values of n_s calculated with Eq. 2.17.

The T-series 2 and the F-series are shown in the bandgap-vs.-lattice diagram in Fig. 6.2 for comparison. In the following, for bandgap calculations, a constant and high bowing parameter of $b_{AlInN} = 5.2\,\text{eV}$ for AlInN is used [91]. This value accurately describes AlInGaN compositions with a bandgap larger than the one of GaN and, hence, this constant value can replace the In-dependent bowing parameter $b_{AlInN} = A_1/(1+A_2 \cdot x_{In}^2)$ in that region [98, 242]. The contour lines in the quaternary area illustrate P_{total} of quaternary barriers, pseudomorphically grown on GaN [104].

Starting from the most tensile strained samples F1 and T6 with high Al contents, which are located in the blue-colored high-polarization regime, both series evolve towards larger lattices and smaller bandgaps. While the T-series 2 remains in the vicinity of the AlInN line by a dominant change in the In content from 5 % to 17 %, the F-series is moving towards GaN by a reduction of the Al-to-Ga content ratio.

For the T-series 2, the large amount of In leads to a change in the strain state from high tensile in-plane strain (ε_{xx}) of 0.948 % for sample T6 to high compressive

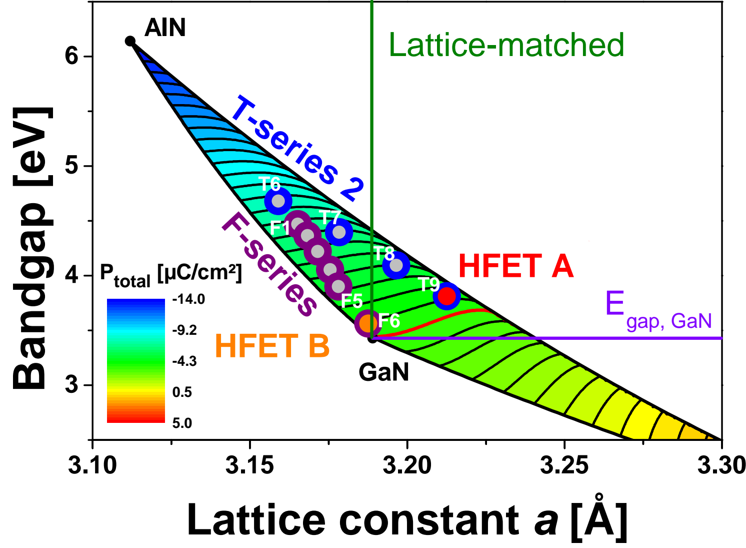

Figure 6.2.: Bandgap diagramm plotted over the lattice constant a. Blue circles represent the T-series 2 and purple circles represent the F-series. Bandgaps and polarization values are calculated with a weighted bandgap formula.

strain ε_{xx} of -0.733 % for sample T9 (also marked as HFET A in red color). The latter results in a very low P_{total} of -3.99 µC·cm^{-2}.

A different way in the bandgap-vs.-lattice diagram in Fig. 6.2 is described by the F-series. While sample F1 exhibits a high tensile strain state with an ε_{xx} of 0.75 %, sample F6 (also marked as HFET B in orange color) is almost lattice-matched to the GaN buffer with a tensile strain state with an ε_{xx} of only 0.04 %. Hence, P_{piezo} is negligible and P_{total} is equal to P_{spon} of -3.79 µC·cm^{-2}, which itself is small due to the low Al content. As apparent from the contour lines in Fig. 6.2, both HFET samples A (red color) and B (orange color) exhibit similar low P_{total} values.

6.2.1. Comparison of 2DEG characterisctics

The T-series 2 and the F-series are expected to show significant differences in the properties of the 2DEG. This expectation is manifested in the values for n_s, calculated with Eq. 2.17 (Tab. 6.2). In general, samples exhibiting a high Al content and, hence, a high ΔP generate a large n_s.

Measured values of n_s for both the T-series 2 and the F-series together with calculated values of n_s are plotted against the absolute value of ΔP in Fig. 6.3. A increasing trend for n_s as a function of ΔP is predicted for both series. While for the T-series 2, this trend is related to the increasing In content, for the F-series, it is caused by the decreasing Al-to-Ga content ratio. This trend can generally be confirmed by the measured values for both series. However, the agreement of

calculated and measured values is much better for samples grown at high $T_{Surface}$ (T6, F-series) and samples with large P_{total} (T6, T7, F1-F4). All n_s values measured (except for T6) are larger than the predicted ones and the deviation increases with decreasing P_{total}. This can be explained by two effects, which are not considered in the calculation: first, the influence of the AlN spike on n_s; second, the inferior crystal quality for samples grown at lower $T_{Surface}$ (compare RBS channeling measurements in Sec. 4.3.2).

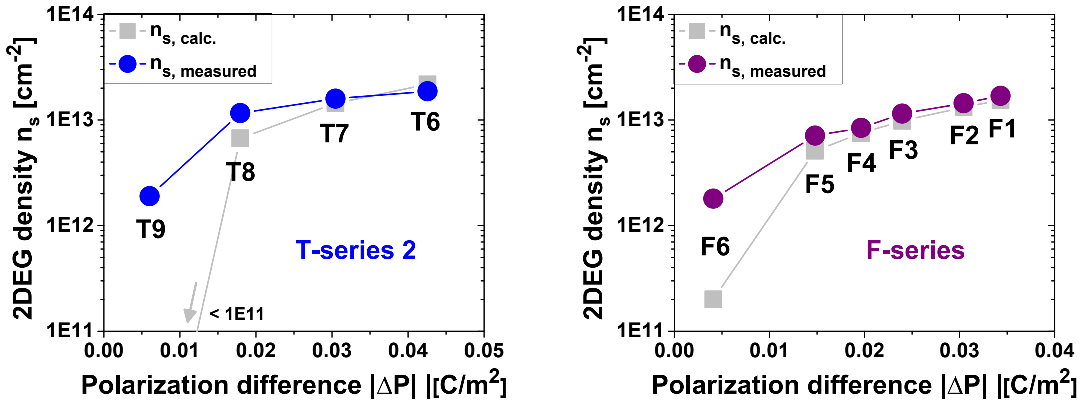

(a) Sample T6 to T9 in the T-series 2.

(b) Sample F1 to F6 in the F-series.

Figure 6.3.: Calculated n_s plotted against the absolute polarization difference $|\Delta P|$ together with measured values for n_s.

Also, the 2DEG mobility values, shown in Fig. 6.4, correspond well to the expectation that samples grown at a higher $T_{Surface}$ show a larger mobility μ. To discuss scattering mechanisms, the mobility μ is plotted against the 2DEG density n_s in Fig. 6.4. The mobilities of the T-series 2 are generally larger than values of the T-series 1 (compare Fig. 6.1b). This is achieved by the AlN spike which was grown at a high value of 815 °C. However, the decrease in the T-series 2 for lowered $T_{Surface}$ is still severe and is very likely to stem from two issues: first, an increased interface roughness at higher In contents (as discussed in Sec. 4.3.2); second, an increased contribution from alloy disorder scattering in the barrier owing to its degraded crystal quality.

For the F-series, the mobility function over n_s shows a maximum of 1820 cm^2/Vs at 300 K and 10900 cm^2/Vs at 77 K for a moderate n_s of $7 \cdot 10^{12}$ cm^{-2}. These values are among the highest in literature reported ones for In-containing barrier layers. Typical values for MOVPE-grown heterostructures are not exceeding 1700 cm^2/Vs [171, 243–245]. Mobilities up to 2500 cm^2/Vs at 300 K have been achieved for AlGaN HFETs, grown by molecular beam epitaxy (MBE) on bulk GaN substrates

[246] and up to 2200 cm^2/Vs for growth on SiC [247]. Recently, record mobility values for lattice-matched AlInN HFETs grown on sapphire up to 2200 cm^2/Vs have been achieved with the CCS MOVPE reactor [151]. However, together with the tunability of n_s, the results shown here demonstrate that 2DEG properties can be adjusted between typical AlGaN and AlInN characteristics with the quaternary material system [248, 249].

The high mobility values are consistent with the low surface roughness of all layers of the F-series in the range of 0.4 nm to 0.6 nm. The overall peak-like shape of the mobility function plotted over n_s illustrates the typical dominant scattering mechanisms in HFET structures in the different n_s regimes [250–252]. The position and the spatial extent of the 2DEG changes with varying n_s. For n_s above $8{\cdot}10^{12}$ cm^{-2}, the distance of the 2DEG to the interface is short and, hence, interface scattering becomes the dominant mechanism. For densities below $8{\cdot}10^{12}$ cm^{-2}, the carrier confinement becomes worse. Consequently, electrons propagate into the GaN buffer and scatter at ionized impurities.

These generally accepted phenomena are confirmed by measurements of the HFET B at two processing steps, as indicated with orange squares in Fig. 6.4. First, a thickness reduction by etching down to 8 nm leads to a very small n_s of $8{\cdot}10^{11}$ cm^{-2} with a lowered μ of 747 cm^2/Vs. Second, when this sample is passivated with 120 nm SiN by plasma-enhanced CVD, both n_s and μ increase to $2.7{\cdot}10^{12}$ cm^{-2} and 1640 cm^2/Vs, respectively. This clearly demonstrates that the mobility reduction at lower n_s is related to the inferior carrier confinement.

6.3. Fabrication of transistors in depletion and enhancement mode

The control over n_s by polarization engineering can be used for shifting V_{th}, according to Eqs. 2.17 and 2.23. This allows for the realization of either depletion mode (d-mode) or enhancement mode (e-mode) transistors. To verify this approach, three samples were fully processed to HFETs with 1 µm gate length. As a d-mode reference HFET, the strongly-tensile strained sample T6 with the highest Al content of 62 % and, hence, the largest n_s of $1.87{\cdot}10^{13}$ cm^{-2} is chosen. The two low-polarization HFETs A and B with low n_s of $1.8{\cdot}10^{12}$ cm^{-2} and $8{\cdot}10^{11}$ cm^{-2}, respectively, are promising for achieving e-mode behavior. Transfer characteristics of these three samples are shown in Fig. 6.5a. One obvious characteristic and the main goal of this comparison is that V_{th} is shifted from large negative values of -5.5 V for the d-mode HFET

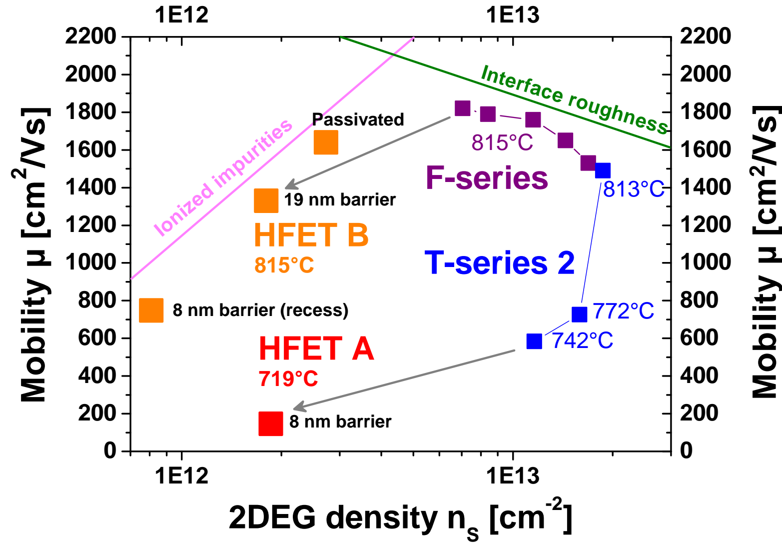

Figure 6.4.: 2DEG mobility μ plotted against the 2DEG density n_s measured by Hall and Van der Pauw.

to positive values of +0.56 V for HFET A and +0.20 V for HFET B, hence, validating the e-mode behavior [253]. This transition is accompanied by a reduction of the drain current (I_D) at V_{th} + 3 V from about 500 mA/mm to 100 mA/mm for HFET A and to 340 mA/mm for HFET B. The decrease of I_D and transconductance (g_m) for the e-mode samples originates from an increase in R_{Sheet} in the access region due to the low n_s.

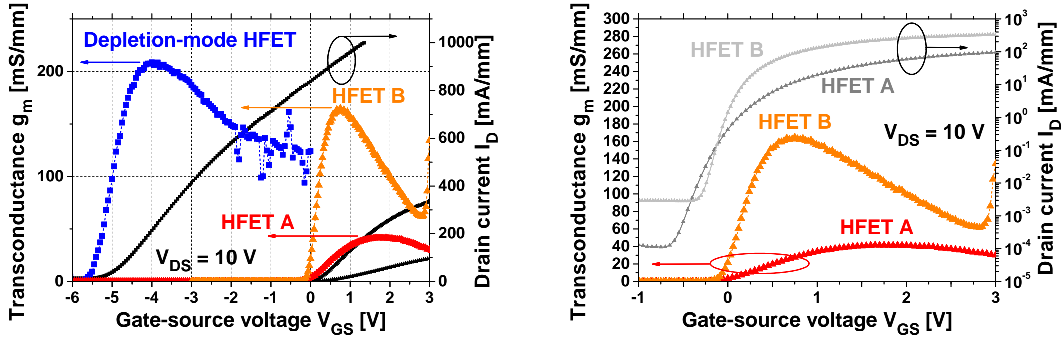

(a) Drain current I_d and transconductance g_m of a reference depletion mode transistor and the two low-polarization HFET samples A and B.

(b) Drain current I_d in semi-logarithmic scale and transconductance g_m in linear scale of only the two low-polarization HFET samples A and B.

Figure 6.5.: Transfer characteristics.

Sample **Composition**	HFET A $Al_{48\%}In_{17\%}Ga_{35\%}N$	HFET B $Al_{11\%}In_{2\%}Ga_{87\%}N$
t_{bar} (recess) [nm]	8	19 (8)
E_{gap} [eV]	3.81	3.56
P_{total} [µC/cm^2]	-3.99	-3.79
P_{spon} [µC/cm^2]	-5.07	-3.75
P_{piezo} [µC/cm^2]	1.08	-0.04
V_{th} [V]	0.56	0.20
$g_{m,max}^{ext./int.}$ [mS/mm]	42 / 64	165 / 370
I_d at 3V [mA/mm]	96	338
$R_{sheet,access}$ [Ω/□]	2.2k	1.4k
ε_{xx} [%]	-0.80	-0.04
n_s (recess) [10^{12} cm^{-2}]	1.8	1.8 (0.8)
μ (recess) [cm^2/Vs]	146	1330 (747)
Roughness rms [nm]	1.5	0.6

Table 6.3.: Electrical and structural properties of the low-polarization HFET A and B [242].

6.3.1. Comparison of enhancement mode transistors

For comparison of both low-polarization HFETs A and B, quantities of electrical and structural properties are summarized in Tab. 6.3. Both HFETs A and B show e-mode behavior with a V_{th} of 0.56 V and 0.20 V, respectively. However, two different device concepts have been employed due to the different layer structures (details can be found in publications [249, 254]). The varying distance of the gate contact to the 2DEG is the most relevant difference in the device design. While for the lattice-matched HFET B the gate-to-2DEG distance is the barrier thickness of 8 nm only, for the compressively strained HFET A it is about 30 nm, consisting of the 8 nm barrier, 12 nm GaN cap, and 10 nm dielectric. The different device geometries make a direct comparison quite difficult. However, bearing this difference in the 2DEG distance in mind, the observed trends in device performance can also be very well correlated to structural properties. Here, the discussion is restricted to some distinct electrical parameters derived from the transfer characteristics of samples A and B (shown in Figs. 6.5a and 6.5b [223]).

The drain current for HFET B at $V_{GS} = 3$ V is 338 mA/mm. This value is three times higher than that of HFET A with 96 mA/mm. The maximum extrinsic transconductance $g_{m,max}^{ext.}$ is improved by a factor of four to 165 mS/mm. The intrinsic transconductance $g_m^{int.}$ is calculated by [255]:

$$g_m^{int} = \frac{g_m^{ext}}{1 - g_m^{ext} \cdot (R_C + L_{GS} \cdot R_{Sheet})}, \tag{6.1}$$

in which R_C is the contact resistance and R_{Sheet} the sheet resistance in the access region. $g_m^{int.}$ is sixfold larger for the almost lattice-matched HFET B. The improved performance is likely to be explained by the following reasons: first, the difference in gate-to-source capacitance by a factor of about four; second, the strong contribution from the lower R_{Sheet} in the access region of $1.4\,\mathrm{k\Omega/\Box}$ for HFET B in comparison to $2.2\,\mathrm{k\Omega/\Box}$ for HFET A; third, the improved 2DEG mobility under the gate ($146\,\mathrm{cm^2/Vs}$ vs. $747\,\mathrm{cm^2/Vs}$ at 300 K). Although at low n_s, interface scattering is not the dominant mechanism in limiting the mobility μ, in this case, the larger value for HFET B is likely related to the smoother interface. HFET A exhibits a large In content of 17 %. As evidenced by the improved morphology in AFM scans, this results in an inferior crystal and interface quality (compare Fig. 4.6).

In conclusion, it has been shown that by a reduction of ΔP between AlInGaN barrier and GaN channel e-mode behavior of HFETs can be realized. However, the reduced ΔP also leads to increased series resistances in the access regions, which has a negative impact on the device performance.

6.3.2. E-mode HFETs with lowered on-resistance by multi-layer barriers

As it was shown in the previous sections, owing to the reduced ΔP between AlInGaN barrier and GaN channel, the device performance is limited by the series resistances in the access regions. Consequently, to achieve low access resistances while simultaneously maintaining the normally-off feature of the active region, the heterostructure design has to be modified. A layer structure which generates a high n_s in the access region and a low n_s under the gate would serve this purpose. Therefore, multi-layer AlInGaN barriers were developed in which high-polarization and low-polarization layers are combined [256]. A similar approach with an AlInGaN capping layer, polarization-matched to an AlGaN barrier below has been shown in literature [257]. In the study presented here, the uppermost AlInGaN as a high-polarization layer serves to enhance n_s.

The layer stacks for the HFETs are shown in Fig. 6.6. All samples are based on HFET B from the previous Sec. 6.2. HFET B1 is identical to HFET B with a single 18 nm thick low-polarization $Al_{11\%}In_{2\%}Ga_{87\%}N$ layer (compare composition of sample F6 from Sec. 4.3.3). HFET B2 and HFET B3 feature exactly the same low-polarization layer. However, its thickness is only 8 nm. On top of this layer, a high-polarization layer with a thickness of 8 nm is deposited. An equal total

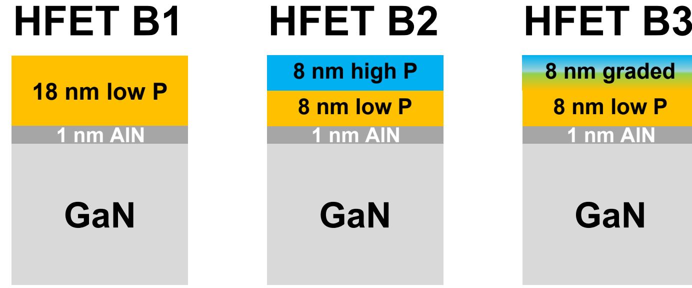

Figure 6.6.: Layer stacks of samples with different AlInGaN barriers, which were processed to HFETs: HFET B1 with a single low-polarization layer; HFET B2 with a double AlInGaN layer; consisting of a low-polarization layer and a high-polarization layer; HFET B3 with a low-polarization layer and a graded AlInGaN high-polarization layer.

barrier thickness was targeted for all samples. For HFET B2, a high-polarization $Al_{43\%}In_{5\%}Ga_{42\%}N$ was chosen (compare composition of sample F3 from Sec. 4.3.3). For HFET B3, a graded AlInGaN layer serves as the high-polarization layer. The grading was performed from the conditions of sample F6 ($Al_{11\%}In_{2\%}Ga_{87\%}N$) to conditions of sample F2 ($Al_{50\%}In_{5\%}Ga_{45\%}N$) (compare Sec. 4.3.3). The slightly higher Al content at the surface of about 50 %, compared to HFET B2 with 43 %, was intentionally adjusted to compensate for the lower Al-containing ramping zone to generate a large n_s.

Simulations of both the conduction band structure and the electron density as a function of the vertical distance are shown for the three HFETs in Fig. 6.7. Obviously in Fig. 6.7, a 2DEG with a high n_s is predicted for all HFETs in the proximity to the thin AlN spike at 0 nm vertical distance.

For HFET B2, a rather large n_s is predicted in the barrier layer at the interface between low and high polarization layers. The reason for the electron accumulation is found in the ΔP between the high-polarization layer and the low-polarization layer, which is accompanied by an abrupt conduction band offset in the bandstructure of HFET B2. This results in a triangular well formation at the interface, in analogy to the one between low-polarization layer and GaN channel.

An improved bandstructure is realized by the design of HFET B3 with a graded high polarization layer. By ramping growth conditions, the composition and, hence, the structural properties are steadily changing, leading to a bandstructure similar to an arsenide-based modulation-doped field effect transistor (MODFET) [258, 259]. This results in an electron density in the barrier, which is 5 orders of magnitude smaller than the density of the 2DEG and hence negligible.

The electron density and mobility determined by Hall and Van der Pauw measure-

HFET	$n_{s,meas.}$ [cm^{-2}]	μ [cm^2/Vs]	R_{Sheet} [$\Omega/\square$]
Multi-layer series			
B1	1.82·10^{12}	1330	2578
B2	5.65·10^{12}	1860	594
B3	4.31·10^{12}	1870	774

Table 6.4.: Electron density, mobility and sheet resistance measured by Hall and van der Pauw for the as-grown HFETs.

ments are given in Tab. 6.4. HFET B1 with its single low-polarization layer shows the lowest density and mobility. For both HFETs with high-polarization layers, the electron density increases with a simultaneous increase in mobility. The latter is due to the lowered Coulomb scattering at ionized impurities [250, 252]. The trend of the measured values of n_s follows the predictions of the simulations. Since the average Al content in the barrier of HFET B3 is not as high as for HFET B2, HFET B2 generates a larger n_s than the ramped HFET B3.

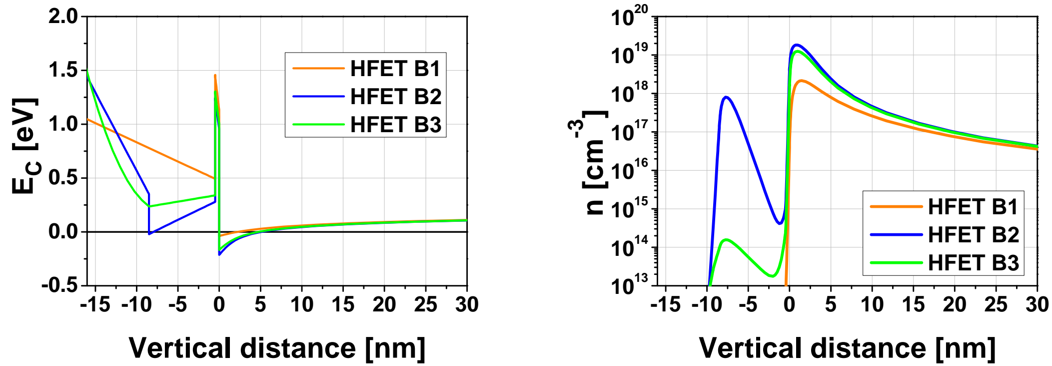

(a) Conduction band along depth.

(b) Electron density n_s along depth.

Figure 6.7.: Simulations for devices B1, B2 and B3. After [260].

Transistor performance

The three samples were processed to HFETs with 1 µm gate length. A gate recess of 11 nm was applied to remove the high polarization layers and, hence, to ensure a positive V_{th}. To realize identical intrinsic devices, the recess was applied to all samples [260].

The transfer characteristics of HFET B1, B2 and B3 are shown in Fig. 6.8. All three devices are normally-off with a similar V_{th} between 0.5 V and 0.6 V. This indicates that also the intrinsic devices are very similar. In agreement to the ex-

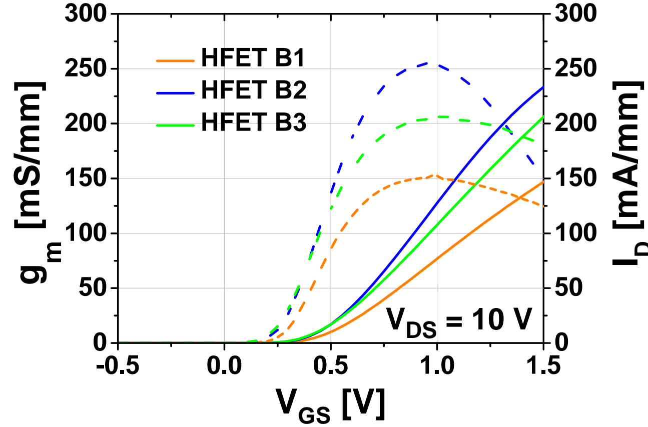

Figure 6.8.: Transfer characteristics for the gate recessed HFETs B1, B2 and B3.

pectations regarding Eq. 6.1, HFET B2 and B3 with the lower R_{Sheet} show larger g_m compared to HFET B1. HFET B2 exhibits a g_m up to 260 mS/mm, which is comparable to conventional AlGaN/GaN HFETs with 1 µm gate length [260].

The drain current I_D in the off-state is limited by the gate leakage current. Before SiN passivation, all devices showed very low leakage currents below 10 nA/mm, which resulted in very high on-off ratios of 10^7 for HFET B1 and 10^8 for HFET B2 and HFET B3. After passivation, this on-off ratio shrunk dramatically to 10^4 due to increased gate leakage current. The gate current at -1 V for HFET B2 increased from $1.5{\cdot}10^{-6}$ mA/mm before passivation to $7.8{\cdot}10^{-3}$ mA/mm. An additional Al_2O_3 gate dielectric was tested successfully to solve this issue [260]. The gate leakage could be reduced for HFET B2 to $3.3{\cdot}10^{-5}$ mA/mm.

In conclusion, polarization engineering has successfully been utilized to obtain both d-mode and e-mode behavior for n-channel HFET. Tensile strained AlInGaN on GaN exhibit a large P_{total} (P_{piezo} and P_{spon} are parallel), which results in d-mode characteristic of HFETs. Compressively strained layers have shown a strongly reduced P_{total} (P_{piezo} and P_{spon} are anti-parallel), which has been utilized for e-mode HFETs. However, the structural degradation for compressively strained AlInGaN with larger In contents results in a lower mobililty μ and, hence, decreased performance of the HFET. Improved e-mode HFET performance has been obtained with almost lattice-matched AlInGaN barriers with low Al contents (P_{piezo} is negligible and P_{spon} is itself small). To improve the performance further, multi-layer AlInGaN barrier HFETs with an additional high-polarization layer in the access region have been introduced. The lowered R_{Sheet} in the access region leads to higher drain currents I_D and transconductances g_m.

Chapter 7

HFET structures with AlInGaN backbarriers for 2DHG accumulation

In analogy to the methodology used in Chap. 6 for polarization engineering in heterostructures with a two-dimensional electron gas (2DEG), heterostructures with a two-dimensional hole gas (2DHG) are investigated here. The 2DHG is induced by the polarization difference (ΔP) between an AlInGaN backbarrier and a GaN channel on top. It is shown that by changing the AlInGaN composition and, hence, by changing ΔP, the electrical properties of the 2DHG can be engineered in a wide range. By appropriate polarization engineering, the threshold voltage of p-channel heterostructure field effect transistors (HFETs) can be controlled according to the corresponding 2DHG density, which allows for the realization of both d-mode and e-mode p-type transistors.

7.1. Preface to Mg doping of GaN

In contrast to the simple task of doping GaN n-type with Si [261, 262], p-type doping of GaN is challenging. Mg is the typical group II element used as the p-dopant. Depending on the acceptor concentration, Mg has a large activation energy between 125 meV and 180 meV [263–267]. Owing to the large activation energy, the doping efficiency of bulk GaN:Mg is only in the order of 1 %-2 % after appropriate annealing steps [268, 269]. The annealing is necessary to activate the Mg acceptors, which are normally passivated with H atoms after epitaxy [270]. Further, GaN grown by MOVPE suffers from a typical n-type autodoping caused by the large background impurity level in the gas phase as compared to ultra-high vacuum epitaxy techniques, e.g. MBE [271, 272]. Within the impurity spectrum in unintentionally doped (uid)-GaN, C, O and H can be found in relatively high concentrations in the range of typical dopant concentrations. The actual impurity concentrations depend on growth conditions [269]. While O is dominantly of donor-type with an ionization energy of merely 30 meV [273, 274], C is mainly a deep acceptor located at

0.9 eV above the valence band [275] and is, hence, often intentionally incorporated to achieve semi-insulating GaN buffers for high-power applications [276]. However, it has also been reported that C_N-O_N complexes form deep donors, which are likely to compensate Mg acceptors [269]. The largest activation efficiencies for Mg p-doping are achieved for layers with low residual C concentrations, which is obtained at high growth surface temperature ($T_{Surface}$), pressure and V/III ratio. In conclusion, due to the high n-type autodoping and the compensation effect, the Mg acceptor concentration needs to be relatively large for sufficient p-type conductivity in MOVPE-grown GaN [277–280]. So far, the hole density in bulk GaN has never been reported to be in excess of $1{\cdot}10^{18}$ cm^{-3}.

A further limitation for a high p-conductivity is the low hole mobility. To illustrate the reported p-type conductivities, literature values for hole density and hole mobility at room temperature are summarized in Fig. 7.1. Plotted are values for both holes in bulk GaN:Mg and holes in a 2DHG. The upper and lower axes are correlated by the assumption that the spatial width of the 2DHG is 5 nm. The gray area in the lower left corner marks the upper limits for MOVPE bulk p-GaN. The limits are a bulk hole density of about $1{\cdot}10^{18}$ cm^{-3} and a mobility of 15 cm^2/Vs. Bulk samples are shown as circles in this plot. Even in MBE p-GaN, shown in red color in the plot, the maximum hole density is only slightly larger with $1.4{\cdot}10^{18}$ cm^{-3} at a mobility of 7.5 cm^2/Vs. Further, MBE p-GaN exhibits large mobilities up to 24 cm^2/Vs for densities in the low 10^{17} cm^{-3} regime [80]. This trend can be understood by the reduced Coulomb scattering in low-impurity bulk p-GaN. However, the specific resistance even under optimized annealing conditions is restricted to values above 0.5 Ωcm [281].

To achieve higher hole densities, different approaches have been proposed. By introducing a modulation-doped p-type AlGaN/GaN superlattice, the hole density can be increased to the range of 1-4 $\cdot 10^{18}$ cm^{-3} [282–284]. These samples are shown as triangles in the plot. In such a superlattice, the ΔP between the AlGaN barrier and the GaN well leads to a periodic oscillation of the valence band edge. This results in an accumulation of holes at these interfaces resulting in a slightly more efficient Mg doping. Still, due to the modulation doping, the hole mobility remains below 10 cm^2/Vs for MOVPE layers. Again, low-impurity MBE layers show a significantly increased mobility [284], confirming that scattering at ionized impurities is still very dominant in such superlattice structures.

The most advanced approach in raising both the hole density and mobility is the realization of a single 2DHG. As described in Sec. 2.4.3, this can be realized by forming a deep valence band quantum well at the interface between a backbarrier and

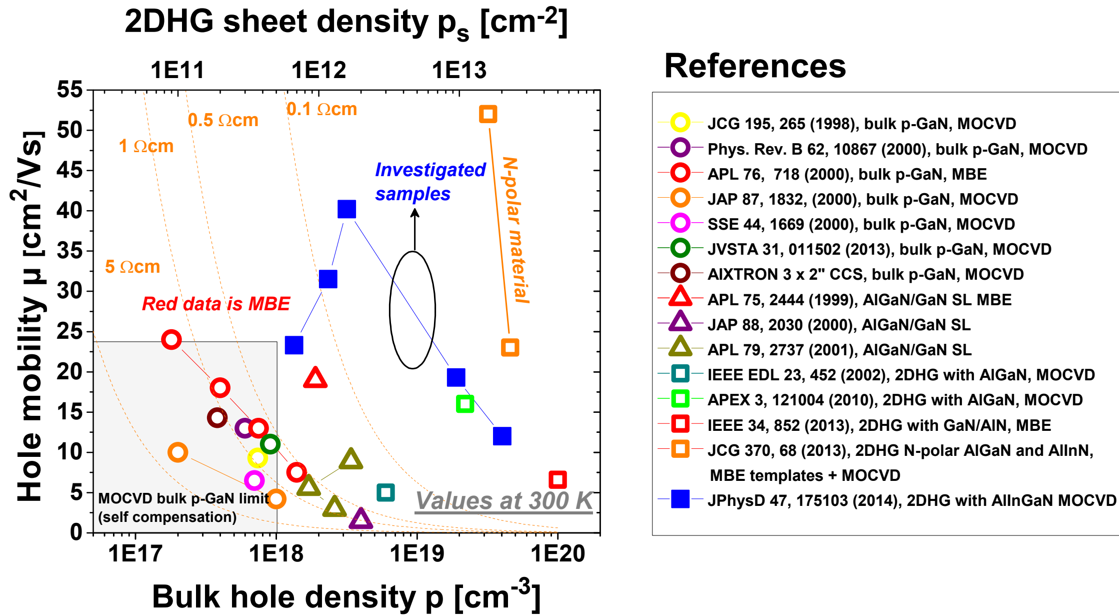

Figure 7.1.: Hole mobility μ plotted either versus the bulk hole density p (for holes in GaN:Mg) or versus the 2DHG sheet density p_s (for holes in a 2DHG). The correlation between p and p_s is calculated by assuming a spatial width of the 2DHG of 5 nm.

a GaN channel. Such samples are shown as squares in the plot. The confinement of holes at the interface leads to the highest possible hole mobilities. Here, ΔP is the important parameter to control the hole density. In the past, only a few publications have reported on 2DHG due to the issues mentioned before, e.g. n-type autodoping. As manifested by the low hole mobilities (not exceeding 16 cm^2/Vs), these heterostructures were far from being mature [48–54]. Only recently, research on 2DHGs has returned into focus and very large mobilities above 50 cm^2/Vs have been reported for N-polar HFET structures deposited with MOVPE on MBE templates [55]. In another study, an MBE HFET with an AlN backbarrier has been presented with the highest ever reported hole density of up to $5 \cdot 10^{13}$ cm^{-2} [56]. These results are far outperforming any conventional doping approach. Further, p-channel transistors have been fabricated using this high-density 2DHG [56].

A systematic study of the influence of the built-in polarization on the 2DHG and on the transistor characteristics is presented here and has been published in [285]. To give a comparison to the results from literature, the values for hole density and mobility are also shown as full blue squares in Fig. 7.1. Clearly visible is that for very large 2DHG densities above $1 \cdot 10^{13}$ cm^{-2}, the results are comparable to the published values from other groups [52–54, 56]. This trend indicates that in this density range

the mobility is limited by a fundamental effect, which will be addressed in a following section. For lower hole densities, however, a strong increase in the mobility above 40 cm^2/Vs is observed due to the absence of a large impurity concentration in the hole channel.

7.2. p-channel HFET structures utilizing a 2DHG

The layer stack of the p-channel HFETs fabricated for this thesis is depicted in Fig. 7.2a. It consists of a GaN/AlN buffer, which is identical to the one used for n-channel HFETs presented in Sec. 4.1, followed by a 35 nm thick AlInGaN backbarrier and a GaN channel on top. A schematic of the corresponding bandstructure for a metal-polar heterostructure is shown in Fig. 7.2b. Due to internal electric fields, both the conduction band and the valence band form potential wells at the heterointerfaces. While the conduction band well is formed at the lower AlInGaN/GaN interface, the valence band well is located at the upper GaN/AlInGaN interface. When the whole structure consists of uid-layers, the n-type autodoping leads to a shift of the Fermi level towards the conduction band (gray drawing). Thus, a 2DEG (E_C crosses E_F) is formed below the AlInGaN layer in analogy to a conventional barrier/GaN heterostructure. To form a quantum well in the valence band (E_V crosses E_F) in the upper GaN channel, compensation of the n-autodoping with Mg acceptors is necessary. Only in this case, as illustrated in the bandstructure (blue drawing) in Fig. 7.2b, a 2DHG can be formed at this upper interface.

The Mg doping level in the upper GaN channel is one of the key issues for inducing a 2DHG with a sufficiently large density and for enabling ohmic contacts. In detail, the 33 nm thick GaN consists of a 3 nm unintentional doped uid-GaN channel, a 20 nm weakly Mg-doped layer and a 10 nm topmost highly doped GaN:Mg^{++} cap for which first the Mg concentration was gradually increased to a high level and for which then, the high level was applied constantly. The 3 nm uid GaN cap in the proximity to the AlInGaN barrier was grown before the heating step to GaN channel growth conditions. This cap fulfills two functions: first, it works as a protection layer for the AlInGaN to prevent In outdiffusion while heating; second, the 2DHG is located in this cap and the mobility is likely to be enhanced due to a reduced scattering probability at ionized dopants. The weak Mg doping in the following 20 nm was applied for compensation of the n-type autodoping. The highly doped GaN:Mg^{++} cap is necessary for ohmic contact formation. Although there is an ongoing controversial discussion about the mechanisms of p-ohmic contact formation, in either case, a clear dependence of contact resistivity on doping concentration has

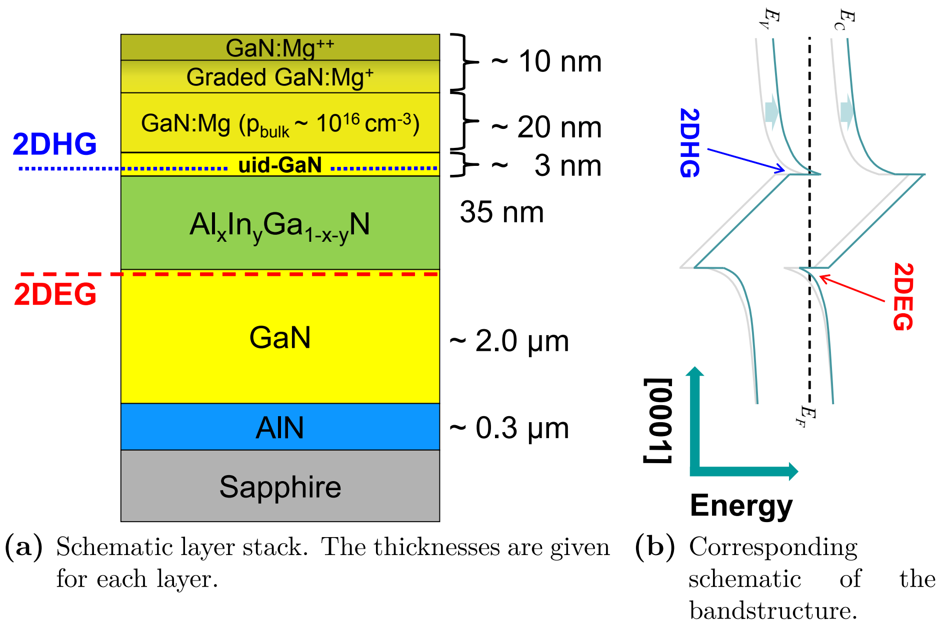

(a) Schematic layer stack. The thicknesses are given for each layer.

(b) Corresponding schematic of the bandstructure.

Figure 7.2.: Layer stack and corresponding schematic bandstructure of p-channel HFETs grown by MOVPE for two cases: Without any Mg doping (grey curve) and with Mg compensation doping in the upper GaN channel (blue curve). The highly doped GaN:Mg^{++} cap is neglected in the bandstructure for simplicity.

been reported [286–289].

For efficient Mg acceptor activation, all heterostructures were annealed before electrical characterization in an open furnace with an applied nitrogen flow at 700 °C for 20 min.

7.2.1. Mg compensation doping

In a first experimental series, the Mg acceptor concentration in the upper GaN channel, which is required for 2DHG formation, is investigated. For determination of the effective bulk hole concentration p for different Cp_2Mg-to-TMGa molar flow gas phase ratios, reference samples without backbarriers are regarded. These are marked as p-GaN stack. Samples with an AlInGaN backbarrier for 2DHG formation are marked as 2DHG stack. Cross sections for both investigated layer stacks are shown in Fig. 7.3a.

In a first experimental series, two different Cp_2Mg-to-TMGa molar flow gas phase ratios were applied: 0.12 % and 0.36 %. The exact doping profiles, measured by secondary ion mass spectroscopy (SIMS), are shown for both ratios for the p-GaN stack in Fig. 7.3b. As obvious from the right hand side of the profile, the SIMS

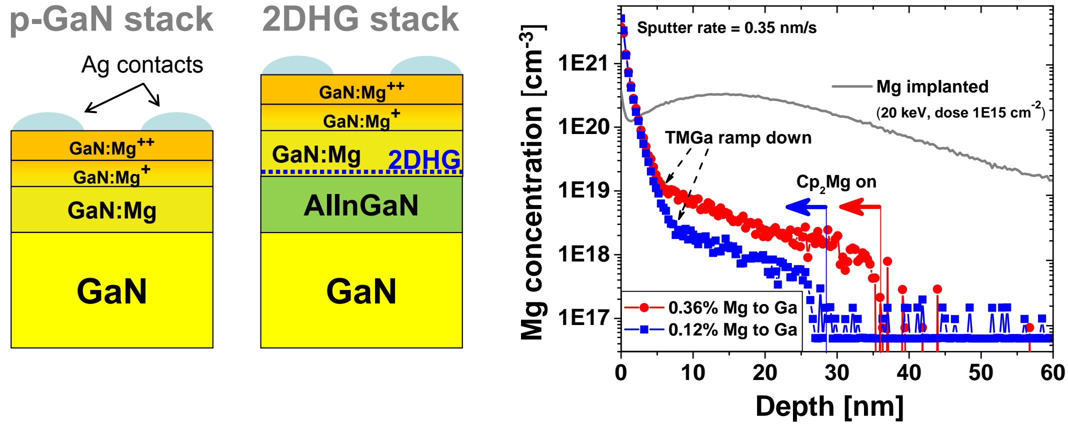

(a) Schematic of the layer stacks used (p-GaN and 2DHG). **(b)** Mg concentration profiles of the p-GaN stacks.

Figure 7.3.: Layer stacks used (p-GaN and 2DHG) and SIMS measurements of p-GaN samples with two different Cp_2Mg-to-TMGa gas phase ratios: 0.36% (red curve with circles) and 0.12% (blue curve with squares). The profile of a Mg-implanted GaN sample which serves as a reference for the determination of the relative sensitivity factors is also shown (gray line).

detection limit is slightly below 10^{17} cm^{-3}. In terms of the absolute doping level, the SIMS results confirm the expected higher Mg incorporation for the increased precursor flow. The measurement curves show two characteristic regions: first, the region with a weak Mg doping; second, the region near the surface, which shows a strong increase of the Mg concentration in growth direction. Although a constant Cp_2Mg flow was applied for the weakly doped p-GaN, the Mg profiles for both samples show a gradual increase by more than one order of magnitude. This appearance is caused by the so called delay effect, which is the adsorption of Mg precursor molecules on reactor parts [290–292]. Consequently, the available effective Mg precursor concentration increases with growth time. Furthermore, this delay effect will extend over a longer time span for lower Cp_2Mg flows, since in this case the reactor saturation will occur later. This mechanism also explains the apparently delayed onset of the Mg doped region for the low-doped sample. Although the delay effect is not intended, for the working principle of the final device, the resulting graded Mg profile is quite advantageous. The Mg doping profile enables a spatial separation of the GaN/AlInGaN interface, at which the 2DHG is accumulated, to the region with larger ionized impurity concentration. Hence, larger mobilities can be expected. For the last 7 nm below the surface, the Mg concentration increases strongly, peaking for both dopant ratios at the same level of about $6 \cdot 10^{21}$ cm^{-3}. This

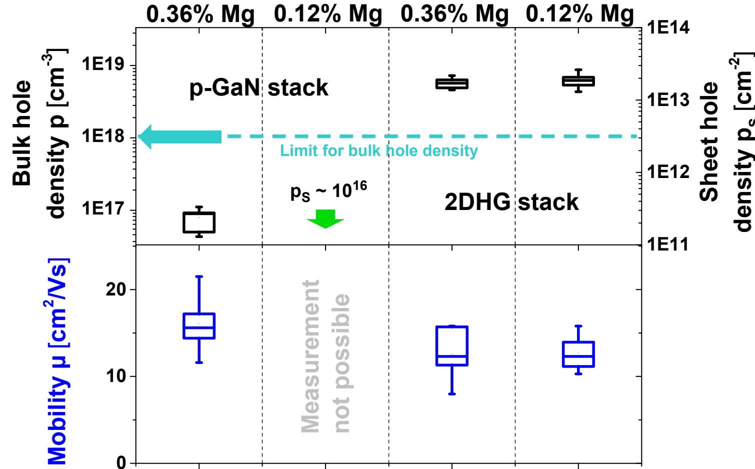

Figure 7.4.: 2DHG density and mobility plotted for a layer stack without AlInGaN (p-GaN) and one with AlInGaN (2DHG), both grown twice with different Cp_2Mg-to-TMGa gas phase ratios.

is in agreement with the reactor conditions, as for both samples, the process ramps to the same Cp_2Mg-to-TMGa ratio of 2.7 %. This profile is mainly achieved by ramping the TMGa flow down. This results in a lower growth rate and, hence, a higher doping level.

Electrical properties

Hall and Van der Pauw measurements were carried out on 5 mm by 5 mm pieces of the as-grown wafers with provisional ohmic contacts formed by Ag paint. The measured bulk hole density p for the reference p-GaN stacks and the p_s for the 2DHG stacks with corresponding mobility values are shown in Fig. 7.4. The sample with the larger Cp_2Mg-to-TMGa ratio of 0.36 % exhibits a bulk hole density p of $6.6{\cdot}10^{16}$ cm^{-3}. From this value, the activation efficiency is estimated to be between 0.7 % and 1.1 %. This value is reasonable in comparison to values reported in the literature for similar doping levels and annealing temperatures [277–280]. The density of the sample with 0.12 % Cp_2Mg-to-TMGa ratio was not accessible via Hall measurements, because of a very high sheet resistance. By assuming an equal activation efficiency and taking results from SIMS measurements into account, the hole density p is estimated to be in the range of low 10^{16} cm^{-3}.

By the insertion of an $Al_{42\%}In_{3\%}Ga_{55\%}N$ backbarrier, the measured hole density increases by two orders of magnitude. A p_s of $2{\cdot}10^{13}$ cm^{-2} is measured for both 2DHG stack samples with the same AlInGaN backbarrier but different Cp_2Mg-to-TMGa ratios (Fig. 7.4). Assuming a total GaN thickness of 30 nm, such a p_s value would

correspond to $p = 7{\cdot}10^{18}\,\text{cm}^{-3}$, which is far exceeding the limit for bulk hole densities of $1{\cdot}10^{18}\,\text{cm}^{-3}$ [277–280].

These observations confirm that holes are accumulated in the proximity to the GaN/AlInGaN interface (as shown in 7.2). The spatial width of such a 2DHG is very small and not exceeding 5 nm. In this region, the acceptor level is above the Fermi level and, hence, a higher number of Mg acceptors is activated. Even by assuming each Mg atom to contribute a hole and by taking the Mg concentration from SIMS into account, a theoretical p_s of only a few times 10^{12}cm^{-2} for the high Cp_2Mg-to-TMGa ratio of 0.36 % would be reached. Hence, despite the likely possibility of the Mg acceptor to serve as a hole source, the origin for the very large p_s is a polarization-induced 2DHG.

The low Cp_2Mg-to-TMGa ratio of 0.12 %, which results in an average Mg concentration of about $1.4{\cdot}10^{18}\,\text{cm}^{-3}$ in the low doped region, is sufficient to compensate for the n-type background doping. Further, measurements of additional samples without Mg doping in the upper GaN layer were performed. These tests revealed that the hole density was not accessible via our measurement setup. Hence, a weak compensation doping with Mg is necessary for the functionality of p-channel HFETs. Thus, all samples discussed in the following exhibit a weak Mg doping.

7.3. AlInGaN backbarrier composition

In this section, the influence of ΔP on the 2DHG characteristics is studied. Five samples A to E, which differ only in the composition of the AlInGaN backbarrier, are compared. Sample properties are given in Tab. 7.1. The different AlInGaN compositions were selected such that the range of achievable values for the total polarization (P_{total}) and, hence, for ΔP was maximized while simultaneously maintaining a high crystal quality. The latter was obtained by adjusting a relatively large $T_{Surface}$ between 793 °C and 820 °C, which results in an In content at a level below 5 %. Very low RBS channeling values $\chi_{\text{RBS,min}}$ of 1.2-1.8% were measured.

As discussed in Sec. 6.2, P_{total} is most effectively changed by adjusting the Al-to-Ga content ratio in the AlInGaN layer. This was achieved by a reduction of the TMAl molar flow from 20.9 µmol·min^{-1} to 5.2 µmol·min^{-1} and by an increase of the TMGa molar flow from 8.8 µmol·min^{-1} to 22.0 µmol·min^{-1}. The resulting TMAl-to-TMGa molar flow ratio were between 0.2 and 2.4 (as given in Tab. 7.1). The TMIn flow was kept at a constant value of 31.5 µmol·min^{-1}.

As intended, between the samples, a large difference is found in the Al content. It decreases from 54 % for sample A to 14 % for sample E. On the other hand, the In

Sample	T_S [°C]	$\frac{TMAl}{TMGa}$	Al [%]	In [%]	Ga [%]	t_{bar} [nm]	ΔP [Ccm^{-2}]	$p_{s,calc./meas.}$ [10^{12}cm^{-2}]	μ [cm^2/Vs]
2DHG-series									
A_{2DHG}	820	2.4	54	4	42	33	-0.036	16.10 / 20.27	12
B_{2DHG}	815	1.2	42	3	55	35	-0.027	10.47 / 9.79	19
C_{2DHG}	807	0.6	25	2	73	33	-0.014	2.87 / 2.24	30
D_{2DHG}	798	0.4	20	2	78	36	-0.010	0.80 / 1.18	29
E_{2DHG}	793	0.2	14	2	84	36	-0.006	- / 0.63	23

Table 7.1.: MOVPE conditions, structural and electrical properties of 2DHG stack samples with AlInGaN backbarriers grown at different TMAl-to-TMGa molar ratios.

content remained almost stable with values of 2 % for samples C-E and 3 % and 4 % for sample B and A, respectively. Although the In incorporation is mainly driven by $T_{Surface}$, also TMAl has a catalytic effect[1] [213, 223–227]. Hence, to maintain a reasonable amount of In in the quaternary layers for the less strained samples, $T_{Surface}$ was reduced for each sample by about 5-10 K with a simultaneous reduction in the TMAl flow.

As shown in Fig. 7.5, the changing composition of the AlInGaN layers for the samples is manifested in the position of the reflexes in XRD measurements. In Fig. 7.5a, HRXRD (0002) 2Θ-ω scans are shown. The GaN peak located at around 34.5 ° and the AlN peak at around 36.1 ° remain stable for each sample, indicating reproducible buffer growth. The AlInGaN peak is located in-between the peaks of GaN and AlN and is shifted to lower diffraction angles from sample A, with high Al content, to sample E, with low Al content. All scans show pronounced fringe oscillations indicating very good interface quality. A closer look at the scans reveals superoscillations on the AlInGaN peak with a specific periodicity corresponding to the total GaN channel thickness grown on top of the AlInGaN backbarrier. The fitting of the HRXRD 2Θ-ω scans is consistent with RBS compositional analysis and can be used to estimate the thicknesses. The AlInGaN thickness which is comparable for all samples is about 35 nm. This corresponds to a growth rate of about 4.7 nm/min. The merged HRXRD ($10\bar{1}5$) RSMs depicted in Fig. 7.5b reveal equal in-plane lattice parameters for AlInGaN and GaN, which demonstrates pseudomorphic growth for all AlInGaN layers. The stars in matching colors represent the theoretical position of fully relaxed AlInGaN layers. Larger distances of theoretical positions and the measured peaks indicate larger residual strain in the respective layers.

[1] The catalytic effect is related to an enhanced In clustering for larger Al contents in tensile strained AlInGaN (compare Sec. 4.3.3).

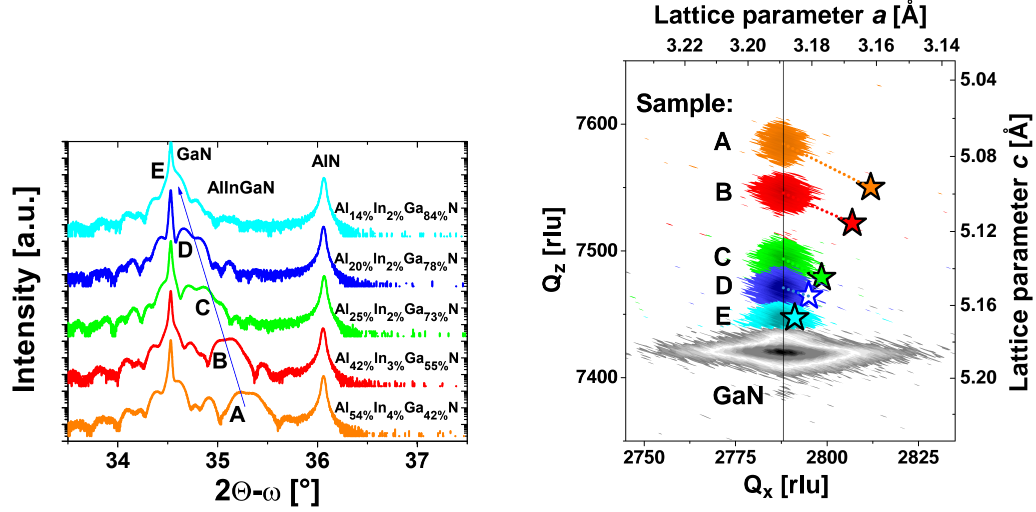

(a) 2Θ-ω (0002) scans. The blue arrow in the figure indicates the quaternary peak position.

(b) Merged (10$\bar{1}$5) RSMs. The stars in matching colors represent the theoretical position of the corresponding fully relaxed AlInGaN layers. Obviously, all samples are pseudomorphically grown on GaN.

Figure 7.5.: HRXRD analysis for samples A to E, which were grown at different reactor conditions.

For sample A, the residual strain was calculated to be 0.87 %. This strain state would correspond to pseudomorphic AlGaN with 35 % Al. The critical thickness of such a layer, however, is below 30 nm [75]. This indicates that the critical thickness of AlInGaN is likely to be larger compared to that of AlGaN layers at equal strain states [293]. The In atoms in an AlGaN lattice are likely counterbalancing local strain peaks by acting as a joint preventing relaxation.

To visualize further consequences of the composition change, the calculated bandgap E_g is plotted in Fig. 7.6 against the nominal lattice constant a. In all calculations, the compositions extracted from the RBS measurements were employed. All AlInGaN layers in this series exhibit a smaller nominal lattice constant than GaN. Hence, the layers are tensile strained on GaN. They also have a larger bandgap than GaN, which is a requirement for 2DHG formation at the GaN/AlInGaN interface.

Further, a subsequent reduction in tensile strain from high Al contents for sample A to lower Al contents for sample E is obvious. This results in a decrease of the piezoelectric polarization (P_{piezo}) accompanied by a decrease of the spontaneous polarization (P_{spon}) due to the lowered Al content. Thus, ΔP to GaN decreases, which is clearly visualized in the approach from sample A to E to the red polarization-matching line to GaN.

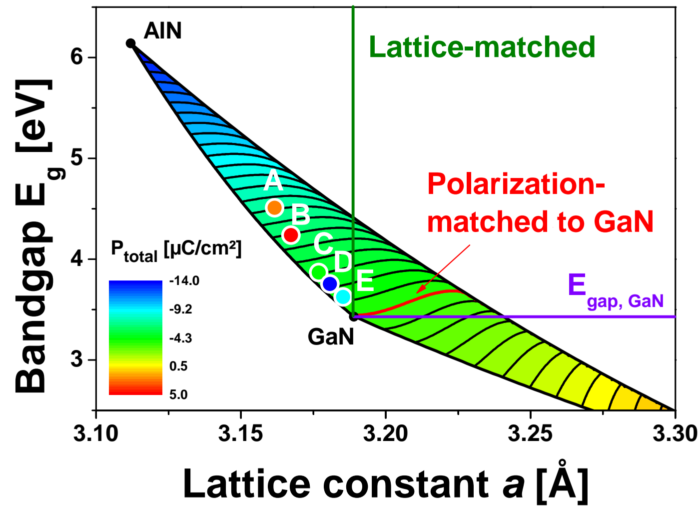

Figure 7.6.: Illustration of the compositions of AlInGaN backbarriers for sample A to E in the bandgap vs. lattice constant diagramm.

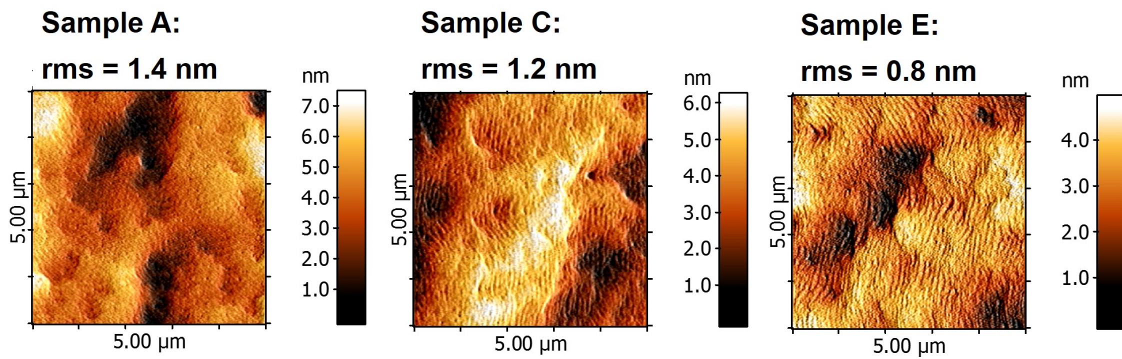

Figure 7.7.: AFM images illustrate smooth surfaces for samples A, C and E. A slight trend to a lower surface roughness is observed from the highly tensile strained sample A to the almost unstrained sample E.

The as-grown surface morphology of samples A, C and E are shown in Fig. 7.7. All samples exhibit a reasonably smooth surface with an atomic step flow pattern in the nanoscale. In the µm scale, however, a clear trend from a wavy surface for sample A to a smoother surface for sample E leads to a reduction of the root mean square roughness (rms) from 1.4 nm to 0.8 nm. This leads to the conclusion that high tensile strain results in a slight degradation of the surface and possibly also of the GaN/AlInGaN interface.

7.3.1. Electrical properties

In the following analysis, Hall and Van der Pauw measurements are presented for samples A to E with different ΔP. Therefore, ohmic contacts were realized on the different samples via e-beam evaporation of 20 nm Ni and 20 nm Au and subsequent annealing in air at 495 °C for 10 min.

In Fig. 7.8, the median values of the measured hole density $p_{s,measured}$ (red circles) as well as the measured mobility μ (blue circles) are plotted against ΔP. Additionally, theoretical values for the hole density $p_{s,calc.}$(gray squares), calculated with Eq. 2.21, are plotted. With rising ΔP, steadily increasing values for $p_{s,measured}$ from $6{\cdot}10^{11}$ cm^{-2} to $2{\cdot}10^{13}$ cm^{-2} are obtained. This is in agreement to the expectation that $p_{s,calc.}$ increases for larger ΔP. This trend sets the 2DHG density in correlation to the AlInGaN backbarrier composition and clearly proves that a polarization-induced 2DHG is the dominant conductive path in these heterostructures. The shape of the mobility plot shows an apparent peak for sample C with a moderate 2DHG density of $2.2{\cdot}10^{12}$ cm^{-2}. As illustrated by the error bar in Fig. 7.8, a large spread of the measured values is apparent only for sample C. For this sample, a median mobility of 30 cm^{2}V^{-1}s^{-1} is derived. However, on one test structure on sample C, a mobility of 43 cm^{2}V^{-1}s^{-1} was measured at a p_s of $1.3{\cdot}10^{12}$ cm^{-2}. At a low measurement temperature of 77 K, hole mobilities for sample D with a maximum of up to 109 cm^2/Vs for a 2DHG density of $1.0{\cdot}10^{12}$ cm^{-2} were measured. These values demonstrate a record for holes in GaN-based heterostructures. For both smaller and larger ΔP, the mobility decreases.

The aforementioned slight increase in interface roughness for samples with larger residual strain might only play a role for samples with large 2DHG densities and, hence, a small 2DHG-to-interface distance. However, fringe oscillations in HRXRD scans are similar for all samples. Thus, the interface quality is comparable for all samples. As a conclusion, the interface roughness is not the root cause for the different mobilities. The overall peak shape of the mobility function, in particular,

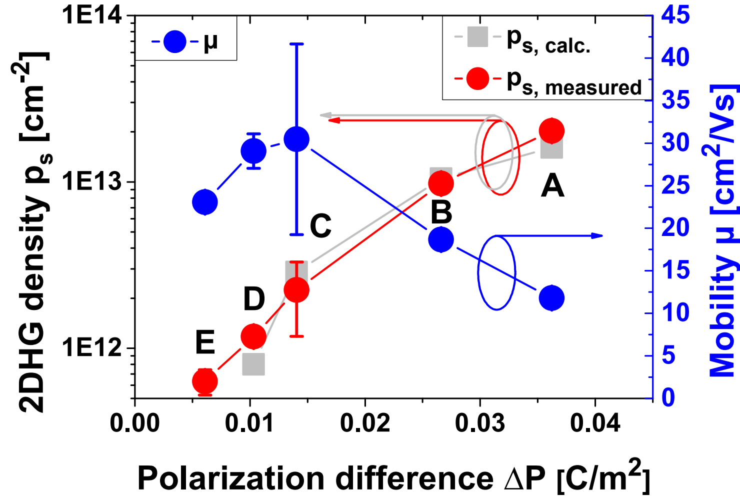

Figure 7.8.: Median values of measured $p_{s,measured}$ (red circles) and calculated $p_{s,calc.}$ (grey squares) as well as the mobility (blue circles) plotted against ΔP for samples A-E. The error bars illustrate the standard deviation for measurements of different structures on a single wafer.

the decrease of the mobilities for samples D and E with very smooth surfaces, must find its origin in other scattering phenomena, which are addressed in the following.

To compare the behavior of the mobility of a 2DHG and a 2DEG, in Fig. 7.9, μ vs. n_s plots of both the 2DHG-series (samples A-E) from this section and the 2DEG-series (samples F1$_{2DEG}$-F6$_{2DEG}$[2]) from Sec. 6.2 are superimposed. This direct comparison is permissible, because the epitaxy conditions and, hence, the AlInGaN compositions of the respective sample combinations are very similar. The values for samples F6$_{2DEG}$^{p} (p for passivated) and F6$_{2DEG}$^{r} (r for recessed), are taken from Fig. 6.4.

Apparently, the mobility values show the same shape for each type of carriers with a maximum at a specific density. For both lower and higher densities, n_s and p_s, the respective mobilities μ_n and μ_p decrease. It can be concluded from this similarity that equal scattering mechanisms are dominant for electrons in a 2DEG and for holes in a 2DHG. While for large densities in a 2DEG, interface scattering plays a major role due to a strong confinement at the interface, for low densities, scattering at ionized impurities is the dominant mechanism [250–252]. This behavior can also be expected for holes in a 2DHG. However, different physical properties have to be accounted for. First, the hole mobilities are about 2 orders of magnitude lower than for electrons. This is mainly due to the higher effective mass m_{eff}. Compared to

[2]For distinction, the 2DEG samples are marked with a subscript $_{2DEG}$ in this section.

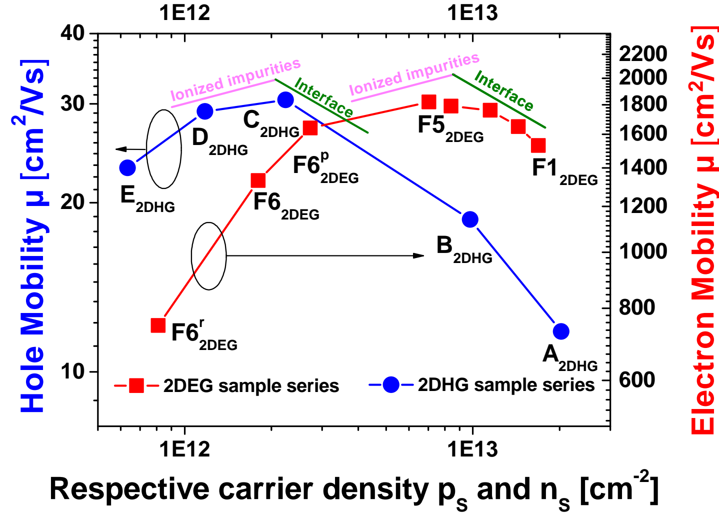

Figure 7.9.: Carrier mobility for holes in a 2DHG and electrons in a 2DEG plotted against the 2DHG and 2DEG density, respectively. The values for the 2DHG are those of the samples presented here, whereas the values for the 2DEG are taken from the TMAl-toTMGa series presented in Sec. 6.2.

the effective mass of electrons of $m_{eff,e}$ =0.22·m_0 [68], the effective mass of holes in the heavy hole band $m_{eff,h}$ is above 2·m_0 [64, 70]. Second, the mobility peak is shifted to lower carrier densities from 7.1·10^{12} cm^{-2} for electrons to 2.2·10^{12} cm^{-2} for holes. This effect is also related to the different effective masses m_{eff} of electrons and holes leading to different spatial charge distributions. The 2DHG-to-interface distance is smaller than the 2DEG-to-interface distance. This results in an increased probability of interface scattering for holes in a 2DHG compared to electrons in a 2DEG. Generally, for higher densities, the center of the charge distribution is moving towards the interface and, hence, the confinement of carriers becomes stronger. Both effects can explain that the hole mobility peak is located at lower carrier densities in comparison to electrons.

7.3.2. p-Channel transistor performance

HFETs with 1 µm gate length were processed on samples A-E. A schematic cross section of the processed structures is given in Fig. 7.10. Ohmic contacts were realized on the highly Mg-doped GaN cap layers by employing a Ni/Au metal stack [286]. In initial experiments and in agreement with published results, it has been found that an equal thickness for Ni and Au yields the lowest value for specific contact resistivity [294]. A stack of 20 nm Ni and 20 nm Au is used here. Although the exact mechanism for ohmic contact formation are still controversially discussed, it

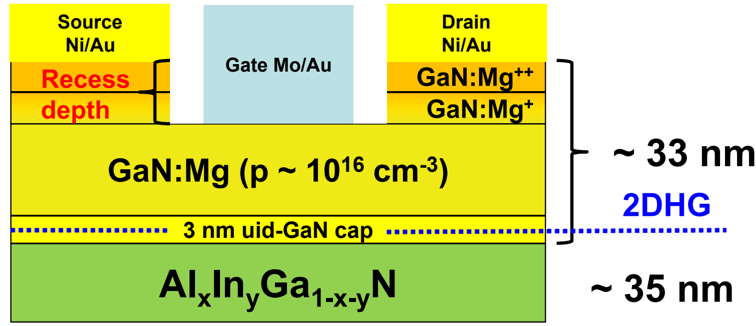

Figure 7.10.: A schematic cross section of processed p-channel HFETs utilizing the polarization-induced 2DHG. Ni/Au metal stacks are used for source and drain ohmic contacts, and Mo/Au metal stacks were used for a Schottky gate. Prior to the gate metallization, a recess of 7 nm was applied to all samples to remove the highly Mg-doped GaN cap layers between the ohmic contacts.

is commonly agreed upon that Ni reacts with O and diffuses to the top of the stack, resulting in a NiO/Au/p-GaN stack. Furthermore, Au diffuses to the GaN interface and can partly form GaAu alloys. Oxygen also promotes the out-diffusion of Ga. Both effects lead to the formation of Ga vacancies below the contact. These act as acceptors leading to a low contact resistance R_C [287, 288].

For the 2DHG-series, R_C is strongly dependent on the sheet resistance R_{Sheet} of the samples, which is higher for sample E than for sample A. While sample A with a low R_{Sheet} exhibits an R_C of 43 Ωmm, R_C increases to 800 Ωmm for sample E with a high R_{Sheet}.

For the gate, a 50 nm Mo / 200 nm Au stack is used, which has been found to be the optimum for a p-type Schottky barrier [112]. This gate metal stack was deposited on the 7 nm recessed GaN channel to form a Schottky barrier with reasonable blocking characteristics in the reverse direction. Furthermore, an access region etch of 7 nm suppresses leakage currents in the forward direction. The optimum access and gate recess depth of 7 nm in matters of device performance has been found in previous experiments, published elsewhere in more detail [295]. This depth is exactly matching the thickness of the highly doped GaN:Mg^{++} cap determined by SIMS in Fig. 7.3b.

Output characteristics for sample A are shown in Fig. 7.11a. Obviously, the drain current is negative for a negative drain source voltage V_{DS}, which demonstrates the p-channel characteristics of this device. An absolute drain current $|I_d|$ of above 40 mA/mm is reached at a negative gate source voltage V_{GS} of -3 V. For GaN-based p-channel devices, this value is considered as being high. Although p-channel devices with larger drain currents above 100 mA/mm have been reported for a GaN/AlN

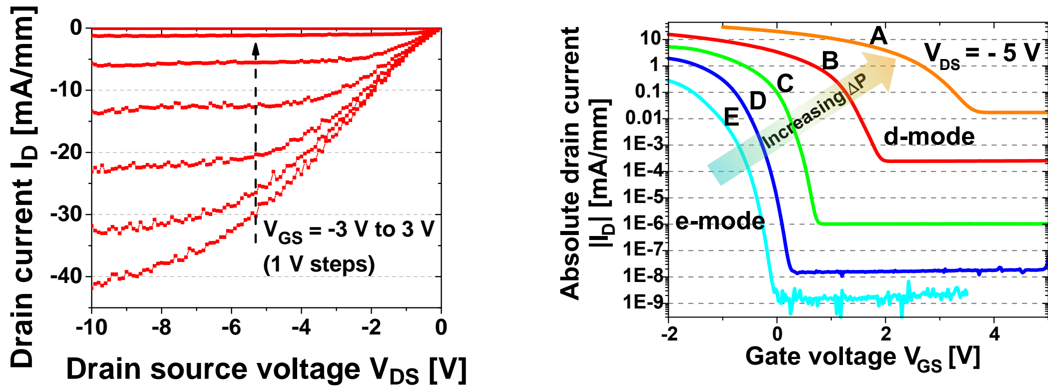

(a) Drain current I_d as a function of drain source voltage V_{DS} for the d-mode sample A (V_{GS} = 3 V to -3 V).

(b) Absolute drain current $|I_d|$ as a function of gate voltage V_{GS} (V_{DS} = -5 V). The threshold voltage shifts from negative values (e-mode) to positive values (d-mode) for increasing ΔP.

Figure 7.11.: Output and transfer characteristics for p-channel HFETs utilizing a 2DHG.

heterostructure [56] (due to the largest possible ΔP in GaN-based HFETs), these transistors show high off-state currents, which result in low on-off ratios of only one order of magnitude. As apparent in Fig. 7.11b, by applying a positive gate source voltage V_{GS} of 3.5 V, sample A can be pinched off properly with an off-current as low as 0.02 mA/mm, resulting in an on-off ratio above 10^3.

The impact of different ΔP owing to changing AlInGaN backbarrier compositions on electrical characteristics is obvious in the semi-logarithmic transfer characteristics of samples A to E in Fig. 7.11b. The applied V_{DS} was -5 V. The largest positive V_{th} is observed for sample A with a value of 3.5 V. For samples B-D, a V_{th} shift to lower voltages is apparent. This is in agreement with the lowered ΔP. Finally, sample E with the lowest ΔP, shows a negative V_{th}. The transistor is fully pinched off at 0 V, demonstrating true e-mode behavior.

The changing ΔP also influences the absolute currents of the devices. A general trend to both lowered on- and off- currents is observed for reduced ΔP. While the d-mode sample A exhibits an absolute drain current $|I_d|$ above 40 mA/mm with a maximum transconductance $g_{m,max}$ of 9 mS/mm, the e-mode sample E shows a lowered $|I_d|$ of 0.7 mA/mm with a $g_{m,max}$ of 0.2 mS/mm. The decreased on-currents for lower ΔP are reasonable, since sheet and contact resistances are increased. However, while on-currents are reduced only by two orders of magnitude, the off-currents, which are also dependent on ΔP, decrease by seven orders of magnitude. This results in an on-off ratio of 10^8 for the e-mode sample E, which is the best value ever

achieved for p-channel transistors.

Based on transistors of sample A, it was also possible to extract small-signal data and cut-off frequencies of a p-channel HFET for the first time [81]. A transit frequency f_t of 206 MHz and a maximum oscillation frequency f_{max} of 640 MHz were achieved [112].

In summary, a double heterostructure with an embedded AlInGaN backbarrier has been used for the generation of a 2DHG. The best practice for polarization engineering in n-channel HFETs has also been applied for p-channel HFETs. In analogy to the n-channel HFETs, both d-mode and e-mode behavior has been shown for p-channel HFETs. Record performances have been achieved for p-channel HFETs utilizing a 2DHG, which demonstrates the high maturity of the fabricated heterostructures.

III.

Light emitting diodes with polarization-engineered AlInGaN layers

Chapter 8

Light emitting diodes with AlInGaN barrier layers

In optoelectronics, light emitting diodes (LEDs) with active InGaN/GaN multiple quantum wells (MQWs) are commercially well established [9, 10]. Despite their high level of maturity, these devices still have a lot of potential for improvement. In paticular, polar LEDs suffer from several issues owing to their internal electric fields: first, the so-called quantum-confined Stark effect (QCSE), which causes a current-density-dependent emission color due to compensation of polarization-induced internal electric fields by increased non-equilibrium carrier concentration [296–298]; second, the reduced external quantum efficiency at higher drive currents [299], the so-called droop. These main drawbacks are motivating research on alternative well and barrier nitride alloys to control the polarization difference (ΔP) and, hence, the internal electric fields in the active MQW. In a MQW, GaN barriers with their fixed and large total polarization (P_{total}) have been replaced by AlInGaN layers with their variable P_{total} [57, 58, 300–302]. Theoretically, it is possible to find an AlInGaN composition with a P_{total} matching to the one of InGaN, which is expected to improve LED performance [103]. It has successfully been shown that the emission wavelength is more stable with drive current [59] and that the efficiency droop can be suppressed to a certain amount [60, 61]. Recently, AlInGaN layers have also been tested as wells [303, 304] and the authors have claimed that conditions to give zero internal field in a MQW can only be achieved with AlInGaN wells. However, in the case of a pseudomorphic MQW on a relaxed GaN buffer this is not the case [104]. Thus, to study the influence of AlInGaN layers on the internal electric fields, the present chapter focuses on LEDs, in which quaternary AlInGaN layers are utilized as barrier layers in MQW structures. The influence of different ΔP on LED properties and performance is studied.

8.1. Internal electric fields

The internal electric fields in a MQW are caused by ΔP between the barriers and the InGaN wells. Exemplarily, in Fig. 8.1, schematic band diagrams are shown for a

compressively strained InGaN single quantum well embedded between either GaN barriers (Fig. 8.1a) or AlInGaN barriers (Fig. 8.1b). The smallest distance between conduction and valence band is denoted as the effective bandgap E_{eff}. In the case of GaN barriers, E_{eff} is lowered due to the fixed and large ΔP compared to AlInGaN with lower ΔP. Electrons and holes, which are confined in the InGaN quantum well, recombine and emit photons with an energy E_{ph}, which depends on E_{eff} and, hence, on the ΔP as well as on the quantization energy E_{quant}.

A further aspect is that electrons and holes in the well are spatially separated due to the internal electric fields, which results in a lowered oscillator strength for the transition for larger ΔP [296–298]. By replacing the GaN barriers with AlInGaN with a lower P_{total} than for GaN, the oscillator strength is expected to increase and the emission color is expected to be blue-shifted because of the increased effective bandgap E_{eff}.

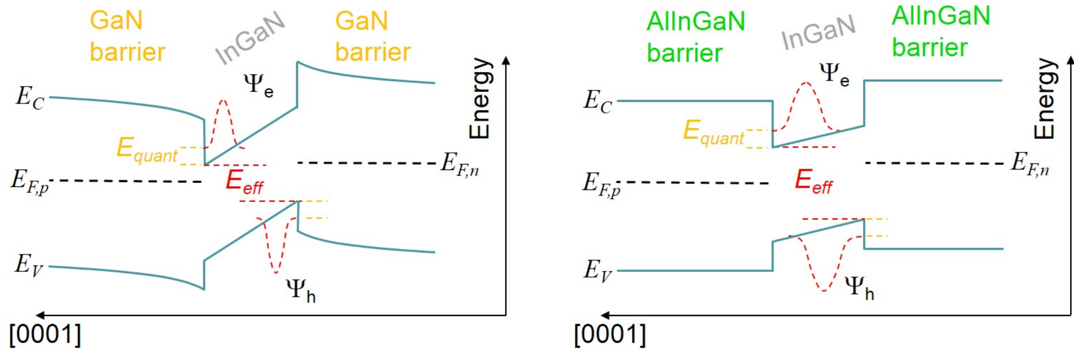

(a) GaN barriers with fixed and large ΔP to the InGaN well.

(b) AlInGaN barriers with lower ΔP to the InGaN well.

Figure 8.1.: Schematic band diagrams of a single InGaN quantum well embedded in (a) GaN barriers or (b) AlInGaN barriers. The overlap of electron and hole wavefunctions is increased for AlInGaN barriers with lower ΔP. Further, the energy of emitted photons increases.

8.2. Structural properties of LEDs

In this section, the influence of the AlInGaN composition on the optical properties of LEDs is investigated. The objective is to vary the internal fields in the MQW by changing the ΔP between barrier and well. To investigate this, LED samples which feature AlInGaN barrier layers with different compositions are fabricated. In a second series, the AlInGaN barrier or the well thickness is changed to optimize LED performance. A conventional LED with GaN barriers serves as a reference.

A schematic cross section of the layer stack, which is used for LED fabrication is shown in Fig. 8.2a. The buffer layer is equivalent to the one used for heterostructure field effect transistors (HFETs), which have been presented in Sec. 4.1. On top of this buffer, the basic LED structure is deposited. It starts with a two-step n-GaN layer with a total thickness of 3 µm. While for the first 2.5 µm, an n-doping level of $5{\cdot}10^{18}\,\mathrm{cm^{-3}}$ was adjusted, for the last 500 nm, the n-doping level was reduced to $1{\cdot}10^{17}\,\mathrm{cm^{-3}}$ to achieve a better balance between electrons and holes in the MQW[1]. On top of the n-GaN, a 5-fold MQW was formed by InGaN wells and AlInGaN barriers. Finally, the topmost layer was realized by 100 nm p-doped GaN with a doping level of about $3{\cdot}10^{17}\,\mathrm{cm^{-3}}$ ionized acceptors.

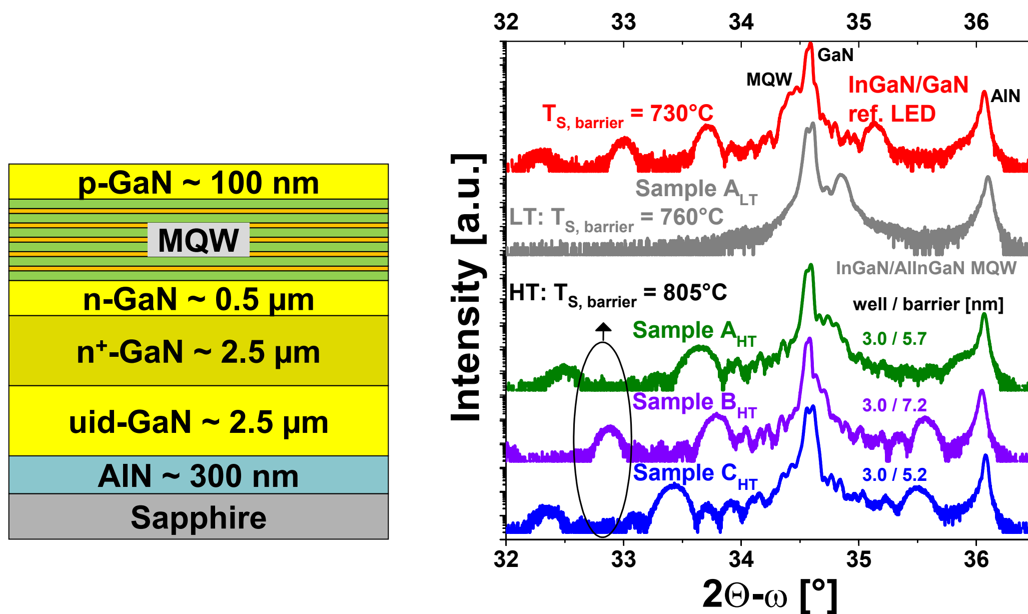

(a) The MQW consists of InGaN wells and either AlInGaN barriers or GaN barriers for the reference LED

(b) LED samples with AlInGaN barriers grown at different reactor conditions. A reference LED has conventional GaN barriers

Figure 8.2.: Schematic cross section of the LED layer stacks (a). Associated HRXRD (0002) 2Θ-ω scans (b).

Different AlInGaN compositions for barrier layers in the MQW

First tests for the development of the LED were carried out by investigating the process window for the barrier growth surface temperature ($T_{S,barrier}$) for AlInGaN layers. Reasonable electroluminescence, qualitatively evaluated by a provisional

[1]Previous optimization test samples have shown a significant increase in brightness by the insertion of a low-doped n-GaN layer below the MQW.

contact method with conductive silver paste, was only observed for a $T_{S,barrier}$ above 800 °C. As shown in Fig. 8.2b, HRXRD (0002) 2Θ-ω scans reveal much more distinct fringe oscillations for LEDs with AlInGaN barriers grown at a high $T_{S,barrier}$ of 805 °C (samples A_{HT}, B_{HT} and C_{HT}) than for an LED sample for which $T_{S,barrier}$ was only 760 °C (sample A_{LT}). For the reference LED with a GaN barrier grown at an even lower $T_{S,barrier}$ of 730 °C, this interface degradation could not be observed, which implies that degradation is only observed for AlInGaN grown at a low $T_{S,barrier}$. As discussed in Sec. 4.3.2, a reduction of $T_{S,barrier}$ leads to an increased In content, which has a strong negative impact on surface roughness, defect densities and alloy disorder. Therefore, high $T_{S,barrier}$ and low In contents in the AlInGaN barrier result in improved LED performance.

In the following, the three high-quality samples A_{HT}, B_{HT} and C_{HT} with $T_{S,barrier}$ of 805 °C are regarded. For these samples, the AlInGaN barrier composition is changed by the TMAl flow, for which the values are listed in Tab. 8.1. The TMGa and the TMIn flow were kept constant at 10.5 µmol/min and 26.2 µmol/min, respectively.

The determination of the composition for both InGaN and AlInGaN is very difficult for an InGaN/AlInGaN MQW. Apart from the issue that several AlInGaN compositions feature an equal lattice constant, an additional degree of freedom arises for the InGaN/AlInGaN superlattice due to the ternary InGaN. Several composition combinations of InGaN and AlInGaN layers show an equal XRD signal. Therefore, the two reference samples are considered for composition determination. For the reference LED with a conventional InGaN/GaN MQW grown at a growth surface temperature ($T_{Surface}$) of 730 °C, it is possible to estimate the In content to be about 20 % from the HRXRD (0002) 2Θ-ω scan. For equal well growth surface temperature ($T_{S,well}$) of 730 °C, it is reasonable to assume the same In incorporation in the well. Hence, all LED samples with InGaN/AlInGaN are expected to exhibit about 20 % In in their wells. Further, a reference sample $C_{HT(Ref)}$ with a 77 nm AlInGaN layer was grown on GaN at barrier growth conditions of sample C_{HT}. RBS analysis yields an AlInGaN composition of 57% Al, 5 % In and 38 % Ga. By taking the results from RBS into account, the compositions of the AlInGaN barriers can finally be estimated by fitting HRXRD (0002) 2Θ-ω scans (Fig. 8.2b). As for the three high-quality samples A_{HT}, B_{HT} and C_{HT}, $T_{S,barrier}$ is equal at 805 °C, it is likely that the In content does not change significantly. The In content is between 2 % - 5 %. Due to the increased TMAl flow, the Al content rises from 28 % for sample A_{HT} to 55 % for sample C_{HT}.

Sample	$T_{S,barrier}$ [°C]	$T_{S,well}$ [°C]	TMAl [µmol/min]	Al [%]	In [%]	Ga [%]	E_g [eV]	t_{bar} [nm]	P_{total} [Ccm^{-2}]
LED samples									
Ref.	730	730	0	0	0	100	3.43	11.2	-0.0340
A_{LT}	760		4.4	-	-	-	-	-	
A_{HT}	805		4.4	28	2	70	3.94	5.7	-0.0503
B_{HT}	805	730	8.7	43	4	53	4.23	7.2	-0.0596
$C_{HT(Ref)}$	805		17.5	55	5	40	4.49	5.2 (77)	-0.0692

Table 8.1.: MOVPE conditions and structural properties of LED samples with AlInGaN barriers grown with different TMAl flows.

8.3. Optical properties of LEDs

PL spectra of the first LED sample series with different AlInGaN barrier compositions and the reference LED are shown in Fig. 8.3a. The reference LED exhibits its emission peak at 2.6 eV. By assuming this value to be the bandgap and neglecting any quantization and polarization effects, this corresponds to an In content of roughly 20 %, according to Eq. 2.10. This is in good agreement with the HRXRD 2Θ-ω scans for a simulation with 2 nm well thickness and 11 nm barrier thickness.

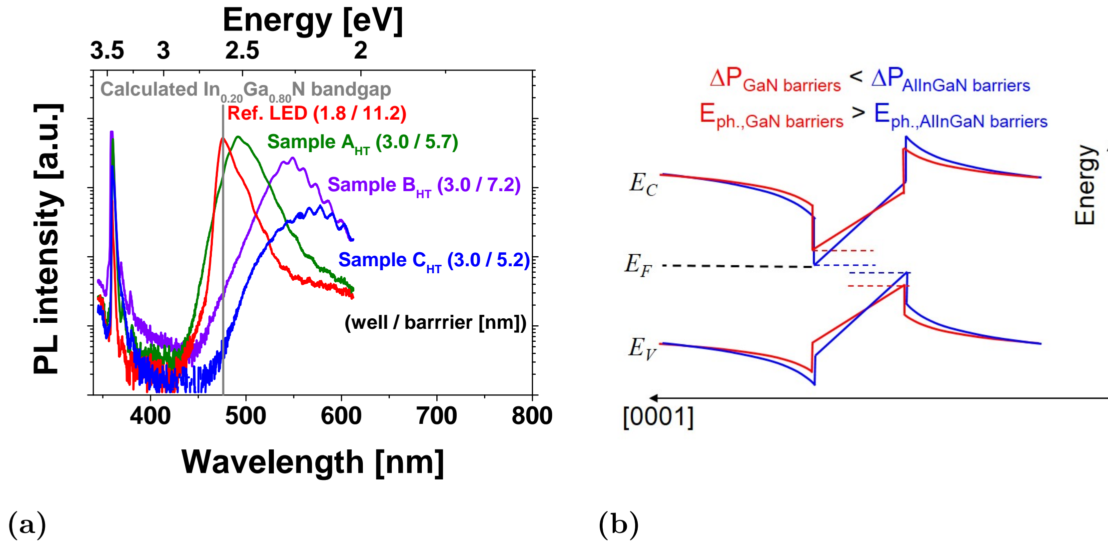

(a) (b)

Figure 8.3.: PL spectra at 10 K of the samples A_{HT}, B_{HT} and C_{HT} with different TMAl precursor fluxes during AlInGaN barrier growth and the reference LED (a). Schematic band diagrams for the reference LED with GaN barriers (red curve) and a sample with high-polaization AlInGaN barriers, illustrating the change in the emission energy (b).

For LED samples with AlInGaN barriers, a red-shift of the emission wavelength is

observed with increasing Al content. This is well correlated to the increasing P_{total} of the AlInGaN barrier, which in turn results in larger electric fields in the MQW [296]. This leads finally to a stronger band tilt in the MQW, as illustrated in the associated band diagrams in Fig. 8.3b. Although the In content in the well is equal for all samples, this effect leads to strong wavelength shift of luminescence from the InGaN well. A further effect of the band tilt is a stronger spatial separation of electron and holes leading to a reduced oscillator strength of the optical transition, which explains the lower intensity in PL spectra [299].

The diode characteristic is exemplarily shown for sample A_{HT} and the reference sample in Fig. 8.4a. The characteristic is very similar for both structures with forward voltages of around 3 V at 20 mA. Photographs of the operating LEDs at a drive current of 5 mA are shown in Fig. 8.4b. The light emission of the LED with AlInGaN barriers seems to be comparable to the conventional LED in matters of intensity and homogeneity. A more quantitatively analysis is given in the following.

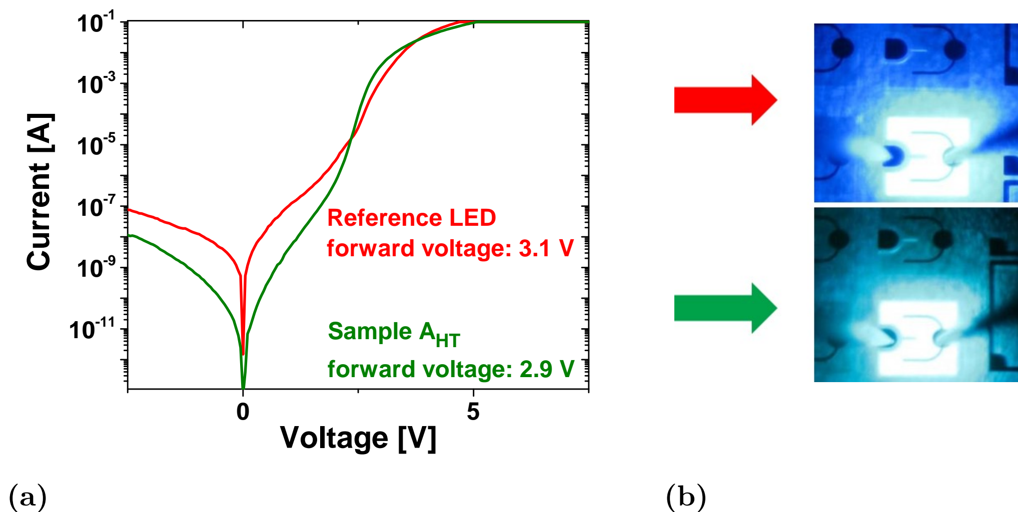

Figure 8.4.: I-V diode characteristic of processed sample A_{HT} and the reference sample (a) and photographs of fully processed LEDs at 5 mA drive current (b).

Luminescence properties of LEDs with various MQW thicknesses

Sample A_{HT} with the lowest P_{total} within the LED series with AlInGaN barriers was chosen to be the starting point for further optimization steps to achieve a high efficiency. Hence, well thickness and AlInGaN barrier thickness were changed by variation of the growth time, while it was ensured that other growth parameters were equal to those of sample A_{HT}.

The PL efficiency, calculated by the ratio of integral intensity of emission spectra and excitation intensity, is plotted as a function of excitation intensity ($I_{exc.}$) in Fig. 8.5a for samples with different well and barrier thicknesses. Additionally, the reference LED is shown for comparison. Obviously, the LED structures with AlInGaN layers cannot reach the efficiency of the conventional layer stack. However, thickness-optimized structures show improved performance. An efficiency optimum is achieved at an InGaN well thickness of 2.3 nm and an AlInGaN barrier thickness of 5.4 nm. At low $I_{exc.}$, a trend to lower efficiencies for both larger well and larger barrier thicknesses is observed.

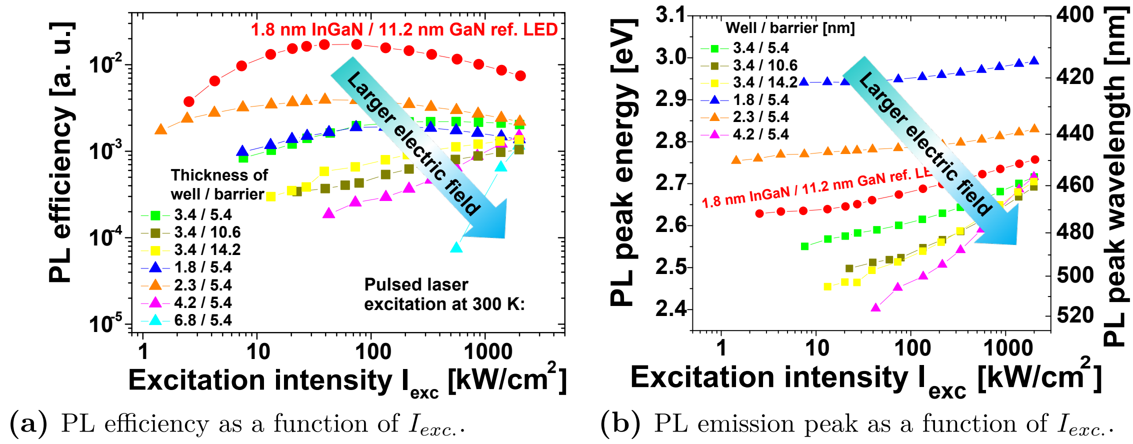

(a) PL efficiency as a function of $I_{exc.}$.

(b) PL emission peak as a function of $I_{exc.}$.

Figure 8.5.: PL studies on samples with varying well and barrier thicknesses, given in the lower/upper corners. Pulsed laser excitation at 300 K, λ_{exc} =337 nm, τ = 10 ns, f = 1kHz.

The position of the PL emission peak is plotted as a function of $I_{exc.}$ in Fig. 8.5b for varying MQW thicknesses. A clear PL wavelength red-shift between the samples is observed for larger well and barrier thicknesses, which is a typical behavior for polar LEDs due to the internal electric fields in the MQW and quantization effects [305]. These observations indicate that a rather large ΔP is apparent in the MQW. Photographs of fully processed LED of the samples with varying well thicknesses, shown in Fig. 8.6, confirm this red-shift with larger well thicknesses in electroluminescence (EL).

By increasing $I_{exc.}$, the emission peak wavelength decreases owing to the QCSE. The induced shift is stronger for increasing well and barrier thicknesses due to the larger band tilt. Generally, at higher $I_{exc.}$, the differences in both efficiency and emission wavelength diminish, which further confirms that polarization-induced internal electric fields strongly determine optical properties of the investigated samples. The

reference LED (red color) and the LED sample with the best efficiency within this series with 2.3 nm well and 5.4 nm AlInGaN barrier (orange color), exhibit a comparable QCSE shift. This indicates similar internal electric fields in these samples.

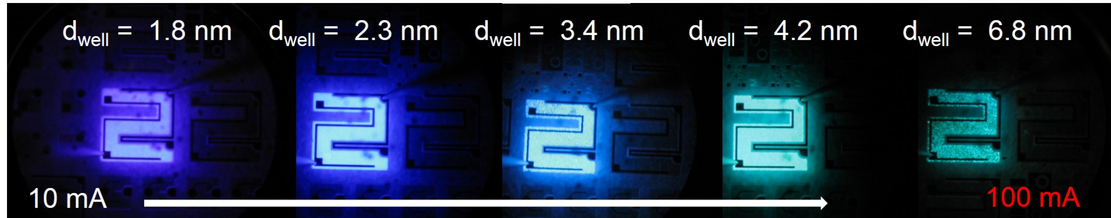

Figure 8.6.: Photographs of fully processed LEDs with different well thicknesses. All samples have AlInGaN barriers with a thickness of 5.6 nm.

In summary, the expectation that by changing P_{total} of the AlInGaN barrier in MQWs it is possible to control the internal electric fields have been confirmed: Lower P_{total} leads to a smaller emission wavelength and an improved oscillator strength. The wavelength shift due to the QCSE for the investigated AlInGaN compositions is similar or stronger to that of conventional InGaN/GaN LED due to a rather high P_{total} of the AlInGaN owing to the large Al contents (28 % - 55 %) and the low In contents (2 % - 5 %) in the AlInGaN barrier. Further compositional studies on InGaN/AlInGaN MQWs with less Al or more In in the barrier should be performed to achieve smaller QCSE-induced wavelength shifts. But, as discussed in the beginning of this section, larger In contents require a lower growth temperature for the AlInGaN barriers, which in turn results in a degradation of crystal quality and LED performance. The challenge remains to deposit high-In-content AlInGaN layers with a high crystal quality.

Chapter 9

LED structures with reversed polarization utilizing a 2DHG

The concept of controlling the polarization difference (ΔP) in a multiple quantum well (MQW) with AlInGaN as barrier layers was discussed in the previous chapter. In this final experimental chapter, a new concept for light emitting diodes (LEDs) to achieve a better carrier confinement in the MQW is proposed. The objective is to inverse the p-n junction in a metal-polar layer stack, which in turn results in a reversed polarization compared to conventional LED. Further, a two-dimensional hole gas (2DHG) as a hole reservoir and as a current spreading layer is employed. The high sheet hole density in such a 2DHG is expected to improve the performance of a LED.

9.1. Preface to inversed p-n junctions

The common crystal orientation of commercially grown LED is metal-polar, i.e. the c-direction ([0001]) of the wurtzite crystal is pointing in growth direction. As shown in Fig. 9.1 in the left part, the conventional LED layer stack consists of a metal-polar p-n diode with n-GaN as the bottom layer and p-GaN as the topmost layer. Normally, an electron blocking layer (EBL) is used above the MQW to mitigate electron leakage which in turn improves the internal quantum efficiency [306, 307]. However, since the EBL is located between the p-GaN and the MQW, holes are also likely to be blocked. A more advanced approach is to design the LED with a reversed polarization relative to the forward-biased induced electric field. As illustrated in Fig. 9.1 in the right part, this can be realized by flipping the p-n junction.

Such an inversed stack is usually avoided because highly Mg-doped bulk p-GaN exhibits inferior crystal quality. The layers on top become rough, which is severe in particular for the MQW [308–310]. Further, Mg might diffuse into subsequently grown layers or Mg might be incorporated from the gas phase due to a memory effect [311]. These problems can be solved by using a backbarrier below the p-down GaN,

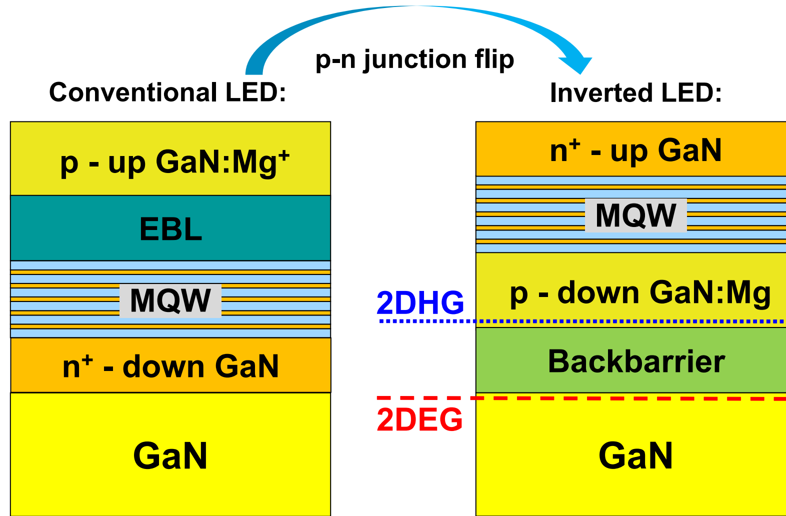

Figure 9.1.: Juxtaposition of the conventional p-up and n-down LED and the inversed p-down and n-up LED. For 2DHG formation in the inversed stack, a backbarrier is used below the p-down GaN.

which induces a 2DHG located at the upper GaN/backbarrier interface (compare Chap. 7). In such a structure, only a weak p-doping level for the compensation of n-autodoping is needed, which allows for subsequent layer growth with a higher crystal quality.

Reversed polarization

To clarify the concept of a reversed polarization, schematic band diagrams for a metal-polar single InGaN quantum well are shown in Fig. 9.2 for both cases: the conventional LED and the inversed LED. For the conventional case, the slope of the bands in the InGaN well due to ΔP to GaN is negative relative to the growth direction ([0001]). This is opposite to the slope, which results from the surrounding p-n junction. The associated conduction band bending leads to injection barriers for both holes and electrons, which in turn results in larger turn-on voltages [312]. Further, the internal electric field in the well drives electrons beyond the quantum well towards the p-GaN, which results in electron leakage.

In the case of an inversed p-n junction in a metal polar stack, a negative slope of the bandstructure develops in growth direction ([0001]), exactly like the slope of the polarization-induced tilt of the wells. This leads to almost flat conduction and valence bands in the barriers in the MQW. As a result, the effective injection barriers are lowered [313]. In addition, the electron confinement is improved, because of the more effectively blocking of the barrier behind of the well. Owing to the inversed p-n junction in a metal-polar stack, the polarization is reversed relative to

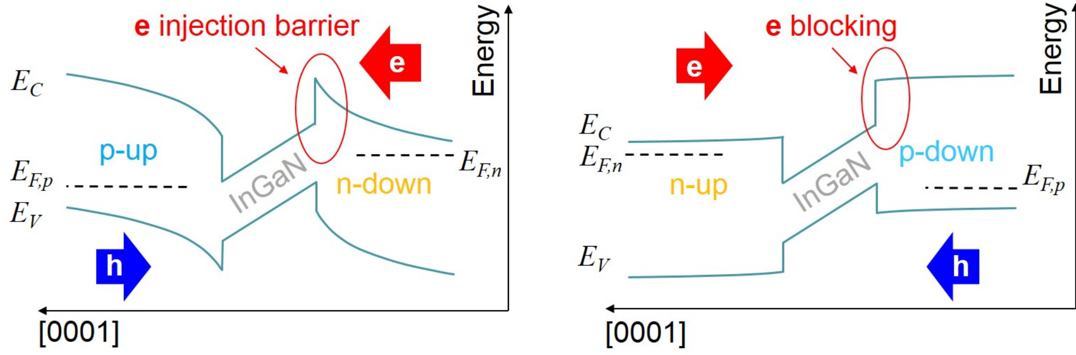

(a) GaN barriers with fixed and large ΔP to the InGaN well.

(b) AlInGaN barriers with lower ΔP to the InGaN well.

Figure 9.2.: Schematic band diagrams of a simplified single InGaN quantum well under forward bias condition for the conventional LED and the inversed pn-junction LED.

the forward-biased induced electric field, similar to the case of N-polar LED stacks with conventional n-down p-up junctions [312].

For a full LED stack as depicted in Fig. 9.1 in the right part, a simulated band structure is shown in Fig. 9.3. The improved blocking characteristics of the active MQW is apparent by the clear steps for each well, which are faced for both electrons and holes. Apart from the improved active zone, the feature of interest is the triangular valence band well at the GaN/backbarrier interface, at which the 2DHG is located. An unintentional buried two-dimensional electron gas (2DEG) is also formed at the lower backbarrier/GaN interface. Nonetheless, by p-doping the AlInGaN backbarrier, the bandstructure can be pulled upwards, which results in a suppression of 2DEG formation. This effect is experimentally confirmed on p-channel reference samples without MQW and n-GaN by an increase of the $R_{sheet,2DEG}$ from $0.5\,\text{k}\Omega/\square$ to $100\,\text{k}\Omega/\square$ with larger Mg doping.

9.2. Fabrication of inversed LEDs

9.2.1. LED stack and its structural properties

The full LED layer stack with an inversed p-n junction is schematically shown in Fig. 9.4a. The bottom stack for 2DHG generation is nominally equal to the stack used for the p-channel heterostructure field effect transistor (HFET) in Chap. 7. For the backbarrier, a high-polarization $Al_{42\%}In_{3\%}Ga_{55\%}N$ was chosen in order to generate a large hole density in the 2DHG. The GaN:Mg layer on top of the AlInGaN

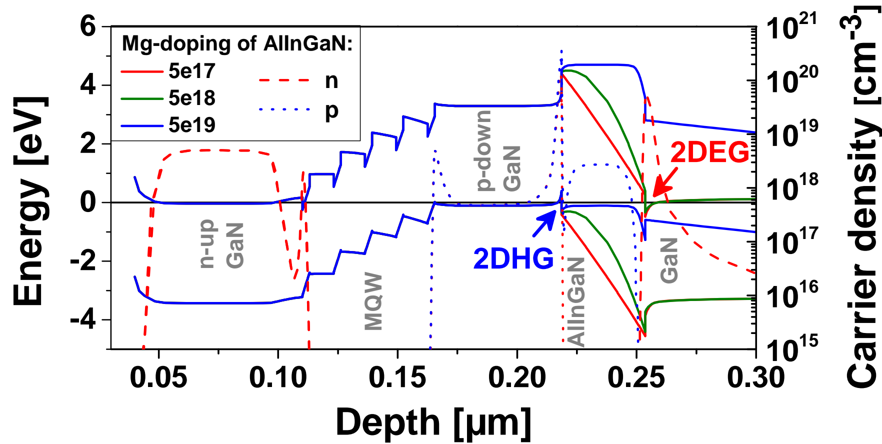

Figure 9.3.: Simulation of an inverted p-n junction LED with AlInGaN backbarrier for 2DHG formation. Different doping levels for the AlInGaN is shown here. The dotted curves represent holes and the dashed curves represent electrons.

backbarrier is weakly doped with a Mg concentration of about $1.4 \cdot 10^{18}\,\mathrm{cm}^{-3}$. The resulting sheet hole density of a reference p-channel HFET was measured to be about $2 \cdot 10^{13}\,\mathrm{cm}^{-2}$. This would be equivalent to a bulk hole density of $5 \cdot 10^{18}\,\mathrm{cm}^{-3}$ assuming the total GaN channel to be 40 nm. This value is five times larger than the uppermost limit for Mg-doped bulk GaN [277–281].

A five-fold MQW is used as the active light-emitting region. It was designed for an emission wavelength in the blue color range around 450 nm and consists of 3 nm InGaN wells and 15 nm GaN barriers. The topmost highly n-doped GaN layer exhibits an electron density of $5 \cdot 10^{18}\,\mathrm{cm}^{-3}$.

A study on structural properties was performed by HRXRD and AFM. In HRXRD (0002) 2Θ-ω scan, shown in Fig. 9.4b, the peak of the AlInGaN is visible between the GaN and AlN buffer peaks. The peak which stems from the MQW is located near the GaN peak on the lower angle side. By simulating the scan, also shown as a red curve, all layer thicknesses were determined. These are also given in the schematic layer stack in Fig. 9.4a. From the distance between the fringe oscillations, the thickness of the periodicity of the MQW can be confirmed.

Further, the very high intensity of fringes up to the fourth order indicates a high crystal quality of the MQW. AFM images (not shown here) of a test sample without MQW and without n-up GaN reveal a roughness of about 1.2 nm (5 µm times 5 µm) for the surface of the GaN:Mg channel. The full LED stack shows no degradation of the surface, which confirms the high quality of subsequent MQW and n-up GaN growth. These results confirm that the low-doped p-down GaN:Mg does not negatively impact subsequent layer growth.

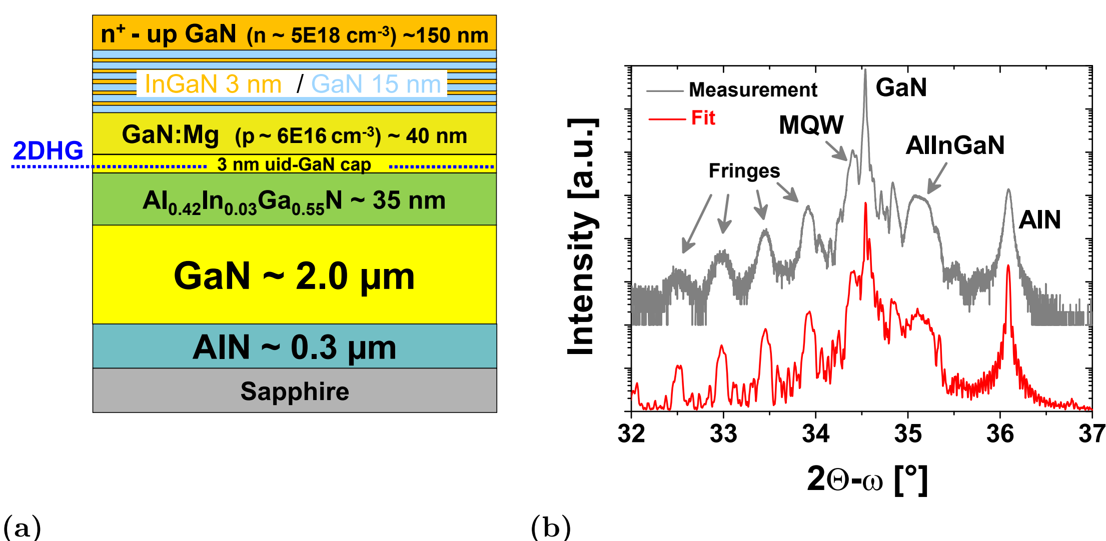

Figure 9.4.: Schematic cross section of the layer stack used for the inversed LEDs (a). Associated HRXRD (0002) 2Θ-ω scan (black) and simulation (red) (b).

9.2.2. Optical properties

Photoluminescence

In the following, three samples A, B and C are regarded, which feature different Mg-doping levels in the GaN barriers in the MQW. The p-doping of the GaN barriers is assumed to improve LED performance, because of an improved carrier balance in the active MQW [62].

To assess and understand optical properties of inverted LED structures, photoluminescence (PL) measurements and simulations of the band structures were carried out, shown in Fig. 9.5. The PL spectra in Fig. 9.5a show significant differences for samples A, B and C. For the undoped sample A, the emission from the InGaN well at 450 nm is suppressed rather strongly. Instead, a pronounced GaN emission peak at 360 nm is apparent, which is very likely to stem from both the n-up GaN:Si layer and the p-down GaN:Mg[1]. By p-doping the GaN barriers in the MQW for sample B, the InGaN peak intensity increases. This is accompanied by a simultaneous suppression of the GaN peak, which indicates that carrier recombination in the MQW becomes more pronounced. For sample C with the highest doping level, the MQW emission becomes very efficient, whereas recombinations in the GaN are even more suppressed. This is indicated by the vanishing near-bandgap GaN peak at 360 nm and by the mitigated broad defect yellow luminescence (YL) between 500 nm and

[1]This can be assumed by regarding the laser penetration depth of several hundreds of nanometers and the a strong diffusion of excited electrons.

600 nm, typically observed for GaN layers [275]. In particular for sample A, the YL is slightly shifted to a lower wavelength and might be attributed to a green luminescence due to In-clustering effects, which have been reported for structures featuring AlInGaN layers [225, 226, 314].

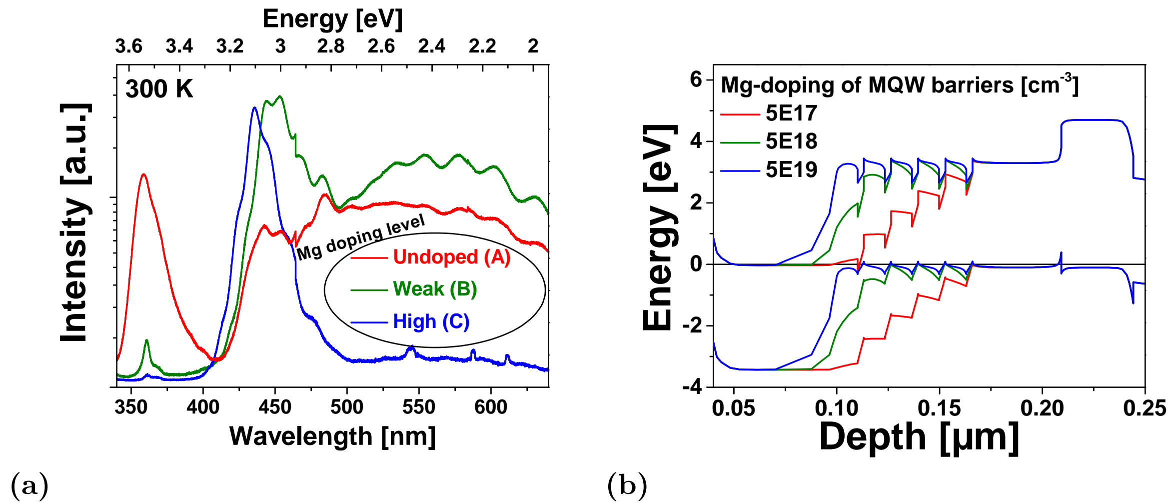

(a) (b)

Figure 9.5.: PL spectra of the inversed LED sample series with Mg-doped GaN barriers in the MQW (a). Associated simulated banddiagrams.

The trends in the PL spectra can be explained using simulations of the band structure shown in Fig. 9.5b. With increasing doping level in the MQW, the bands are strongly pulled upwards in this region. Thus, the MQW region becomes more flat and the valence band InGaN wells are approaching the Fermi level. This leads to an improved hole transport into the MQW. These holes recombine with electrons in the conduction band more efficiently due to a weaker electric field in the active MQW. Hence, electron diffusion to the p-down GaN and AlInGaN backbarrier is suppressed. This explains the decrease of both near-bandgap GaN peak and the GaN YL.

Electroluminescence

Processing these inversed LED is challenging. First, it is difficult to perform the mesa etch accurately. The lower p-GaN channel needs to be contacted and this layer exhibits a thickness of only 20 nm. With lowered p-channel thickness by etching, the hole density decreases. Second, the p-GaN channel is not sufficiently p-doped for ohmic contact formation. Third, etch damage might induce N vacancies in the p-down GaN which in turn lead to an unintentional n-doping [315–317]. All these issues prevent a successful processing of devices at this stage.

Nevertheless, as shown in Fig. 9.6a, a provisional contact method on the as-grown LED wafer is used for a quick electroluminescence test. Due to the inversed p-down n-up junction, the n-probes can directly contact the surface of the wafer. For the p-probes, the wafer was scratched with a diamond file to be able to contact the p-down layers. A conductive silver paste was used for a provisional test. As obvious in the photograph, this layer stack is capable of emitting light.

The EL spectra for different forward voltages are shown in Fig. 9.6b. The blue emission at 450 nm is similar to the PL emission wavelength, which confirms that light is effectively emitted through the active MQW in InGaN wells as expected. The peak shows no wavelength shift with current, indicating that the reversed polarization in the MQW likely suppresses the QCSE. The reason is likely found in the improved band structure, which approaches flat band conditions when forward-biased. However, the applied voltage which was necessary for the LED to emit light is quite high with values between 15 V and 60 V. Hence, the electric field is large for every EL measurement and flat band conditions are probably achieved for all measurements. To prove this, further samples which emit light at smaller voltages need to be investigated.

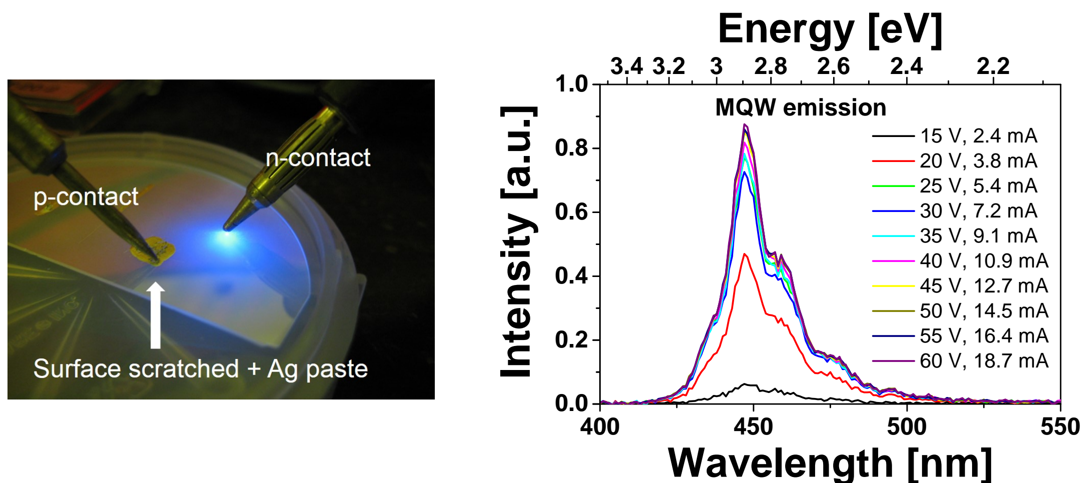

(a) Photographic of a 2-inch as-grown LED wafer with an applied bias.

(b) EL spectra with different applied forward voltages and the respective drive currents.

Figure 9.6.: Electroluminescence of an inversed LED.

A novel concept for an InGaN-based LED has been presented here. An inversed p-n junction in a metal-polar layer stack has been applied, which has resulted in a reversed polarization regarding forward-biased LED devices. This has been realized by utilizing a 2DHG as a hole reservoir and as a current spreading layer at the

bottom p-GaN side. With high-polarization AlInGaN backbarriers, a large sheet hole density in the 2DHG has been achieved. However, processing these inversed LEDs remains challenging. In particular, the bottom p-contact needs to be improved to achieve ohmic contact behavior. Nevertheless, electroluminescence has successfully been demonstrated. The peak wavelength has shown to be independent of the current density, which indicated a reduced QCSE, most likely due to the reversed polarization in the active MQW.

Chapter 10

Summary and outlook

This thesis represents a comprehensive study on the quaternary group III nitride alloy system ($Al_xIn_yGa_{1\text{-}x\text{-}y}N$). The fundamentals and principles of group III nitrides as well as epitaxial growth and characterization methods have been introduced in the beginning. The focus of this thesis has been on the experimental results on nitride heterostructures and their interpretation. These results have been structured in separate parts, in which three substantial topics have been dealt with: first, general aspects on the crystal growth of quaternary AlInGaN; second and third, the fabrication and characterization of electronic and opto-electronic devices, i.e. the heterostructure field effect transistor (HFET) and the light emitting diode (LED).

In the theoretical part, polarization engineering has been introduced as the core methodology for this thesis. The best possible flexibility in adjusting material properties independently, e.g. bandgap E_g and lattice constant a or strain state ε and total polarization (P_{total}), is offered by the AlInGaN alloy system. This offers a unique possibility to control the polarization difference (ΔP) at interfaces and, hence, a possible adjustment of the bandstructure in devices.

Literature research has revealed a controversy regarding the bandgap bowing parameters and the method for bandgap calculation. Due to these uncertainties, the accurate prediction of the bandgap of polarization-matching AlInGaN layers remains difficult. Nevertheless, it has been shown in the experimental parts that polarization-reduction up to a certain level is possible by strain-engineering with AlInGaN layers. The results have demonstrated the high flexibility of heterostructures with AlInGaN barriers and future developments in the area of devices with quaternary AlInGaN are likely to benefit from the gained comprehension.

In the first part, the synthesis and structural properties of quaternary AlInGaN layers on two different substrate templates have been discussed. First and more important for conventional devices is the growth on GaN. Second, conditions for growth on AlN templates have been explored. In both cases, a wide AlInGaN composition range resulting in different strain states from high tensile to high compressive has

been covered by discovering possible process conditions. First, the optimum reactor pressure has been identified to be below 150 hPa to prevent gas phase pre-reactions of the Al precursor (TMAl). Further, and even more critical to control, the growth surface temperature ($T_{Surface}$) has been identified to limit the In incorporation. The Ga content is only weakly dependent on pressure and $T_{Surface}$ and, hence, it can be adjusted by the Ga precursor (TMGa) flow. As a general aspect for AlInGaN growth, it has been confirmed that owing to the weak cracking efficiency of NH_3 at lower temperatures the group V to III ratio must be chosen a factor of 3 to 30 larger than for binary GaN or AlN growth.

It has further been shown that the crystal quality depends strongly on the AlInGaN composition and the strain state. A general trend to lower crystal quality has been observed with increasing In content and larger compressive strain. In the pseudomorphic case for compressively strained AlInGaN, the In incorporation at the interface has been identified to be hampered. With increasing thickness, relaxation accompanied by strong In pulling has occured. For this phenomena, a multi-sublayer model has been developed.

High-quality AlInGaN layers have been achieved at a $T_{Surface}$ of 800 °C, which resulted in an In contents of about 5 %. These layers have been used as barriers in devices. However, the development of epitaxial growth attempts, which allow for a high In incorporation while maintaining crystal quality is ongoing. Here, growth with pulsed precursor supply, which enhances the migration of the adsorped species, is very promising.

Further, direct epitaxial growth of AlInGaN on AlN has been studied. It has been found to be more challenging compared to growth on GaN for the reason that all AlInGaN compositions are under compressive strain. Due to the large lattice mismatch, relaxation and phase separation effects have occured even under optimum reactor conditions. Several trends, which have been observed for AlInGaN growth on GaN, have also been confirmed for the growth on AlN, i.e. higher In contents for smaller $T_{Surface}$ and an effective change of the Ga content by the TMGa flux. A trend to improved crystal quality has been identified for compositions near the AlGaN ternary line, i.e. for lower In contents.

Owing to the possibility to control P_{total}, high-quality AlInGaN layers are promising for the implementation as backbarriers in n-channel double heterostructure field effect transistor (DHFET). A sophisticated multi-layer backbarrier structure with step-wise change of P_{total} could be envisioned.

In the second part, single and double heterostructures containing AlInGaN barriers,

in which two-dimensional carrier gases are induced by ΔP, have been grown. Both n-channel HFETs containing a two-dimensional electron gas (2DEG) and p-channel HFETs containing a two-dimensional hole gas (2DHG) have been realized.

The influence of the AlInGaN composition, determining ΔP, on transport properties in the carrier gases and the impact on HFET characteristics have been in focus. For both 2DEG and 2DHG, larger carrier densities can be induced by compositions with either larger Al contents or lower In contents. Apart from the spontaneous polarization (P_{spon}), the effect is mainly driven by the piezoelectric polarization (P_{piezo}), which either contributes to the P_{spon} in the case of tensilely strained AlInGaN barriers or compensates P_{spon} in the case of compressively strained AlInGaN barriers.

The overall mobility functions plotted against the densities have revealed a peak for both carrier types at moderately densities. Peak mobilities of $1820\,\text{cm}^2\text{V}^{-1}\text{s}^{-1}$ for electrons and $43\,\text{cm}^2\text{V}^{-1}\text{s}^{-1}$ for holes have been observed. The larger effective mass of holes is mainly responsible for the generally lower hole mobilities. However, the hole mobility of $43\,\text{cm}^2\text{V}^{-1}\text{s}^{-1}$ represents a record for MOVPE-grown GaN-based heterostructures. Mobility-measurements at 77 K have revealed strongly increased mobilities by a factor of about 5 for both electrons and holes owing to the reduced phonon-scattering. Apart from phonon-scattering, the peak shape of the overall mobility function at room temperature is due to several other scattering mechanisms. The peak mobilities are achieved at moderate densities for both carrier types. While in the low density regime impurity scattering in the GaN channel is dominant, interface and alloy scattering rules in the high-density regime. Alloy scattering increases for larger In contents in the AlInGaN barrier, which generally leads to a reduced mobility. An AlN interlayer favorably grown at higher $T_{Surface}$ between an AlInGaN barrier and the GaN channel strongly improves the mobility at least for electrons. For holes, a stronger interface hole confinement due to the larger effective mass is responsible for a pronounced interface scattering compared to electrons. As a result, the peak of the mobility function is shifted from a large density of $7.1\cdot10^{12}\,\text{cm}^{-2}$ for electrons to a lower value of $2.2\cdot10^{12}\,\text{cm}^{-2}$ for holes.

It has been demonstrated that polarization engineering with AlInGaN barriers is a powerful approach to shift the threshold voltage for both n-channel and p-channel HFET. Polarization-optimized HFET in matters of carrier density allow for the realization of both depletion and enhancement mode devices. In particular for the less-studied p-channel technology, on-off ratios of up to 10^8 for e-mode transistors have been obtained. The first ever measured small signal data and cut-off frequencies of a p-channel HFET has shown a transit frequency f_t of 206 MHz and a maximum

oscillation frequency f_{max} of 640 MHz.

For future research on p-channel HFET utilizing a 2DHG, the focus should be on the increase of the hole mobility. Here, the most promising concept is valence band engineering. Since in usual heterostructures, the hole properties are determined by the heavy-hole valence band, there is a huge potential for a design, which enables the light-hole band or the crystal field split-off band. The ten times smaller effective light-hole mass compared to the one of heavy-holes would result in a greatly enhanced performance. This could possibly be realized by inducing anisotropic and/or shear strain in semi-polar nitrides.

In the last part, LEDs with polarization-engineered AlInGaN barriers as a replacement of conventional binary GaN barriers have been studied. This has enabled a control of ΔP between barrier and the InGaN well. It has been shown that the built-in electric field in the multiple quantum well (MQW), which originates from ΔP, can be influenced by adjusting the composition of AlInGaN barriers. Indeed, electroluminescence has been observed in the green-to-blue color range and the quantum efficiency has almost reached the one of a conventional GaN-barrier LED.

The wavelength shift due to the QCSE, however, has been similar to that of conventional InGaN/GaN LED due to an AlInGaN composition with a rather large Al content and, hence, a high P_{total}. To achieve smaller QCSE-induced wavelength shifts, compressively strained composition with either small Al contents or large In contents need to be investigated further.

Finally, a novel concept of an LED device has been presented. By flipping the conventional p-up n-down junction to a p-down n-up junction, the polarization is reversed, which has been assumed to be promising for mitigating efficiency droop effects. The flip-design has been realized by the integration of a 2DHG as a hole reservoir and as a current spreading layer at the bottom p-GaN side. A large sheet hole density in the 2DHG has been achieved by using a high-polarization AlInGaN backbarrier. A MQW has successfully been grown on top of a 2DHG stack and luminescence tests have shown blue light emission. The peak wavelength has shown to be stable with the current density. This probably indicates that the QCSE is mitigated by the reversed polarization in the active MQW.

The development of a full process of this inverted p-down n-up LED is ongoing. The biggest challenge remains to contact the buried 2DHG. Here, implantation methods or highly p-doped GaN regrowth, preferably by low-temperature and high-purity deposition processes like MBE might pave a way for a successful processing of the inverted LEDs.

References

[1] Multimedia, *Nobel prize in physics for 2014*, Visited on october 7th 2014, 2014. [Online]. Available: http://www.nobelprize.org/nobel_prizes/physics/laureates/2014/press.html.

[2] H. Amano, M. Kito, K. Hiramatsu, and I. Akasaki, "P-Type Conduction in Mg-Doped GaN Treated with Low-Energy Electron Beam Irradiation LEEBI", *Japanese Journal of Applied Physics*, vol. 28, no. 12A, p. L2112, 1989. [Online]. Available: http://stacks.iop.org/1347-4065/28/i=12A/a=L2112.

[3] S. Nakamura, T. Mukai, and M. Senoh, "High-Power GaN P-N Junction Blue-Light-Emitting Diodes", *Japanese Journal of Applied Physics*, vol. 30, no. 12A, p. L1998, 1991. [Online]. Available: http://stacks.iop.org/1347-4065/30/i=12A/a=L1998.

[4] S. Nakamura, M. Senoh, and T. Mukai, "High power InGaN/GaN double heterostructure violet light emitting diodes", *Applied Physics Letters*, vol. 62, no. 19, pp. 2390–2392, 1993. [Online]. Available: http://scitation.aip.org/content/aip/journal/apl/62/19/10.1063/1.109374.

[5] S. Nakamura, M. Senoh, S. ichi Nagahama, N. Iwasa, T. Yamada, T. Matsushita, H. Kiyoku, and Y. Sugimoto, "InGaN-Based Multi-Quantum-Well-Structure Laser Diodes", *Japanese Journal of Applied Physics*, vol. 35, no. Part 2, No. 1B, pp. L74–L76, 1996. [Online]. Available: http://jjap.jsap.jp/link?JJAP/35/L74/.

[6] S. Nakamura, M. Senoh, and T. Mukai, "P-GaN/InGaN/GaN double - heterostructure blue-light-emitting diodes", *Japanese Journal of Applied Physics*, vol. 32, no. 1A, p. L8, 1993. [Online]. Available: http://stacks.iop.org/1347-4065/32/i=1A/a=L8.

[7] S. P. DenBaars, D. Feezell, K. Kelchner, S. Pimputkar, C.-C. Pan, C.-C. Yen, S. Tanaka, Y. Zhao, N. Pfaff, R. Farrell, M. Iza, S. Keller, U. Mishra, J. S. Speck, and S. Nakamura, "Development of gallium-nitride-based light-emitting diodes and laser diodes for energy-efficient lighting and displays", *Acta Materialia*, vol. 61, no. 3, pp. 945 –951, 2013, The Diamond Jubilee Issue Materials Challenges in Tomorrow's World Selected Topics in Materials Science and Engineering. [Online]. Available: http://www.sciencedirect.com/science/article/pii/S1359645412007896.

[8] Multimedia, *U.S. Department of Energy, Solid-State Lighting Research and Development: Manufacturing Roadmap*, Visited on october 7th 2014, 2014. [Online]. Available: `http://http://www1.eere.energy.gov/buildings/ssl/techroadmaps.html`.

[9] ——, *Osram LED*, Visited on september 23th 2014, 2014. [Online]. Available: `http://www.osram.de/osram_de/news-und-wissen/led-home/index.jsp`.

[10] ——, *Cree lighting*, Visited on september 23th 2014, 2014. [Online]. Available: `http://www.cree.com/Lighting`.

[11] Y. Uemoto, D. Shibata, M. Yanagihara, H. Ishida, H. Matsuo, S. Nagai, N. Batta, M. Li, T. Ueda, T. Tanaka, and D. Ueda, "8300v blocking voltage algan/gan power hfet with thick poly-aln passivation", in *Electron Devices Meeting, 2007. IEDM 2007. IEEE International*, Dec. 2007, pp. 861–864.

[12] I. Hwang, H. Choi, J. Lee, H. S. Choi, J. Kim, J. Ha, C.-Y. Um, S.-K. Hwang, J. Oh, J.-Y. Kim, J.-K. Shin, Y. Park, U.-I. Chung, I.-K. Yoo, and K. Kim, "1.6 kV, 2.9 mΩcm^2 normally-off p-GaN HEMT device", in *Power Semiconductor Devices and ICs (ISPSD), 2012 24th International Symposium*, Jun. 2012, pp. 41–44.

[13] Multimedia, *Cree power*, Visited on september 2nd march 2015, 2015. [Online]. Available: `http://www.cree.com/RF/Products/`.

[14] U. K. Mishra, L. Shen, T. Kazior, and Y.-F. Wu, "GaN-Based RF Power Devices and Amplifiers", *Proceedings of the IEEE*, vol. 96, no. 2, pp. 287–305, Feb. 2008.

[15] Y. F. Wu, M. Moore, A. Saxler, T. Wisleder, and P. Parikh, "40-W/mm double field-plated GaN HEMTs", in *Device Research Conference, 2006 64th*, Jun. 2006, pp. 151–152.

[16] D. C. Look and J. R. Sizelove, "Predicted maximum mobility in bulk GaN", *Applied Physics Letters*, vol. 79, no. 8, pp. 1133–1135, 2001. [Online]. Available: `http://scitation.aip.org/content/aip/journal/apl/79/8/10.1063/1.1394954`.

[17] E. C. H. Kyle, S. W. Kaun, P. G. Burke, F. Wu, Y.-R. Wu, and J. S. Speck, "High-electron-mobility GaN grown on free-standing GaN templates by ammonia-based molecular beam epitaxy", *Journal of Applied Physics*, vol. 115, no. 19, 193702, 2014. [Online]. Available: `http://scitation.aip.org/content/aip/journal/jap/115/19/10.1063/1.4874735`.

[18] E. Johnson, "Physical limitations on frequency and power parameters of transistors", in *1958 IRE International Convention Record*, vol. 13, Mar. 1965, pp. 27–34.

[19] K. Shinohara, D. Regan, Y. Tang, A. Corrion, D. Brown, J. Wong, J. Robinson, H. Fung, A Schmitz, T. Oh, S. Kim, P. Chen, R. Nagele, A. Margomenos, and M. Micovic, "Scaling of GaN HEMTs and Schottky Diodes for Submillimeter-Wave MMIC Applications", *Electron Devices, IEEE Transactions on*, vol. 60, no. 10, pp. 2982–2996, Oct. 2013.

[20] Multimedia, *Macom*, Visited on may 27th 2014, 2014. [Online]. Available: http://www.macom.com/files/live/sites/ma/files/contributed/Gan/ganmanifesto.pdf.

[21] O Ambacher, "Growth and applications of Group III-nitrides", *Journal of Physics D: Applied Physics*, vol. 31, no. 20, p. 2653, 1998. [Online]. Available: http://stacks.iop.org/0022-3727/31/i=20/a=001.

[22] O. Ambacher, J. Smart, J. R. Shealy, N. G. Weimann, K. Chu, M. Murphy, W. J. Schaff, L. F. Eastman, R. Dimitrov, L. Wittmer, M. Stutzmann, W. Rieger, and J. Hilsenbeck, "Two-dimensional electron gases induced by spontaneous and piezoelectric polarization charges in N- and Ga-face AlGaN/GaN heterostructures", *Journal of Applied Physics*, vol. 85, no. 6, pp. 3222–3233, 1999. [Online]. Available: http://scitation.aip.org/content/aip/journal/jap/85/6/10.1063/1.369664.

[23] O Ambacher, J Majewski, C Miskys, A Link, M Hermann, M Eickhoff, M Stutzmann, F Bernardini, V Fiorentini, V Tilak, B Schaff, and L. F. Eastman, "Pyroelectric properties of AlInGaN/GaN hetero- and quantum well structures", *Journal of Physics: Condensed Matter*, vol. 14, no. 13, p. 3399, 2002. [Online]. Available: http://stacks.iop.org/0953-8984/14/i=13/a=302.

[24] F. Bernardini, V. Fiorentini, and D. Vanderbilt, "Spontaneous polarization and piezoelectric constants of III-V nitrides", *Phys. Rev. B*, vol. 56, R10024–R10027, 16 Oct. 1997. [Online]. Available: http://link.aps.org/doi/10.1103/PhysRevB.56.R10024.

[25] F. Bernardini and V. Fiorentini, "Nonlinear macroscopic polarization in III-V nitride alloys", *Phys. Rev. B*, vol. 64, p. 085 207, 8 Aug. 2001. [Online]. Available: http://link.aps.org/doi/10.1103/PhysRevB.64.085207.

[26] A. D. Bykhovski, V. V. Kaminski, M. S. Shur, Q. C. Chen, and M. A. Khan, "Pyroelectricity in gallium nitride thin films", *Applied Physics Letters*, vol. 69, no. 21, pp. 3254–3256, 1996. [Online]. Available: http://scitation.aip.org/content/aip/journal/apl/69/21/10.1063/1.118027.

[27] M. S. Shur, A. D. Bykhovski, and R. Gaska, “Pyroelectric and Piezoelectric Properties of Gan-Based Materials”, in *Symposium G – GaN and Related Alloys*, ser. MRS Proceedings, vol. 537, 1998. [Online]. Available: http://journals.cambridge.org/article_S1946427400287782.

[28] H. Morkoc, *Nitride semiconductors and devices*. Springer, 1999, vol. 32.

[29] S. Yamaguchi, M. Kariya, S. Nitta, H. Kato, T. Takeuchi, C. Wetzel, H. Amano, and I. Akasaki, “Structural and optical properties of AlInN and AlGaInN on GaN grown by metalorganic vapor phase epitaxy”, *Journal of Crystal Growth*, vol. 195, no. 1–4, pp. 309 –313, 1998. [Online]. Available: http://www.sciencedirect.com/science/article/pii/S0022024898006290.

[30] M. Asif Khan, A. Bhattarai, J. N. Kuznia, and D. T. Olson, “High electron mobility transistor based on a GaN/AlGaN heterojunction”, *Applied Physics Letters*, vol. 63, no. 9, pp. 1214–1215, 1993. [Online]. Available: http://scitation.aip.org/content/aip/journal/apl/63/9/10.1063/1.109775.

[31] P. Asbeck, E. Yu, S. Lau, G. Sullivan, J. V. Hove, and J. Redwing, “Piezoelectric charge densities in AlGaN/GaN HFETs”, English, *Electronics Letters*, vol. 33, 1230–1231(1), 14 Jul. 1997. [Online]. Available: http://digital-library.theiet.org/content/journals/10.1049/el_19970843.

[32] E. Yu, G. Sullivan, P. Asbeck, C. Wang, D. Qiao, and S. Lau, “Measurement of piezoelectrically induced charge in GaN/AlGaN heterostructure field-effect transistors”, *Applied Physics Letters*, vol. 71, no. 19, pp. 2794–2796, Oct. 1997.

[33] L. Shen, S. Heikman, B. Moran, R. Coffie, N.-Q. Zhang, D. Buttari, I. Smorchkova, S. Keller, S. DenBaars, and U. Mishra, “AlGaN/AlN/GaN high-power microwave HEMT”, *Electron Device Letters, IEEE*, vol. 22, no. 10, pp. 457–459, Oct. 2001.

[34] R. Gaska, M. Shur, A. Bykhovski, A. Orlov, and G. Snider, “Electron mobility in modulation-doped AlGaN/GaN heterostructures”, *Applied Physics Letters*, vol. 74, no. 2, pp. 287–289, Jan. 1999.

[35] I. P. Smorchkova, C. R. Elsass, J. P. Ibbetson, R. Vetury, B. Heying, P. Fini, E. Haus, S. P. DenBaars, J. S. Speck, and U. K. Mishra, “Polarization-induced charge and electron mobility in AlGaN/GaN heterostructures grown by plasma-assisted molecular-beam epitaxy”, *Journal of Applied Physics*, vol. 86, no. 8, pp. 4520–4526, 1999. [Online]. Available: http://scitation.aip.org/content/aip/journal/jap/86/8/10.1063/1.371396.

[36] S. Keller, Y.-F. Wu, G. Parish, N. Ziang, J. Xu, B. Keller, S. P. DenBaars, and U. K. Mishra, “Gallium nitride based high power heterojunction field effect transistors: process development and present status at UCSB”, *Electron Devices, IEEE Transactions on*, vol. 48, no. 3, pp. 552–559, Mar. 2001.

[37] U. K. Mishra, P. Parikh, Y.-F. Wu, *et al.*, "AlGaN/GaN HEMTs-an overview of device operation and applications", *Proceedings-IEEE*, vol. 90, no. 6, pp. 1022–1031, 2002.

[38] T. Palacios, A Chakraborty, S. Rajan, C. Poblenz, S. Keller, S. DenBaars, J. Speck, and U. Mishra, "High-power AlGaN/GaN HEMTs for Ka-band applications", *Electron Device Letters, IEEE*, vol. 26, no. 11, pp. 781–783, Nov. 2005.

[39] R. Pengelly, S. Wood, J. Milligan, S. Sheppard, and W. Pribble, "A Review of GaN on SiC High Electron-Mobility Power Transistors and MMICs", *Microwave Theory and Techniques, IEEE Transactions on*, vol. 60, no. 6, pp. 1764–1783, Jun. 2012.

[40] H. Sun, A. Alt, H. Benedickter, E. Feltin, J.-F. Carlin, M. Gonschorek, N. Grandjean, and C. Bolognesi, "205-GHz (Al,In)N/GaN HEMTs", *Electron Device Letters, IEEE*, vol. 31, no. 9, pp. 957–959, Sep. 2010.

[41] M. E. Aumer, S. F. LeBoeuf, F. G. McIntosh, and S. M. Bedair, "High optical quality AlInGaN by metalorganic chemical vapor deposition", *Applied Physics Letters*, vol. 75, no. 21, pp. 3315–3317, 1999. [Online]. Available: `http://scitation.aip.org/content/aip/journal/apl/75/21/10.1063/1.125336`.

[42] F. G. McIntosh, K. S. Boutros, J. C. Roberts, S. M. Bedair, E. L. Piner, and N. A. El Masry, "Growth and characterization of AlInGaN quaternary alloys", *Applied Physics Letters*, vol. 68, no. 1, pp. 40–42, 1996. [Online]. Available: `http://scitation.aip.org/content/aip/journal/apl/68/1/10.1063/1.116749`.

[43] R. Wang, G. Li, J. Verma, B. Sensale-Rodriguez, T. Fang, J. Guo, Z. Hu, O. Laboutin, Y. Cao, W. Johnson, *et al.*, "220-GHz quaternary barrier InAlGaN/AlN/GaN HEMTs", *Electron Device Letters, IEEE*, vol. 32, no. 9, pp. 1215–1217, 2011.

[44] R. Wang, G. Li, G. Karbasian, J. Guo, B. Song, Y. Yue, Z. Hu, O. Laboutin, Y. Cao, W. Johnson, *et al.*, "Quaternary barrier InAlGaN HEMTs with f_t/f_{max} of 230/300 GHz", *IEEE Electron Device Lett*, vol. 34, no. 3, pp. 378–380, 2013.

[45] G. Jessen, R. C. Fitch, J. Gillespie, G. Via, A. Crespo, D. Langley, D. Denninghoff, M. Trejo, and E. Heller, "Short-channel effect limitations on high-frequency operation of algan/gan hemts for t-gate devices", *Electron Devices, IEEE Transactions on*, vol. 54, no. 10, pp. 2589–2597, Oct. 2007.

[46] E. T. Yu, X. Z. Dang, P. M. Asbeck, S. S. Lau, and G. J. Sullivan, "Spontaneous and piezoelectric polarization effects in III–V nitride heterostructures", *Journal of Vacuum Science and Technology B*, vol. 17, no. 4, pp. 1742–1749, 1999. [Online]. Available: `http://scitation.aip.org/content/avs/journal/jvstb/17/4/10.1116/1.590818`.

[47] M. A. Khan, J. W. Yang, G. Simin, R. Gaska, M. S. Shur, and A. D. Bykhovski, "Piezoelectric doping in AlInGaN/GaN heterostructures", *Applied Physics Letters*, vol. 75, no. 18, pp. 2806–2808, 1999. [Online]. Available: `http://scitation.aip.org/content/aip/journal/apl/75/18/10.1063/1.125156`.

[48] M. S. Shur, A. D. Bykhovski, R. Gaska, J. W. Yang, G. Simin, and M. A. Khan, "Accumulation hole layer in p-GaN/AlGaN heterostructures", *Applied Physics Letters*, vol. 76, no. 21, pp. 3061–3063, 2000. [Online]. Available: `http://scitation.aip.org/content/aip/journal/apl/76/21/10.1063/1.126579`.

[49] A Link, O. Ambacher, I. Smorchkova, U. K. Mishra, J. S. Speck, and M Stutzmann, "Formation and electronic transport of 2D electron and hole gases in AlGaN/GaN heterostructures", in *Materials Science Forum*, Trans Tech Publ, vol. 353, 2001, pp. 787–790.

[50] M. Shatalov, G. Simin, J. Zhang, V. Adivarahan, A Koudymov, R. Pachipulusu, and M. Asif Khan, "GaN/AlGaN p-channel inverted heterostructure JFET", *Electron Device Letters, IEEE*, vol. 23, no. 8, pp. 452–454, Aug. 2002.

[51] T. Zimmermann, M. Neuburger, M. Kunze, I Daumiller, A Denisenko, A Dadgar, A Krost, and E. Kohn, "P-channel InGaN-HFET structure based on polarization doping", *Electron Device Letters, IEEE*, vol. 25, no. 7, pp. 450–452, Jul. 2004.

[52] A. Nakajima, Y. Sumida, M. H. Dhyani, H. Kawai, and E. M. S. Narayanan, "High density two-dimensional hole gas induced by negative polarization at GaN/AlGaN heterointerface", *Applied Physics Express*, vol. 3, no. 12, p. 121 004, 2010. [Online]. Available: `http://stacks.iop.org/1882-0786/3/i=12/a=121004`.

[53] A. Nakajima, P. Liu, M. Ogura, T. Makino, S. ichi Nishizawa, S. Yamasaki, H. Ohashi, K. Kakushima, and H. Iwai, "Temperature-independent two-dimensional hole gas confined at GaN/AlGaN heterointerface", *Applied Physics Express*, vol. 6, no. 9, p. 091 002, 2013. [Online]. Available: `http://stacks.iop.org/1882-0786/6/i=9/a=091002`.

[54] A. Nakajima, P. Liu, M. Ogura, T. Makino, K. Kakushima, S.-i. Nishizawa, H. Ohashi, S. Yamasaki, and H. Iwai, "Generation and transportation mechanisms for two-dimensional hole gases in GaN/AlGaN/GaN double heterostructures", *Journal of Applied Physics*, vol. 115, no. 15, 153707, 2014. [Online]. Available: `http://scitation.aip.org/content/aip/journal/jap/115/15/10.1063/1.4872242`.

[55] M. Fandrich, T. Mehrtens, T. Aschenbrenner, T. Klein, M. Gebbe, S. Figge, C. Kruse, A. Rosenauer, and D. Hommel, "Nitride based heterostructures with Ga- and N-polarity for sensing applications", *Journal of Crystal Growth*, vol. 370, no. 0, pp. 68 –73, 2013, 16th International Conference on Metalorganic Vapor Phase Epi-

taxy. [Online]. Available: http://www.sciencedirect.com/science/article/pii/S0022024812006100.

[56] G. Li, R. Wang, B. Song, J. Verma, Y. Cao, S. Ganguly, A Verma, J. Guo, H. Xing, and D. Jena, "Polarization-induced GaN-on-insulator E/D mode p-channel heterostructure FETs", *Electron Device Letters, IEEE*, vol. 34, no. 7, pp. 852–854, Jul. 2013.

[57] M. Shatalov, A. Chitnis, V. Adivarahan, A. Lunev, J. Zhang, J. W. Yang, Q. Fareed, G. Simin, A. Zakheim, M. A. Khan, R. Gaska, and M. S. Shur, "Band-edge luminescence in quaternary AlInGaN light-emitting diodes", *Applied Physics Letters*, vol. 78, no. 6, pp. 817–819, 2001. [Online]. Available: http://scitation.aip.org/content/aip/journal/apl/78/6/10.1063/1.1343493.

[58] M. F. Schubert, J. Xu, J. K. Kim, E. F. Schubert, M. H. Kim, S. Yoon, S. M. Lee, C. Sone, T. Sakong, and Y. Park, "Polarization-matched GaInN/AlGaInN multi-quantum-well light-emitting diodes with reduced efficiency droop", *Applied Physics Letters*, vol. 93, no. 4, 041102, 2008. [Online]. Available: http://scitation.aip.org/content/aip/journal/apl/93/4/10.1063/1.2963029.

[59] A. Knauer, H. Wenzel, T. Kolbe, S. Einfeldt, M. Weyers, M. Kneissl, and G. Tränkle, "Effect of the barrier composition on the polarization fields in near UV InGaN light emitting diodes", *Applied Physics Letters*, vol. 92, no. 19, 191912, 2008. [Online]. Available: http://scitation.aip.org/content/aip/journal/apl/92/19/10.1063/1.2930686.

[60] P.-M. Tu, C.-Y. Chang, S.-C. Huang, C.-H. Chiu, J.-R. Chang, W.-T. Chang, D.-S. Wuu, H.-W. Zan, C.-C. Lin, H.-C. Kuo, and C.-P. Hsu, "Investigation of efficiency droop for InGaN-based UV light-emitting diodes with InAlGaN barrier", *Applied Physics Letters*, vol. 98, no. 21, 211107, 2011. [Online]. Available: http://scitation.aip.org/content/aip/journal/apl/98/21/10.1063/1.3591967.

[61] G. Liu, J. Zhang, C. K. Tan, and N. Tansu, "Efficiency-droop suppression by using large-bandgap AlGaInN thin barrier layers in InGaN quantum-well light-emitting diodes", *Photonics Journal, IEEE*, vol. 5, no. 2, pp. 2 201 011–2 201 011, Apr. 2013.

[62] G. Verzellesi, D. Saguatti, M. Meneghini, F. Bertazzi, M. Goano, G. Meneghesso, and E. Zanoni, "Efficiency droop in InGaN/GaN blue light-emitting diodes: physical mechanisms and remedies", *Journal of Applied Physics*, vol. 114, no. 7, 071101, 2013. [Online]. Available: http://scitation.aip.org/content/aip/journal/jap/114/7/10.1063/1.4816434.

[63] L. Pauling, *The nature of the chemical bond and the structure of molecules and crystals: an introduction to modern structural chemistry*. Cornell University Press, 1960, vol. 18.

[64] K. Kim, W. R. L. Lambrecht, B. Segall, and M. van Schilfgaarde, "Effective masses and valence-band splittings in GaN and AlN", *Phys. Rev. B*, vol. 56, pp. 7363–7375, 12 Sep. 1997. [Online]. Available: http://link.aps.org/doi/10.1103/PhysRevB.56.7363.

[65] M. Suzuki and T. Uenoyama, "Strain effect on electronic and optical properties of GaN/AlGaN quantum-well lasers", *Journal of Applied Physics*, vol. 80, no. 12, pp. 6868–6874, 1996. [Online]. Available: http://scitation.aip.org/content/aip/journal/jap/80/12/10.1063/1.363755.

[66] H. Masui, S. Nakamura, S. P. DenBaars, and U. K. Mishra, "Nonpolar and Semipolar III-Nitride Light-Emitting Diodes: Achievements and Challenges", *Electron Devices, IEEE Transactions on*, vol. 57, no. 1, pp. 88–100, Jan. 2010.

[67] N. H. Thillosen, "Spin-Bahn-Wechselwirkung von niedrigdimensionalen AlGaN/GaN-Elektronengasen", PhD thesis, RWTH Aachen university, 2006. [Online]. Available: http://darwin.bth.rwth-aachen.de/opus/volltexte/2006/1639/.

[68] V. W. L. Chin, T. L. Tansley, and T. Osotchan, "Electron mobilities in gallium, indium, and aluminum nitrides", *Journal of Applied Physics*, vol. 75, no. 11, pp. 7365–7372, 1994. [Online]. Available: http://scitation.aip.org/content/aip/journal/jap/75/11/10.1063/1.356650.

[69] G. D. Chen, M. Smith, J. Y. Lin, H. X. Jiang, S. H. Wei, M. Asif Khan, and C. J. Sun, "Fundamental optical transitions in GaN", *Applied Physics Letters*, vol. 68, no. 20, pp. 2784–2786, 1996. [Online]. Available: http://scitation.aip.org/content/aip/journal/apl/68/20/10.1063/1.116606.

[70] M. Suzuki, T. Uenoyama, and A. Yanase, "First-principles calculations of effective-mass parameters of AlN and GaN", *Phys. Rev. B*, vol. 52, pp. 8132–8139, 11 Sep. 1995. [Online]. Available: http://link.aps.org/doi/10.1103/PhysRevB.52.8132.

[71] Q. Yan, P. Rinke, M. Scheffler, and C. G. Van de Walle, "Role of strain in polarization switching in semipolar InGaN/GaN quantum wells", *Applied Physics Letters*, vol. 97, no. 18, 181102, 2010. [Online]. Available: http://scitation.aip.org/content/aip/journal/apl/97/18/10.1063/1.3507289.

[72] A. A. Yamaguchi, "Theoretical investigation on polarization control of semipolar-oriented InGaN quantum-well emission using AlInGaN alloy substrates", *Applied Physics Letters*, vol. 94, no. 20, 201104, 2009. [Online]. Available: http://scitation.aip.org/content/aip/journal/apl/94/20/10.1063/1.3139080.

[73] L. Vegard, "Die Konstitution der Mischkristalle und die Raumfüllung der Atome", German, *Zeitschrift für Physik*, vol. 5, no. 1, pp. 17–26, 1921. [Online]. Available: http://dx.doi.org/10.1007/BF01349680.

[74] U. W. Pohl, *Epitaxy of Semiconductors*. Springer, 1999, vol. 32.

[75] S. R. Lee, D. D. Koleske, K. C. Cross, J. A. Floro, K. E. Waldrip, A. T. Wise, and S. Mahajan, "In situ measurements of the critical thickness for strain relaxation in AlGaN/GaN heterostructures", *Applied Physics Letters*, vol. 85, no. 25, pp. 6164–6166, 2004. [Online]. Available: http://scitation.aip.org/content/aip/journal/apl/85/25/10.1063/1.1840111.

[76] J. D. Albrecht, R. P. Wang, P. P. Ruden, M. Farahmand, and K. F. Brennan, "Monte Carlo calculation of electron transport properties of bulk AlN", *Journal of Applied Physics*, vol. 83, no. 3, pp. 1446–1449, 1998. [Online]. Available: http://scitation.aip.org/content/aip/journal/jap/83/3/10.1063/1.366848.

[77] V. M. Polyakov and F. Schwierz, "Low-field electron mobility in wurtzite InN", *Applied Physics Letters*, vol. 88, no. 3, 032101, 2006. [Online]. Available: http://scitation.aip.org/content/aip/journal/apl/88/3/10.1063/1.2166195.

[78] C. G. Rodrigues, u. R. Vasconcellos, R. Luzzi, and V. N. Freire, "Nonlinear transport properties of III nitrides in electric field", *Journal of Applied Physics*, vol. 98, no. 4, 043702, 2005. [Online]. Available: http://scitation.aip.org/content/aip/journal/jap/98/4/10.1063/1.1999024.

[79] K. T. Tsen, C. Poweleit, D. K. Ferry, H. Lu, and W. J. Schaff, "Observation of large electron drift velocities in InN by ultrafast Raman spectroscopy", *Applied Physics Letters*, vol. 86, no. 22, 222103, 2005. [Online]. Available: http://scitation.aip.org/content/aip/journal/apl/86/22/10.1063/1.1931048.

[80] I. P. Smorchkova, E. Haus, B. Heying, P. Kozodoy, P. Fini, J. P. Ibbetson, S. Keller, S. P. DenBaars, J. S. Speck, and U. K. Mishra, "Mg doping of GaN layers grown by plasma-assisted molecular-beam epitaxy", *Applied Physics Letters*, vol. 76, no. 6, pp. 718–720, 2000. [Online]. Available: http://scitation.aip.org/content/aip/journal/apl/76/6/10.1063/1.125872.

[81] H. Hahn, B. Reuters, A. Pooth, A. Noculak, H. Kalisch, and A. Vescan, "First small-signal data of GaN-based p-channel heterostructure field effect transistors", *Japanese Journal of Applied Physics*, vol. 52, no. 12R, p. 128 001, 2013. [Online]. Available: http://stacks.iop.org/1347-4065/52/i=12R/a=128001.

[82] M. Higashiwaki and T. Matsui, "Estimation of band-gap energy of intrinsic InN from photoluminescence properties of undoped and Si-doped InN films grown by plasma-assisted molecular-beam epitaxy", *Journal of Crystal Growth*, vol. 269, no. 1, pp. 162 –166, 2004, Proceedings of the First ONR International Indium Nitride Workshop. [Online]. Available: http://www.sciencedirect.com/science/article/pii/S0022024804006256.

[83] P. Schley, R. Goldhahn, G. Gobsch, M. Feneberg, K. Thonke, X. Wang, and A. Yoshikawa, "Influence of strain on the band gap energy of wurtzite InN", *physica status solidi (b)*, vol. 246, no. 6, pp. 1177–1180, 2009. [Online]. Available: http://dx.doi.org/10.1002/pssb.200880924.

[84] T. Onuma, S. Chichibu, Y. Uchinuma, T. Sota, S. Yamaguchi, S. Kamiyama, H. Amano, and I. Akasaki, "Recombination dynamics of localized excitons in AlInN epitaxial films on GaN templates grown by metalorganic vapor phase epitaxy", *Journal of Applied Physics*, vol. 94, no. 4, pp. 2449–2453, 2003. [Online]. Available: http://scitation.aip.org/content/aip/journal/jap/94/4/10.1063/1.1592868.

[85] W Walukiewicz, S. Li, J Wu, K. Yu, J. A. III, E. Haller, H. Lu, and W. J. Schaff, "Optical properties and electronic structure of InN and In-rich group III-nitride alloys", *Journal of Crystal Growth*, vol. 269, no. 1, pp. 119 –127, 2004, Proceedings of the First ONR International Indium Nitride Workshop. [Online]. Available: http://www.sciencedirect.com/science/article/pii/S0022024804006190.

[86] R. Goldhahn, P. Schley, A. T. Winzer, G. Gobsch, V. Cimalla, O. Ambacher, M. Rakel, C. Cobet, N. Esser, H. Lu, and W. J. Schaff, "Detailed analysis of the dielectric function for wurtzite InN and In-rich InAlN alloys", *physica status solidi (a)*, vol. 203, no. 1, pp. 42–49, 2006. [Online]. Available: http://dx.doi.org/10.1002/pssa.200563507.

[87] I. Vurgaftman, J. R. Meyer, and L. R. Ram-Mohan, "Band parameters for III–V compound semiconductors and their alloys", *Journal of Applied Physics*, vol. 89, no. 11, pp. 5815–5875, 2001. [Online]. Available: http://scitation.aip.org/content/aip/journal/jap/89/11/10.1063/1.1368156.

[88] I. Vurgaftman and J. R. Meyer, "Band parameters for nitrogen-containing semiconductors", *Journal of Applied Physics*, vol. 94, no. 6, pp. 3675–3696, 2003. [Online]. Available: http://scitation.aip.org/content/aip/journal/jap/94/6/10.1063/1.1600519.

[89] L. Liu and J. H. Edgar, "Substrates for gallium nitride epitaxy", *Materials Science and Engineering: R: Reports*, vol. 37, no. 3, pp. 61 –127, 2002. [Online]. Available: http://www.sciencedirect.com/science/article/pii/S0927796X02000086.

[90] F. Yun, M. A. Reshchikov, L. He, T. King, H. Morkoç, S. W. Novak, and L. Wei, "Energy band bowing parameter in AlGaN alloys", *Journal of Applied Physics*, vol. 92, no. 8, pp. 4837–4839, 2002. [Online]. Available: http://scitation.aip.org/content/aip/journal/jap/92/8/10.1063/1.1508420.

[91] E. Sakalauskas, B. Reuters, L. R. Khoshroo, H. Kalisch, M. Heuken, A. Vescan, M. Röppischer, C. Cobet, G. Gobsch, and R. Goldhahn, “Dielectric function and optical properties of quaternary AlInGaN alloys”, *Journal of Applied Physics*, vol. 110, no. 1, 013102, 2011. [Online]. Available: http://scitation.aip.org/content/aip/journal/jap/110/1/10.1063/1.3603015.

[92] E. Sakalauskas, . Tuna, A. Kraus, H. Bremers, U. Rossow, C. Giesen, M. Heuken, A. Hangleiter, G. Gobsch, and R. Goldhahn, “Dielectric function and bowing parameters of InGaN alloys”, *physica status solidi (b)*, vol. 249, no. 3, pp. 485–488, 2012. [Online]. Available: http://dx.doi.org/10.1002/pssb.201100334.

[93] M. van Schilfgaarde, A. Sher, and A.-B. Chen, “Theory of AlN, GaN, InN and their alloys”, *Journal of Crystal Growth*, vol. 178, no. 1–2, pp. 8 –31, 1997. [Online]. Available: http://www.sciencedirect.com/science/article/pii/S0022024897000730.

[94] M. Goano, E. Bellotti, E. Ghillino, C. Garetto, G. Ghione, and K. F. Brennan, “Band structure nonlocal pseudopotential calculation of the III-nitride wurtzite phase materials system. Part II. Ternary alloys AlGaN, InGaN, and InAlN”, *Journal of Applied Physics*, vol. 88, no. 11, pp. 6476–6482, 2000. [Online]. Available: http://scitation.aip.org/content/aip/journal/jap/88/11/10.1063/1.1309047.

[95] M. J. Lukitsch, Y. V. Danylyuk, V. M. Naik, C. Huang, G. W. Auner, L. Rimai, and R. Naik, “Optical and electrical properties of AlInN films grown by plasma source molecular-beam epitaxy”, *Applied Physics Letters*, vol. 79, no. 5, pp. 632–634, 2001. [Online]. Available: http://scitation.aip.org/content/aip/journal/apl/79/5/10.1063/1.1388883.

[96] Q. Guo, T. Tanaka, M. Nishio, and H. Ogawa, “Optical Bandgap Energy of Wurtzite In-Rich AlInN Alloys”, *Japanese Journal of Applied Physics*, vol. 42, no. 2B, p. L141, 2003. [Online]. Available: http://stacks.iop.org/1347-4065/42/i=2B/a=L141.

[97] K. Wang, R. Martin, D. Amabile, P. Edwards, S. Hernandez, E. Nogales, K. ODonnell, K. Lorenz, E. Alves, V. Matias, A Vantomme, D. Wolverson, and I. M. Watson, “Optical energies of AlInN epilayers”, *Journal of Applied Physics*, vol. 103, no. 7, pp. 073 510–073510–3, Apr. 2008.

[98] W. Terashima, S.-B. Che, Y. Ishitani, and A. Yoshikawa, “Growth and characterization of AlInN ternary alloys in whole composition range and fabrication of InN/AlInN multiple quantum wells by RF molecular beam epitaxy”, *Japanese Journal of Applied Physics*, vol. 45, no. 6L, p. L539, 2006. [Online]. Available: http://stacks.iop.org/1347-4065/45/i=6L/a=L539.

[99] F. Wang, S.-S. Li, J.-B. Xia, H. X. Jiang, J. Y. Lin, J. Li, and S.-H. Wei, "Effects of the wave function localization in AlInGaN quaternary alloys", *Applied Physics Letters*, vol. 91, no. 6, 061125, 2007. [Online]. Available: http://scitation.aip.org/content/aip/journal/apl/91/6/10.1063/1.2769958.

[100] E. Iliopoulos, A. Adikimenakis, C. Giesen, M. Heuken, and A. Georgakilas, "Energy bandgap bowing of InAlN alloys studied by spectroscopic ellipsometry", *Applied Physics Letters*, vol. 92, no. 19, 191907, 2008. [Online]. Available: http://scitation.aip.org/content/aip/journal/apl/92/19/10.1063/1.2921783.

[101] E Sakalauskas, H Behmenburg, C Hums, P Schley, G Rossbach, C Giesen, M Heuken, H Kalisch, R. H. Jansen, J Bläsing, A Dadgar, A Krost, and R Goldhahn, "Dielectric function and optical properties of Al-rich AlInN alloys pseudomorphically grown on GaN", *Journal of Physics D: Applied Physics*, vol. 43, no. 36, p. 365 102, 2010. [Online]. Available: http://stacks.iop.org/0022-3727/43/i=36/a=365102.

[102] D. Jena, J. Simon, A. K. Wang, Y. Cao, K. Goodman, J. Verma, S. Ganguly, G. Li, K. Karda, V. Protasenko, C. Lian, T. Kosel, P. Fay, and H. Xing, "Polarization-engineering in group III-nitride heterostructures: New opportunities for device design", *physica status solidi (a)*, vol. 208, no. 7, pp. 1511–1516, 2011. [Online]. Available: http://dx.doi.org/10.1002/pssa.201001189.

[103] M.-H. Kim, M. F. Schubert, Q. Dai, J. K. Kim, E. F. Schubert, J. Piprek, and Y. Park, "Origin of efficiency droop in GaN-based light-emitting diodes", *Applied Physics Letters*, vol. 91, no. 18, p. 183 507, 2007. [Online]. Available: http://scitation.aip.org/content/aip/journal/apl/91/18/10.1063/1.2800290.

[104] N Ketteniss, L. R. Khoshroo, M Eickelkamp, M Heuken, H Kalisch, R. H. Jansen, and A Vescan, "Study on quaternary AlInGaN/GaN HFETs grown on sapphire substrates", *Semiconductor Science and Technology*, vol. 25, no. 7, p. 075 013, 2010. [Online]. Available: http://stacks.iop.org/0268-1242/25/i=7/a=075013.

[105] M. Takeuchi, H. Shimizu, R. Kajitani, K. Kawasaki, T. Kinoshita, K. Takada, H. Murakami, Y. Kumagai, A. Koukitu, T. Koyama, S. Chichibu, and Y. Aoyagi, "Al- and N-polar AlN layers grown on c-plane sapphire substrates by modified flow-modulation MOCVD", *Journal of Crystal Growth*, vol. 305, no. 2, pp. 360 –365, 2007, Proceedings of the 4th International Workshop on Bulk Nitride Semiconductors IV. [Online]. Available: http://www.sciencedirect.com/science/article/pii/S0022024807003740.

[106] Y. Kumagai, K. Akiyama, R. Togashi, H. Murakami, M. Takeuchi, T. Kinoshita, K. Takada, Y. Aoyagi, and A. Koukitu, "Polarity dependence of AlN decomposition in flowing H_2", *Journal of Crystal Growth*, vol. 305, no. 2, pp. 366 –371, 2007,

Proceedings of the 4th International Workshop on Bulk Nitride Semiconductors IV. [Online]. Available: http://www.sciencedirect.com/science/article/pii/S0022024807003739.

[107] M. Imura, K. Nakano, N. Fujimoto, N. Okada, K. Balakrishnan, M. Iwaya, S. Kamiyama, H. Amano, I. Akasaki, T. Noro, T. Takagi, and A. Bandoh, "High-temperature metal-organic vapor phase epitaxial growth of AlN on sapphire by multi transition growth mode method varying V/III ratio", *Japanese Journal of Applied Physics*, vol. 45, no. 11R, p. 8639, 2006. [Online]. Available: http://stacks.iop.org/1347-4065/45/i=11R/a=8639.

[108] B. K. Ridley, O Ambacher, and L. F. Eastman, "The polarization-induced electron gas in a heterostructure", *Semiconductor Science and Technology*, vol. 15, no. 3, p. 270, 2000. [Online]. Available: http://stacks.iop.org/0268-1242/15/i=3/a=308.

[109] B. K. Ridley, "Polarization-induced electron populations", *Applied Physics Letters*, vol. 77, no. 7, pp. 990–992, 2000. [Online]. Available: http://scitation.aip.org/content/aip/journal/apl/77/7/10.1063/1.1288817.

[110] B. K. Ridley, "Analytical models for polarization-induced carriers", *Semiconductor Science and Technology*, vol. 19, no. 3, p. 446, 2004. [Online]. Available: http://stacks.iop.org/0268-1242/19/i=3/a=027.

[111] J. Shealy, T. Prunty, E. Chumbes, and B. Ridley, "Growth and passivation of AlGaN/GaN heterostructures", *Journal of Crystal Growth*, vol. 250, no. 1–2, pp. 7–13, 2003, Proceedings of the Fourteenth American Conference on Crystal Grow th and Epitaxy. [Online]. Available: http://www.sciencedirect.com/science/article/pii/S0022024802021875.

[112] H. Hahn, "Threshold voltage engineering of GaN-based n-channel and p-channel heterostructure field effect transistors", PhD thesis, RWTH Aachen university, 2014.

[113] H. Hahn, B. Reuters, S. Geipel, M. Schauerte, F. Benkhelifa, O. Ambacher, H. Kalisch, and A. Vescan, "Charge balancing in GaN-based 2-D electron gas devices employing an additional 2-D hole gas and its influence on dynamic behaviour of GaN-based heterostructure field effect transistors", *Journal of Applied Physics*, vol. 117, no. 10, 104508, 2015. [Online]. Available: http://scitation.aip.org/content/aip/journal/jap/117/10/10.1063/1.4913857.

[114] T. Drummond, H. Morkoc, K. Lee, and M. Shur, "Model for modulation doped field effect transistor", *Electron Device Letters, IEEE*, vol. 3, no. 11, pp. 338–341, Nov. 1982.

[115] D. Delagebeaudeuf and N. T. Linh, “Metal-(n) AlGaAs-GaAs two-dimensional electron gas FET”, *Electron Devices, IEEE Transactions on*, vol. 29, no. 6, pp. 955–960, Jun. 1982.

[116] Multimedia, *AIXTRON SE*, Visited on may 27th 2014, 2014. [Online]. Available: `http://www.aixtron.com/en/products/technologies/`.

[117] ——, *LayTec AG*, Visited on may 27th 2014, 2014. [Online]. Available: `http://www.laytec.de/compounds-physical:`.

[118] ——, *AIXTRON Close Coupled Showerhead*, Visited on march 31th 2015, 2015. [Online]. Available: `http://www.aixtron.com/fileadmin/documents/matrix/r_d_systems/CCS_3x2_6x2_inch_01.pdf`.

[119] R. P. Parikh and R. A. Adomaitis, “An overview of gallium nitride growth chemistry and its effect on reactor design: application to a planetary radial-flow CVD system”, *Journal of Crystal Growth*, vol. 286, no. 2, pp. 259 –278, 2006. [Online]. Available: `http://www.sciencedirect.com/science/article/pii/S0022024805010973`.

[120] D. A. Neumayer and J. G. Ekerdt, “Growth of Group III Nitrides. A Review of Precursors and Techniques”, *Chemistry of Materials*, vol. 8, no. 1, pp. 9–25, 1996. [Online]. Available: `http://pubs.acs.org/doi/abs/10.1021/cm950108r`.

[121] S. S. Liu and D. A. Stevenson, “Growth kinetics and catalytic effects in the vapor phase epitaxy of gallium nitride”, *Journal of The Electrochemical Society*, vol. 125, no. 7, pp. 1161–1169, 1978. [Online]. Available: `http://jes.ecsdl.org/content/125/7/1161.abstract`.

[122] D. D. Koleske, A. E. Wickenden, R. L. Henry, W. J. DeSisto, and R. J. Gorman, “Growth model for GaN with comparison to structural, optical, and electrical properties”, *Journal of Applied Physics*, vol. 84, no. 4, pp. 1998–2010, 1998. [Online]. Available: `http://scitation.aip.org/content/aip/journal/jap/84/4/10.1063/1.368353`.

[123] C. Larsen, N. Buchan, S. Li, and G. Stringfellow, “Decomposition mechanisms of trimethylgallium”, *Journal of Crystal Growth*, vol. 102, no. 1–2, pp. 103 –116, 1990. [Online]. Available: `http://www.sciencedirect.com/science/article/pii/002202489090891N`.

[124] A. H. McDaniel and M. D. Allendorf, “Autocatalytic behavior of trimethylindium during thermal decomposition”, *Chemistry of Materials*, vol. 12, no. 2, pp. 450–460, 2000. [Online]. Available: `http://pubs.acs.org/doi/abs/10.1021/cm990497f`.

[125] E. L. Piner, M. K. Behbehani, N. A. El-Masry, F. G. McIntosh, J. C. Roberts, K. S. Boutros, and S. M. Bedair, “Effect of hydrogen on the indium incorporation in InGaN epitaxial films”, *Applied Physics Letters*, vol. 70, no. 4, pp. 461–463, 1997. [Online]. Available: `http://scitation.aip.org/content/aip/journal/apl/70/4/10.1063/1.118181`.

[126] S. Pearton, “GaN and ZnO-based materials and devices”, vol. 156, 2012.

[127] A. Dadgar, “Sixteen years GaN on Si”, *physica status solidi (b)*, n/a–n/a, 2015. [Online]. Available: `http://dx.doi.org/10.1002/pssb.201451656`.

[128] A. Krost and A. Dadgar, “GaN-based optoelectronics on silicon substrates”, *Materials Science and Engineering: B*, vol. 93, no. 1–3, pp. 77 –84, 2002. [Online]. Available: `http://www.sciencedirect.com/science/article/pii/S0921510702000430`.

[129] A. Krost, A. Dadgar, G. Strassburger, and R. Clos, “GaN-based epitaxy on silicon: stress measurements”, *physica status solidi (a)*, vol. 200, no. 1, pp. 26–35, 2003. [Online]. Available: `http://dx.doi.org/10.1002/pssa.200303428`.

[130] A. Able, W. Wegscheider, K. Engl, and J. Zweck, “Growth of crack-free GaN on Si(111) with graded AlGaN buffer layers”, *Journal of Crystal Growth*, vol. 276, no. 3–4, pp. 415 –418, 2005. [Online]. Available: `http://www.sciencedirect.com/science/article/pii/S0022024804019554`.

[131] N. Sawaki, T. Hikosaka, N. Koide, S. Tanaka, Y. Honda, and M. Yamaguchi, “Growth and properties of semi-polar GaN on a patterned silicon substrate”, *Journal of Crystal Growth*, vol. 311, no. 10, pp. 2867 –2874, 2009, Proceedings of the 2nd International Symposium on Growth of III Nitrides. [Online]. Available: `http://www.sciencedirect.com/science/article/pii/S0022024809000554`.

[132] Z. H. Wu, T. Tanikawa, T. Murase, Y.-Y. Fang, C. Q. Chen, Y. Honda, M. Yamaguchi, H. Amano, and N. Sawaki, “Partial strain relaxation by stacking fault generation in InGaN multiple quantum wells grown on (1-101) semipolar GaN”, *Applied Physics Letters*, vol. 98, no. 5, pp. 051 902–051902–3, Jan. 2011.

[133] G.-T. Chen, S.-P. Chang, J.-I. Chyi, and M.-N. Chang, “Growth and characterization of crack-free semipolar (1-101) InGaN/GaN multiple-quantum well on V-grooved (001)Si substrates”, *Applied Physics Letters*, vol. 92, no. 24, 241904, 2008. [Online]. Available: `http://scitation.aip.org/content/aip/journal/apl/92/24/10.1063/1.2946655`.

[134] S. Nakamura, S. Pearton, and G. Fasol, *The blue laser diode: the complete story.* Springer, 2000.

[135] E. A. Soares, M. A. Van Hove, C. F. Walters, and K. F. McCarty, "Structure of the α-Al_2O_3 (0001) surface from low-energy electron diffraction: Al termination and evidence for anomalously large thermal vibrations", *Phys. Rev. B*, vol. 65, p. 195 405, 19 Apr. 2002. [Online]. Available: `http://link.aps.org/doi/10.1103/PhysRevB.65.195405`.

[136] Y. A. Xi, K. X. Chen, F. Mont, J. K. Kim, C. Wetzel, E. F. Schubert, W. Liu, X. Li, and J. A. Smart, "Very high quality AlN grown on (0001) sapphire by metal-organic vapor phase epitaxy", *Applied Physics Letters*, vol. 89, no. 10, 103106, 2006. [Online]. Available: `http://scitation.aip.org/content/aip/journal/apl/89/10/10.1063/1.2345256`.

[137] Q. Paduano, D. Weyburne, J. Jasinski, and Z. Liliental-Weber, "Effect of initial process conditions on the structural properties of AlN films", *Journal of Crystal Growth*, vol. 261, no. 2–3, pp. 259 –265, 2004, Proceedings of the 11th Biennial (US) Workshop on Organometallic Vapor Phase Epitaxy (OMVPE). [Online]. Available: `http://www.sciencedirect.com/science/article/pii/S0022024803020207`.

[138] J. Jasinski, Z. Liliental-Weber, Q. S. Paduano, and D. W. Weyburne, "Inversion domains in AlN grown on (0001) sapphire", *Applied Physics Letters*, vol. 83, no. 14, pp. 2811–2813, 2003. [Online]. Available: `http://scitation.aip.org/content/aip/journal/apl/83/14/10.1063/1.1616191`.

[139] G. Stringfellow, "Fundamental aspects of organometallic vapor phase epitaxy", *Materials Science and Engineering: B*, vol. 87, no. 2, pp. 97 –116, 2001. [Online]. Available: `http://www.sciencedirect.com/science/article/pii/S0921510701007127`.

[140] M. Krysko, G. Franssen, T. Suski, M. Albrecht, B. Lucznik, I. Grzegory, S. Krukowski, R. Czernecki, S. Grzanka, I. Makarowa, M. Leszczynski, and P. Perlin, "Correlation between luminescence and compositional striations in InGaN layers grown on miscut GaN substrates", *Applied Physics Letters*, vol. 91, no. 21, 211904, 2007. [Online]. Available: `http://scitation.aip.org/content/aip/journal/apl/91/21/10.1063/1.2815921`.

[141] V. Thévenot, V. Souliere, H. Dumont, Y. Monteil, J. Bouix, P. Regreny, and T.-M. Duc, "Behaviour of vicinal InP surfaces grown by MOVPE: exploitation of AFM images", *Journal of Crystal Growth*, vol. 170, no. 1–4, pp. 251 –256, 1997, Metalorganic Vapour Phase Epitaxy 1996. [Online]. Available: `http://www.sciencedirect.com/science/article/pii/S002202489600615X`.

[142] M. A. Moram and M. E. Vickers, "X-ray diffraction of III-nitrides", *Reports on Progress in Physics*, vol. 72, no. 3, p. 036 502, 2009. [Online]. Available: `http://stacks.iop.org/0034-4885/72/i=3/a=036502`.

[143] V. Srikant, J. S. Speck, and D. R. Clarke, “Mosaic structure in epitaxial thin films having large lattice mismatch”, *Journal of Applied Physics*, vol. 82, no. 9, pp. 4286–4295, 1997. [Online]. Available: http://scitation.aip.org/content/aip/journal/jap/82/9/10.1063/1.366235.

[144] A. D. Kurtz, S. A. Kulin, and B. L. Averbach, “Effect of dislocations on the minority carrier lifetime in semiconductors”, *Phys. Rev.*, vol. 101, pp. 1285–1291, 4 Feb. 1956. [Online]. Available: http://link.aps.org/doi/10.1103/PhysRev.101.1285.

[145] X. Zheng, H. Chen, Z. Yan, Y. Han, H. Yu, D. Li, Q. Huang, and J. Zhou, “Determination of twist angle of in-plane mosaic spread of GaN films by high-resolution X-ray diffraction”, *Journal of Crystal Growth*, vol. 255, no. 1–2, pp. 63 –67, 2003. [Online]. Available: http://www.sciencedirect.com/science/article/pii/S0022024803012119.

[146] C. Dunn and E. Kogh, “Comparison of dislocation densities of primary and secondary recrystallization grains of Si-Fe”, *Acta Metallurgica*, vol. 5, no. 10, pp. 548 –554, 1957. [Online]. Available: http://www.sciencedirect.com/science/article/pii/0001616057901220.

[147] T. Metzger, R. Höpler, E. Born, O. Ambacher, M. Stutzmann, R. Stömmer, M. Schuster, H. Göbel, S. Christiansen, M. Albrecht, and H. P. Strunk, “Defect structure of epitaxial GaN films determined by transmission electron microscopy and triple-axis X-ray diffractometry”, *Philosophical Magazine A*, vol. 77, no. 4, pp. 1013–1025, 1998. [Online]. Available: http://dx.doi.org/10.1080/01418619808221225.

[148] J. Ayers, “The measurement of threading dislocation densities in semiconductor crystals by X-ray diffraction”, *Journal of Crystal Growth*, vol. 135, no. 1–2, pp. 71 –77, 1994. [Online]. Available: http://www.sciencedirect.com/science/article/pii/0022024894907277.

[149] B Holländer, H Heer, M Wagener, H Halling, and S Mantl, “New high-precision 5-axes RBS/channeling goniometer for ion beam analysis of 150 mm wafers”, *Nuclear Instruments and Methods in Physics Research Section B: Beam Interactions with Materials and Atoms*, vol. 161–163, no. 0, pp. 227 –230, 2000. [Online]. Available: http://www.sciencedirect.com/science/article/pii/S0168583X99007478.

[150] B. Reuters, M. Finken, A. Wille, B. Holländer, M. Heuken, H. Kalisch, and A. Vescan, “Relaxation and critical strain for maximum in incorporation in AlInGaN on GaN grown by metal organic vapour phase epitaxy”, *Journal of Applied Physics*, vol. 112, no. 9, 093524, 2012. [Online]. Available: http://scitation.aip.org/content/aip/journal/jap/112/9/10.1063/1.4764342.

[151] H. Behmenburg, “Comprehensive study on MOVPE of InAlN/GaN HEMT structures and GaN nanowires”, PhD thesis, RWTH Aachen university, 2013. [Online]. Available: http://darwin.bth.rwth-aachen.de/opus3/volltexte/2013/4542/.

[152] T. Böttcher, S. Einfeldt, S. Figge, R. Chierchia, H. Heinke, D. Hommel, and J. S. Speck, “The role of high-temperature island coalescence in the development of stresses in GaN films”, *Applied Physics Letters*, vol. 78, no. 14, pp. 1976–1978, 2001. [Online]. Available: http://scitation.aip.org/content/aip/journal/apl/78/14/10.1063/1.1359780.

[153] S. Nakamura, “GaN Growth Using GaN Buffer Layer”, *Japanese Journal of Applied Physics*, vol. 30, no. Part 2, No. 10A, pp. L1705–L1707, 1991. [Online]. Available: http://jjap.jsap.jp/link?JJAP/30/L1705/.

[154] H. Amano, N. Sawaki, I. Akasaki, and Y. Toyoda, “Metalorganic vapor phase epitaxial growth of a high quality GaN film using an AlN buffer layer”, *Applied Physics Letters*, vol. 48, no. 5, pp. 353–355, 1986. [Online]. Available: http://scitation.aip.org/content/aip/journal/apl/48/5/10.1063/1.96549.

[155] D. Koleske, M. Coltrin, K. Cross, C. Mitchell, and A. Allerman, “Understanding GaN nucleation layer evolution on sapphire”, *Journal of Crystal Growth*, vol. 273, no. 1–2, pp. 86 –99, 2004. [Online]. Available: http://www.sciencedirect.com/science/article/pii/S0022024804009923.

[156] M. Miyoshi, H. Ishikawa, T. Egawa, K. Asai, M. Mouri, T. Shibata, M. Tanaka, and O. Oda, “High-electron-mobility AlGaN/AlN/GaN heterostructures grown on 100-mm-diam epitaxial AlN/sapphire templates by metalorganic vapor phase epitaxy”, *Applied Physics Letters*, vol. 85, no. 10, pp. 1710–1712, 2004. [Online]. Available: http://scitation.aip.org/content/aip/journal/apl/85/10/10.1063/1.1790073.

[157] H. Yu, M. K. Ozturk, S. Ozcelik, and E. Ozbay, “A study of semi-insulating GaN grown on AlN buffer/sapphire substrate by metalorganic chemical vapor deposition”, *Journal of Crystal Growth*, vol. 293, no. 2, pp. 273 –277, 2006. [Online]. Available: http://www.sciencedirect.com/science/article/pii/S0022024806005501.

[158] V. A. Joshkin, C. A. Parker, S. M. Bedair, J. F. Muth, I. K. Shmagin, R. M. Kolbas, E. L. Piner, and R. J. Molnar, “Effect of growth temperature on point defect density of unintentionally doped GaN grown by metalorganic chemical vapor deposition and hydride vapor phase epitaxy”, *Journal of Applied Physics*, vol. 86, no. 1, pp. 281–288, 1999. [Online]. Available: http://scitation.aip.org/content/aip/journal/jap/86/1/10.1063/1.370727.

[159] C. Mavroidis, J. J. Harris, M. J. Kappers, N. Sharma, C. J. Humphreys, and E. J. Thrush, “Observation of thermally activated conduction at a GaN-sapphire interface”, *Applied Physics Letters*, vol. 79, no. 8, pp. 1121–1123, 2001. [Online]. Available: http://scitation.aip.org/content/aip/journal/apl/79/8/10.1063/1.1395525.

[160] W. Seifert, R. Franzheld, E. Butter, H. Sobotta, and V. Riede, “On the origin of free carriers in high-conducting n-GaN”, *Crystal Research and Technology*, vol. 18, no. 3, pp. 383–390, 1983. [Online]. Available: http://dx.doi.org/10.1002/crat.2170180314.

[161] M. G. Cheong, K. S. Kim, C. S. Oh, N. W. Namgung, G. M. Yang, C.-H. Hong, K. Y. Lim, E.-K. Suh, K. S. Nahm, H. J. Lee, D. H. Lim, and A. Yoshikawa, “Conductive layer near the GaN/sapphire interface and its effect on electron transport in unintentionally doped n-type GaN epilayers”, *Applied Physics Letters*, vol. 77, no. 16, pp. 2557–2559, 2000. [Online]. Available: http://scitation.aip.org/content/aip/journal/apl/77/16/10.1063/1.1318728.

[162] C. Wetzel, T. Suski, J. W. Ager III, E. R. Weber, E. E. Haller, S. Fischer, B. K. Meyer, R. J. Molnar, and P. Perlin, “Pressure Induced Deep Gap State of Oxygen in GaN”, *Phys. Rev. Lett.*, vol. 78, pp. 3923–3926, 20 May 1997. [Online]. Available: http://link.aps.org/doi/10.1103/PhysRevLett.78.3923.

[163] C. Kim, I. K. Robinson, J. Myoung, K. Shim, M. C. Yoo, and K. Kim, “Critical thickness of GaN thin films on sapphire (0001)”, *Applied Physics Letters*, vol. 69, no. 16, pp. 2358–2360, 1996. [Online]. Available: http://scitation.aip.org/content/aip/journal/apl/69/16/10.1063/1.117524.

[164] A. D. Bykhovski, B. L. Gelmont, and M. S. Shur, “Elastic strain relaxation and piezoeffect in GaN-AlN, GaN-AlGaN and GaN-InGaN superlattices”, *Journal of Applied Physics*, vol. 81, no. 9, pp. 6332–6338, 1997. [Online]. Available: http://scitation.aip.org/content/aip/journal/jap/81/9/10.1063/1.364368.

[165] M. Higashiwaki, T. Mimura, and T. Matsui, “AlGaN/GaN Heterostructure Field-Effect Transistors on 4H-SiC Substrates with Current-Gain Cutoff Frequency of 190 GHz”, *Applied Physics Express*, vol. 1, no. 2, p. 021 103, 2008. [Online]. Available: http://stacks.iop.org/1882-0786/1/i=2/a=021103.

[166] S. Mathis, A. Romanov, L. Chen, G. Beltz, W. Pompe, and J. Speck, “Modeling of threading dislocation reduction in growing GaN layers”, *Journal of Crystal Growth*, vol. 231, no. 3, pp. 371 –390, 2001, Proceedings of the International Specialist Meeting on Bulk Nitrides and Related Techniques. [Online]. Available: http://www.sciencedirect.com/science/article/pii/S0022024801014683.

[167] I. Booker, L. Rahimzadeh Khoshroo, J. F. Woitok, V. Kaganer, C. Mauder, H. Behmenburg, J. Gruis, M. Heuken, H. Kalisch, and R. H. Jansen, “Dislocation density assessment via X-ray GaN rocking curve scans”, *physica status solidi (c)*, vol. 7, no. 7-8, pp. 1787–1789, 2010. [Online]. Available: http://dx.doi.org/10.1002/pssc.200983615.

[168] V. M. Kaganer, O. Brandt, A. Trampert, and K. H. Ploog, “X-ray diffraction peak profiles from threading dislocations in GaN epitaxial films”, *Phys. Rev. B*, vol. 72, p. 045 423, 4 Jul. 2005. [Online]. Available: http://link.aps.org/doi/10.1103/PhysRevB.72.045423.

[169] R Butté, J.-F. Carlin, E Feltin, M Gonschorek, S Nicolay, G Christmann, D Simeonov, A Castiglia, J Dorsaz, H. J. Buehlmann, S Christopoulos, G. B. H. von Högersthal, A. J. D. Grundy, M Mosca, C Pinquier, M. A. Py, F Demangeot, J Frandon, P. G. Lagoudakis, J. J. Baumberg, and N Grandjean, “Current status of AlInN layers lattice-matched to GaN for photonics and electronics”, *Journal of Physics D: Applied Physics*, vol. 40, no. 20, p. 6328, 2007. [Online]. Available: http://stacks.iop.org/0022-3727/40/i=20/a=S16.

[170] A Teke, S Gökden, R Tülek, J. H. Leach, Q Fan, J Xie, . Özgür, H Morkoç, S. B. Lisesivdin, and E Özbay, “The effect of AlN interlayer thicknesses on scattering processes in lattice-matched AlInN/GaN two-dimensional electron gas heterostructures”, *New Journal of Physics*, vol. 11, no. 6, p. 063 031, 2009. [Online]. Available: http://stacks.iop.org/1367-2630/11/i=6/a=063031.

[171] R. Tülek, A. Ilgaz, S. Gökden, A. Teke, M. K. Öztürk, M. Kasap, S. Özçelik, E. Arslan, and E. Özbay, “Comparison of the transport properties of high quality AlGaN/AlN/GaN and AlInN/AlN/GaN two-dimensional electron gas heterostructures”, *Journal of Applied Physics*, vol. 105, no. 1, 013707, 2009. [Online]. Available: http://scitation.aip.org/content/aip/journal/jap/105/1/10.1063/1.2996281.

[172] I. P. Smorchkova, L. Chen, T. Mates, L. Shen, S. Heikman, B. Moran, S. Keller, S. P. DenBaars, J. S. Speck, and U. K. Mishra, “AlN/GaN and AlGan/AlN/GaN two-dimensional electron gas structures grown by plasma-assisted molecular-beam epitaxy”, *Journal of Applied Physics*, vol. 90, no. 10, pp. 5196–5201, 2001. [Online]. Available: http://scitation.aip.org/content/aip/journal/jap/90/10/10.1063/1.1412273.

[173] M. Higashiwaki and T. Matsui, “InAlN/GaN heterostructure field-effect transistors grown by plasma-assisted molecular-beam epitaxy”, *Japanese Journal of Applied Physics*, vol. 43, no. 6B, p. L768, 2004. [Online]. Available: http://stacks.iop.org/1347-4065/43/i=6B/a=L768.

[174] Y. Cao and D. Jena, "High-mobility window for two-dimensional electron gases at ultrathin AlN/GaN heterojunctions", *Applied Physics Letters*, vol. 90, no. 18, 182112, 2007. [Online]. Available: http://scitation.aip.org/content/aip/journal/apl/90/18/10.1063/1.2736207.

[175] M. Gonschorek, J.-F. Carlin, E. Feltin, M. A. Py, and N. Grandjean, "High electron mobility lattice-matched AlInN/GaN field-effect transistor heterostructures", *Applied Physics Letters*, vol. 89, no. 6, 062106, 2006. [Online]. Available: http://scitation.aip.org/content/aip/journal/apl/89/6/10.1063/1.2335390.

[176] N. Grandjean and J. Massies, "GaN and AlGaN molecular beam epitaxy monitored by reflection high-energy electron diffraction", *Applied Physics Letters*, vol. 71, no. 13, pp. 1816–1818, 1997. [Online]. Available: http://scitation.aip.org/content/aip/journal/apl/71/13/10.1063/1.119408.

[177] K. Jeganathan, T. Ide, M. Shimizu, and H. Okumura, "Strain relaxation correlated with the transport properties of AlN/GaN heterostructure grown by plasma-assisted molecular-beam epitaxy", *Journal of Applied Physics*, vol. 93, no. 4, pp. 2047–2050, 2003. [Online]. Available: http://scitation.aip.org/content/aip/journal/jap/93/4/10.1063/1.1537458.

[178] A. Kondratyev, R. Talalaev, W. Lundin, A. Sakharov, A. Tsatsul'nikov, E. Zavarin, A. Fomin, and D. Sizov, "Aluminum incorporation control in AlGaN MOVPE: experimental and modeling study", *Journal of Crystal Growth*, vol. 272, no. 1–4, pp. 420 –425, 2004, The Twelfth International Conference on Metalorganic Vapor Phase Epitaxy. [Online]. Available: http://www.sciencedirect.com/science/article/pii/S0022024804011418.

[179] J. Stellmach, M. Pristovsek, . Sava, J. Schlegel, E. Yakovlev, and M. Kneissl, "High aluminium content and high growth rates of AlGaN in a close-coupled showerhead MOVPE reactor", *Journal of Crystal Growth*, vol. 315, no. 1, pp. 229 –232, 2011, 15th International Conference on Metalorganic Vapor Phase Epitaxy ICMOVPE-XV. [Online]. Available: http://www.sciencedirect.com/science/article/pii/S0022024810004367.

[180] J. E. Northrup, L. T. Romano, and J. Neugebauer, "Surface energetics, pit formation, and chemical ordering in InGaN alloys", *Applied Physics Letters*, vol. 74, no. 16, pp. 2319–2321, 1999. [Online]. Available: http://scitation.aip.org/content/aip/journal/apl/74/16/10.1063/1.123837.

[181] T. Sadler, M. Kappers, and R. Oliver, "The effect of temperature and ammonia flux on the surface morphology and composition of InAlN epitaxial layers", *Journal of Crystal Growth*, vol. 311, no. 13, pp. 3380 –3385, 2009. [Online]. Available: http://www.sciencedirect.com/science/article/pii/S002202480900414X.

[182] A. Yamamoto, Y. Murakami, K. Koide, M. Adachi, and A. Hashimoto, “Growth temperature dependences of MOVPE InN on sapphire substrates”, *physica status solidi (b)*, vol. 228, no. 1, pp. 5–8, 2001. [Online]. Available: `http://dx.doi.org/10.1002/1521-3951(200111)228:1<5::AID-PSSB5>3.0.CO;2-E`.

[183] A. Yamamoto, M. Adachi, and A. Hashimoto, “Enhanced two-dimensional growth of MOVPE InN films on sapphire substrates”, *Journal of Crystal Growth*, vol. 230, no. 3–4, pp. 351 –356, 2001, Proceedings of the Fourth European Workshop on Gallium Nitride. [Online]. Available: `http://www.sciencedirect.com/science/article/pii/S0022024801012611`.

[184] N. Yoshimoto, T. Matsuoka, T. Sasaki, and A. Katsui, “Photoluminescence of InGaN films grown at high temperature by metalorganic vapor phase epitaxy”, *Applied Physics Letters*, vol. 59, no. 18, pp. 2251–2253, 1991. [Online]. Available: `http://scitation.aip.org/content/aip/journal/apl/59/18/10.1063/1.106086`.

[185] J. Leitner, J. Stejskal, and P. Vonka, “Thermodynamic modeling of AlGaInN growth by MOVPE”, *Journal of Crystal Growth*, vol. 267, no. 1–2, pp. 8 –16, 2004. [Online]. Available: `http://www.sciencedirect.com/science/article/pii/S0022024804003318`.

[186] J. Creighton, G. T. Wang, W. G. Breiland, and M. E. Coltrin, “Nature of the parasitic chemistry during AlGaInN OMVPE”, *Journal of Crystal Growth*, vol. 261, no. 2–3, pp. 204 –213, 2004, Proceedings of the 11th Biennial (US) Workshop on Organometallic Vapor Phase Epitaxy (OMVPE). [Online]. Available: `http://www.sciencedirect.com/science/article/pii/S0022024803020128`.

[187] A. Lobanova, K. Mazaev, R. Talalaev, M. Leys, S. Boeykens, K. Cheng, and S. Degroote, “Effect of V/III ratio in AlN and AlGaN MOVPE”, *Journal of Crystal Growth*, vol. 287, no. 2, pp. 601 –604, 2006, The 16th American Conference on Crystal Growth and Epitaxy ACCGE, The 12th Biennial Workshop on OMVPE OMVPE. [Online]. Available: `http://www.sciencedirect.com/science/article/pii/S0022024805012248`.

[188] F. Nakamura, S. Hashimoto, M. Hara, S. Imanaga, M. Ikeda, and H. Kawai, “AlN and AlGaN growth using low-pressure metalorganic chemical vapor deposition”, *Journal of Crystal Growth*, vol. 195, no. 1–4, pp. 280 –285, 1998. [Online]. Available: `http://www.sciencedirect.com/science/article/pii/S002202489800668X`.

[189] T. Matsuoka, “Calculation of unstable mixing region in wurtzite InGaAlN”, *Applied Physics Letters*, vol. 71, no. 1, pp. 105–106, 1997. [Online]. Available: `http://scitation.aip.org/content/aip/journal/apl/71/1/10.1063/1.119440`.

[190] V. Deibuk and A. Voznyi, “Thermodynamic stability and redistribution of charges in ternary AlGaN, InGaN, and InAlN alloys”, English, *Semiconductors*, vol. 39, no. 6, pp. 623 –628, 2005. [Online]. Available: `http://dx.doi.org/10.1134/1.1944849`.

[191] S. Y. Karpov, N. I. Podolskaya, I. A. Zhmakin, and A. I. Zhmakin, “Statistical model of ternary group-III nitrides”, *Phys. Rev. B*, vol. 70, p. 235 203, 23 Dec. 2004. [Online]. Available: `http://link.aps.org/doi/10.1103/PhysRevB.70.235203`.

[192] M. Ferhat and F. Bechstedt, “First-principles calculations of gap bowing in InGaN and InAlN alloys: relation to structural and thermodynamic properties”, *Phys. Rev. B*, vol. 65, p. 075 213, 7 Feb. 2002. [Online]. Available: `http://link.aps.org/doi/10.1103/PhysRevB.65.075213`.

[193] B. P. Burton, A. van de Walle, and U. Kattner, “First principles phase diagram calculations for the wurtzite-structure systems AlN–GaN, GaN–InN, and AlN–InN”, *Journal of Applied Physics*, vol. 100, no. 11, 113528, 2006. [Online]. Available: `http://scitation.aip.org/content/aip/journal/jap/100/11/10.1063/1.2372309`.

[194] T. Takayama, M. Yuri, K. Itoh, T. Baba, and J. Harris, “Analysis of phase-separation region in wurtzite group III nitride quaternary material system using modified valence force field model”, *Journal of Crystal Growth*, vol. 222, no. 1–2, pp. 29 –37, 2001. [Online]. Available: `http://www.sciencedirect.com/science/article/pii/S0022024800008691`.

[195] C. Hums, J. Bläsing, A. Dadgar, A. Diez, T. Hempel, J. Christen, A. Krost, K. Lorenz, and E. Alves, “Metal-organic vapor phase epitaxy and properties of AlInN in the whole compositional range”, *Applied Physics Letters*, vol. 90, no. 2, 022105, 2007. [Online]. Available: `http://scitation.aip.org/content/aip/journal/apl/90/2/10.1063/1.2424649`.

[196] X. A. Cao and Y. Yang, “Electroluminescence observation of nanoscale phase separation in quaternary AlInGaN light-emitting diodes”, *Applied Physics Letters*, vol. 96, no. 15, 151109, 2010. [Online]. Available: `http://scitation.aip.org/content/aip/journal/apl/96/15/10.1063/1.3397987`.

[197] S. Yu, S. Chang, R. Lin, Y. Lin, Y. Lu, S. Chang, and Y. Chiou, “Growth of quaternary AlInGaN with various TMI molar rates”, *Journal of Crystal Growth*, vol. 312, no. 12–13, pp. 1920 –1924, 2010. [Online]. Available: `http://www.sciencedirect.com/science/article/pii/S0022024810002149`.

[198] C. H. Chen, L. Y. Huang, Y. F. Chen, H. X. Jiang, and J. Y. Lin, "Mechanism of enhanced luminescence in InAlGaN quaternary alloys", *Applied Physics Letters*, vol. 80, no. 8, pp. 1397–1399, 2002. [Online]. Available: http://scitation.aip.org/content/aip/journal/apl/80/8/10.1063/1.1455147.

[199] C. H. Chen, Y. F. Chen, Z. H. Lan, L. C. Chen, K. H. Chen, H. X. Jiang, and J. Y. Lin, "Mechanism of enhanced luminescence in InAlGaN quaternary epilayers", *Applied Physics Letters*, vol. 84, no. 9, pp. 1480–1482, 2004. [Online]. Available: http://scitation.aip.org/content/aip/journal/apl/84/9/10.1063/1.1650549.

[200] J. P. Liu, R. Q. Jin, J. C. Zhang, J. F. Wang, M Wu, J. J. Zhu, D. G. Zhao, Y. T. Wang, and H Yang, "Indium mole fraction effect on the structural and optical properties of quaternary AlInGaN epilayers", *Journal of Physics D: Applied Physics*, vol. 37, no. 15, p. 2060, 2004. [Online]. Available: http://stacks.iop.org/0022-3727/37/i=15/a=003.

[201] I. Gorczyca, S. P. Łepkowski, T. Suski, N. E. Christensen, and A. Svane, "Influence of indium clustering on the band structure of semiconducting ternary and quaternary nitride alloys", *Phys. Rev. B*, vol. 80, p. 075 202, 7 Aug. 2009. [Online]. Available: http://link.aps.org/doi/10.1103/PhysRevB.80.075202.

[202] A. Fischer, H. Kühne, and H. Richter, "New approach in equilibrium theory for strained layer relaxation", *Phys. Rev. Lett.*, vol. 73, pp. 2712–2715, 20 Nov. 1994. [Online]. Available: http://link.aps.org/doi/10.1103/PhysRevLett.73.2712.

[203] R. People and J. C. Bean, "Calculation of critical layer thickness versus lattice mismatch for GeSi/Si strained-layer heterostructures", *Applied Physics Letters*, vol. 47, no. 3, pp. 322–324, 1985. [Online]. Available: http://scitation.aip.org/content/aip/journal/apl/47/3/10.1063/1.96206.

[204] D. Holec, P. Costa, M. Kappers, and C. Humphreys, "Critical thickness calculations for InGaN/GaN", *Journal of Crystal Growth*, vol. 303, no. 1, pp. 314 –317, 2007, Proceedings of the Fifth Workshop on Modeling in Crystal Growth IWMCG-5. [Online]. Available: http://www.sciencedirect.com/science/article/pii/S002202480601623X.

[205] K. Lorenz, N. Franco, E. Alves, S. Pereira, I. Watson, R. Martin, and K. O'Donnell, "Relaxation of compressively strained AlInN on GaN", *Journal of Crystal Growth*, vol. 310, no. 18, pp. 4058 –4064, 2008. [Online]. Available: http://www.sciencedirect.com/science/article/pii/S0022024808005587.

[206] A. Polian, M. Grimsditch, and I. Grzegory, "Elastic constants of gallium nitride", *Journal of Applied Physics*, vol. 79, no. 6, pp. 3343–3344, 1996. [Online]. Available: `http://scitation.aip.org/content/aip/journal/jap/79/6/10.1063/1.361236`.

[207] A. F. Wright, "Elastic properties of zinc-blende and wurtzite AlN, GaN, and InN", *Journal of Applied Physics*, vol. 82, no. 6, pp. 2833–2839, 1997. [Online]. Available: `http://scitation.aip.org/content/aip/journal/jap/82/6/10.1063/1.366114`.

[208] F. M. Morales, J. M. Mánuel, R García, B Reuters, H Kalisch, and A Vescan, "Evaluation of interpolations of InN, AlN and GaN lattice and elastic constants for their ternary and quaternary alloys", *Journal of Physics D: Applied Physics*, vol. 46, no. 24, p. 245 502, 2013. [Online]. Available: `http://stacks.iop.org/0022-3727/46/i=24/a=245502`.

[209] M. Lopuszynski and J. A. Majewski, "Composition dependence of elastic constants in wurtzite AlGaInN alloys", *Journal of Applied Physics*, vol. 111, no. 3, 033502, 2012. [Online]. Available: `http://scitation.aip.org/content/aip/journal/jap/111/3/10.1063/1.3678002`.

[210] R. A. Oliver, M. J. Kappers, C. J. Humphreys, and G. A. D. Briggs, "Growth modes in heteroepitaxy of InGaN on GaN", *Journal of Applied Physics*, vol. 97, no. 1, 013707, 2005. [Online]. Available: `http://scitation.aip.org/content/aip/journal/jap/97/1/10.1063/1.1823581`.

[211] S. M. de Sousa Pereira, K. P. O'Donnell, and E. J. da Costa Alves, "Role of nanoscale strain inhomogeneity on the light emission from InGaN epilayers", *Advanced Functional Materials*, vol. 17, no. 1, pp. 37–42, 2007. [Online]. Available: `http://dx.doi.org/10.1002/adfm.200600650`.

[212] Y. Liu, T. Egawa, H. Ishikawa, B. Zhang, and M. Hao, "Influence of growth temperature on quaternary AlInGaN epilayers for ultraviolet emission grown by metalorganic chemical vapor deposition", *Japanese Journal of Applied Physics*, vol. 43, no. 5R, p. 2414, 2004. [Online]. Available: `http://stacks.iop.org/1347-4065/43/i=5R/a=2414`.

[213] J.-P. Ahl, J. Hertkorn, H. Koch, B. Galler, B. Michel, M. Binder, and B. Hollnder, "Morphology, growth mode and indium incorporation of MOVPE grown InGaN and AlInGaN: a comparison", *Journal of Crystal Growth*, vol. 398, no. 0, pp. 33 –39, 2014. [Online]. Available: `http://www.sciencedirect.com/science/article/pii/S0022024814002619`.

[214] G. S. Bales and A. Zangwill, “Morphological instability of a terrace edge during step-flow growth”, *Phys. Rev. B*, vol. 41, pp. 5500–5508, 9 May 1990. [Online]. Available: http://link.aps.org/doi/10.1103/PhysRevB.41.5500.

[215] M. Rusanen, I. Koponen, and J. Kallunki, “Mixing length scales: step meandering and island nucleation on vicinal surfaces”, English, *The European Physical Journal B - Condensed Matter and Complex Systems*, vol. 36, no. 1, pp. 141–147, 2003. [Online]. Available: http://dx.doi.org/10.1140/epjb/e2003-00327-8.

[216] P. Boguslawski, K. Rapcewicz, and J. J. Bernholc, “Surface segregation and interface stability of AlN/GaN, GaN/InN, and AlN/InN (0001) epitaxial systems”, *Phys. Rev. B*, vol. 61, pp. 10 820–10 826, 16 Apr. 2000. [Online]. Available: http://link.aps.org/doi/10.1103/PhysRevB.61.10820.

[217] U. Großner, J. Furthmüller, and F. Bechstedt, “Initial stages of III-nitride growth”, *Applied Physics Letters*, vol. 74, no. 25, pp. 3851–3853, 1999. [Online]. Available: http://scitation.aip.org/content/aip/journal/apl/74/25/10.1063/1.124201.

[218] S. Pereira, M. R. Correia, E. Pereira, K. P. O’Donnell, C. Trager-Cowan, F. Sweeney, and E. Alves, “Compositional pulling effects in InGaN/GaN layers: a combined depth-resolved cathodoluminescence and Rutherford backscattering / channeling study”, *Phys. Rev. B*, vol. 64, p. 205 311, 20 Nov. 2001. [Online]. Available: http://link.aps.org/doi/10.1103/PhysRevB.64.205311.

[219] G. Stringfellow, “Microstructures produced during the epitaxial growth of InGaN alloys”, *Journal of Crystal Growth*, vol. 312, no. 6, pp. 735 –749, 2010. [Online]. Available: http://www.sciencedirect.com/science/article/pii/S0022024809011014.

[220] M. Finken, A. Wille, B. Reuters, B. Holländer, M. Heuken, H. Kalisch, and A. Vescan, “Growth properties and electrochemical characterization of InGaN photoanodes with different In concentrations”, *physica status solidi (c)*, vol. 11, no. 3-4, pp. 746–749, 2014. [Online]. Available: http://dx.doi.org/10.1002/pssc.201300414.

[221] M. E. Vickers, M. J. Kappers, T. M. Smeeton, E. J. Thrush, J. S. Barnard, and C. J. Humphreys, “Determination of the indium content and layer thicknesses in InGaN/GaN quantum wells by X-ray scattering”, *Journal of Applied Physics*, vol. 94, no. 3, pp. 1565–1574, 2003. [Online]. Available: http://scitation.aip.org/content/aip/journal/jap/94/3/10.1063/1.1587251.

[222] B. Jogai, “Effect of in-plane biaxial strains on the band structure of wurtzite GaN”, *Phys. Rev. B*, vol. 57, pp. 2382–2386, 4 Jan. 1998. [Online]. Available: http://link.aps.org/doi/10.1103/PhysRevB.57.2382.

[223] B. Reuters, A. Wille, N. Ketteniss, H. Hahn, B. Holländer, M. Heuken, H. Kalisch, and A. Vescan, “Polarization-engineered enhancement-mode high-electron-mobility transistors using quaternary AlInGaN barrier layers”, English, *Journal of Electronic Materials*, vol. 42, no. 5, pp. 826–832, 2013. [Online]. Available: `http://dx.doi.org/10.1007/s11664-013-2473-7`.

[224] M. Marques, L. K. Teles, L. M. R. Scolfaro, L. G. Ferreira, and J. R. Leite, “Microscopic description of the phase separation process in AlGaInN quaternary alloys”, *Phys. Rev. B*, vol. 70, p. 073 202, 7 Aug. 2004. [Online]. Available: `http://link.aps.org/doi/10.1103/PhysRevB.70.073202`.

[225] S. Nagarajan, T. S. Oh, M. S. Kumar, C.-H. Hong, and E.-K. Suh, “Structural and optical properties of In-rich InAlGaN/InGaN heterostructures for white light emission”, *Japanese Journal of Applied Physics*, vol. 47, no. 6R, p. 4413, 2008. [Online]. Available: `http://stacks.iop.org/1347-4065/47/i=6R/a=4413`.

[226] S Nagarajan, Y. S. Lee, M. S. Kumar, O. H. Cha, C.-H. Hong, and E.-K. Suh, “White light generation from In-rich InAlGaN/InGaN heterostructures”, *Journal of Physics D: Applied Physics*, vol. 41, no. 1, p. 012 001, 2008. [Online]. Available: `http://stacks.iop.org/0022-3727/41/i=1/a=012001`.

[227] W. Jiao, W. Kong, J. Li, K. Collar, T.-H. Kim, and A. S. Brown, “The relationship between depth-resolved composition and strain relaxation in InAlN and InGaN films grown by molecular beam epitaxy”, *Applied Physics Letters*, vol. 103, no. 16, 162102, 2013. [Online]. Available: `http://scitation.aip.org/content/aip/journal/apl/103/16/10.1063/1.4825143`.

[228] H. K. Cho, J. Y. Lee, and G. M. Yang, “Characterization of pit formation in III-nitrides grown by metalorganic chemical vapor deposition”, *Applied Physics Letters*, vol. 80, no. 8, pp. 1370–1372, 2002. [Online]. Available: `http://scitation.aip.org/content/aip/journal/apl/80/8/10.1063/1.1454215`.

[229] I.-H. Kim, H.-S. Park, Y.-J. Park, and T. Kim, “Formation of V-shaped pits in InGaN/GaN multiquantum wells and bulk InGaN films”, *Applied Physics Letters*, vol. 73, no. 12, pp. 1634–1636, 1998. [Online]. Available: `http://scitation.aip.org/content/aip/journal/apl/73/12/10.1063/1.122229`.

[230] H. K. Cho, K. H. Lee, S. W. Kim, K. S. Park, Y.-H. Cho, and J. H. Lee, “Influence of growth temperature and reactor pressure on microstructural and optical properties of InAlGaN quaternary epilayers”, *Journal of Crystal Growth*, vol. 267, no. 1–2, pp. 67 –73, 2004. [Online]. Available: `http://www.sciencedirect.com/science/article/pii/S0022024804003690`.

[231] J. P. Liu, Y. T. Wang, H. Yang, D. S. Jiang, U. Jahn, and K. H. Ploog, "Investigations on V-defects in quaternary AlInGaN epilayers", *Applied Physics Letters*, vol. 84, no. 26, pp. 5449–5451, 2004. [Online]. Available: http://scitation.aip.org/content/aip/journal/apl/84/26/10.1063/1.1767959.

[232] L. Naixin, W. Junxi, Y. Jianchang, L. Zhe, R. Jun, and L. Jinmin, "Characterization of quaternary AlInGaN epilayers and polarization-reduced InGaN/AlInGaN MQW grown by MOCVD", *Journal of Semiconductors*, vol. 30, no. 11, p. 113 003, 2009. [Online]. Available: http://stacks.iop.org/1674-4926/30/i=11/a=113003.

[233] C. B. Soh, S. J. Chua, S. Tripathy, S. Y. Chow, D. Z. Chi, and W. Liu, "Influence of composition pulling effect on the two-dimensional electron gas formed at AlInGaN/GaN interface", *Journal of Applied Physics*, vol. 98, no. 10, 103704, 2005. [Online]. Available: http://scitation.aip.org/content/aip/journal/jap/98/10/10.1063/1.2132090.

[234] H Lahrèche, P Vennéguès, B Beaumont, and P Gibart, "Growth of high-quality GaN by low-pressure metal-organic vapour phase epitaxy (LP-MOVPE) from 3D islands and lateral overgrowth", *Journal of Crystal Growth*, vol. 205, no. 3, pp. 245 –252, 1999. [Online]. Available: http://www.sciencedirect.com/science/article/pii/S0022024899002997.

[235] B. Reuters, J. Strate, H. Hahn, M. Finken, A. Wille, M. Heuken, H. Kalisch, and A. Vescan, "Selective MOVPE of InGaN-based LED structures on non-planar Si (111) facets of patterned Si (100) substrates", *Journal of Crystal Growth*, vol. 391, no. 0, pp. 33 –40, 2014. [Online]. Available: http://www.sciencedirect.com/science/article/pii/S0022024814000050.

[236] T. Kehagias, G. P. Dimitrakopulos, J. Kioseoglou, H. Kirmse, C. Giesen, M. Heuken, A. Georgakilas, W. Neumann, T. Karakostas, and P. Komninou, "Indium migration paths in V-defects of InAlN grown by metal-organic vapor phase epitaxy", *Applied Physics Letters*, vol. 95, no. 7, 071905, 2009. [Online]. Available: http://scitation.aip.org/content/aip/journal/apl/95/7/10.1063/1.3204454.

[237] A. Minj, D. Cavalcoli, and A. Cavallini, "Indium segregation in AlInN/AlN/GaN heterostructures", *Applied Physics Letters*, vol. 97, no. 13, 132114, 2010. [Online]. Available: http://scitation.aip.org/content/aip/journal/apl/97/13/10.1063/1.3489433.

[238] L. Rahimzadeh Khoshroo, N. Ketteniss, C. Mauder, H. Behmenburg, J. F. Woitok, I. Booker, J. Gruis, M. Heuken, A. Vescan, H. Kalisch, and R. H. Jansen, "Quaternary nitride heterostructure field effect transistors", *physica status solidi (c)*, vol. 7,

no. 7-8, pp. 2001–2003, 2010. [Online]. Available: http://dx.doi.org/10.1002/pssc.200983614.

[239] J. Xie, X. Ni, M. Wu, J. H. Leach, m. Özgür, and H. Morkoç, "High electron mobility in nearly lattice-matched AlInN/AlN/GaN heterostructure field effect transistors", *Applied Physics Letters*, vol. 91, no. 13, 132116, 2007. [Online]. Available: http://scitation.aip.org/content/aip/journal/apl/91/13/10.1063/1.2794419.

[240] A. Dadgar, F. Schulze, J. Bläsing, A. Diez, A. Krost, M. Neuburger, E. Kohn, I. Daumiller, and M. Kunze, "High-sheet-charge–carrier-density AlInN/GaN field-effect transistors on Si(111)", *Applied Physics Letters*, vol. 85, no. 22, pp. 5400–5402, 2004. [Online]. Available: http://scitation.aip.org/content/aip/journal/apl/85/22/10.1063/1.1828580.

[241] A. M. Dabiran, A. M. Wowchak, A. Osinsky, J. Xie, B. Hertog, B. Cui, D. C. Look, and P. P. Chow, "Very high channel conductivity in low-defect AlN/GaN high electron mobility transistor structures", *Applied Physics Letters*, vol. 93, no. 8, 082111, 2008. [Online]. Available: http://scitation.aip.org/content/aip/journal/apl/93/8/10.1063/1.2970991.

[242] B. Reuters, A. Wille, B. Holländer, E. Sakalauskas, N. Ketteniss, C. Mauder, R. Goldhahn, M. Heuken, H. Kalisch, and A. Vescan, "Growth studies on quaternary AlInGaN layers for HEMT application", English, *Journal of Electronic Materials*, vol. 41, no. 5, pp. 905–909, 2012. [Online]. Available: http://dx.doi.org/10.1007/s11664-012-1989-6.

[243] Y. Liu, H. Jiang, S. Arulkumaran, T. Egawa, B. Zhang, and H. Ishikawa, "Demonstration of undoped quaternary AlInGaN/GaN heterostructure field-effect transistor on sapphire substrate", *Applied Physics Letters*, vol. 86, no. 22, pp. 223 510–223510–3, May 2005.

[244] Y. Liu, T. Egawa, H. Jiang, B. Zhang, and H. Ishikawa, "Novel quaternary AlInGaN/GaN heterostructure field effect transistors on sapphire substrate", *Japanese Journal of Applied Physics*, vol. 45, no. 7R, p. 5728, 2006. [Online]. Available: http://stacks.iop.org/1347-4065/45/i=7R/a=5728.

[245] T. Lim, R. Aidam, L. Kirste, P. Waltereit, R. Quay, S. Müller, and O. Ambacher, "Compositional variation of nearly lattice-matched InAlGaN alloys for high electron mobility transistors", *Applied Physics Letters*, vol. 96, no. 25, 252108, 2010. [Online]. Available: http://scitation.aip.org/content/aip/journal/apl/96/25/10.1063/1.3456561.

[246] C. Skierbiszewski, K. Dybko, W. Knap, M. Siekacz, W. Krupczyski, G. Nowak, M. Bokowski, J. usakowski, Z. R. Wasilewski, D. Maude, T. Suski, and S. Porowski, "High mobility two-dimensional electron gas in AlGaN/GaN heterostructures grown on bulk GaN by plasma assisted molecular beam epitaxy", *Applied Physics Letters*, vol. 86, no. 10, 102106, 2005. [Online]. Available: http://scitation.aip.org/content/aip/journal/apl/86/10/10.1063/1.1873056.

[247] J. Chung, W. E. Hoke, E. Chumbes, and T. Palacios, "AlGaN/GaN HEMT with 300-GHz f_{max}", *Electron Device Letters, IEEE*, vol. 31, no. 3, pp. 195–197, Mar. 2010.

[248] V. Jain, *Physics of semiconductors devices*. Springer, 2014.

[249] N Ketteniss, A Askar, B Reuters, A Noculak, B Holländer, H Kalisch, and A Vescan, "Polarization-reduced quaternary InAlGaN/GaN HFET and MISHFET devices", *Semiconductor Science and Technology*, vol. 27, no. 5, p. 055 012, 2012. [Online]. Available: http://stacks.iop.org/0268-1242/27/i=5/a=055012.

[250] M. N. Gurusinghe, S. K. Davidsson, and T. G. Andersson, "Two-dimensional electron mobility limitation mechanisms in AlGaN/GaN heterostructures", *Phys. Rev. B*, vol. 72, p. 045 316, 4 Jul. 2005. [Online]. Available: http://link.aps.org/doi/10.1103/PhysRevB.72.045316.

[251] D. Jena, Y. Smorchkova, C. Elsass, A. C. Gossard, and U. K. Mishra, "Electron transport and intrinsic mobility limits in two-dimensional electron gases of III-V nitride heterostructures", *eprint arXiv:cond-mat/0103461*, Mar. 2001, Provided by the SAO/NASA Astrophysics Data System. [Online]. Available: http://adsabs.harvard.edu/abs/2001cond.mat..3461J.

[252] J. Antoszewski, M. Gracey, J. M. Dell, L. Faraone, T. A. Fisher, G. Parish, Y.-F. Wu, and U. K. Mishra, "Scattering mechanisms limiting two-dimensional electron gas mobility in $Al_{0.25}Ga_{0.75}N$/GaN modulation-doped field-effect transistors", *Journal of Applied Physics*, vol. 87, no. 8, pp. 3900–3904, 2000. [Online]. Available: http://scitation.aip.org/content/aip/journal/jap/87/8/10.1063/1.372432.

[253] A. Vescan, H. Hahn, B. Reuters, and H. Kalisch, "Novel GaN-based transistors using polarization engineering", in *10th International Conference on Advanced Semiconductor Devices Microsystems (ASDAM)*, Oct. 2014, pp. 1–4.

[254] H. Hahn, B. Reuters, A. Wille, N. Ketteniss, F. Benkhelifa, O. Ambacher, H. Kalisch, and A. Vescan, "First polarization-engineered compressively strained AlInGaN barrier enhancement-mode MISHFET", *Semiconductor Science and Technology*, vol. 27, no. 5, p. 055 004, 2012. [Online]. Available: http://stacks.iop.org/0268-1242/27/i=5/a=055004.

[255] R. Dietrich, *AlGaN/GaN HEMTs für HF-Leistungsanwendungen*. Shaker, 2001.

[256] N. Ketteniss, B. Reuters, B. Hollander, H. Hahn, H. Kalisch, and A. Vescan, "Quaternary nitride enhancement mode HFET with 260 mS/mm and a threshold voltage of +0.5 V", in *Device Research Conference (DRC), 2012 70th Annual*, Jun. 2012, pp. 161–162.

[257] S. Nakazawa, T. Ueda, K. Inoue, T. Tanaka, H. Ishikawa, and T. Egawa, "Recessed-gate AlGaN/GaN HFETs with lattice-matched InAlGaN quaternary alloy capping layers", *Electron Devices, IEEE Transactions on*, vol. 52, no. 10, pp. 2124–2128, 2005.

[258] P. Solomon and H. Morkoc, "Modulation-doped GaAs/AlGaAs heterojunction field-effect transistors (MODFETs), ultrahigh-speed device for supercomputers", *Electron Devices, IEEE Transactions on*, vol. 31, no. 8, pp. 1015–1027, Aug. 1984.

[259] A. Ketterson, W. Masselink, J. Gedymin, J. Klem, C.-K. Peng, W. Kopp, H. Morkoc, and K. Gleason, "Characterization of InGaAs/AlGaAs pseudomorphic modulation-doped field-effect transistors", *Electron Devices, IEEE Transactions on*, vol. 33, no. 5, pp. 564–571, May 1986.

[260] N. Ketteniss, "GaN-based heterostructure field effect transistors with ternary and quaternary InAlGaN barrier layers", PhD thesis, RWTH Aachen university, 2013. [Online]. Available: `http://darwin.bth.rwth-aachen.de/opus3/volltexte/2013/4609/`.

[261] N. Koide, H. Kato, M. Sassa, S. Yamasaki, K. Manabe, M. Hashimoto, H. Amano, K. Hiramatsu, and I. Akasaki, "Doping of GaN with Si and properties of blue m/i/n/n+ GaN LED with Si-doped n+-layer by MOVPE", *Journal of Crystal Growth*, vol. 115, no. 1–4, pp. 639 –642, 1991. [Online]. Available: `http://www.sciencedirect.com/science/article/pii/002202489190818P`.

[262] L. B. Rowland, K. Doverspike, and D. K. Gaskill, "Silicon doping of GaN using disilane", *Applied Physics Letters*, vol. 66, no. 12, pp. 1495–1497, 1995. [Online]. Available: `http://scitation.aip.org/content/aip/journal/apl/66/12/10.1063/1.113666`.

[263] D. Seghier and H. P. Gislason, "Electrical characterization of Mg-related energy levels and the compensation mechanism in GaN:Mg", *Journal of Applied Physics*, vol. 88, no. 11, pp. 6483–6487, 2000. [Online]. Available: `http://scitation.aip.org/content/aip/journal/jap/88/11/10.1063/1.1312834`.

[264] T. Tanaka, A. Watanabe, H. Amano, Y. Kobayashi, I. Akasaki, S. Yamazaki, and M. Koike, "P-type conduction in Mg-doped GaN and AlGaN grown by metalorganic vapor phase epitaxy", *Applied Physics Letters*, vol. 65, no. 5, pp. 593–594, 1994. [Online]. Available: http://scitation.aip.org/content/aip/journal/apl/65/5/10.1063/1.112309.

[265] J. W. Huang, T. F. Kuech, H. Lu, and I. Bhat, "Electrical characterization of Mg-doped GaN grown by metalorganic vapor phase epitaxy", *Applied Physics Letters*, vol. 68, no. 17, pp. 2392–2394, 1996. [Online]. Available: http://scitation.aip.org/content/aip/journal/apl/68/17/10.1063/1.116144.

[266] W. Götz, N. M. Johnson, J. Walker, D. P. Bour, and R. A. Street, "Activation of acceptors in Mg-doped GaN grown by metalorganic chemical vapor deposition", *Applied Physics Letters*, vol. 68, no. 5, pp. 667–669, 1996. [Online]. Available: http://scitation.aip.org/content/aip/journal/apl/68/5/10.1063/1.116503.

[267] C. Johnson, J. Y. Lin, H. X. Jiang, M. A. Khan, and C. J. Sun, "Metastability and persistent photoconductivity in Mg-doped p-type GaN", *Applied Physics Letters*, vol. 68, no. 13, pp. 1808–1810, 1996. [Online]. Available: http://scitation.aip.org/content/aip/journal/apl/68/13/10.1063/1.116020.

[268] W. Götz, N. M. Johnson, and D. P. Bour, "Deep level defects in Mg-doped, p-type GaN grown by metalorganic chemical vapor deposition", *Applied Physics Letters*, vol. 68, no. 24, pp. 3470–3472, 1996. [Online]. Available: http://scitation.aip.org/content/aip/journal/apl/68/24/10.1063/1.116075.

[269] J. Yang, D. G. Zhao, D. S. Jiang, P. Chen, Z. S. Liu, L. C. Le, X. J. Li, X. G. He, J. P. Liu, S. M. Zhang, H. Wang, J. J. Zhu, and H. Yang, "Investigation on the compensation effect of residual carbon impurities in low temperature grown Mg doped GaN films", *Journal of Applied Physics*, vol. 115, no. 16, 163704, 2014. [Online]. Available: http://scitation.aip.org/content/aip/journal/jap/115/16/10.1063/1.4873957.

[270] J. Neugebauer and C. G. Van de Walle, "Role of hydrogen in doping of GaN", *Applied Physics Letters*, vol. 68, no. 13, pp. 1829–1831, 1996. [Online]. Available: http://scitation.aip.org/content/aip/journal/apl/68/13/10.1063/1.116027.

[271] D. Koleske, A. Wickenden, R. Henry, and M. Twigg, "Influence of MOVPE growth conditions on carbon and silicon concentrations in GaN", *Journal of Crystal Growth*, vol. 242, no. 1–2, pp. 55 –69, 2002. [Online]. Available: http://www.sciencedirect.com/science/article/pii/S0022024802013489.

[272] J. Neugebauer and C. G. Van de Walle, "Gallium vacancies and the yellow luminescence in GaN", *Applied Physics Letters*, vol. 69, no. 4, pp. 503–505, 1996. [Online]. Available: http://scitation.aip.org/content/aip/journal/apl/69/4/10.1063/1.117767.

[273] T. Mattila and R. M. Nieminen, "Ab initio study of oxygen point defects in GaAs, GaN and AlN", *Phys. Rev. B*, vol. 54, pp. 16 676–16 682, 23 Dec. 1996. [Online]. Available: http://link.aps.org/doi/10.1103/PhysRevB.54.16676.

[274] J. C. Zolper, R. G. Wilson, S. J. Pearton, and R. A. Stall, "Ca and O ion implantation doping of GaN", *Applied Physics Letters*, vol. 68, no. 14, pp. 1945–1947, 1996. [Online]. Available: http://scitation.aip.org/content/aip/journal/apl/68/14/10.1063/1.115634.

[275] J. L. Lyons, A. Janotti, and C. G. Van de Walle, "Carbon impurities and the yellow luminescence in GaN", *Applied Physics Letters*, vol. 97, no. 15, p. 152 108, 2010. [Online]. Available: http://scitation.aip.org/content/aip/journal/apl/97/15/10.1063/1.3492841.

[276] S. Kato, Y. Satoh, H. Sasaki, I. Masayuki, and S. Yoshida, "C-doped GaN buffer layers with high breakdown voltages for high-power operation AlGaN/GaN HFETs on 4-in Si substrates by MOVPE", *Journal of Crystal Growth*, vol. 298, no. 0, pp. 831 –834, 2007, Thirteenth International Conference on Metal Organic Vapor Phase Epitaxy ICMOVPE XIII. [Online]. Available: http://www.sciencedirect.com/science/article/pii/S0022024806011146.

[277] H Obloh, K. Bachem, U Kaufmann, M Kunzer, M Maier, A Ramakrishnan, and P Schlotter, "Self-compensation in Mg doped p-type GaN grown by MOCVD", *Journal of Crystal Growth*, vol. 195, no. 1–4, pp. 270 –273, 1998. [Online]. Available: http://www.sciencedirect.com/science/article/pii/S0022024898005788.

[278] M Lachab, D.-H Youn, R. Q. Fareed, T Wang, and S Sakai, "Characterization of Mg-doped GaN grown by metalorganic chemical vapor deposition", *Solid-State Electronics*, vol. 44, no. 9, pp. 1669 –1677, 2000. [Online]. Available: http://www.sciencedirect.com/science/article/pii/S0038110100000721.

[279] U. Kaufmann, P. Schlotter, H. Obloh, K. Köhler, and M. Maier, "Hole conductivity and compensation in epitaxial GaN:Mg layers", *Phys. Rev. B*, vol. 62, pp. 10 867–10 872, 16 Oct. 2000. [Online]. Available: http://link.aps.org/doi/10.1103/PhysRevB.62.10867.

[280] P. Kozodoy, H. Xing, S. P. DenBaars, U. K. Mishra, A. Saxler, R. Perrin, S. Elhamri, and W. C. Mitchel, "Heavy doping effects in Mg-doped GaN", *Journal of Applied Physics*, vol. 87, no. 4, pp. 1832–1835, 2000. [Online]. Available: http://scitation.aip.org/content/aip/journal/jap/87/4/10.1063/1.372098.

[281] W. Lu, D. Aplin, A. R. Clawson, and P. K. L. Yu, “Effects of the gas ambient in thermal activation of Mg-doped p-GaN on Hall effect and photoluminescence”, *Journal of Vacuum Science and Technology A*, vol. 31, no. 1, p. 011 502, 2013. [Online]. Available: http://scitation.aip.org/content/avs/journal/jvsta/31/1/10.1116/1.4768174.

[282] P. Kozodoy, M. Hansen, S. P. DenBaars, and U. K. Mishra, “Enhanced Mg doping efficiency in AlGaN/GaN superlattices”, *Applied Physics Letters*, vol. 74, no. 24, pp. 3681–3683, 1999. [Online]. Available: http://scitation.aip.org/content/aip/journal/apl/74/24/10.1063/1.123220.

[283] K. Kumakura, T. Makimoto, and N. Kobayashi, “Enhanced hole generation in Mg-doped AlGaN/GaN superlattices due to piezoelectric field”, *Japanese Journal of Applied Physics*, vol. 39, no. 4S, p. 2428, 2000. [Online]. Available: http://stacks.iop.org/1347-4065/39/i=4S/a=2428.

[284] E. L. Waldron, J. W. Graff, and E. F. Schubert, “Improved mobilities and resistivities in modulation-doped p-type AlGaN/GaN superlattices”, *Applied Physics Letters*, vol. 79, no. 17, pp. 2737–2739, 2001. [Online]. Available: http://scitation.aip.org/content/aip/journal/apl/79/17/10.1063/1.1410340.

[285] B Reuters, H Hahn, A Pooth, B Holländer, U Breuer, M Heuken, H Kalisch, and A Vescan, “Fabrication of p-channel heterostructure field effect transistors with polarization-induced two-dimensional hole gases at metal–polar GaN/AlInGaN interfaces”, *Journal of Physics D: Applied Physics*, vol. 47, no. 17, p. 175 103, 2014. [Online]. Available: http://stacks.iop.org/0022-3727/47/i=17/a=175103.

[286] J.-O. Song, J.-S. Ha, and T.-Y. Seong, “Ohmic-Contact Technology for GaN-Based Light-Emitting Diodes: Role of P-Type Contact”, *Electron Devices, IEEE Transactions on*, vol. 57, no. 1, pp. 42–59, Jan. 2010.

[287] H. W. Jang, S. Y. Kim, and J.-L. Lee, “Mechanism for ohmic contact formation of oxidized Ni/Au on p-type GaN”, *Journal of Applied Physics*, vol. 94, no. 3, pp. 1748–1752, Aug. 2003.

[288] C.-S. Lee, Y.-J. Lin, and C.-T. Lee, “Investigation of oxidation mechanism for ohmic formation in Ni/Au contacts to p-type GaN layers”, *Applied Physics Letters*, vol. 79, no. 23, pp. 3815–3817, 2001. [Online]. Available: http://scitation.aip.org/content/aip/journal/apl/79/23/10.1063/1.1425065.

[289] Y. Koide, T. Maeda, T. Kawakami, S. Fujita, T. Uemura, N. Shibata, and M. Murakami, “Effects of annealing in an oxygen ambient on electrical properties of ohmic contacts to p-type GaN”, English, *Journal of Electronic Materials*, vol. 28, no. 3, pp. 341–346, 1999. [Online]. Available: http://dx.doi.org/10.1007/s11664-999-0037-7.

[290] Y. Ohba and A. Hatano, "A study on strong memory effects for Mg doping in GaN metalorganic chemical vapor deposition", *Journal of Crystal Growth*, vol. 145, no. 1–4, pp. 214 –218, 1994. [Online]. Available: `http://www.sciencedirect.com/science/article/pii/0022024894910537`.

[291] B. Kuhn, M. Welsch, M. Kessler, and F. Scholz, "The influence of growth conditions on the electrical properties of magnesium-doped GaN grown by MOVPE", *physica status solidi (a)*, vol. 176, no. 1, pp. 787–792, 1999. [Online]. Available: http://dx.doi.org/10.1002/(SICI)1521-396X(199911)176:1<787::AID-PSSA787>3.0.CO;2-J.

[292] M. R. Islam, K. Sugita, M. Horie, A. Hashimoto, and A. Yamamoto, "Mg doping behavior of MOVPE InGaN", *Journal of Crystal Growth*, vol. 311, no. 10, pp. 2817 –2820, 2009, Proceedings of the 2nd International Symposium on Growth of III Nitrides. [Online]. Available: `http://www.sciencedirect.com/science/article/pii/S0022024809000414`.

[293] Y. Kobayashi, Y. Yamauchi, and N. Kobayashi, "Structural and optical properties of AlGaInN/GaN grown by MOVPE", *Japanese Journal of Applied Physics*, vol. 42, no. 4S, p. 2300, 2003. [Online]. Available: `http://stacks.iop.org/1347-4065/42/i=4S/a=2300`.

[294] J.-K. Ho, C.-S. Jong, C. C. Chiu, C.-N. Huang, K.-K. Shih, L.-C. Chen, F.-R. Chen, and J.-J. Kai, "Low-resistance ohmic contacts to p-type gan achieved by the oxidation of ni/au films", *Journal of Applied Physics*, vol. 86, no. 8, pp. 4491–4497, 1999. [Online]. Available: `http://scitation.aip.org/content/aip/journal/jap/86/8/10.1063/1.371392`.

[295] H. Hahn, B. Reuters, A Pooth, B. Hollander, M. Heuken, H. Kalisch, and A Vescan, "p-Channel Enhancement and Depletion Mode GaN-Based HFETs With Quaternary Backbarriers", *Electron Devices, IEEE Transactions on*, vol. 60, no. 10, pp. 3005–3011, Oct. 2013.

[296] T. Takeuchi, S. Sota, M. Katsuragawa, M. Komori, H. Takeuchi, H. Amano, and I. Akasaki, "Quantum-confined Stark effect due to piezoelectric fields in GaInN strained quantum wells", *Japanese Journal of Applied Physics*, vol. 36, no. 4A, p. L382, 1997. [Online]. Available: `http://stacks.iop.org/1347-4065/36/i=4A/a=L382`.

[297] T. Takeuchi, C. Wetzel, S. Yamaguchi, H. Sakai, H. Amano, I. Akasaki, Y. Kaneko, S. Nakagawa, Y. Yamaoka, and N. Yamada, "Determination of piezoelectric fields in strained GaInN quantum wells using the quantum-confined Stark effect", *Applied Physics Letters*, vol. 73, no. 12, pp. 1691–1693, Sep. 1998.

[298] M. Leroux, N. Grandjean, M. Laügt, J. Massies, B. Gil, P. Lefebvre, and P. Bigenwald, "Quantum confined Stark effect due to built-in internal polarization fields in AlGaN/GaN quantum wells", *Phys. Rev. B*, vol. 58, R13371–R13374, 20 Nov. 1998. [Online]. Available: http://link.aps.org/doi/10.1103/PhysRevB.58.R13371.

[299] Y. Yamane, K. Fujiwara, and J. K. Sheu, "Largely variable electroluminescence efficiency with current and temperature in a blue (In,Ga)N multiple-quantum-well diode", *Applied Physics Letters*, vol. 91, no. 7, p. 073 501, 2007. [Online]. Available: http://scitation.aip.org/content/aip/journal/apl/91/7/10.1063/1.2769754.

[300] M.-Y. Ryu, C. Q. Chen, E. Kuokstis, J. W. Yang, G. Simin, and M. A. Khan, "Luminescence mechanisms in quaternary AlInGaN materials", *Applied Physics Letters*, vol. 80, no. 20, pp. 3730–3732, 2002. [Online]. Available: http://scitation.aip.org/content/aip/journal/apl/80/20/10.1063/1.1481766.

[301] V. Perez-Solorzano, A. Groening, R. Haerle, H. Schweizer, and M. Jetter, "Characterisation of quaternary AlInGaN thick layers and quantum wells grown by MOVPE", *Journal of Crystal Growth*, vol. 272, no. 1–4, pp. 386 –392, 2004, The Twelfth International Conference on Metalorganic Vapor Phase Epitaxy. [Online]. Available: http://www.sciencedirect.com/science/article/pii/S0022024804010383.

[302] M.-Y. Ryu, J. Song, C. Chen, and M. A. Khan, "Indium incorporation effects on luminescence mechanisms in quaternary AlInGaN layers", *Solid State Communications*, vol. 142, no. 10, pp. 569 –572, 2007. [Online]. Available: http://www.sciencedirect.com/science/article/pii/S0038109807002578.

[303] S.-H. Park, Y.-T. Moon, D.-S. Han, J. Seo Park, M.-S. Oh, and D. Ahn, "Light emission enhancement in blue InGaAlN/InGaN quantum well structures", *Applied Physics Letters*, vol. 99, no. 18, 181101, 2011. [Online]. Available: http://scitation.aip.org/content/aip/journal/apl/99/18/10.1063/1.3657141.

[304] S.-H. Park and D. Ahn, "Spontaneous emission and optical gain characteristics of blue InGaAlN/InGaN quantum well structures with reduced internal field", *Journal of Applied Physics*, vol. 112, no. 4, 043107, 2012. [Online]. Available: http://scitation.aip.org/content/aip/journal/jap/112/4/10.1063/1.4747841.

[305] M. Leroux, N. Grandjean, J. Massies, B. Gil, P. Lefebvre, and P. Bigenwald, "Barrier-width dependence of group-III nitrides quantum-well transition energies", *Phys. Rev. B*, vol. 60, pp. 1496–1499, 3 Jul. 1999. [Online]. Available: http://link.aps.org/doi/10.1103/PhysRevB.60.1496.

[306] Y.-K. Kuo, S.-H. Yen, and J.-R. Chen, "Numerical simulation of AlInGaN ultraviolet light-emitting diodes", in *Proc. SPIE*, vol. 6368, 2006, pp. 636 812–636812–10. [Online]. Available: http://dx.doi.org/10.1117/12.685897.

[307] H. J. Kim, S. Choi, S.-S. Kim, J.-H. Ryou, P. D. Yoder, R. D. Dupuis, A. M. Fischer, K. Sun, and F. A. Ponce, "Improvement of quantum efficiency by employing active-layer-friendly lattice-matched InAlN electron blocking layer in green light-emitting diodes", *Applied Physics Letters*, vol. 96, no. 10, 101102, 2010. [Online]. Available: `http://scitation.aip.org/content/aip/journal/apl/96/10/10.1063/1.3353995`.

[308] C.-H. Ko, Y.-K. Su, S.-J. Chang, T.-M. Kuan, C.-I. Chiang, W.-H. Lan, W.-J. Lin, and J. Webb, "P-down InGaN/GaN multiple quantum wells light-emitting diode structure grown by metal-organic vapor-phase epitaxy", *Japanese Journal of Applied Physics*, vol. 41, no. 4S, p. 2489, 2002. [Online]. Available: `http://stacks.iop.org/1347-4065/41/i=4S/a=2489`.

[309] Y. Su, S. Chang, C.-H. Ko, J. Chen, T.-M. Kuan, W.-H. Lan, W.-J. Lin, Y.-T. Cherng, and J. Webb, "InGaN/GaN light emitting diodes with a p-down structure", *Electron Devices, IEEE Transactions on*, vol. 49, no. 8, pp. 1361–1366, Aug. 2002.

[310] M. L. Reed, E. D. Readinger, H. Shen, M. Wraback, A. Syrkin, A. Usikov, O. V. Kovalenkov, and V. A. Dmitriev, "N-InGaN p-GaN single heterostructure light emitting diode with p-side down", *Applied Physics Letters*, vol. 93, no. 13, 133505, 2008. [Online]. Available: `http://scitation.aip.org/content/aip/journal/apl/93/13/10.1063/1.2992582`.

[311] H. Xing, D. S. Green, H. Yu, T. Mates, P. Kozodoy, S. Keller, S. P. DenBaars, and U. K. Mishra, "Memory effect and redistribution of mg into sequentially regrown gan layer by metalorganic chemical vapor deposition", *Japanese Journal of Applied Physics*, vol. 42, no. 1R, p. 50, 2003. [Online]. Available: `http://stacks.iop.org/1347-4065/42/i=1R/a=50`.

[312] F. Akyol, D. N. Nath, S. Krishnamoorthy, P. S. Park, and S. Rajan, "Suppression of electron overflow and efficiency droop in N-polar GaN green light emitting diodes", *Applied Physics Letters*, vol. 100, no. 11, 111118, 2012. [Online]. Available: `http://scitation.aip.org/content/aip/journal/apl/100/11/10.1063/1.3694967`.

[313] W.-H. Lan, "Wavelength shift of gallium nitride light emitting diode with p-down structure", *Electron Devices, IEEE Transactions on*, vol. 52, no. 6, pp. 1217–1219, Jun. 2005.

[314] S.-W. Feng, Y.-C. Cheng, Y.-Y. Chung, C. C. Yang, K.-J. Ma, C.-C. Yan, C. Hsu, J. Y. Lin, and H. X. Jiang, "Strong green luminescence in quaternary InAlGaN thin films", *Applied Physics Letters*, vol. 82, no. 9, pp. 1377–1379, 2003. [Online]. Available: `http://scitation.aip.org/content/aip/journal/apl/82/9/10.1063/1.1556965`.

[315] R. J. Shul, L. Zhang, A. G. Baca, C. G. Willison, J. Han, S. J. Pearton, and F. Ren, “Inductively coupled plasma-induced etch damage of GaN p-n junctions”, *Journal of Vacuum Science and Technology A*, vol. 18, no. 4, pp. 1139–1143, 2000. [Online]. Available: `http://scitation.aip.org/content/avs/journal/jvsta/18/4/10.1116/1.582313`.

[316] J. Eddy C.R. and B. Molnar, “Plasma etch-induced conduction changes in gallium nitride”, English, *Journal of Electronic Materials*, vol. 28, no. 3, pp. 314–318, 1999. [Online]. Available: `http://dx.doi.org/10.1007/s11664-999-0033-y`.

[317] X. A. Cao, A. P. Zhang, G. T. Dang, F. Ren, S. J. Pearton, R. J. Shul, and L. Zhang, “Schottky diode measurements of dry etch damage in n- and p-type GaN”, *Journal of Vacuum Science and Technology A*, vol. 18, no. 4, pp. 1144–1148, 2000. [Online]. Available: `http://scitation.aip.org/content/avs/journal/jvsta/18/4/10.1116/1.582314`.

Publications

[1] H. Hahn, B. Reuters, S. Geipel, M. Schauerte, F. Benkhelifa, O. Ambacher, H. Kalisch, and A. Vescan, “Charge balancing in GaN-based 2-D electron gas devices employing an additional 2-D hole gas and its influence on dynamic behaviour of GaN-based heterostructure field effect transistors”, *Journal of Applied Physics*, vol. 117, no. 10, 104508, 2015. [Online]. Available: `http://scitation.aip.org/content/aip/journal/jap/117/10/10.1063/1.4913857`.

[2] M. Finken, A. Wille, B. Reuters, M. Heuken, H. Kalisch, and A. Vescan, “Investigations of the electrochemical stability of ingan photoanodes in different electrolytes”, *physica status solidi (b)*, n/a–n/a, 2014. [Online]. Available: `http://dx.doi.org/10.1002/pssb.201451576`.

[3] A. Vescan, H. Hahn, B. Reuters, and H. Kalisch, “Novel GaN-based transistors using polarization engineering”, in *10th International Conference on Advanced Semiconductor Devices Microsystems (ASDAM)*, Oct. 2014, pp. 1–4.

[4] B Reuters, H Hahn, A Pooth, B Holländer, U Breuer, M Heuken, H Kalisch, and A Vescan, “Fabrication of p-channel heterostructure field effect transistors with polarization-induced two-dimensional hole gases at metal–polar GaN/AlInGaN interfaces”, *Journal of Physics D: Applied Physics*, vol. 47, no. 17, p. 175 103, 2014. [Online]. Available: `http://stacks.iop.org/0022-3727/47/i=17/a=175103`.

[5] B. Reuters, J. Strate, H. Hahn, M. Finken, A. Wille, M. Heuken, H. Kalisch, and A. Vescan, “Selective MOVPE of InGaN-based LED structures on non-planar Si (111) facets of patterned Si (100) substrates”, *Journal of Crystal Growth*, vol. 391, no. 0, pp. 33 –40, 2014. [Online]. Available: `http://www.sciencedirect.com/science/article/pii/S0022024814000050`.

[6] H. Hahn, B. Reuters, A. Pooth, H. Kalisch, and A. Vescan, “Characterization of GaN-based p-channel device structures at elevated temperatures”, *Semiconductor Science and Technology*, vol. 29, no. 7, p. 075 002, 2014. [Online]. Available: `http://stacks.iop.org/0268-1242/29/i=7/a=075002`.

[7] H. Hahn, B. Reuters, S. Kotzea, G. Lukens, S. Geipel, H. Kalisch, and A. Vescan, “First monolithic integration of GaN-based enhancement mode n-channel and p-channel heterostructure field effect transistors”, in *Device Research Conference (DRC), 2014 72nd Annual*, Jun. 2014, pp. 259–260.

[8] A. Wille, B. Reuters, M. Finken, F. Heyroth, G. Schmidt, M. Heuken, H. Kalisch, and A. Vescan, “Strain relief mechanisms and growth behavior of superlattice distributed Bragg reflectors”, *physica status solidi (c)*, vol. 11, no. 3-4, pp. 758–761, 2014. [Online]. Available: `http://dx.doi.org/10.1002/pssc.201300444`.

[9] M. Finken, A. Wille, B. Reuters, B. Holländer, M. Heuken, H. Kalisch, and A. Vescan, “Growth properties and electrochemical characterization of InGaN photoanodes with different In concentrations”, *physica status solidi (c)*, vol. 11, no. 3-4, pp. 746–749, 2014. [Online]. Available: `http://dx.doi.org/10.1002/pssc.201300414`.

[10] B. Reuters, A. Wille, N. Ketteniss, H. Hahn, B. Holländer, M. Heuken, H. Kalisch, and A. Vescan, “Polarization-engineered enhancement-mode high-electron-mobility transistors using quaternary AlInGaN barrier layers”, English, *Journal of Electronic Materials*, vol. 42, no. 5, pp. 826–832, 2013. [Online]. Available: `http://dx.doi.org/10.1007/s11664-013-2473-7`.

[11] B. Reuters, H. Hahn, H. Behmenburg, M. Heuken, H. Kalisch, and A. Vescan, “Insulating behavior of interfaces in regrown AlGaN/GaN double heterostructures on AlGaN back-barrier templates”, *physica status solidi (c)*, vol. 10, no. 5, pp. 799–802, 2013. [Online]. Available: `http://dx.doi.org/10.1002/pssc.201200607`.

[12] W Witte, B Reuters, D Fahle, H Behmenburg, K. R. Wang, A Trampert, B Holländer, H Hahn, H Kalisch, M Heuken, and A Vescan, “AlGaN/GaN heterostructure field-effect transistors regrown on nitrogen implanted templates”, *Semiconductor Science and Technology*, vol. 28, no. 8, p. 085 006, 2013. [Online]. Available: `http://stacks.iop.org/0268-1242/28/i=8/a=085006`.

[13] H. Hahn, B. Reuters, A Pooth, B. Hollander, M. Heuken, H. Kalisch, and A Vescan, “P-Channel enhancement and depletion mode GaN-based HFETs with quaternary backbarriers”, *Electron Devices, IEEE Transactions on*, vol. 60, no. 10, pp. 3005–3011, Oct. 2013.

[14] H. Hahn, B. Reuters, A. Pooth, A. Noculak, H. Kalisch, and A. Vescan, “First small-signal data of GaN-based p-channel heterostructure field effect transistors”, *Japanese Journal of Applied Physics*, vol. 52, no. 12R, p. 128 001, 2013. [Online]. Available: `http://stacks.iop.org/1347-4065/52/i=12R/a=128001`.

[15] H. Hahn, B. Reuters, H. Kalisch, and A. Vescan, “AlN barrier HFETs with AlGaN channels to shift the threshold voltage to higher positive values: a proposal”, *Semiconductor Science and Technology*, vol. 28, no. 7, p. 074 017, 2013. [Online]. Available: `http://stacks.iop.org/0268-1242/28/i=7/a=074017`.

[16] F. M. Morales, J. M. Mánuel, R García, B Reuters, H Kalisch, and A Vescan, "Evaluation of interpolations of InN, AlN and GaN lattice and elastic constants for their ternary and quaternary alloys", *Journal of Physics D: Applied Physics*, vol. 46, no. 24, p. 245 502, 2013. [Online]. Available: `http://stacks.iop.org/0022-3727/46/i=24/a=245502`.

[17] E. V. Lutsenko, M. V. Rzheutski, V. N. Pavlovskii, E. V. Muravitskaya, G. P. Yablonskii, C. Mauder, B. Reuters, H. Kalisch, M. Heuken, and A. Vescan, "Temperature resolved photoluminescence of nonpolar InGaN/GaN multiple quantum well heterostructures grown on $LiAlO_2$", *physica status solidi (c)*, vol. 10, no. 3, pp. 532–535, 2013. [Online]. Available: `http://dx.doi.org/10.1002/pssc.201200677`.

[18] B. Reuters, A. Wille, B. Holländer, E. Sakalauskas, N. Ketteniss, C. Mauder, R. Goldhahn, M. Heuken, H. Kalisch, and A. Vescan, "Growth studies on quaternary AlInGaN layers for HEMT application", English, *Journal of Electronic Materials*, vol. 41, no. 5, pp. 905–909, 2012. [Online]. Available: `http://dx.doi.org/10.1007/s11664-012-1989-6`.

[19] B. Reuters, M. Finken, A. Wille, B. Holländer, M. Heuken, H. Kalisch, and A. Vescan, "Relaxation and critical strain for maximum In incorporation in AlInGaN on GaN grown by metal organic vapour phase epitaxy", *Journal of Applied Physics*, vol. 112, no. 9, 093524, 2012. [Online]. Available: `http://scitation.aip.org/content/aip/journal/jap/112/9/10.1063/1.4764342`.

[20] H. Hahn, B. Reuters, A. Wille, N. Ketteniss, F. Benkhelifa, O. Ambacher, H. Kalisch, and A. Vescan, "First polarization-engineered compressively strained AlInGaN barrier enhancement-mode MISHFET", *Semiconductor Science and Technology*, vol. 27, no. 5, p. 055 004, 2012. [Online]. Available: `http://stacks.iop.org/0268-1242/27/i=5/a=055004`.

[21] N Ketteniss, A Askar, B Reuters, A Noculak, B Holländer, H Kalisch, and A Vescan, "Polarization-reduced quaternary InAlGaN/GaN HFET and MISHFET devices", *Semiconductor Science and Technology*, vol. 27, no. 5, p. 055 012, 2012. [Online]. Available: `http://stacks.iop.org/0268-1242/27/i=5/a=055012`.

[22] N. Ketteniss, B. Reuters, B. Hollander, H. Hahn, H. Kalisch, and A. Vescan, "Quaternary nitride enhancement mode HFET with 260 mS/mm and a threshold voltage of +0.5 V", in *Device Research Conference (DRC), 2012 70th Annual*, Jun. 2012, pp. 161–162.

[23] E. Sakalauskas, B. Reuters, L. R. Khoshroo, H. Kalisch, M. Heuken, A. Vescan, M. Röppischer, C. Cobet, G. Gobsch, and R. Goldhahn, "Dielectric function and optical properties of quaternary AlInGaN alloys", *Journal of Applied Physics*, vol.

110, no. 1, 013102, pp. –, 2011. [Online]. Available: http://scitation.aip.org/content/aip/journal/jap/110/1/10.1063/1.3603015.

[24] C Netzel, C Mauder, T Wernicke, B Reuters, H Kalisch, M Heuken, A Vescan, M Weyers, and M Kneissl, "Strong charge carrier localization interacting with extensive nonradiative recombination in heteroepitaxially grown m-plane InGaN quantum wells", *Semiconductor Science and Technology*, vol. 26, no. 10, p. 105 017, 2011. [Online]. Available: http://stacks.iop.org/0268-1242/26/i=10/a=105017.

[25] C. Mauder, B. Reuters, K. Wang, D. Fahle, A. Trampert, M. Rzheutskii, E. Lutsenko, G. Yablonskii, J. Woitok, M. Chou, M. Heuken, H. Kalisch, and R. Jansen, "Effect of indium incorporation on optical and structural properties of m-plane InGaN/GaN MQW on $LiAlO_2$ substrates", *Journal of Crystal Growth*, vol. 315, no. 1, pp. 246 –249, 2011, 15th International Conference on Metalorganic Vapor Phase Epitaxy (ICMOVPE-XV). [Online]. Available: http://www.sciencedirect.com/science/article/pii/S0022024810004811.

[26] C. Mauder, B. Reuters, H. Behmenburg, R. A. De Souza, J. F. Woitok, M. M. C. Chou, M. Heuken, H. Kalisch, and R. H. Jansen, "Mechanisms of impurity incorporation during MOVPE growth of m-plane GaN layers on $LiAlO_2$", *physica status solidi (c)*, vol. 8, no. 7-8, pp. 2050–2052, 2011. [Online]. Available: http://dx.doi.org/10.1002/pssc.201001027.

[27] C. Mauder, E. V. Lutsenko, M. V. Rzheutski, B. Reuters, V. Z. Zubialevich, V. N. Pavlovskii, G. P. Yablonskii, M. Heuken, H. Kalisch, and A. Vescan, "Irregular spectral position of E parallel c component of polarized photoluminescence from m-plane InGaN/GaN multiple quantum wells grown on $LiAlO_2$", *Applied Physics Letters*, vol. 99, no. 23, 232114, 2011. [Online]. Available: http://scitation.aip.org/content/aip/journal/apl/99/23/10.1063/1.3667199.

[28] C. Mauder, K. R. Wang, B. Reuters, H. Behmenburg, L. R. Khoshroo, Q. Wan, A. Trampert, M. V. Rzheutskii, E. V. Lutsenko, G. P. Yablonskii, J. F. Woitok, M. Heuken, H. Kalisch, and R. H. Jansen, "Anisotropic properties of MOVPE-grown m-plane GaN layers on $LiAlO_2$ substrates", *physica status solidi (b)*, vol. 247, no. 7, pp. 1750–1752, 2010. [Online]. Available: http://dx.doi.org/10.1002/pssb.200983521.

[29] C. Mauder, B. Reuters, L. R. Khoshroo, M. Rzheutskii, E. Lutsenko, G. Yablonskii, J. Woitok, M. Heuken, H. Kalisch, and R. Jansen, "Development of m-plane GaN anisotropic film properties during movpe growth on $LiAlO_2$ substrates", *Journal of Crystal Growth*, vol. 312, no. 11, pp. 1823 –1827, 2010. [Online]. Available: http://www.sciencedirect.com/science/article/pii/S0022024810001697.

[30] C. Mauder, L. Rahimzadeh Khoshroo, H. Behmenburg, B. Reuters, M. Bösing, M. V. Rzheutskii, E. V. Lutsenko, G. P. Yablonskii, J. F. Woitok, M. M. C. Chou, M. Heuken, H. Kalisch, and R. H. Jansen, "Impact of nitridation on structural and optical properties of MOVPE-grown m-plane GaN layers on $LiAlO_2$", *physica status solidi (c)*, vol. 6, no. S2, S482–S485, 2009. [Online]. Available: `http://dx.doi.org/10.1002/pssc.200880790`.

[31] L. R. Khoshroo, C. Mauder, H. Behmenburg, J. Woitok, W. Zander, J. Gruis, B. Reuters, J. Schubert, A. Vescan, M. Heuken, H. Kalisch, and R. H. Jansen, "Epitaxy and characterisation of AlInGaN heterostructures for HEMT application", *physica status solidi (c)*, vol. 6, no. S2, S470–S473, 2009. [Online]. Available: `http://dx.doi.org/10.1002/pssc.200880944`.

List of figures

2.1. Structure of the wurtzite crystal and the simulated bandstructure of GaN at the Γ symmetry point after [65]. 6
2.2. Illustration of the elastic deformation for pseudomorphic growth for three different cases: the tensile strained case $a_{nom} < a_{GaN}$, the lattice-matched case $a_{nom} = a_{GaN}$ and the compressively strained case $a_{nom} > a_{GaN}$. A ball-and-stick model is shown in every case to indicate the changing dipole length. 9
2.3. Bandgap of nitride binaries and ternaries plotted against the in-plane lattice constant a. While the bowing for AlGaN and InGaN is commonly accepted to be constant, the bowing for AlInN is controversially discussed. 11
2.4. Bandgap contour plot in a ternary diagram for all metal contents possible in a quaternary nitride layer. The orange lines mark the compositions with bandgaps equal to that of GaN. The yellow-to-red colored areas indicate larger bandgaps than the one of GaN. 13
2.5. Location of fixed interface charges in a metal-polar two-fold heterostructure and the corresponding bandstructure. 15
2.6. Band diagram of a double heterostructure consisting of a lower GaN n-channel and an upper GaN p-channel with an embedded barrier. Conduction and valence bands as well as the accumulated 2DHG (blue) and 2DEG (red) densities. The associated polarization charges are given at each interface. After [112]. 17
2.7. Schematic illustration of the HFET device principle including source, drain and gate contacts. 18

2.8. Bandgap diagrams plotted over the lattice constant a with different bowing parameters for AlInN. Either a non-weighted a), c) and e) or a weighted bandgap equation b), d) and f) is applied. The calculated bandgap values for the typical ternary barrier layers $Al_{0.25}Ga_{0.75}N$ (purple star) and $Al_{0.83}In_{0.17}N$ (orange star) as well as measured bandgap values for several AlInN layers (red circles) with different compositions are shown. 20

3.1. Schematic drawings of the MOVPE reactors used in this thesis. . . . 24
3.2. Schematic cross section through the reciprocal space. The Ewald construction with $\underline{\mathbf{S}}=\underline{\mathbf{k}}_{\mathbf{d}}-\underline{\mathbf{k}}_{\mathbf{i}}$ is also included. The relevant reflexes for the analysis in this thesis are shown exemplarily for fully relaxed GaN and AlN schematically. The movement of the scattering vector $\underline{\mathbf{S}}$ with changing goniometer angles is illustrated by the arrows. The grey area is measureable in skew geometry. 29
3.3. Exemplary HRXRD measurements on a sample with a lattice-matched $Al_{83\%}In_{17\%}N$ barrier with a thickness of 42 nm on a GaN/AlN buffer. 31
3.4. Example of RBS measurements of a AlInGaN/AlN heterostructure. . 32

4.1. Typical layer stack sequence on a sapphire substrate. 36
4.2. Overview of the different sample series which are most relevant for this thesis. On the underlying bandgap contour plot, the different samples are shown in dependence of composition. 40
4.3. Compositions determined by RBS (upper plot), nominal strain ε_{nom}, residual strain ε_{res} and $\chi_{\mathrm{RBS,min}}$ channeling values (bottom plot) for different reactor pressures. 42
4.4. XRD $(10\bar{1}5)$ RSM taken with an open detector of sample P3. The dashed red line in the image illustrates the Q_x position of the GaN buffer peak. The red triangles illustrate the theoretical positions of sample P3 assumed to be pseudomorphically grown (R = 0 %) or fully relaxed (R = 100 %). 43
4.5. HRXRD $(10\bar{1}5)$ RSMs in triple axis geometry. 45
4.6. AFM 5 µm · 5 µm scans of the HT-sample (top) and the LT-sample (bottom) in planar illustration (left) and 3D perspective (right). . . . 46
4.7. RBS spectra: The blue dots represent the random measurement, the green squares represent the channeling signal, and the red curves are simulations. The compositions are given in the insets. 47

4.8. HRXRD (0002) 2Θ-ω scan for the LT-sample (grey curve). The fit based on the six-fold multi-layer model derived by RBS is also shown (red curve). 48
4.9. Relaxation (grey curve), In content (red curve), nominal strain (green curve) and residual strain (orange curve) as functions of the AlInGaN layer thickness for the LT-sample. 49
4.10. HRXRD (0002) 2Θ-ω scans for a sample series, for which $T_{Surface}$ is different. The quaternary peak is shifted to lower angles for an increasing In content due to a larger nominal lattice constant c. . . . 51
4.11. Effect of $T_{Surface}$ on In incorporation and crystal quality. 51
4.12. Bandgap diagram plotted over the lattice constant a. Blue triangles represent theoretical values for samples T1 to T5 with a non-weighted bandgap. Green triangles represent values with a weighted bandgap. The red triangles are values measured by SE. 52
4.13. HRXRD (0002) 2Θ-ω scans for sample series F, for which the TMAl-to-TMGa molar flow ratio is changed. The quaternary peak is shifted to lower angles for an increasing Ga content due to a larger nominal lattice constant c. Also shown are the first and the second fringe oscillations, which are of equal intensity indicating a similar interface quality in these heterostructures. 55
4.14. Morphological development of AlInGaN samples with growth conditions of sample F6 and different thicknesses of 70 nm, 200 nm and 500 nm. 56

5.1. Experimental concept of a MOVPE experiment using different templates grown in previous epitaxy runs on sapphire. The GaN template consists of 1 µm AlN and 3 µm GaN and the AlN template consists of only 1 µm AlN. 60
5.2. Illustration of the composition in the bandgap-vs.-lattice diagram. The arrows indicate the shift in the composition due to the increased TMGa flow for growth on AlN (red) and for growth on GaN (light blue). 61
5.3. HRXRD (0002) 2Θ-ω scans for samples grown with different TMGa fluxes. The red curves are samples grown on AlN templates. The light blue curves are samples on GaN templates, shown for comparison. 61

5.4. Merged HRXRD (10$\bar{1}$5) RSM of samples of the "temperature" series. A pseudomorphic phase is apparent for all $T_{Surface}$. For lower $T_{Surface}$ phase segregation leads to an additional fully relaxed AlInGaN phase. 63

6.1. Hall and van der Pauw measurements on samples of the T-series 1. . 69
6.2. Bandgap diagramm plotted over the lattice constant a. Blue circles represent the T-series 2 and purple circles represent the F-series. Bandgaps and polarization values are calculated with a weighted bandgap formula. 72
6.3. Calculated n_s plotted against the absolute polarization difference $|\Delta P|$ together with measured values for n_s. 73
6.4. 2DEG mobility μ plotted against the 2DEG density n_s measured by Hall and Van der Pauw. 75
6.5. Transfer characteristics. 75
6.6. Layer stacks of samples with different AlInGaN barriers, which were proccessed to HFETs: HFET B1 with a single low-polarization layer; HFET B2 with a double AlInGaN layer; consisting of a low-polarization layer and a high-polarization layer; HFET B3 with a low-polarization layer and a graded AlInGaN high-polarization layer. 78
6.7. Simulations for devices B1, B2 and B3. After [260]. 79
6.8. Transfer characteristics for the gate recessed HFETs B1, B2 and B3. . 80

7.1. Hole mobility μ plotted either versus the bulk hole density p (for holes in GaN:Mg) or versus the 2DHG sheet density p_s (for holes in a 2DHG). The correlation between p and p_s is calculated by assuming a spatial width of the 2DHG of 5 nm. 83
7.2. Layer stack and corresponding schematic bandstructure of p-channel HFETs grown by MOVPE for two cases: Without any Mg doping (grey curve) and with Mg compensation doping in the upper GaN channel (blue curve). The highly doped GaN:Mg^{++} cap is neglected in the bandstructure for simplicity. 85
7.3. Layer stacks used (p-GaN and 2DHG) and SIMS measurements of p-GaN samples with two different Cp_2Mg-to-TMGa gas phase ratios: 0.36% (red curve with circles) and 0.12% (blue curve with squares). The profile of a Mg-implanted GaN sample which serves as a reference for the determination of the relative sensitivity factors is also shown (gray line). 86

7.4. 2DHG density and mobility plotted for a layer stack without AlInGaN (p-GaN) and one with AlInGaN (2DHG), both grown twice with different Cp_2Mg-to-TMGa gas phase ratios. 87
7.5. HRXRD analysis for samples A to E, which were grown at different reactor conditions. 90
7.6. Illustration of the compositions of AlInGaN backbarriers for sample A to E in the bandgap vs. lattice constant diagramm. 91
7.7. AFM images illustrate smooth surfaces for samples A, C and E. A slight trend to a lower surface roughness is observed from the highly tensile strained sample A to the almost unstrained sample E. 91
7.8. Median values of measured $p_{s,measured}$ (red circles) and calculated $p_{s,calc.}$ (grey squares) as well as the mobility (blue circles) plotted against ΔP for samples A-E. The error bars illustrate the standard deviation for measurements of different structures on a single wafer. . 93
7.9. Carrier mobility for holes in a 2DHG and electrons in a 2DEG plotted against the 2DHG and 2DEG density, respectively. The values for the 2DHG are those of the samples presented here, whereas the values for the 2DEG are taken from the TMAl-toTMGa series presented in Sec. 6.2. 94
7.10. A schematic cross section of processed p-channel HFETs utilizing the polarization-induced 2DHG. Ni/Au metal stacks are used for source and drain ohmic contacts, and Mo/Au metal stacks were used for a Schottky gate. Prior to the gate metallization, a recess of 7 nm was applied to all samples to remove the highly Mg-doped GaN cap layers between the ohmic contacts. 95
7.11. Output and transfer characteristics for p-channel HFETs utilizing a 2DHG. 96

8.1. Schematic band diagrams of a single InGaN quantum well embedded in (a) GaN barriers or (b) AlInGaN barriers. The overlap of electron and hole wavefunctions is increased for AlInGaN barriers with lower ΔP. Further, the energy of emitted photons increases. 102
8.2. Schematic cross section of the LED layer stacks (a). Associated HRXRD (0002) 2Θ-ω scans (b). 103

8.3. PL spectra at 10 K of the samples A_{HT}, B_{HT} and C_{HT} with different TMAl precursor fluxes during AlInGaN barrier growth and the reference LED (a). Schematic band diagrams for the reference LED with GaN barriers (red curve) and a sample with high-polaization AlInGaN barriers, illustrating the change in the emission energy (b). 105
8.4. I-V diode characteristic of processed sample A_{HT} and the reference sample (a) and photographs of fully processed LEDs at 5 mA drive current (b). 106
8.5. PL studies on samples with varying well and barrier thicknesses, given in the lower/upper corners. Pulsed laser excitation at 300 K, λ_{exc} =337 nm, τ = 10 ns, f = 1kHz. 107
8.6. Photographs of fully processed LEDs with different well thicknesses. All samples have AlInGaN barriers with a thickness of 5.6 nm. 108

9.1. Juxtaposition of the conventional p-up and n-down LED and the inversed p-down and n-up LED. For 2DHG formation in the inversed stack, a backbarrier is used below the p-down GaN. 110
9.2. Schematic band diagrams of a simplified single InGaN quantum well under forward bias condition for the conventional LED and the inversed pn-junction LED. 111
9.3. Simulation of an inverted p-n junction LED with AlInGaN backbarrier for 2DHG formation. Different doping levels for the AlInGaN is shown here. The dotted curves represent holes and the dashed curves represent electrons. 112
9.4. Schematic cross section of the layer stack used for the inversed LEDs (a). Associated HRXRD (0002) 2Θ-ω scan (black) and simulation (red) (b). 113
9.5. PL spectra of the inversed LED sample series with Mg-doped GaN barriers in the MQW (a). Associated simulated banddiagrams. 114
9.6. Electroluminescence of an inversed LED. 115

List of tables

2.1. Structural parameters for the binary nitride alloys in the wurtzite phase. If not otherwise mentioned, taken from [87–89]. 8

4.1. MOVPE conditions and structural properties of AlInGaN layers grown either at varying reactor pressure P (samples P1, P2 and P3) or at varying $T_{Surface}$ (samples HT and LT). Published in [150]. 42
4.2. MOVPE conditions and structural properties of the T-series 1 with AlInGaN layers grown at varying $T_{Surface}$. 50
4.3. MOVPE conditions and structural properties of AlInGaN layers grown at different TMAl-to-TMGa molar flow ratios. The TMIn flux is constant at 31.5 µmol/min. $T_{Surface}$ and reactor pressure are equal for all samples with values of 815°C and 70 hPa, respectively. 54

5.1. MOVPE conditions and structural properties of AlInGaN layers grown with either different TMGa flux or at varying $T_{Surface}$ on both GaN (G1 to G5) and AlN (A1 to A5). Reactor pressure P is equal for all samples at 70 hPa. 60

6.1. Growth surface temperature $T_{Surface}$, AlInGaN composition, thickness t_{bar}, bandgap E_g, theoretical and measured values of the electron density $n_{s,calc./meas.}$ as well as the measured mobility μ for samples T1-T5 in the T-series 1. The bandgap values marked with * are determined by SE. For samples with the bandgap of the barrier smaller than the one of GaN, the measured $n_{s,measured}$ and mobility μ values marked with *. Here, no 2DEG is formed. 68
6.2. Growth surface temperature T_S, TMAl-to-TMGa molar flow ratio, AlInGaN composition and bandgap E_g for the T-series 2 and the F-series (F for flow). Additionally, theoretical and measured values of the electron density n_s and the measured mobility μ in the 2DEG are given. 71
6.3. Electrical and structural properties of the low-polarization HFET A and B [242]. 76

6.4. Electron density, mobility and sheet resistance measured by Hall and van der Pauw for the as-grown HFETs. 79

7.1. MOVPE conditions, structural and electrical properties of 2DHG stack samples with AlInGaN backbarriers grown at different TMAl-to-TMGa molar ratios. 89

8.1. MOVPE conditions and structural properties of LED samples with AlInGaN barriers grown with different TMAl flows. 105

List of abbreviations

$\chi_{\text{RBS,min}}$ . . . . RBS channeling value

E_{gap} . . . . bandgap

I_D . . . . drain current

$I_{exc.}$ . . . . excitation intensity

P_{piezo} . . . . piezoelectric polarization

P_{spon} . . . . spontaneous polarization

P_{total} . . . . total polarization

R_{Sheet} . . . . sheet resistance

$T_{S,barrier}$ . . . . barrier growth surface temperature

$T_{S,well}$ . . . . well growth surface temperature

T_{Set} . . . . process set temperature

$T_{Surface}$ . . . . growth surface temperature

V_{bd} . . . . breakdown voltage

V_{th} . . . . threshold voltage

ΔP . . . . polarization difference

ε_{xx} . . . . in-plane strain

f_t . . . . transit frequency

f_{max} . . . . maximum oscillation frequency

g_m . . . . transconductance

n_s . . . . sheet electron density

p_s . . . . sheet hole density

2DEG . . . . two-dimensional electron gas

2DHG . . . . two-dimensional hole gas

AFM . . . . atomic force microscope

CCS . . . . close-coupled showerhead

DHFET . . . . double heterostructure field effect transistor

DMGa . . . . dimethylgallium

EBL . . . . electron blocking layer

EL . . . . electroluminescence

ELOG . . . . epitaxial lateral overgrowth

FWHM . . . . full width at half maximum

H_2 . . . . hydrogen

HEMT . . . . high electron mobility transistor

HFET . . . . heterostructure field effect transistor

HRXRD . . . . high-resolution X-ray diffraction

JFoM . . . . Johnson figure of merit

LD . . . . laser diode

LED . . . . light emitting diode

MBE . . . . molecular beam epitaxy

MESFET . . . . metal semiconductor field effect transistor

MMGa . . . . monomethylgallium

MOCVD . . . . metal-organic chemical vapor deposition

MODFET . . . . modulation-doped field effect transistor

MOVPE . . . . metal-organic vapor phase epitaxy

MQW . . . . multiple quantum well

MRD . . . . material research diffractometer

N_2 . . . . nitrogen

NH_3 . . . . ammonia

OMVPE . . . . organo-metallic vapor phase epitaxy

PL . . . . photoluminescence

QCSE . . . . quantum-confined Stark effect

RBS . . . . Rutherford backscattering spectroscopy

RF . . . . radio frequency

RSM . . . . reciprocal space mapping

SE . . . . spectroscopic ellipsometry

SIMS . . . . secondary ion mass spectroscopy

TEGa . . . . triethylgallium

TMAl . . . . trimethylaluminum

TMGa . . . . trimethylgallium

TMIn . . . . trimethylindium

uid . . . . unintentionally doped

XRD . . . . X-ray diffraction

YL . . . . yellow luminescence

Acknowledgements/Danksagung

Ich möchte mich bei allen Personen bedanken, die mich bei der Anfertigung dieser Arbeit unterstützt und motiviert haben.

- Herrn Prof. Dr.-Ing. Andrei Vescan, der mir die Möglichkeit gegeben hat, am Lehr- und Forschungsgebiet GaN-Bauelementtechnologie zu promovieren. Insbesondere möchte ich mich für die Freiheit bedanken, mit der ich meinen eigenen Ideen folgen konnte.

- Herrn Prof. Dr. rer. nat. Ferdinand Scholz für die Übernahme des zweiten Gutachtens.

- Herrn Prof. Dr.-Ing. Michael Heuken für die stetige Begleitung meiner Forschungsarbeit.

- Herrn Prof. Dr. sc. techn. Renato Negra für eine angenehme Prüfungsatmosphäre.

- Herrn Dr. rer. nat. Holger Kalisch für die fachliche Diskussion von Ergebnissen und die ausdauernden Korrekturen meiner Veröffentlichungen.

- Herrn Dr.-Ing. Herwig Hahn für die herausragend gute Zusammenarbeit und die entstandene tiefe Freundschaft.

- Mr. Justin Payne for the personal relationship marked by profound friendship and cooperation.

- Herrn M.Sc. Matthias Finken und Frau M.Sc. Ada Wille für die stets gute Arbeitsatmosphäre im Büro und die Zusammenarbeit am „GaNdalf“.

- Herrn Dipl.-Phys. Frank Jessen für praktische Tipps im Labor und seine Unterstützung im Bereich der Technologie.

- Herrn Gerrit Kuivenhofen für seine große Hilfsbereitschaft in allen technischen Belangen.

- Herrn Dr. rer. nat. Bernd Holländer vom Forschungszentrum Jülich für viele Messungen und deren Analyse, aber auch für die netten Gespräche.
- Frau Gabriele Nogueira-Glenski und Frau Sonja Buchholz-Trappe für ihre Unterstützung im Bereich der Lithographie, vor allem aber für die freundschaftlichen Gespräche.
- Frau Marita Söhndel für ihre Unterstützung bei allen organisatorischen Fragen.
- Allen weiteren wissenschaftlichen Mitarbeitern und Studenten bei GaNBET für die tolle Arbeitsatmosphäre während meiner Zeit am Institut.
- Allen Mitarbeiten von Kooperationspartnern (AIXTRON SE, Forschungszentrum Jülich, JARA-FIT, SIMAERA Shanghai).

Außerordentlicher Dank richtet sich an meine Familie. Nur durch den stetigen Zuspruch und die unermüdliche Unterstützung meiner Frau, Dipl.-Math. Anke Reuters, konnte ich diese Arbeit fertig stellen. Ich bin ihr sehr dankbar für die Geburt meiner beiden gesunden Kinder während meiner Promotionszeit.
Besonderer Dank gebührt meinen Eltern, die mir durch ihre ausdauernde Unterstützung mein Studium erst ermöglichten. Nur aufgrund ihrer Erziehung zum freien Denken war es mir möglich, meine Promotion erfolgreich zu meistern.